POINT TARGET INTERFEROMETRY AS APPLIED TO THE CHARACTERIZATION OF LOCALIZED DEFORMATION FEATURES

A Dissertation presented to the Faculty of the Graduate School
University of Missouri – Columbia

In Partial Fulfillment
Of the Requirements for the Degree

Doctor of Philosophy

---

by

DEEPAK MANJUNATH

Dr. Brent Rosenblad, Dissertation Supervisor

MAY 2008

The undersigned, appointed by the Dean of the Graduate School,
Have examined the dissertation entitled

POINT TARGET INTERFEROMETRY AS APPLIED TO THE CHARACTERIZATION OF LOCALIZED DEFORMATION FEATURES

Presented by Deepak Manjunath

A candidate for the degree of Doctor of Philosophy in Civil Engineering

And hereby certify that in their opinion it is worthy of acceptance.

_____
Professor Brent L. Rosenblad

_____
Professor John J. Bowders Jr.

_____
Professor Erik J. Loehr

_____
Professor Francisco Gomez

_____
Professor Justin J. Legarsky

OM SAI RAM

ACKNOWLEDGEMENTS

I owe thanks to a lot of people for enabling me realize this dream. First and foremost, I thank my family for being supportive and for being patient with me all the way. A lot of thanks also goes to my fiance', Indrani Tulasi, who always encouraged me to pursue my interests. I would like to express deep gratitude to Dr. Eric Sandvol and Kristin Sandvol for giving me the opportunity that opened up avenues for pursuing this degree. Paco Gomez, has been a great mentor and friend. I thank him for his time, patience, guidance, for encouraging me to think creatively and for all the conversations over coffee.

The Geotechnical Engineering program has been instrumental in instilling virtues of commitment, dedication and hard work in me. The ever-enthusiastic and supportive trio of Dr. Bowders, Dr. Loehr and Dr. Rosenblad, have always been encouraging and have always had their doors open for discussion.

I consider myself fortunate to have been in the company of excellent human beings who have made my stay at the University of Missouri, Columbia memorable.

TABLE OF CONTENTS

LIST OF FIGURES

LIST OF TABLES

ABSTRACT

Monitoring of ground deformation is a critical component of geotechnical engineering practice. This study investigated the application of synthetic aperture radar interferometry (InSAR) using point target analysis (IPTA) for detecting and characterizing localized deformation features that are often associated with geotechnical engineering activities. In contrast to discrete point in-situ deformation measurement techniques, InSAR can be used to obtain a broader view of deformation processes at a site.

The objectives of this research were to (1) evaluate the feasibility of using IPTA to detect localized deformation features, (2) investigate the influence of SAR data characteristics on the ability to successfully apply IPTA processing and (3) quantify the dependence of the IPTA-derived deformation estimates on the number of SAR acquisitions used to constrain the analysis. To address these objectives, 52 SAR scenes acquired over Los Angeles, CA, during construction of the Los Angeles Metro Rail Red Line between 1992 and 2000 were used. This site was chosen due to the availability of extensive SAR data and the known occurrence of localized settlements along the Red Line alignment during construction.

Results from IPTA processing of the complete dataset successfully demonstrated the ability to detect the localized deformations associated with the subway construction. Deformation time histories for points along the Red Line alignment exhibited episodic settlements that were not observed for points located away from the alignment.

To address the second objective of this study, IPTA processing was applied to subsets of the 52 SAR acquisitions available for the site. The number of interferometric pairs required for successfully applying point target analysis without patch errors was found to range between 20 and 25. The average baseline of interferograms constituting a dataset was hypothesized to have a dominant influence on the ability to successfully apply IPTA processing to a dataset. However, no clear baseline dependence was identified.

To address the third objective, the variability of the estimated rate of deformation was estimated using the standard deviation from one thousand runs of the IPTA analysis as applied to datasets of varying sizes. Irrespective of the deformation rate of a point target, the variability of the estimated deformation rates was found to vary inversely with the size of the dataset used to constrain the analysis. In addition, the coefficient of variation of deformation rates was observed to decrease with an increase in the size of the dataset used for analysis. Irrespective of the deformation rate of a point target, both the mean and the standard deviation of the associated uncertainty (U_G) was observed to decrease with an increase in the size of the dataset used for IPTA analysis.

1. INTRODUCTION

1.1 Introduction

Monitoring of ground deformation is a critical component of geotechnical engineering practice. Examples of ground deformation problems include deformation induced by earth pressure on retaining structures, settlement due to consolidation of soil, and settlements during construction of underground facilities.

Current in-situ deformation measuring techniques are performed at discrete points of interest at a site. Although this method provides the ability to monitor specific points of interest at a site, supplementing such information with a broader image of the overall deformation process, affecting the site as a whole would be extremely valuable. However, doing this with current in-situ monitoring techniques would prove to be strategically as well as economically unfeasible.

Initially used to infer earthquake induced deformation, Synthetic Aperture Radar interferometry (InSAR) is a remote sensing technique that enables the derivation of spatially continuous deformation fields. Satellite imagery acquired before and after a deformation event can be quantitatively manipulated to discern regions in the satellite image that deformed between the two acquisitions. The resolution of the satellite imagery used in deriving such deformation fields controls the fineness of detail achievable from InSAR. In addition, the technique is attractive since it provides the option of using satellite imagery acquired in the past for interferometric calculations. This enables the assessment of the

deformation history for a site despite not having in-situ instrument monitoring deformations during the time of interest. The spatial separation between the satellite positions during the times of the before and after image acquisitions, referred to as the baseline, combined with the prevailing topographic relief, dictates the quality of the computed deformation field for a site of interest. The use of large baseline acquisitions to perform interferometry, results in low quality deformation fields that can be difficult to interpret.

To overcome these short-comings, an approach called Interferometric Point Target Analysis (IPTA), confines the computational processing characteristic of InSAR to only those pixels in the satellite imagery with scattering properties that are temporally stable. Point target information can be used to discern deformation fields even for image pairs acquired from spatial positions of the satellite defining large baselines. Temporal stability of scattering properties ensures the quality of information derived from the stable scattering pixels over time and enables the computation of a reliable temporal deformation history.

1.2 Motivation

The IPTA method has not been extensively studied for application to detect small spatial-scale deformation features that are common in civil engineering practice. The advantages provided by IPTA over conventional InSAR, make it an attractive option to quantify the deformation history of a site. IPTA analysis relies on having sufficient information in terms of the number of satellite images available for analysis. However, the number of satellite acquisitions available for a study area can be variable depending on factors

beyond the control of the user. In circumstances where IPTA is useful to infer important deformation information, knowledge of the affect of the number of images used in the analysis on the reliability of the derived deformation estimates is crucial. One way to study such dependencies is to analyze a site for which plenty of satellite imagery is available. Comparison of deformation histories obtained by processing subsets of data having varying numbers of the available satellite imagery can provide useful insights into the influence of the number of images used in the analysis on the deformation estimates derived using IPTA. The availability of fifty-two satellite images, acquired between 1992 and 2000, which bracket the construction period of underground tunnels for the Los Angeles Redline, made this an ideal site for this study.

1.3 Objectives

The following three research objectives were identified for this study:

1. Evaluate the feasibility of using IPTA to detect small spatial-scale deformation features by computing the deformation time histories resulting from the construction of the Red Line in Los Angeles,
2. Investigate the influence of dataset characteristics on the application of the conventional IPTA processing flow, and
3. Quantify the dependence of the IPTA-derived deformation time history on the number of satellite acquisitions used to constrain the analysis.

With respect to the second objective, it was hypothesized that the average perpendicular baseline calculated from all interferograms constituting a dataset, would influence the ability to successfully apply the IPTA processing flow.

1.4 Organization of Thesis

This manuscript is divided into a total of six chapters inclusive of the current chapter. Details of the adopted technique and specifics of the study designed to achieve the objectives are presented in the five chapters that follow.

The concept of the Synthetic Aperture Radar (SAR) and details pertaining to how ground deformation can be determined using SAR data are presented in the second chapter. In addition, a brief history of the development of the technique and a summary of currently operating SAR systems is provided. Mathematical expressions relating important SAR parameters are presented to enhance understanding of the technique.

The third chapter builds on the information provided in the second chapter and presents details pertaining to the Interferometric Point Target Analysis (IPTA). A literature review summarizing the development of the technique and its applications to non-tectonic problems is presented.

The fourth chapter provides the data and methods adopted to accomplish the three objectives of this study. Specifics regarding the satellite imagery used and IPTA processing flow adopted are provided.

Results obtained from the study and a detailed discussion of the results is presented in the fifth chapter. The sixth chapter presents conclusions derived from this study and recommendations for future work.

2. BACKGROUND

2.1 Introduction

This chapter introduces the concepts relating to Synthetic Aperture Radar (SAR) and the technique of interferometry as applied to SAR data. A brief history pertaining to the development of SAR is presented. The general processing flow used to perform interferometric calculations, with details pertaining to each step as reviewed from relevant literature, is also presented.

2.2 Overview of Synthetic Aperture Radar

The synthetic aperture radar concept, initially referred to as Doppler beam sharpening, is attributed to Carl Wiley who in 1951 made the observation that it was possible to use the difference in Doppler frequency shift induced by two distinct targets within a radar beam to improve the resolving power of the moving radar in the direction of its flight (Curlander and McDonough, 1991). The synthetic aperture radar, as it is known today, is a pulsed-radar that uses the forward motion of the platform carrying it in order to simulate an antenna with a larger aperture.

The antenna aperture can be defined as “the physical area of the antenna projected onto a plane perpendicular to the direction of the antenna beam” (Maini and Agrawal, 2007). The antenna beam is a channel of electromagnetic energy radiated by the antenna (Skolnik, 1962). Large apertures are necessary to achieve measurements characterized by high spatial resolution. A very large and

impractical real aperture antenna (RAR) would be required to match the resolution achievable using a SAR. Using SAR, the infeasibility of mounting a large real aperture radar on a moving platform (like aircrafts or satellites) is overcome by synthesizing a large antenna length from the forward motion of the antenna during imaging. In other words, during SAR data acquisition, an object on the ground is imaged from many different locations on the satellite's flight track.

During imaging, the component of electromagnetic energy reflected by objects on the ground back towards the antenna is called backscatter. The redundancy in information, obtained by recording the backscatter from the object when imaged from different perspectives, is then used to generate high resolution digital imagery. The resolution in a direction parallel to the motion of the SAR also referred to as the *azimuth*, is independent of the altitude of the sensor during imaging and can be expressed as approximately one-half the length of the imaging antenna (Jensen, 2000). A detailed derivation of the azimuth resolution as provided in Curlander and McDonough (1991) is presented in Section 2.2.4.2. As an illustration, an azimuth resolution of approximately 4 m can be achieved when data acquired by the 10-m long antenna mounted on board the European Remote Sensing satellites (ERS-1 and ERS-2) is processed.

Synthetic aperture radar interferometry (InSAR) is a remote sensing technique that can be used to derive high resolution deformation maps as well as topographic maps of an imaged area (Burgmann et al., 2000). In this study, the technique was used for deformation mapping. The technique can be applied

when at least two synthetic aperture radar (SAR) images of the same area on the ground, acquired from slightly different look angles, are available for analysis.

Electromagnetic radiations with frequencies ranging from 1-GHz to 300-GHz define the microwave region of the electromagnetic spectrum. Satellite-borne SAR systems operate in the 1-GHz to 10-GHz range of microwave frequencies and are classified according to the specific frequency bands they adopt for imaging. All SAR systems are active microwave remote sensing systems, meaning that the radar illuminates the target to be imaged with electromagnetic radiation with frequencies in the microwave region of the electromagnetic spectrum (Figure 2.1).

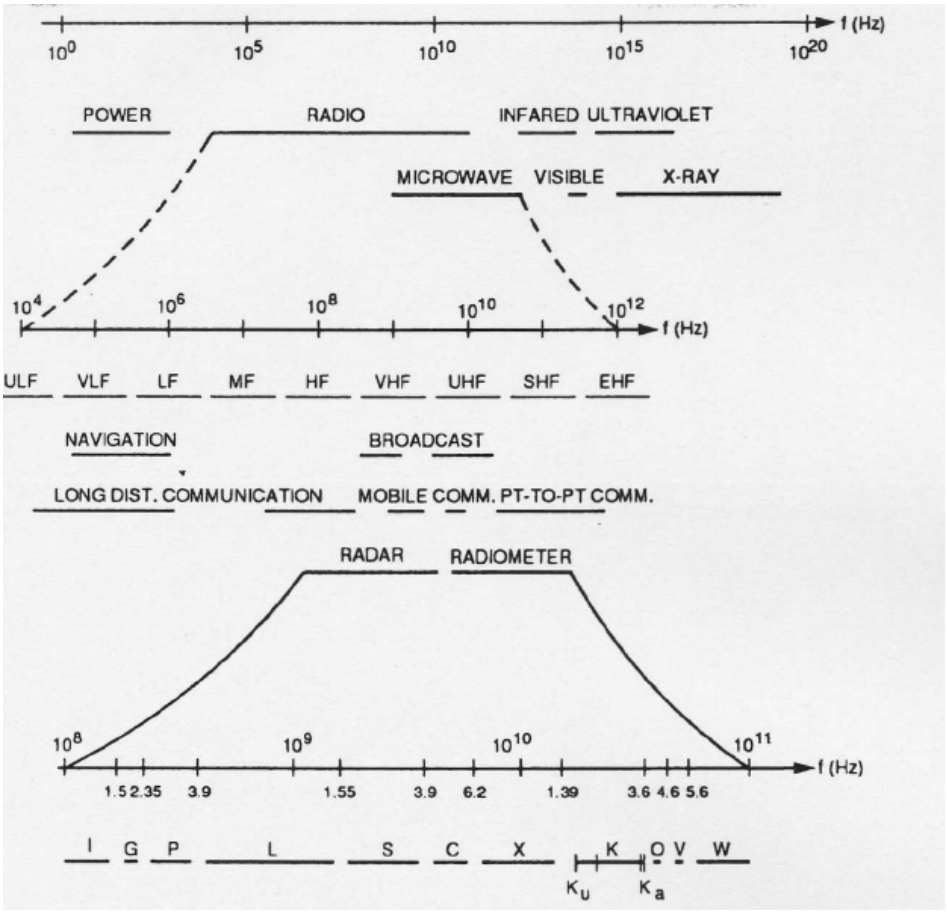

Figure 2.1 The electromagnetic spectrum (Curlander and McDonough, 1991)

Active remote sensing enables night-time data acquisition. In addition, the long wavelengths characteristic of microwave frequencies enable cloud penetration. Besides SAR system design issues, the primary factors influencing the choice of radar wavelengths employed by SAR systems include:

1. **Atmospheric transmission**: Figure 2.2, illustrates the capability of different wavelengths in the electromagnetic spectrum to penetrate the Earth's atmosphere. Higher transmission percentages represent greater penetration abilities. As can be inferred from Figure 2.2, radiation with wavelengths greater than that represented by the X-band (3 cm) can completely penetrate the earth's atmosphere.
2. **Scattering behavior induced by the radiation**: The amplitude of backscatter received from any imaged surface is a function of the wavelength of the incident electromagnetic energy. This will be explained in more detail in Section 2.2.3.
3. **Sensitivity to imaged topography and deformation:** In the case of interferometric applications, greater sensitivity to imaged topography can be achieved by using shorter wavelengths or by ensuring a bigger imaging baseline. This will be explained in more detail in Section 2.3.1.

Currently operational satellite-borne SAR systems operate in one of the following microwave frequency bands:

1. X band – with a wavelength of 3 cm or a frequency of 10 GHz,
2. C band – with a wavelength of 5.6 cm or a frequency of 5.3 GHz, and
3. L band – with a wavelength of 24 cm or a frequency of 1.3 GHz.

Short wavelengths (X-band and C-band) induce a higher sensitivity to deformation but cannot penetrate vegetation and snow cover. On the other hand, SAR systems imaging with larger wavelengths (L-band) are relatively less

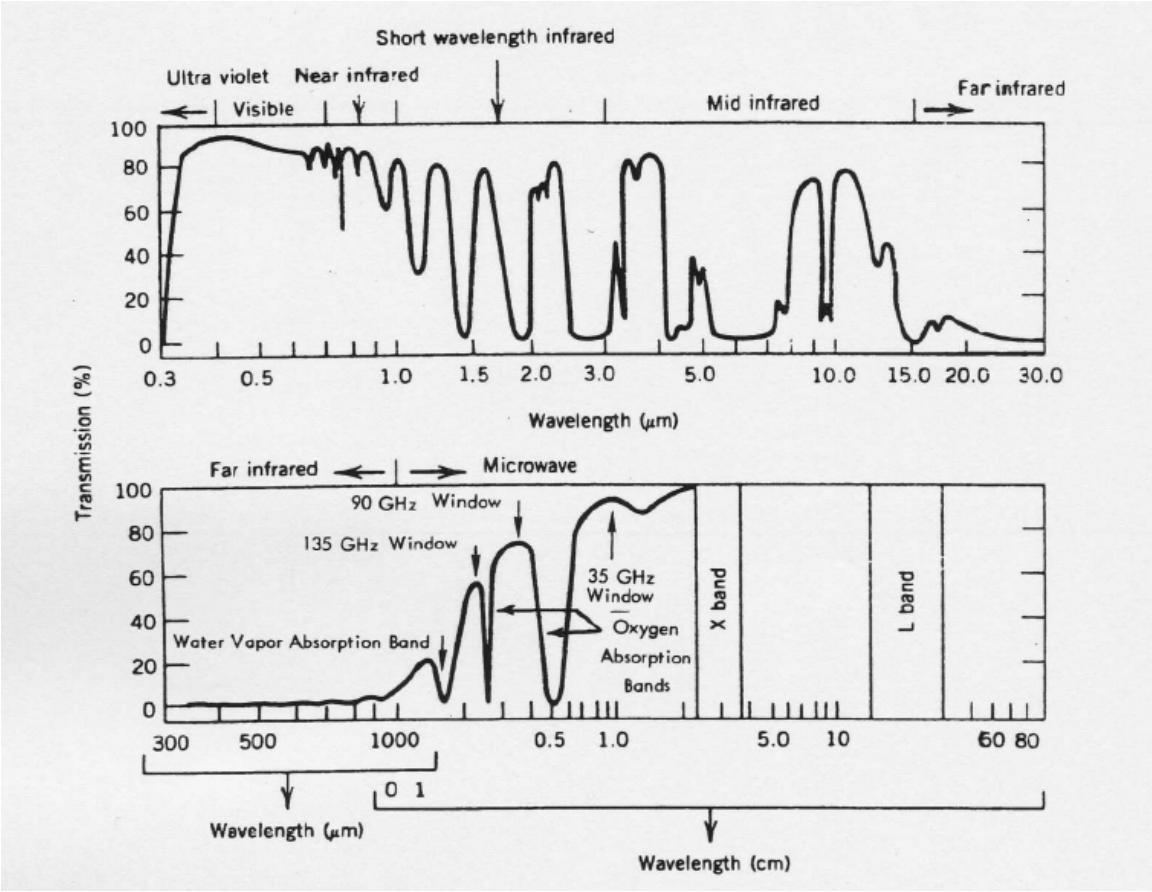

Figure 2.2 Atmospheric transmission as a function of radiation wavelength (Curlander and McDonough, 1991)

sensitive to deformation but have the ability to penetrate vegetation and snow cover.

2.2.1 SAR Imaging modes

SAR systems are capable of imaging in different modes. Some of the common imaging modes include:

1. Strip-map mode,
2. Burst mode,
3. Scan SAR mode,
4. Spot light mode, and
5. Polarimetric mode.

Strip-map mode: Imagery in this mode of operation is obtained by an antenna that maintains a constant inclination of its *look vector* relative to the direction of flight. The vector defining the slant range direction, as shown in Figure 2.3, is known as the look vector. High-resolution imagery can be processed from raw data acquired from the strip map mode by using backscatter information of an object that is available for the time period during which the object remained in the field of illumination of the radar (Chang et al., 1996).

Burst mode: Imagery in this mode of operation is acquired by recording the backscatter of a group of pulses that are transmitted in regular bursts. Imagery obtained in this mode has lower azimuth resolutions than are achievable from the strip-map mode. The burst mode was used by Magellan to image the surface of Venus (Chang et al., 1996).

Scan SAR mode: This mode of operation enables wide swath data acquisition. The swath is illustrated in Figure 2.3 and defines the width of the footprint imaged by the SAR. Data for each sub-swath is obtained in the burst mode thus resulting in lower azimuth resolution (Chang et al., 1996).

Spotlight mode: Data acquired in this mode of operation is characterized by an azimuth resolution greater than that attainable from the strip map imaging mode.

The higher resolution is a result of longer object illumination times made possible by electronically steering the radar beam in the direction of the area of interest. In other words, increasing the illumination time for a target synthesizes an antenna length that is longer than that which can be synthesized in the strip-map mode. It should, however, be noted that increased azimuth resolution achievable in this mode comes at the cost of spatial coverage since extended illumination time can be achieved for only specific sections of the traditional SAR data frame (Canada Center for Remote Sensing, 2005).

Polarimetric mode: In this mode of operation, data is acquired by emitting and receiving electromagnetic radiation that is polarized in either the horizontal or the vertical plane or both. A fully polarimetric system emits and receives radiation polarized in both directions hence making it possible to obtain full polarimetric information about the imaged surface hence enabling comprehensive quantification of its scattering properties. On the other hand, dual polarization systems are those in which the transmitted radiation is polarized in one direction whereas radiation polarized in both orthogonal components are received. The dual polarization imaging mode is also referred to as the compact imaging mode (Ainsworth et al., 2007). Complete polarization information of the imaged surface cannot be acquired from dual polarization data.

2.2.2 Satellite-based SAR Systems

Synthetic Aperture Radars (SAR's) used to acquire data for interferometry are usually mounted on either satellite or airborne platforms. Data used in this study

was acquired by satellite-based SAR systems, a brief overview of which is provided in this section. Some examples of satellite borne SAR systems include

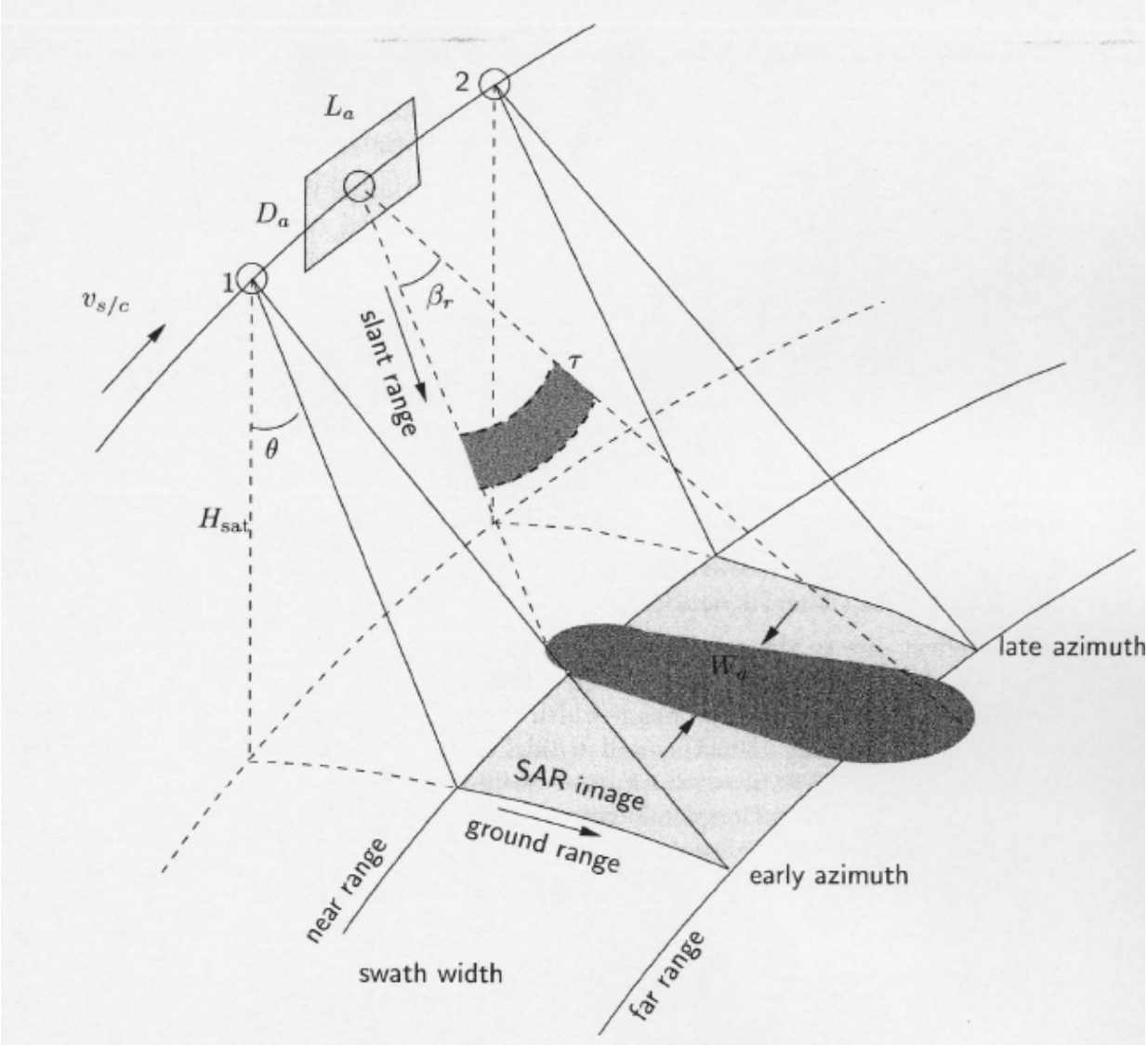

Figure 2.3 SAR imaging geometry (Hanssen, 2001).

Seasat, SIR-A/B/C, X-SAR, ERS-1/2, Envisat, JERS-1, RADARSAT-1/2, and TerraSAR-X.

The Seasat system, operating in the L-band of microwave frequencies was launched by the United States of America (USA) in 1978 to facilitate ocean

studies (Curlander and McDonough, 1991; Hanssen, 2001). Operations of the Seasat system were managed by the National Aeronautics and Space Administration's (NASA) Jet Propulsion Lab (JPL). Launching of the Shuttle Imaging Radar–A (SIR-A) in 1981 was followed by SIR-B that was launched in 1984. Both the SIR satellites were launched by the USA and operated in the L-band. While data acquired from the SIR-A was optically processed, the data acquired from SIR-B was subjected to digital processing (Curlander and McDonough, 1991). Polarimetric data was made available following the launch of the SIR-C and X-SAR missions in 1994 with the uniqueness that data were available in three frequency bands namely, L-band, C-band, and X–band respectively (Curlander and McDonough, 1991; Hanssen, 2001).

The European Remote Sensing Satellite (ERS-1) was launched by the European Space Agency in 1991 and remained in orbit until March 2000. The ERS-2 was launched in April, 1995 and was similar to the ERS-1. From August 1995 to May 1996, the ERS-2 followed the ERS-1 on the same orbit making it possible to acquire imagery temporally spaced one day apart (Ferretti et al., 2007). Such image pairs are also referred to as tandem pairs. Both ERS satellites operate in the C band. The launch of ERS-1 was followed by the launch of Japanese Earth Resources satellite (JERS-1) in 1992 which remained in orbit until October 1998 and operated in the L-band (Hanssen, 2001). RADARSAT-1 was developed and launched by Canada on November 4, 1995 and was primarily intended for earth observation. The Envisat system was launched by the European Space Agency (ESA) in 2002 and carried an Advanced Synthetic

Aperture Radar (ASAR) operating in the C-band. The ASAR is a versatile instrument that is capable of operating in different image acquisition modes besides being capable of acquiring imagery in different polarizations and steering the radar beam over a range of off-nadir angles (Ferretti et al., 2007).

The TerraSAR–X, launched on June 15, 2007 carries a SAR operating in the X-band. The TerraSAR-X was developed jointly by the German Aerospace Center and European Aeronautic Defence and Space Company. The satellite is capable of operating in Spotlight (1-m resolution), Strip map (3-m resolution) and ScanSAR (16-m resolution) modes (Infoterra, 2007). Specifications of some satellite-borne SAR systems are provided in Table 2.1. The repeat cycle defines the time period between successive visits by the satellite to image the same site on the ground. The operating frequency defining a mission is directly related to the wavelength of microwave radiation used for imaging.

Table 2.1 Specifications of some satellite-borne SAR systems

Mission	**Launched** (year)	**Repeat Cycle** (days)	**Satellite Altitude** (km)	**Frequency** (GHz)	**Bandwidth** (MHz)	**Look Angle** (degrees)
ERS-1	1991	35	790	5.3	15.55	23
ERS-2	1995	35	790	5.3	15.55	23
JERS-1	1992	44	568	1.275	15	39
Radarsat-1	1995	24	792	5.3	11-30	20-49
ENVISAT	2001	35	800	5.3	14	20-50
ALOS	2002	45	700	1.27	28	8-60
TerraSAR-X	2007	11	514	10	150	~35

(Hanssen, 2001 and Eineder et al., 2004)

A detailed description of the relationship between the bandwidth and range resolution is provided in Section 2.2.4.1. The look angle (θ) in Table 2.1 is the

look angle at the center of the swath. The look angle and swath width are illustrated in Figure 2.3.

2.2.3 SAR Data Acquisition

During data acquisition, the SAR transmits electromagnetic waves with microwave frequencies ranging from 1 GHz – 10 GHz towards the earth and records the magnitude and phase of the fraction of the incident energy reflected back towards the satellite. Such systems recording both the amplitude and phase of the reflected energy or echoes are known as coherent imaging systems (Curlander and McDonough, 1991). During data acquisition, the SAR is pointed towards the earth in a plane that is orthogonal to the direction of flight of the platform carrying it. The angle made by the radar look vector with respect to the vertical is known as the off-nadir angle or the look angle and gives rise to the side looking geometry of the SAR during data acquisition, as illustrated in Figure 2.3.

The SAR images a particular object on the ground from several different locations during the satellite's orbit. For example, an object on the ground is typically imaged from around 1000 different locations in the orbit of the ERS-1 (ESA, 2007). These various responses are then digitally processed in order to assign the object a distinct amplitude and phase. The distance on the satellite's trajectory defining the time period during which an object on the ground begins and stops being imaged or detected by the SAR is known as the length of the synthesized aperture. As an example, the 10-m long imaging radar mounted on the ERS-1 images objects on the ground for a distance of 4 km during its orbit. In

other words, the ERS-1 synthesizes the resolution achievable with a 4-km long antenna using an antenna that is only 10-m long (ESA, 2007). As mentioned before, this results in an azimuth resolution of approximately 4 m.

An image of the radar footprint in side-looking geometry can be constructed by similar processing of the acquired raw data. The processed SAR image is composed of several evenly spaced pixels. Each pixel denotes the information corresponding to a *ground resolution cell* (Hanssen, 2001). A ground resolution cell, whose dimensions are defined by the ground range resolution and ground azimuth resolution of a SAR system, can be defined as the area on the ground that corresponds to a single pixel as mapped in a SAR image. The electromagnetic radiation reflected towards the SAR system from all elements located within a ground resolution cell (e.g. buildings, roads, etc.), contributes to the backscatter that is associated with the pixel representing the ground resolution cell in the SAR image. SAR data resolution is discussed in more detail in Section 2.2.4.

The data corresponding to each pixel in a SAR image can be represented as a complex number having amplitude and phase. Resolution cells characterized with high amplitudes of backscatter show up as bright pixels on the processed SAR image whereas those with low backscatter are characterized by darker colors. Due to details pertaining to the process in which raw SAR data are processed into a SAR image and owing to the complex number representation of data for each pixel in the SAR image, the processed SAR image is often referred to as a *Single Look Complex* (SLC) image.

The amplitude of a pixel is a function of its overall “roughness”. Rough surfaces reflect more of the incident electromagnetic energy back to the radar resulting in high amplitudes whereas smooth surfaces reflect the incident energy in a direction away from the satellite and result in low amplitudes. The perception of roughness by a satellite depends on the relation between the wavelength of the radiation used by the radar and the root-mean-square (RMS) height of the surface being imaged. Surfaces having a RMS height of the same order as the radar wavelength reflect most of the incident energy back in the direction of the radar and are hence perceived as rough surfaces. On the other hand, surfaces having RMS heights less than the wavelength of the incident radiation behave as smooth surfaces.

Besides roughness, the backscatter corresponding to a pixel is also influenced by the angle of incidence of the radar beam. The relationship between the backscattering coefficient and the angle of incidence of the radar beam for different frequencies in the microwave region of the electromagnetic spectrum is shown in Figure 2.4 (Curlander and McDonough, 1991).

The *differential path delay phase* of a scattering element in a SAR image resolution cell represents the change in phase between the transmitted and received signals due to the time taken by the signal to traverse the two-way distance between the satellite and the element on the ground. The mathematical expression for the differential path delay phase (ϕ) of an elemental scatterer within a resolution cell is:

$$\phi = -\frac{2\pi}{\lambda}(2R) = -\frac{4\pi}{\lambda}R, \qquad (2.1)$$

where, 2R represents the round trip distance traversed by the pulse emitted by the SAR (with R denoting the slant range) and λ represents the wavelength of the radiation. The negative sign accounts for the change in phase of echoes received from a scatterer being inversely related to the change in range to the scatterer

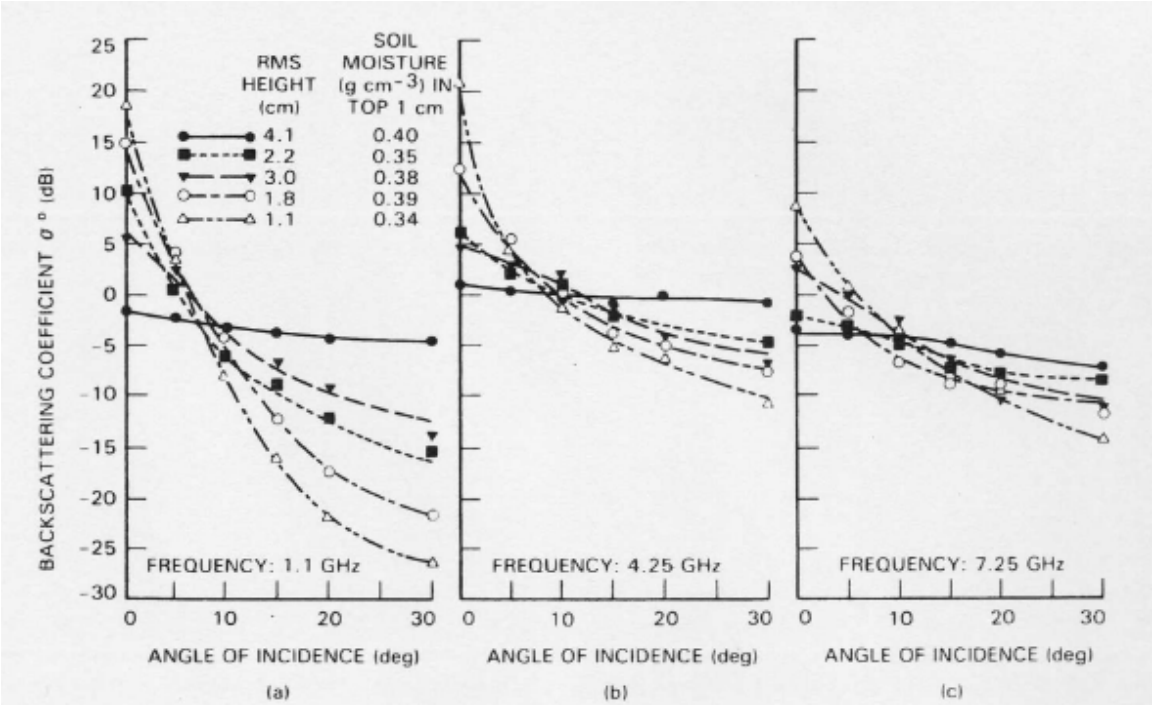

Figure 2.4 Relationship between backscatter coefficient, angle of incidence and frequency of electromagnetic radiation (Curlander and McDonough, 1991).

(Hanssen, 2001). In other words, during imaging, a decreasing range to a scatterer on the ground results in a positive frequency shift of the echoes received from the target, whereas an increasing range to a scatterer results in a negative frequency shift. This principle known as the *Doppler frequency shift* is exploited to increase the azimuth resolution in SAR images. More details on this principle and how it is applied are provided in Section 2.2.4.2. It can be inferred

from Eq. 2.1, that the propagation phase of a scatterer within a pixel is directly proportional to its slant range distance.

However, due to the periodic nature of the emitted pulse, similar phase values are recorded for all scatterers located at distances of integer multiples of the wavelength from the satellite. Hence, the true phase representing a scatterer is encrypted within the range of phase values representing one whole wavelength of the emitted pulse. In other words the phase is *wrapped* between $-\pi$ and $+\pi$. The amplitude and phase recorded for a scatterer during SAR data acquisition can be represented as a *phasor*. A phasor is a vector representation of a complex number where the length of the vector represents the amplitude and the angle describing the vectors orientation represents the phase. The complex phasor representing each element within the cell has components corresponding to *backscatter phase* and *differential path delay phase.* The scattering mechanism of each elemental scatterer contributes to the backscatter phase associated with it (Hanssen, 2001). The slant-range distance, which defines the differential path delay phase, is measured with respect to a reference surface oriented in a direction normal to the radar look direction (Rosen et al., 2000).

A ground resolution cell, whose dimension depends on the imaging radar specifications, is composed of several elemental scatterers. During SAR image acquisition, each elemental scatterer located within a ground resolution cell, reflects some of the incident electromagnetic signal back towards the SAR antenna. Hence, each elemental scatterer can be associated with backscatter

phase and differential path delay phase components in addition to amplitude. The complex phasor corresponding to the pixel representing such a ground resolution cell in a SAR image is derived by the coherent summation of complex phasors representing each elemental scatterer within that cell. Coherent summation is a vector summation operation where each individual vector being summed represents the complex phasor corresponding to the respective elemental scatterer within the ground resolution cell under consideration (ESA, 2007).

2.2.4 SAR Data Resolution

The resolution of conventional real aperture radar (RAR) systems is a function of the *angular resolution* of the radar beam and its altitude of operation. The angular resolution is inversely proportional to the length of the antenna aperture. Hence, high operating altitudes will need to be compensated by long antenna apertures to preserve the resolution of such systems. However, desired resolutions would entail impractically long antennas (several kilometers) to be mounted on imaging platforms. As previously mentioned, this shortcoming is overcome by synthesizing a long antenna aperture by moving the imaging radar in the along-track or flight direction while simultaneously imaging in the range. SAR systems resolve objects in two directions, namely the *range* and the *azimuth*. The direction perpendicular to the along-track/flight direction and parallel to the radar look direction is called the range. The along-track/flight direction determines the azimuth (Figure 2.3). Factors governing SAR image resolutions in both these directions are discussed in the following sections.

2.2.4.1 Range Resolution

Pulse travel times to and from points on the ground are used to resolve their location in the range direction. In addition, range resolution is a function of *pulse width* or the time period of the pulse. Shorter pulse widths result in increased range resolution. The *slant range resolution* (Δr) of a SAR can be expressed as:

$$\Delta r = \frac{c\tau}{2}, \tag{2.2}$$

where c is the velocity of light (3 x 10^8 m/sec) and τ is the pulse width. The pulse width is inversely proportional to the radar bandwidth and can be expressed as:

$$\tau = \frac{1}{B}, \tag{2.3}$$

where B is the *radar bandwidth*. From Eq. 2.2, it is evident that the slant range resolution is independent of the altitude of the satellite during data acquisition. However, shortening of pulse widths results in a decrease in its energy thus affecting the strength of backscatter or amplitude. Therefore, it is not feasible to reduce pulse widths below typical lower-bounds. *Pulse or chirp compression* is a procedure that is used to reduce the effective pulse width, thus increasing the resolution of SAR data. For an ERS sensor, pulse compression is used to reduce the pulse width from from 37.1 μs to 64 ns, thereby increasing the ground range resolution from 5.5 km to approximately 25 m (Curlander and McDonough, 1991; Hanssen, 2001).

2.2.4.2 Azimuth Resolution

Typically, the ability to resolve any two targets in the azimuth direction depends on the fineness of the beam in the horizontal direction. The angular resolution of the beam in the horizontal direction (θ_h) can be expressed as

$$\theta_h = \frac{\lambda}{L_a}, \tag{2.4}$$

where λ is the wavelength of the radiation and L_a is the length of the radar antenna. Conventionally, the locations of any two targets located within the radar beam cannot be resolved by the radar hence limiting the achievable azimuth resolution. The azimuth resolution (Δx) in such cases can be expressed as:

$$\Delta x = \frac{\lambda R}{L_a}, \tag{2.5}$$

where R denotes the slant range to the target. SAR systems overcome this limitation by using the Doppler frequency shift principle to resolve the locations of targets even when they are illuminated by the radar beam simultaneously.

The Doppler shift technique, first proposed by Carl Wiley and referred to as Doppler beam sharpening, forms the basis for high azimuth resolution that can be synthesized from SAR data (Curlander and McDonough, 1991). Due to the fineness of the radar beam, any two targets illuminated by the radar beam simultaneously can be assumed to be located at the same slant range. The degree of fineness of radar beams is representative of the angular resolution that can be achieved. Greater fineness makes greater angular resolution achievable. The *Doppler Effect* is the phenomena that results in the observation of an increase or decrease in frequency of radar echoes received from targets

illuminated by the radar beam. This frequency change results from the relative motion between the satellite and the target and can be observed for the time period during which a target is illuminated by the radar.

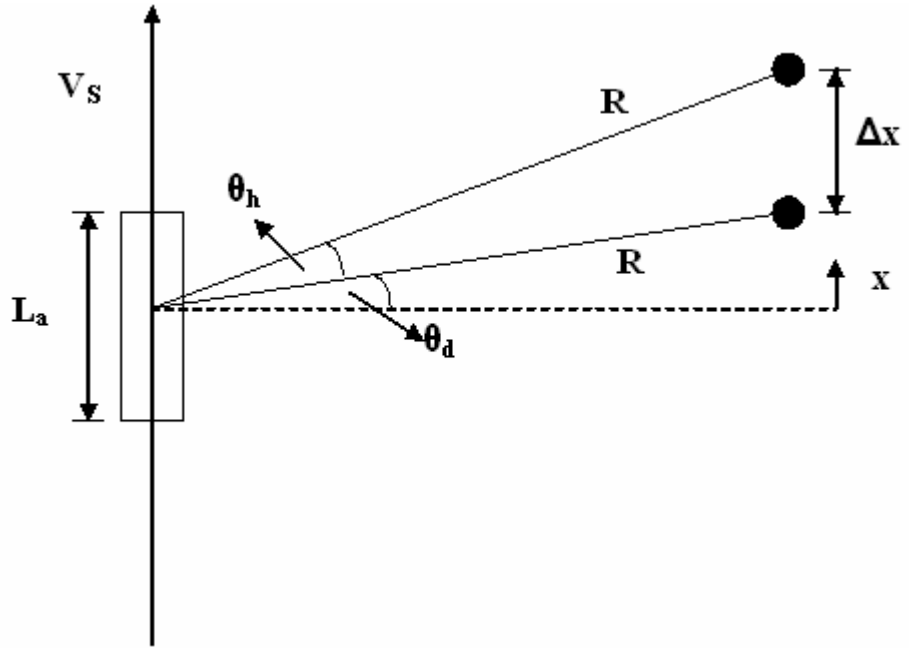

Figure 2.5 Plan view of SAR imaging geometry (modified from Curlander and McDonough, 1991)

With reference to Figure 2.5, the Doppler frequency shift (f_d) can be expressed as:

$$f_d = \frac{2V_s \sin\theta_d}{\lambda} \quad , \tag{2.6}$$

where V_s is the relative velocity of the satellite with respect to the earth, θ_d is the angle made by the look vector to the target with respect to a plane perpendicular to the satellite flight direction and λ is the wavelength used for imaging. Since θ_d is small, f_d can be approximated as:

$$f_d = \frac{2V_s x}{\lambda R}, \tag{2.7}$$

where x is the distance between the target and the plane perpendicular to the satellite flight direction measured in the direction of flight and R is the slant range to the target. Rearranging Eq. 2.7, the azimuth resolution (Δx) can be expressed as:

$$\Delta x = \frac{\lambda R \Delta f_d}{2V_s} \tag{2.8}$$

As can be seen from Eq. 2.8, the azimuth resolution is a function of the resolution with which the Doppler frequency (Δf_d) can be measured. If the resolution of measuring the Doppler frequency is considered to be the reciprocal of the time span defining the length of time a particular target is illuminated by the radar beam, Eq. 2.8 can be rearranged as:

$$\Delta x = \left(\frac{\lambda R}{2V_s}\right)\left(\frac{L_a V_s}{R\lambda}\right) = \frac{L_a}{2}, \tag{2.9}$$

where L_a denotes the length of the radar antenna measured in a direction along the satellite flight direction (Curlander and McDonough, 1991).

It is evident from Eq. 2.9 that the azimuth resolution of SAR data, just like the range resolution of SAR data, is independent of the altitude of the satellite during image acquisition. This is in contrast to the resolution of data acquired by conventional RAR systems, where the achievable resolution is a function of the altitude of operation of the satellite system. *Azimuth compression* is the procedure that is adopted in order to realize the full azimuth resolution (Hanssen, 2001). Figure 2.6 illustrates the radar viewing geometry in a plane perpendicular to the along-track direction. Points on the ground in the near-range are illuminated by the radar beam for time periods shorter than that for points in the

far-range. This redundancy provides useful information needed to offset the loss of resolution in the far-range resulting from an oblique look vector. It should, however, be noted that the look angle varies as a function of the range at which an object is imaged with farther ranges requiring greater look angles. Typically the look angle for ERS-1/2 varies between 18° at the near range to 24° at the far range.

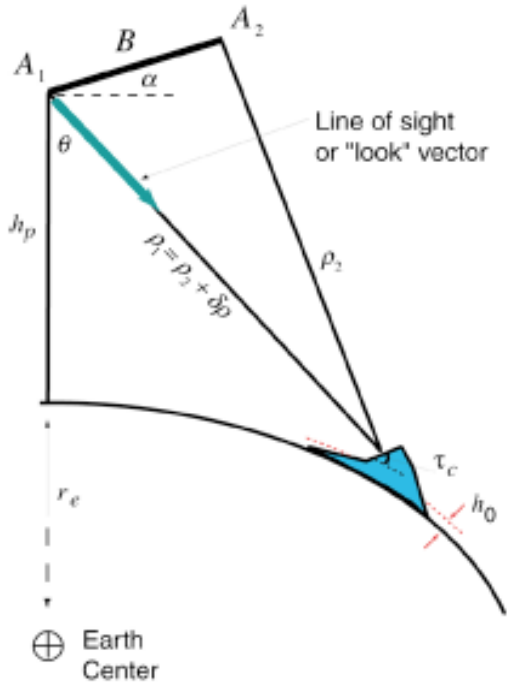

Figure 2.6 Radar viewing geometry in a plane perpendicular to flight track (Rosen et al., 2000). A_1 and A_2 are the two sensors separated by baseline B. r_e is the radius of the Earth, h_p is the elevation of the reference satellite position from Earth' s surface, τ_c represents the terrain slope in the cross-track direction, ho is the elevation of the constant elevation reference surface used for interferogram flattening. ρ_1 and ρ_2 are the ranges to the imaged point from sensor positions A_1 and A_2 respectively. $\delta\rho$ represents the range change that occurred between the two acquisitions. θ is the satellite look angle.

2.2.5 Pulse Repetition Frequency

As discussed in Section 2.2.4.1 and 2.2.4.2, the effective pulse width directly influences the achievable slant range resolution whereas the azimuth resolution depends only on the length of the antenna (L_a) used in data acquisition. As shown in Section 2.2.4.2, the azimuth resolution is a function of the resolution with which the Doppler frequency shift can be determined. For any target, the variation of Doppler frequency shift can be represented by a waveform having a spread about a central frequency. The central frequency is called the Doppler centroid frequency and the spread about the central frequency is referred to as the *Doppler bandwidth*. The Doppler bandwidth can be expressed as:

$$B_{dop} = \frac{2V_s\theta_h}{\lambda}, \tag{2.10}$$

Since SAR systems are pulsed in nature, the pulse repetition frequency (PRF) should be chosen such that the Doppler bandwidth is sampled adequately in order to facilitate its correct reconstruction during data processing. More specifically, the PRF should be greater than the Doppler bandwidth being sampled (Hanssen, 2001). Substituting Eq. (2.4) in Eq. (2.10), the Doppler bandwidth can be expressed as:

$$B_{dop} = \frac{2V_s}{L_a}, \tag{2.11}$$

The requirement that the PRF be greater than the Doppler bandwidth can therefore be mathematically expressed as

$$PRF > \frac{2V_s}{L_a}, \tag{2.12}$$

where V_s denotes the satellite velocity relative to the earth and L_a denotes the antenna length. Hence, in order to ensure adequate sampling of the Doppler bandwidth, it is necessary for the SAR system to emit a pulse for every distance of L/2 traveled by the satellite along its track.

This condition sets the lower bound for the PRF that can be employed during SAR data acquisition. The upper bound is defined by the pulse width that ensures that the radar can distinguish between pulse returns originating from the near-range and the far-range. The upper bound for the PRF can be expressed as

$$PRF_{\max} = \frac{1}{t_2 - t_1}, \tag{2.13}$$

where t_1 and t_2 are the times taken by the radar echoes to travel to the satellite from the near-range and the far-range respectively. If θ_1 and θ_2 represent the inclination of the look vector to the near-range and far-range respectively, the upper bound for the PRF can be expressed as:

$$PRF_{\max} = \frac{c}{2H}\left(\frac{1}{\sec(\theta_2) - \sec(\theta_1)}\right), \tag{2.14}$$

where H denotes the altitude of the satellite during image acquisition.

2.2.6 Effect of Topography on Resolution

On flat ground, the ground resolution cell dimension (R) can be related to the slant range resolution as:

$$R = \frac{\Delta r}{\sin \theta}, \tag{2.15}$$

where Δr denotes the slant range resolution and θ denotes the SAR look angle. However, as the local terrain slope deviates from a flat relief, the dimension of the ground resolution cell imaged within a single slant range resolution cell changes, as shown in Figure 2.7. An increase in the local terrain slope results in an increase in the magnitude of the ground resolution cell imaged. This is known as *foreshortening*. As the local terrain slope approaches the off-nadir angle in magnitude, the ground resolution cell approaches infinity and translates into a complete loss of ground range resolution.

A limiting case of foreshortening is known as *layover* which causes scatterers in a ground resolution cell located on terrain sloped greater than the off-nadir angle to be imaged in reverse order. A decrease in the local terrain slope results in the opposite effect of a decrease in the magnitude of the imaged ground resolution cell. When the negative local terrain slope equals the off-nadir angle in magnitude, the ground range resolution becomes equal to the slant range resolution. Any further decrease in the local terrain slope translates in an inability to image scatterers on such slopes. Such regions that cannot be imaged owing to their location on excessively negative terrain slopes are known as *radar shadow* regions (Ferretti et al., 2007).

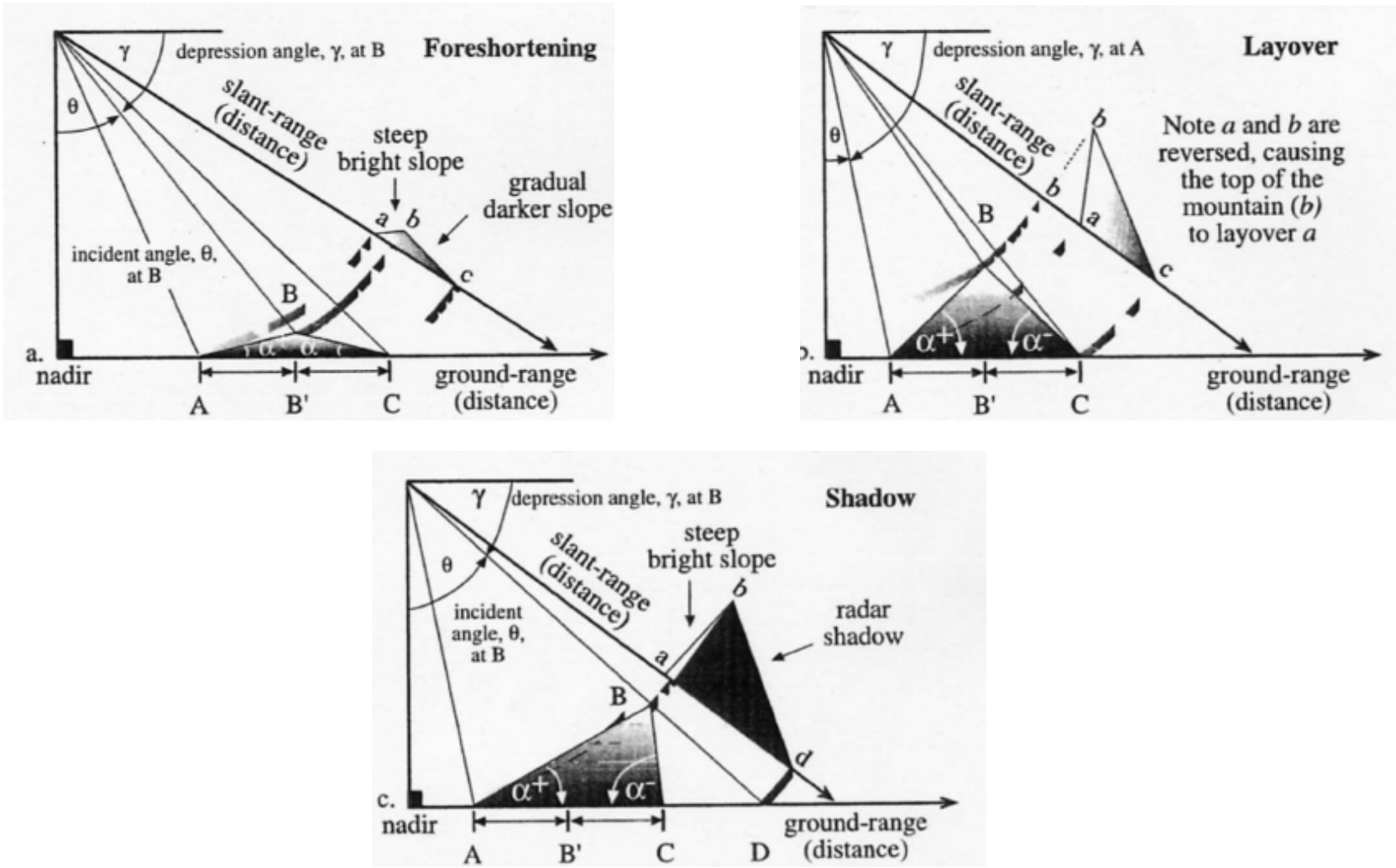

Figure 2.7 Foreshortening, Layover and Shadow effects (Jensen, 2000).

2.3 Interferometry

As explained before, interferometry can be performed when at least two SAR images acquired from slightly varying positions in space are available for analysis. The necessity for at least two acquisitions can be illustrated with the help of Figure 2.8.

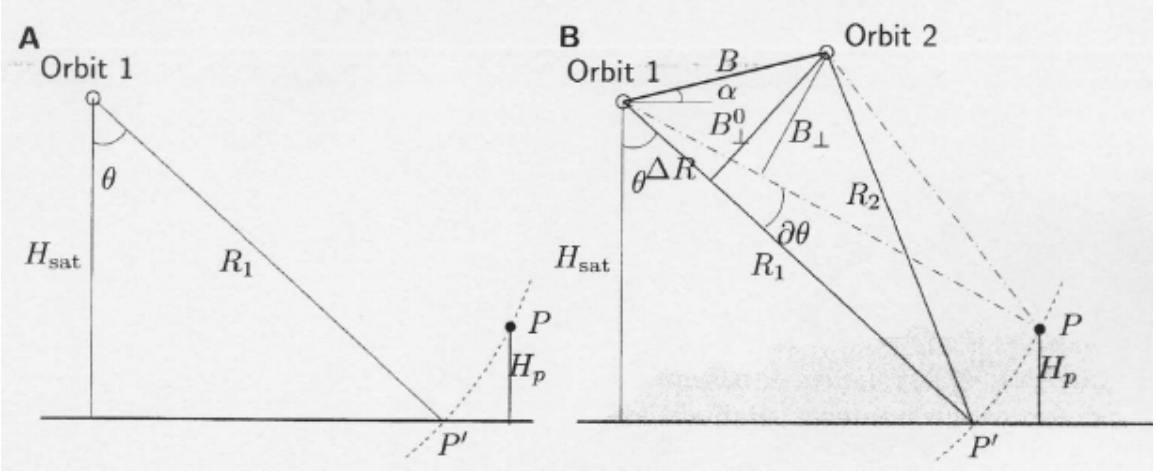

Figure 2.8 (A) Inherent nature of radar to discern objects based only on their range from the radar and the resulting insensitivity to terrain variation. (B) Sensitivity to height variations is obtained by imaging the terrain with two radars separated by a baseline (Hanssen, 2001).

Due to the inherent ranging nature of the imaging radar, a single acquisition gives information relating only to the relative range distance between two targets. Hence, irrespective of their relative angular separation, any two targets located at the same range from the imaging radar are mapped into the same slant range resolution cell. The image does not provide any information about the angular separation between mapped targets.

However, if the same two targets are imaged from another radar located at a slightly different position in space, it is possible to geometrically relate the

elevation difference between the two imaged targets to the spatial separation of the points of acquisition of the two images and the slant range distance of each of the two targets from the two imaging positions. In other words, acquiring imagery from slightly different imaging positions facilitates depth perception (Hanssen, 2001).

The two SAR images may be acquired simultaneously or may be separated in time. If the two acquisitions are separated in time, any surface deformation that may have occurred during that time period can be derived by multiplying the complex phasors of all pixels in one acquisition by the conjugate of the complex phasors of all corresponding pixels in the other. This operation yields an image known as an *interferogram*. The complex multiplication on a pixel by pixel basis is equivalent to differencing the phases representing each pixel in both the acquisitions while multiplying their respective amplitudes (Burgmann et al., 2000).

With reference to the imaging geometry depicted in Figure 2.6, the interferometric phase for the imaged point on the ground derived from the two acquisitions- A1 (at time 1) and A2 (at time 2), can be expressed as:

$$\phi = -\frac{4\pi}{\lambda}(\rho_1 - \rho_2) \tag{2.16}$$

where ρ_1 and ρ_2 represent the slant range distance from satellite positions A_1 and A_2 respectively, to the point imaged on the ground. The interferometric phase component, which is proportional to differential path delay, enables resolution of image pixels in the third dimension. The procedure of relating differential path delay phase to elevation changes is analogous to the

phenomenon of *parallax* that relates the observed angular separation between resolution elements in a stereo pair to their relative elevation differences. However, it should be noted that the sensitivity of stereo-pairs to elevation changes is of the order of several meters as compared to millimeter or centimeter level accuracy that is achievable with InSAR.

For baseline (B) values significantly smaller than the slant ranges from the two satellite positions to a target on the ground, the two look vectors can be approximated to be parallel to each other (Zebker and Goldstein, 1986) and Eq. 2.16 can be expressed as:

$$\phi = -\frac{4\pi}{\lambda} B \sin(\theta - \alpha), \tag{2.17}$$

where, $B\sin(\theta-\alpha)$ denotes $(\rho_1 - \rho_2)$. Physical quantities denoted by all symbols used in Eq. (2.16) and Eq. (2.17) are evident from Figure 2.6. The resolution of an interferogram equals that of the two images used in its derivation.

All pixels in an interferogram representing corresponding ground resolution cells can be represented as complex numbers. As mentioned in Section 2.2.3, the phase representing any imaged target is directly proportional to its slant range distance from the satellite. Two acquisitions being separated in time requires that the same area be imaged during a satellite revisit. This kind of interferometry is referred to as *repeat pass interferometry*. It is desired that the repeat orbit be as close as possible to that followed during the initial acquisition. This is, however, not possible in practice thus giving rise to the same area being imaged from two slightly different look angles.

SAR images acquired from slightly different radar look angles have pixels representing the same ground resolution cells with nearly the same backscatter phase but with different path delay phase. During interferogram formation, the common backscatter phase corresponding to the same ground resolution cells is cancelled, thus yielding a phase term that is related to the differential path delay phase. The following sections introduce and discuss important InSAR concepts with emphasis on processing steps and parameters.

2.3.1 Baseline Dependence

The spatial separation between satellites during any two passes for acquisition of the same frame of raw data is known as the baseline between the two acquisitions. The baseline can be represented by the *normal baseline* and *cross-track baseline* components or the *parallel baseline* and *perpendicular baseline* components. These baseline components are illustrated in Figure 2.9. Interferograms generated using two acquisitions separated by perpendicular baselines other than zero will have phase contributions due to topography of the area imaged by the two acquisitions, in addition to earth curvature and deformation phase.

The *topographic phase* contribution in an interferogram is induced by the difference in slant range distances from the two satellite positions, during image acquisition, to the same point on the ground. Greater perpendicular baselines are more sensitive to topographic phase than smaller ones. The sensitivity of an interferogram to deformation is a function of the wavelength of radiation used for

imaging whereas the sensitivity to topography is a function of the perpendicular baseline.

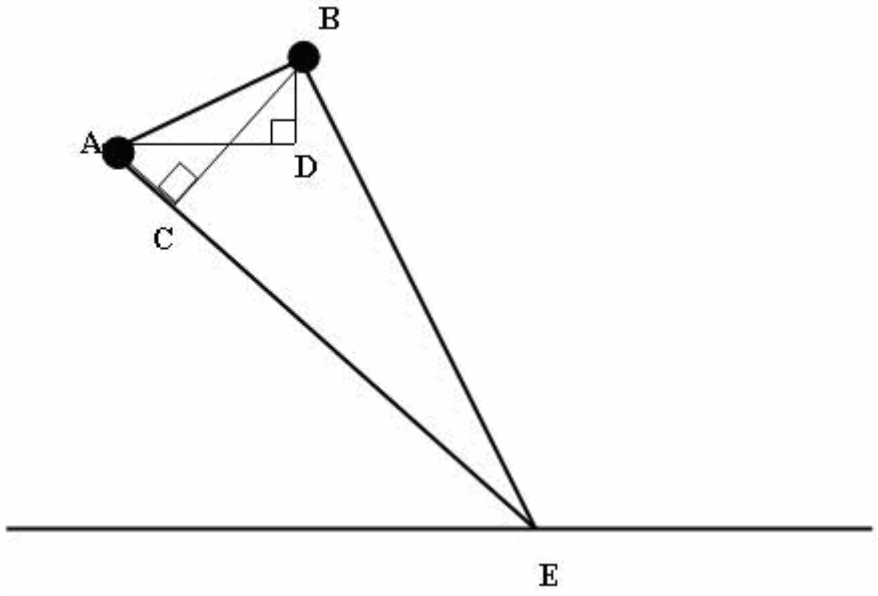

Figure 2.9 Interferometric baseline and its components. AE and BE are the look vectors from satellites A and B to a point E on the ground. BC represents the perpendicular baseline, AC represents the parallel baseline, BD represents the normal baseline and AD represents the across-track baseline.

The sensitivity to topography can be inferred from the *ambiguity height*. This quantity defines the topographic elevation change that induces an interferometric phase change of one cycle or 2π radians. With reference to the geometry shown in Figure 2.6, the ambiguity height can be expressed as:

$$h_{ambig} = 2\pi\left(\frac{\delta h}{\delta\phi}\right) = \frac{\lambda\rho_1 \sin\theta}{2B_\perp}, \tag{2.18}$$

where $\left(\frac{\delta h}{\delta\phi}\right)$ represents the change in topographic height with respect to the interferometric phase, ρ_1 is the slant range distance from the satellite in the reference image, θ is the look angle and $B_\perp$ is the perpendicular baseline

(Burgmann et al., 2000). With reference to Figure 2.6, the perpendicular baseline can be expressed as:

$$B_{\perp} = B\cos(\theta - \alpha)\,, \tag{2.19}$$

On the other hand, a surface deformation component equal to half the imaging wavelength measured along the satellite look vector and occurring between two SAR acquisitions induces one whole phase cycle in the interferogram calculated from those two acquisitions.

The process of simulating the topographic phase contribution from baseline information and subtraction from the interferogram is known as *Differential Interferometry or DInSAR*. The topography for a frame can be obtained from existing Digital Elevation Models (DEM) for the region in the case of *two-pass interferometry* or from *multiple-pass interferometry*. In order to be able to perform two-pass differential interferometry, it is necessary to coregister the DEM to the geometry of the master SLC prior to simulating the topographic phase contribution from it. Multiple-pass interferometry consists of using more than two acquisitions such that at least one pair brackets the period when no surface deformation is recorded. An interferogram calculated between such pairs contains only topographic phase which after simulating and scaling to the baseline defining the pair bracketing the deformation of interest, can be subtracted to obtain a *differential interferogram* (Rosen et al., 2000).

2.4 InSAR Processing Flow

The flow chart shown in Figure 2.10 illustrates the conventional processing steps related to differential interferometry in sequential order. A

detailed description of each processing step is provided in this section.

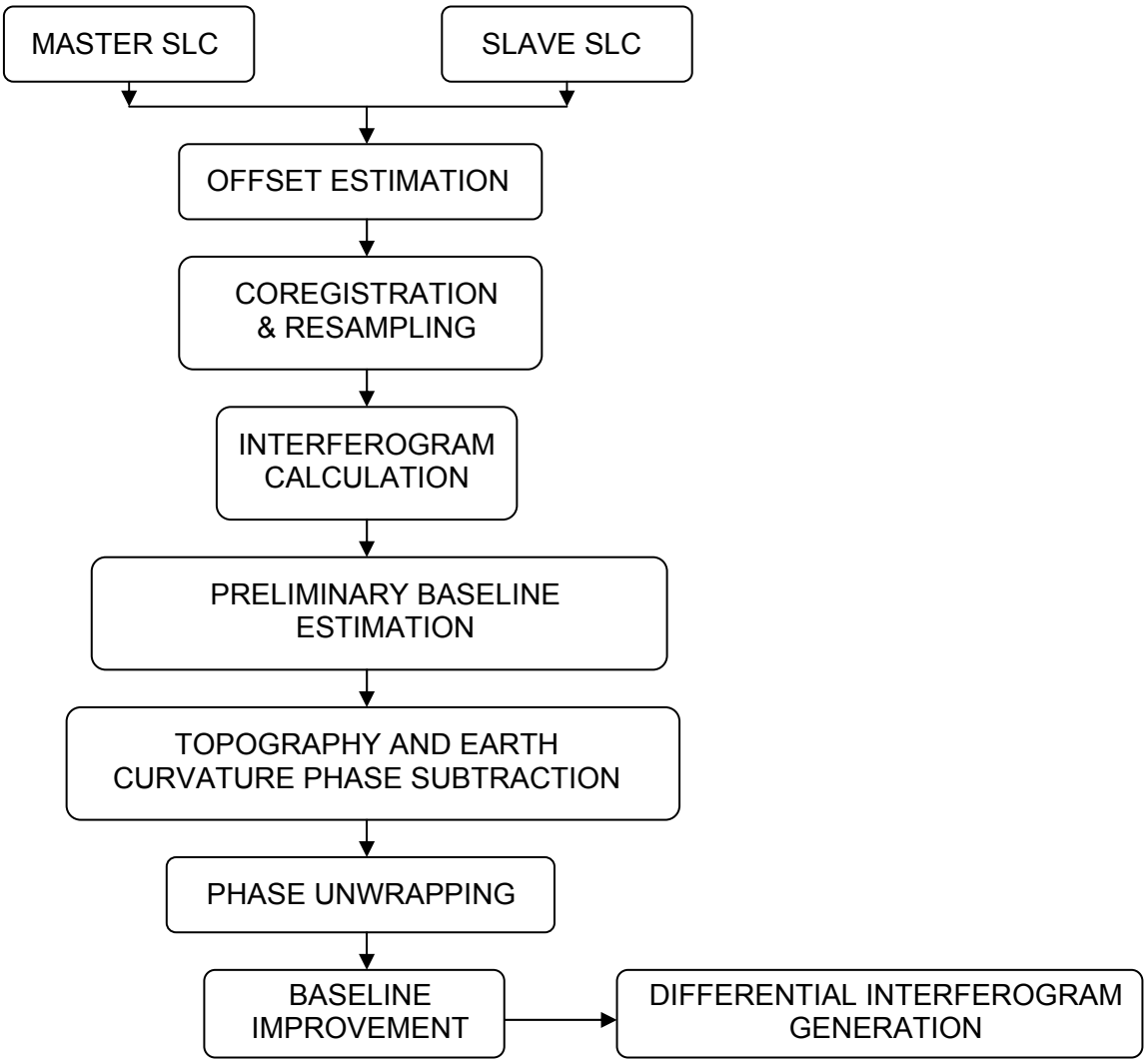

.

Figure 2.10 Processing flow for generation of differential interferogram.

A detailed description of each of the steps mentioned in the flowchart above follows.

2.4.1 Offset Estimation and Coregistration

The accuracy of topographic elevations or displacements derived from satellite interferometry is highly dependent on this step in the processing flow.

Acquisition of SAR data from two satellite geometries results in a relative shift or offset in the positioning of pixels between the two SAR images used for interferometry. The shift between images in the range direction is a function of the baseline separating the two imaging geometries, whereas, a relative shift in the azimuth direction results due to differing relative times of imaging the same area during the two data takes (Hanssen, 2001). The relative shift between the images results in the same ground resolution cell being assigned different pixel locations in the two images.

Coregistration is the process of aligning the pixels corresponding to the same ground resolution cell in two different SAR images. The two SAR images used for interferogram calculation must be coregistered in order to ensure that phases used for interferometric calculations correspond only to those pixels, in the two SAR images, that represent the same ground resolution cell. Among the two SLC's used in interferogram calculation, pixel locations corresponding to one SLC are used as a reference for coregistration. The reference SLC is referred to as the *master*, whereas the image(s) being coregistered into the reference geometry is referred to as the *slave*. Coregistration accuracies equivalent to $1/8^{th}$ to $1/10^{th}$ of a pixel are recommended for interferometry. The *coherence* (γ) of an interferogram depends on the accuracy of coregistration. Coherence is defined as the "normalized complex correlation coefficient of the complex backscatter intensities" corresponding to the master and slave SLC's (Werner et al., 2002). Coherence, as shown in Eq. 2.20, is calculated as an average over a specified

number of pixels defined by a range and azimuth window and is expressed as a number between 0 and 1 with higher numbers indicating better coherence.

$$\gamma = \left| \frac{\left\langle s_2 s_1^* \right\rangle}{\sqrt{\left\langle s_1 s_1^* \right\rangle \left\langle s_2 s_2^* \right\rangle}} \right|, \tag{2.20}$$

where s_1 and s_2 represent the backscatter intensities of corresponding pixels in the master and slave images respectively. As mentioned in Hanssen (2001), it has been shown that a coregistration accuracy of $1/8^{th}$ of a pixel preserves 96% of the coherence in interferograms derived from SAR acquisitions characterized by small Doppler centroids (Just and Bamler, 1994). Usually, one of the image geometries is chosen as the reference for coregistration.

Coregistration is usually achieved by estimating coefficients that can be used to interpolate every pixel in the slave to the appropriate positions relative to the master. This is achieved by dividing the images into small tiles after which the coregistration coefficient for each tile is calculated based on the cross-correlation of the amplitudes of each tile (Ferretti et al., 2007).

During cross correlation, amplitude signatures from the image tiles are compared for similarity. Threshold values of signal-to-noise ratio representing the ratio of the peak to the mean of the calculated cross-correlation function are used as measures to accept or reject the offset vectors computed for each tile. The estimated coregistration coefficients are then used to estimate a polynomial so that the slave image can be interpolated into the geometry of the master.

Due to different imaging geometries, similar areas on the ground are represented in slightly shifted grids representing the different SAR images,

although the grid spacing in both images remains the same. Hence a ground resolution cell contributing to a single pixel in the slave may be contributing only to a part of a pixel in the master. In order to be able to perform interferometric calculations, the complex phase values of the slave image need to be calculated for the pixel locations of the master as implied by the coregistration coefficients.

As mentioned in Hanssen and Bamler (1999), the phase values at the new pixel locations can be obtained by reconstructing the continuous phase field from the sampled data corresponding to the slave and then *resampling* the reconstructed phase field at the inherent sampling rate of the master. Reconstruction of the continuous phase field from sampled data entails interpolation. Choice of appropriate interpolation kernels warrants careful consideration due to their direct influence on interferogram coherence and processing time (Bamler and Hanssen, 1997). The nearest neighbor, piece-wise linear, 4-point cubic and 6-point cubic interpolation kernels were evaluated by Hanssen and Bamler (1999). Lower phase errors and higher mean total coherence were found to be characteristic of the 6-point cubic interpolation kernels as compared to other kernels analyzed in their study.

2.4.2 Interferogram Calculation

Image coregistration and resampling is followed by interferogram calculation. As mentioned in Section 2.3, an interferogram is computed on a pixel-by-pixel basis by multiplying the complex phasor of a pixel in the master by the complex conjugate of the corresponding pixel in the slave. Corresponding pixels are those that represent the complex contribution from the same ground

resolution cell. Hence, accurate coregistration is critical in ensuring accurate interferogram calculation. Following the notation used in Hanssen (2001), interferogram calculation can be expressed as:

$$y_1 y_2^* = |y_1|\exp(j\psi_1)|y_2|\exp(-j\psi_2) = |y_1||y_2|\exp(j(\psi_1 - \psi_2)), \qquad (2.21)$$

where y_1 and y_2 depict the complex phasors of corresponding pixels in both the images used in interferogram calculation, y_2^* depicts the conjugate of the complex phasor for the pixel in the slave image, and ψ_1 and ψ_2 represent the phase of corresponding pixels in the master and slave images.

2.4.3 Baseline Estimation

In deformation mapping applications, accuracy in simulating the phase contribution from topography and the curvature of the earth dictate the accuracy in the relative deformation estimated using differential interferometry. When the phase contribution due to earth curvature is subtracted from an interferogram, the resulting phase image contains phase contributions due only to the topography of the imaged area and any deformation bracketed by the two images used in interferogram calculation. This operation of subtracting the earth-curvature phase contribution is known as *interferogram flattening*. Accuracy in these operations is dictated by the accuracy of baseline estimation.

As can be inferred from Eq. 2.18 in Section 2.3.1, the accuracy of the perpendicular baseline estimate has a direct bearing on the inferred ambiguity height and hence the accuracy of topographic maps derived using interferometric calculations. During the course of a satellite orbit, the spatial location of the

satellite is expressed in the form of *state vectors* which constrain the satellite location in terms of position, velocity and time. The state vectors are determined from satellite tracking data, gravity models and estimated atmospheric drag effects from dynamic models (Hanssen, 2001). Tracking data are obtained through satellite laser ranging (SLR) in which the travel time of a laser emitted from a network of ground stations is used to estimate the distance from the network stations to the satellite at various points during its orbit. Due to the inability of the laser to penetrate clouds, the availability of SLR tracking data is dependent on local weather conditions prevalent during the satellite orbit. In addition, the measured range between the satellite and the ground stations need to be corrected for path delay effects induced due to local tropospheric and atmospheric conditions.

The accuracy of SLR tracking data is reported to range from 1 cm to 20 cm. The distribution of SLR tracking system ground stations is so sparse that an ERS satellite in orbit cannot be tracked by three satellites simultaneously (Scharroo et al., 2000). Since the number of SLR ground stations is limited, the state vectors in the intermediate positions need to be interpolated using information from the gravity and dynamic models. Hence the accuracy of these intermediate state vectors is a function of the accuracy of gravity and dynamic models used in their derivation.

Other ways of tracking the satellite position during its orbit are by measuring the Doppler frequency shift between transmitted and received microwave signals emitted from the satellite. This principle is used in conjunction

with round-trip travel time measurements to track the satellite velocity and location by Precise Range and Range-Rate Equipment (PRARE) and Doppler Orbitography and Radiopositioning Integrated by Satellite (DORIS) systems. In both systems, microwave radiations in the C and X band are emitted where the C band frequency is utilized to estimate and compensate for the ionospheric influence on measurements. In contrast to the 1 cm – 20 cm positioning accuracy range characteristic of SLR tracking systems, positioning accuracies of around 4.5 cm by PRARE systems and 5 cm by DORIS systems are achievable (ESA, 2007). ERS-1 orbits were mainly derived from SLR tracking data whereas the ERS-2 uses a combination of SLR and PRARE tracking data to constrain the satellite's orbit.

As explained in Section 2.3.1, the baseline vector can be represented by its perpendicular and parallel components or by its cross-track and normal components. Several algorithms have been proposed for accurate interferometric baseline estimation According to Ren et al. (2003), all baseline estimation methods can be broadly classified as belonging to one of three methods, namely:

1. Orbit method,
2. Tie point method, and
3. Frequency method.

Orbit methods use the precise state vectors to derive interferometric baseline estimates. In such cases, the phase contribution due to earth curvature and the topography of the region imaged can be estimated accurately. This entails a state vector positioning accuracy of about 1 mm whereas the current positioning

accuracy for ERS state vectors is of the order a few centimeters (Hanssen, 2001).

In cases where satellite orbits of the required precision are unavailable, the interferometric baseline is estimated from the unwrapped phase data. The tie point methods use unwrapped phase values corresponding to ground control points with predetermined geographic position and elevation to solve for the baseline. Small et al. (1993) verify the accuracy of baseline estimates derived iteratively using a non-linear least squares procedure and ground control point phase data. Seymour and Cumming (1996) present a method that iteratively solves for the interferometric baseline by using two coregistered tandem SAR images and an available DEM of the imaged area coregistered to the master SAR image. The advantage of this method is that it does not use unwrapped phase data for baseline estimation. Frequency methods derive baseline estimates by relating the baseline to the observed *fringe frequency* in flat areas of the unwrapped interferogram. The fringe frequency, expressed in cycles-per-meter (cycles/m), is the number of cycles of phase present in one meter of an interferogram.

Goyal and Verma (1996) have shown that the cross-track and normal baseline components can be estimated from geometrical calculations performed on three points each spaced one fringe apart from each other. The derivation is made based on the assumption that the distance between two consecutive fringes is small hence making it feasible to neglect earth curvature from the formulation. Fang et al. (2004) formulate a method of baseline estimation by

relating the baseline to the periodicity of interferometric fringes in regions of the interferogram characterized by flat terrain. Despite the reduced accuracy of orbit information derived from available state vectors, the topographic and earth curvature phase contributions estimated from the same can be used to reduce the fringe gradient of the complex interferogram hence making phase unwrapping easy and less error prone.

2.4.4 Phase Unwrapping

As explained in Section 2.2.3, a complex interferogram represents differential path delay phase for each pixel by phase values wrapped in the range $(-\pi, \pi)$. Determination of the absolute phase value for these pixels entails the addition of an integer number of whole cycles of phase or integer multiples of 2π radians to the complex phase of each pixel. The absolute phase representing the displacement or range change for each pixel is determined in two steps.

The first step is performed to find the integer number of whole cycles that need to be added in order to achieve the correct relative phase difference of all pixels relative to a reference pixel. This procedure is known as *phase unwrapping*. Once the complex phase of all pixels is unwrapped with respect to the phase of a reference point in the interferogram, the absolute unwrapped phase determination step consists of determining the constant multiple of 2π that should be added to the relative phase of all pixels as determined from the phase unwrapping step (Rosen at al., 2000).

The phase unwrapping stage is the most critical step in interferometry and is often very difficult. Various algorithms have been proposed to achieve reliable

phase unwrapping. Phase unwrapping is an under-constrained inverse problem. Its solution, hence, entails some assumptions, the validity of which dictates the correctness of the solution obtained. The common assumptions made are:

1. The wrapped phase gradients equal the unwrapped phase gradients, and
2. The unwrapped phase field is smoothly varying with the absolute phase difference between adjacent pixels in the interferogram not exceeding half a cycle (Hanssen, 2001).

These assumptions are valid when the interferograms in question are characterized by good coherence and when the relief of the area represented in the interferograms varies gradually. Given the two dimensional nature of SAR data, the addition of integer multiples of 2π needs to be accomplished in a sequential fashion starting from a chosen reference point. This step is usually referred to as phase gradient integration. When the assumptions are valid, the same unwrapped phase field will result irrespective of the direction chosen for phase gradient integration. However, when the assumptions are not valid, different solutions can be obtained based on the direction chosen for phase gradient integration. This can be explained with the help of Figure 2.11(a) and Figure 2.11 (b) that were adopted directly from Madsen and Zebker (1999).

0.2	0.2	0.2	0.2
0.4	0.2	0.2	0.4
0.6	0.8	0.8	0.6
0.8	0.8	0.8	0.8

(a)

0.2	0.2	0.2	0.2
0.4	0.2	0.2	0.4
0.6	-0.2	-0.2	0.6
0.8	-0.2	-0.2	0.8

(b)

Figure 2.11 Effect of residue points on phase unwrapping.

If every cell shown in Figure 2.11 (a) represents a pixel in a wrapped interferogram, the values denoted in each cell represent the wrapped phase value of the corresponding pixel normalized by 2π. Unwrapping these values would entail adding an integer number of cycles normalized by 2π, to the normalized wrapped phase values represented in each cell in Figure 2.11 (a), such that the difference between the unwrapped values corresponding to neighboring pixels do not exceed 0.5. If the difference between the wrapped values of neighboring pixels in Figure 2.11(a) does not exceed 0.5, no operation would be necessary. Since the phase values are laid out in a two-dimensional matrix, unwrapping can be accomplished in one of the following two ways:

1. By unwrapping the first column and then using the unwrapped values in each cell of the first column to unwrap each row, or
2. By unwrapping the first row and then using the unwrapped values in each cell of the first row to unwrap each column.

Using either of the two approaches must necessarily yield the same result. Unwrapping the values shown in Figure 2.11 (a) by adopting the first approach yields a matrix that is identical to the wrapped phase matrix shown in Figure 2.11 (a). However, unwrapping the values shown in Figure 2.11 (a) by adopting the second approach yields the unwrapped matrix shown in Figure 2.11(b). Obviously, the solutions adopted by the two approaches are not the same. The different solutions result due to unwrapping errors that propagate from a group of four neighboring pixels whose wrapped phase differences add up to a non-zero value (Figure 2.12).

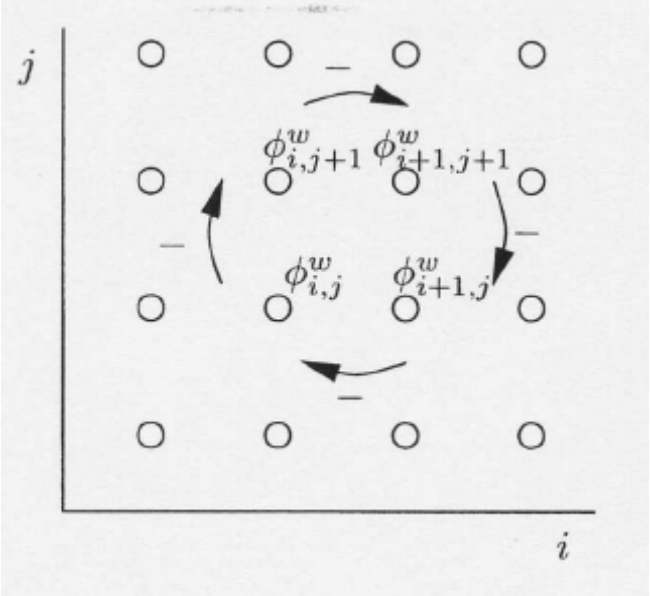

Figure 2.12 Residue calculation. i and j depict the range and azimuth respectively and the circles depict the centers of pixels. The arrows show the direction of phase difference summation (Hanssen, 2001).

These pixels are known as *residue points* (Madsen and Zebker, 1999). Residues can be either negative or positive and their detection indicates the presence of discontinuities in the phase field. Unwrapping errors hence result from the addition of incorrect multiples of 2π. Therefore, unwrapping errors in interferograms can be identified by looking for discontinuities in the unwrapped phase field which are characterized by phase jumps or cycle skips.

Hence, inherent *fringe gradients*, expressed in phase cycles per pixel, dictate the difficulty in unwrapping an interferogram correctly. High fringe gradients increase the difficulty in phase unwrapping. Fringe gradients in an interferogram depend on three main parameters, namely:

1. Perpendicular baseline,
2. Terrain slope with respect to look vector, and

3. Wavelength used for imagery (Rosen et al., 2000).

Fringe gradients increase with increase in baselines. Terrains sloping toward the sensor induce greater fringe gradients than those sloping away. Fringe gradients are inversely proportional to wavelength with short wavelengths yielding high fringe gradients. As mentioned in Gens (2003), most of the techniques proposed to accomplish phase unwrapping can be broadly classified under two methods, namely:

1. Path following methods, and
2. Minimum norm methods.

Path following methods operate by identifying and delineating branch cuts and restricting the unwrapping direction to regions bounded by them. Branch cuts are lines joining a pair of oppositely polarized residues. Hence regions bounded by branch cuts are zones characterized by smoothly varying phase fields which can be unwrapped using the traditional assumptions.

As mentioned in Gens (2003), the branch-cut algorithm (Goldstein, et al., 1988), Flynn's minimum discontinuity algorithm (Flynn, 1997), minimum cost flow networks (Constantini, 1998) and minimum spanning tree algorithm (Chen and Zebker 2000) are some path following methods proposed to achieve two dimensional phase unwrapping. The minimum cost flow algorithm formulates the unwrapping problem as a network flow problem (Gens, 2003) and positions branch cuts by solving for the optimum flow required in a network of arcs to yield a minimum total cost for the network (Werner et al., 2002) so that the interferometric phase can be unwrapped.

Minimum-norm methods solve the problem mathematically and achieve unwrapping by solving for the integer multiples of 2π that mimimize the difference between the wrapped and unwrapped phase gradients in the range and azimuth directions (Gens, 2003; Feretti et al., 2007). Both weighted and unweighted least squares phase unwrapping methods have been proposed to achieve phase unwrapping in the minimum norm sense (Ghiglia and Romero, 1994; Fornaro et al., 1996a Fornaro et al., 1996b). More details on the topic can be found in Ghiglia and Pritt (1998).

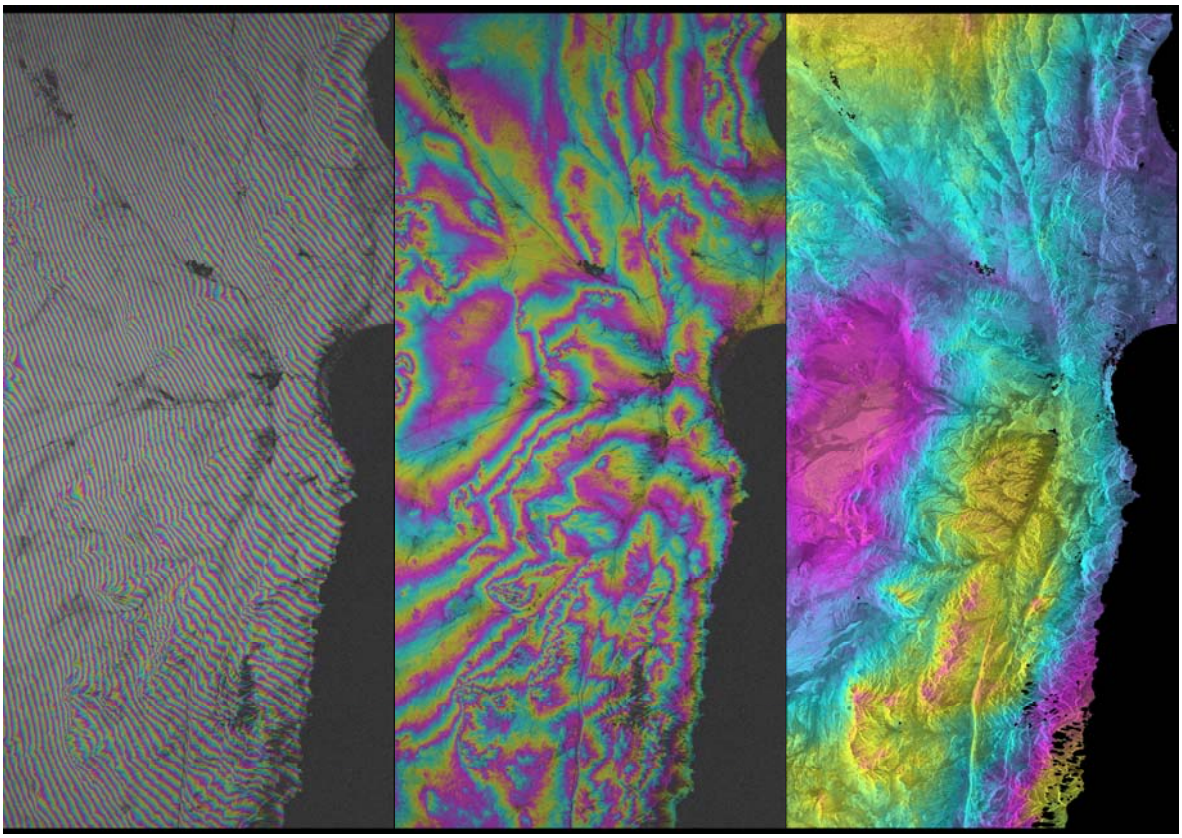

(a) **(b)** **(c)**

Figure 2.13 (a) Interferogram between March 1996 ERS1 and March 2000 ERS2 acquisitions over Mejillones peninsula, (b) the interferogram with earth curvature removed and (c) the unwrapped differential interferogram. The acquisitions are separated by a 20 m baseline. All figures above are in descending satellite look geometry.

2.4.5 Preprocessing for Unwrapping

Preprocessing involves steps to reduce phase noise and phase complexity to aid in phase unwrapping. *Multi-looking* and *filtering* are two commonly adopted preprocessing steps.

Multi-looking is a process by which phase values of a specified number of interferogram pixels are averaged in order to reduce noise (Hanssen, 2001). Multi-looking results in loss of resolution or low sampling rates which can be disadvantageous when applied to interferograms with high fringe gradients. However, multi-looking can be effectively applied to datasets with smooth phase fields and low fringe gradients. In addition, multi-looking helps reduce processing time by reducing data set sizes.

Filtering on the other hand, aids in reducing phase noise while maintaining the data set resolution. Care should be taken while adopting filter parameters in order to avoid generation of filtering artifacts in regions of non-uniform phase fields or loss of whole phase cycles owing to over filtering. Both these effects induce errors during phase unwrapping (Werner et al., 2002).

2.5 Summary

An introduction to Synthetic Aperture Radar and the technique of interferometry were provided in this chapter. The concepts introduced in this chapter are fundamental to the point target interferometry technique, which was adopted for deformation history analysis of the study area. The fundamentals of point target interferometry and its applications are presented in the next chapter.

3. INTERFEROMETRIC POINT TARGET ANALYSIS

3.1 Introduction

Details pertaining to the use of conventional InSAR techniques to infer ground deformation details were provided in Chapter 2. This chapter introduces the concept of point target interferometry or *interferometric point target analysis* (IPTA) which was used for analyzing data in this study. All principles introduced in the previous chapter apply to point target interferometry, except that the interferometric calculations are applied to only those pixels that demonstrate stable scattering properties. These pixels are stable in the sense that their phase values do not decorrelate over long baselines or long time periods. Such stable behavior renders long-baseline, long-time-period interferograms useful for deformation inference.

In contrast, conventional InSAR can be used to derive deformation information from only relatively short-baseline, short-time-span interferometric pairs. The increased utilization of available data for a site of interest, resulting from the increased number of acquisitions that can be used to derive coherent interferograms, makes it possible to model the phase contributions to interferometric phase and to derive deformation time history estimates for these stable scattering pixels. The phase model is constrained with multiple interferograms spanning different time intervals and different baselines.

A detailed description of the approach including the conventional processing flow adopted for this study is presented. In addition, a literature

review outlining the application of point target interferometry to derive non-tectonic deformation estimates with an emphasis on civil engineering applications is provided.

3.2 Contributions to Interferometric Phase

3.2.1 Unwrapped Phase Components

Interferometric phase is composed of differential path delay components resulting due to the topography of the imaged area, deformation occurring between acquisitions, water vapor inhomogeneities in the troposphere, and noise. Deformation of a given pixel, when expressed as a function of time, is composed of both *time linear* and *non-linear* components. Time linear deformation represents the component of deformation that varies linearly as a function of time, whereas non-linear deformation represents the component that does not vary linearly with time. Phase contributions due to errors in Digital Elevation Models (DEM) used to derive topographic phase, baseline estimation errors and atmospheric path delay can sometimes obscure phase contribution due to small deformations. In such cases, resolving interferometric phase into its constituent components becomes critical. The IPTA, which is a multi-temporal statistical approach, aims at resolving interferometric phase into its components in order to derive reliable estimates of deformation phase and associated uncertainties. Statistical robustness is achieved by constraining the phase model with multiple interferograms computed from a stack of complex images bracketing the time period of interest. The unwrapped interferometric phase can be represented by the summation of phase contributions from linear deformation

($\phi_{lin-def}$), topography (ϕ_{topo}) and residual phase (ϕ_{res}) as shown in Eq. 3.1. As shown in Eq. 3.2, the residual phase is composed of phase contributions due to *atmospheric path delay* (ϕ_{atm}), non-linear deformation ($\phi_{non-lin-def}$) and *noise* (ϕ_{noise}).

$$\phi_{unw} = \phi_{lin-def} + \phi_{topo} + \phi_{res} \tag{3.1}$$

where,

$$\phi_{res} = \phi_{atm} + \phi_{non-lin-def} + \phi_{noise} \tag{3.2}$$

3.2.2 Residual Phase Components

Variation of spectral characteristics of the residual phase in spatial and temporal domains is used to characterize phase contributions from its constituent components. The accuracy of the estimates of atmospheric phase, non-linear deformation phase and phase noise is a function of the accuracy of inherent assumptions with respect to the spatial and temporal variation of spectral characteristics made to constrain their solution (Werner et al., 2003).

Water vapor in the troposphere increases the travel time of microwave frequency electromagnetic radiation. Thus, the phase value assigned to a point on the ground (given by difference in the phase values recorded at the beginning and end of the two-way transit of microwaves to a point on the ground) that is imaged during such tropospheric conditions will be representative of the slant range distance between the satellite and the point on the ground in addition to atmospheric path delay induced phase difference. The lack of knowledge of tropospheric conditions during image acquisition or the inability to account for

such induced path delay, can lead to erroneously considering the entire phase contribution for an imaged point as resulting due only to the slant range distance between the imaged point and the satellite.

The tropospheric condition prevailing at the time of acquisition of a satellite image (SLC), controls whether the image is characterized by atmospheric path delay phase or not. An interferogram calculated using two SLCs with either one characterized by atmospheric path delay, will have phase contributions resulting due to atmospheric path delay. On the other hand, an interferogram calculated between two SLCs acquired during exactly similar tropospheric conditions will not contain atmospheric path delay phase.

Figure 3.1 compares two differential interferograms to illustrate the spatial expression of atmospheric path delay phase. The interferograms were computed from SLCs processed by concatenating raw data that was acquired for two SLC frames (4023 and 4041) along ERS Track 368 over Northern Chile. Each frame of data acquired by the ERS contains data corresponding to a 100 km by 100 km area on the ground. Hence, concatenation of data corresponding to two consecutive frames, results in an SLC containing data for a 100 km by 200 km area on the ground. The interferogram shown on the left is characterized by phase signature that is characteristic of small deformation while the interferogram on the right has a pronounced atmospheric path delay signature.

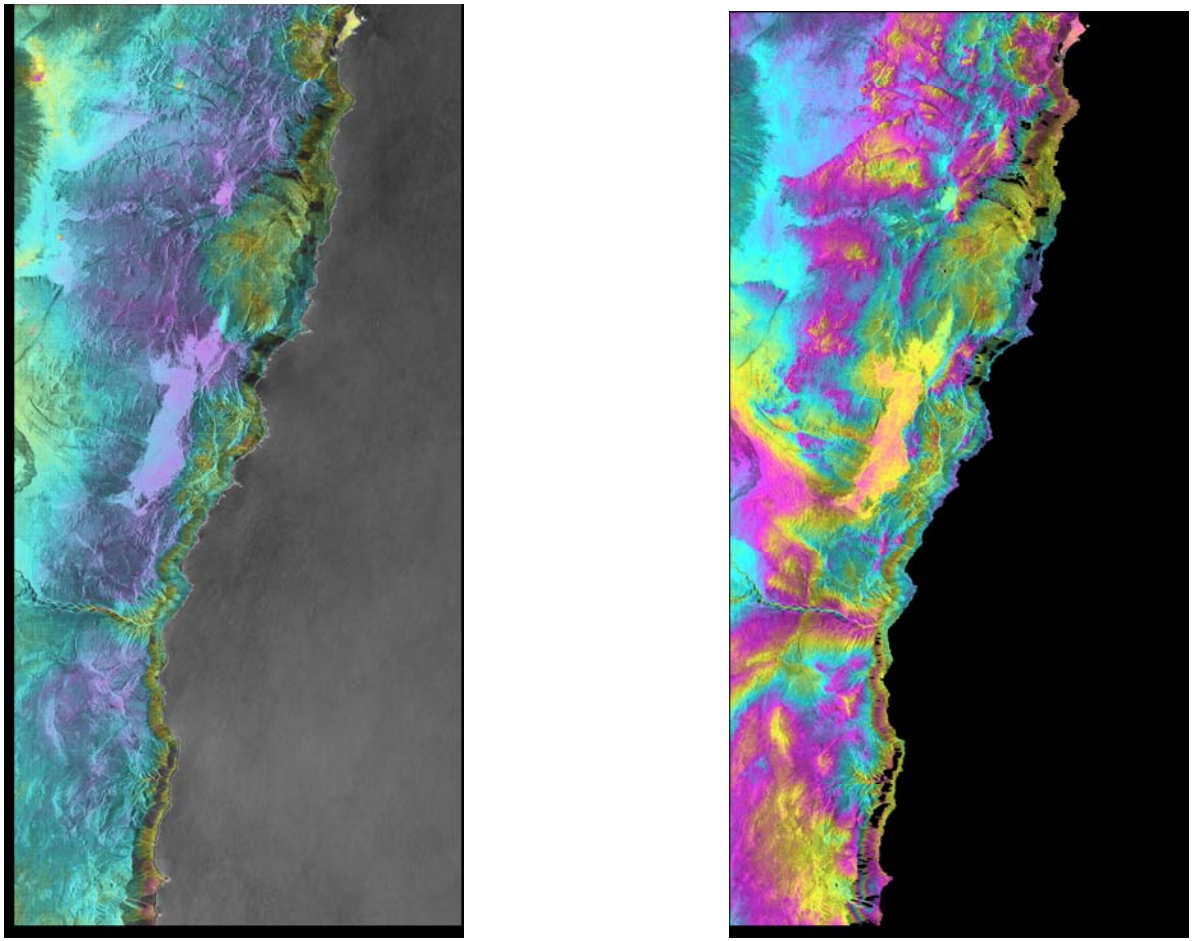

(a) (b)

Figure 3.1 (a) Differential interferogram without atmospheric path delay phase and (b) Differential interferogram with atmospheric path delay phase. Both interferograms are shown in satellite viewing geometry. One color cycle corresponds with 2π radians of phase or 28 mm of displacement in the satellite line-of-sight direction.

As stated in Werner et al. (2003), the expected spatial and temporal signatures of the residual phase components can be summarized as follows:

1. The atmospheric path delay phase can be spatially correlated while being uncorrelated or random in the temporal domain.
2. The non-linear component of deformation can vary from being spatially and temporally correlated to being uncorrelated in both domains.
3. Baseline errors correlate spatially but can be uncorrelated in time.
4. Phase noise is random in both spatial and temporal domains.

Among the components that constitute residual phase, non-linear deformation is the only parameter that is desired in deformation mapping. The spatial and temporal characteristics of the different phase components constituting the residual phase are used to estimate and filter the undesirable phase components so that an accurate estimate of non-linear deformation can be obtained.

3.3 Point Targets for Statistical Analysis

3.3.1 Point Target Attributes

Temporal decorrelation and *geometric decorrelation* result in loss of phase data due to the loss of coherence and limits the use of SAR acquisitions in constraining reliable phase models. Temporal decorrelation results from varying scattering properties of radar pulse reflectors on the ground and is particularly evident in interferograms derived from SLCs acquired on dates separated by long time periods. Geometric decorrelation is characterized by loss of coherence in interferograms derived from long-baseline SAR acquisitions.

The *permanent scatterer* (PS) technique (Ferretti et al., 2000, 2001) developed at the Politecnico di Milano (POLIMI), Italy is a multi-temporal, multi-baseline statistical approach that limits analysis of phase history to those SAR image pixels known to possess stable scattering behavior. Such permanent scatterer pixels represent ground resolution cells that are composed of elemental reflectors that dominate the backscatter of the resolution element in which they are located. Such reflecting abilities induce stable behavior, in the sense that the phase values of permanent scattering pixels do not decorrelate over long spatial and temporal baseline acquisitions (Ferretti et al., 2001). Such stable behavior enables the complete use of data stacks available for a particular site of interest since interferometric processing need not be restricted to only short spatial and temporal baseline pairs.

Permanent scatterers are also referred to as *coherent scatterers* (Schnieder et al., 2006), *coherent pixels* (Mallorqui et al., 2006), and *point targets* (Werner et al., 2003). Since all data processing for the work presented in this document was accomplished using the Interferometric Point Target Analysis (IPTA) package developed by Gamma Remote Sensing, future references to the above described stable scatterers will be made using the term *point targets*. Details on criterion used in point target identification can be found in the Section 3.3.2.

From the above explanation, it is evident that phase history of point targets can be exploited over only those time periods that define stable behavior. Accurate identification of such point targets is critical in ensuring complete use of

phase data and deriving a robust phase model. Corner reflectors possessing dihedral and trihedral shapes, high radar cross section, and oriented in the look direction of the satellite are good examples of reflectors that exhibit stable behavior.

Radar cross section (RCS) of a target is defined as “the area intercepting that amount of power which, when scattered equally in all directions, produces an echo at the radar equal to that from the target” (Skolink, 1962). In other words, the radar cross section is proportional to the ratio of the power reflected by a radar target towards the radar to the power density incident on the target. Hence, larger targets tend to have larger values of RCS. Metallic edges on building roof-tops and guard-rails along highways and bridges are some examples of man-made stable reflectors.

The density of SAR acquisitions in the temporal domain dictates the accuracy in identification of point targets. A dense stack of SLCs assures good sampling of phase histories of candidate points, based on which appropriate quality control procedures can be adopted to monitor the deviation of point phases with respect to a general fit. All points with characteristic phase values within the acceptable deviation from a general fit are considered point targets for statistical analysis. Ferretti et al. (2000) report that urban areas are characterized by a minimum persistent scattered density of at least 100 per km^2 with a phase variance of less than 0.25 radians with respect to a best fitting phase model.

3.3.2 Criteria for Point Target Identification

The IPTA reference manual lists the following primary criteria that should be met by the complex data stack selected for point target identification and analysis:

1. Accurate *focusing*,
2. Accurate co-registration, and
3. Accurate *radiometric calibration*.

The process of forming a SAR image or an SLC by processing pulse returns as received by the SAR is known as “SAR focusing” or “synthetic aperture processing”(Hanssen, 2001). Radiometric calibration can be defined as “the process of characterizing the performance of the end-to-end SAR system, in terms of its ability to measure the amplitude and phase of the backscattered signal” (Curlander and McDonough, 1991).

In the IPTA package, *temporal variability* and *spectral diversity* of the radar backscatter are two criteria used to identify point targets in a data stack containing acquisitions satisfying the above mentioned primary criteria.

3.3.2.1 Temporal Variability

Temporal variability can be defined as the ratio of the mean to the standard deviation (MSR) of backscatter from a pixel. The IPTA reference manual recommends using MSR values of about 1.5 in order to identify point targets. The MSR as defined in the IPTA manual is the reciprocal of the parameter referred to as *amplitude dispersion* or *dispersion index* in Ferretti et al. (2000). In other words, the amplitude dispersion or dispersion index is the ratio of

the standard deviation to the mean of backscatter received from a pixel. As explained in Ferretti et al. (2000), the rationale behind using the amplitude dispersion for persistent scatterer identification is that the parameter serves as a good approximation of phase dispersion for scatterers characterized by a high signal-to-noise ratio (SNR). According to the IPTA reference manual, identifying point targets from MSR values is reliable for data stacks containing more than 25-30 acquisitions due to the better estimate of MSR that can be inferred from more samples.

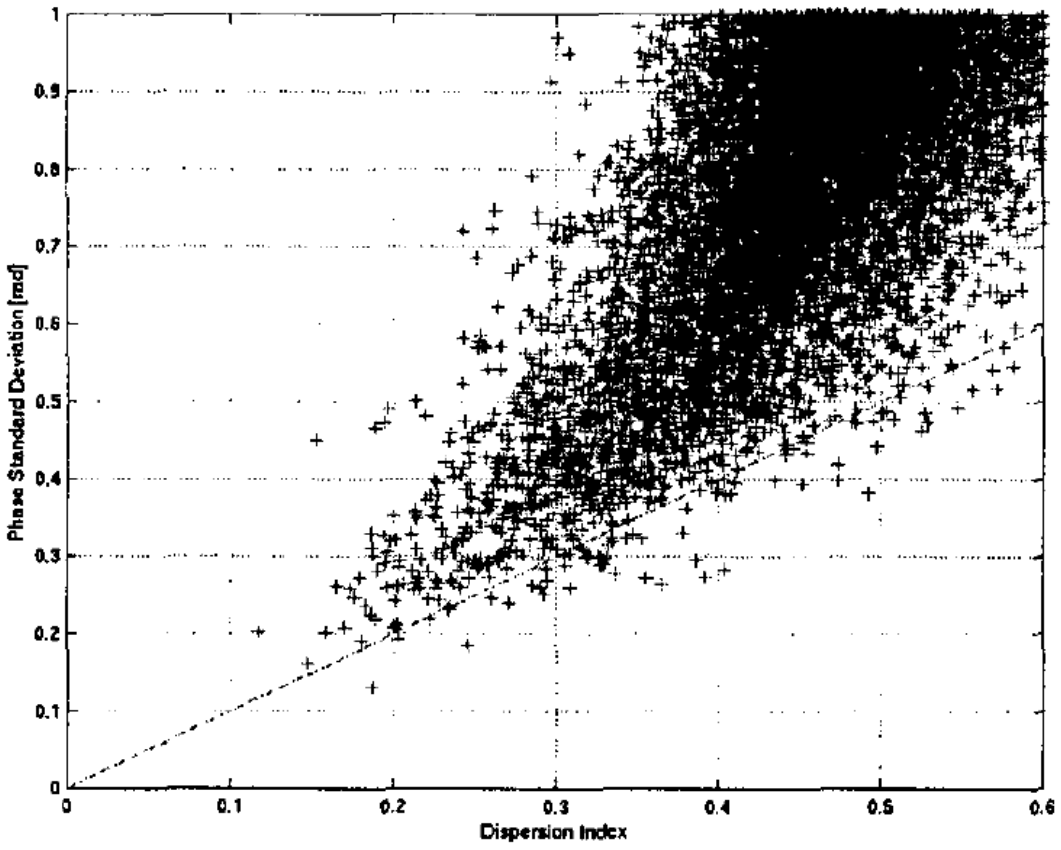

Figure 3.2 Correlation between phase standard deviation and dispersion index (Ferretti et al., 2000).

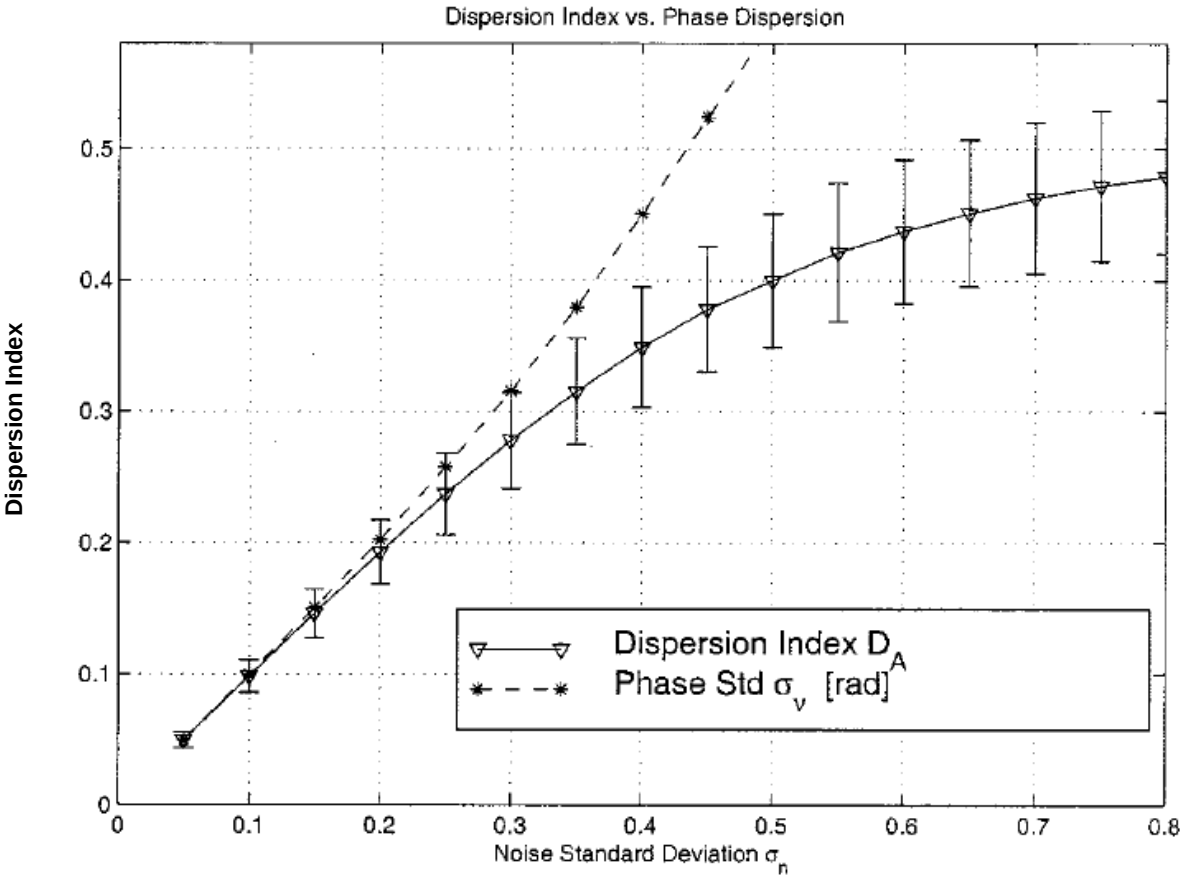

Figure 3.3 Dispersion index- phase dispersion relation (Ferretti et al., 2001).

A correlation between phase standard deviation and dispersion index is shown in Figure 3.2 (Ferretti et al., 2000). Numerical simulation results shown in Figure 3.3 show that dispersion index values lower than 0.25 approximate the phase standard deviation better than higher values (Ferretti et al., 2001). As per the IPTA reference manual, identification of pixels located in radar shadow regions as potential point targets can be avoided by restricting point target selection to only those pixels characterized with a backscatter greater than the spatial average.

3.3.2.2 Spectral Diversity

For data stacks containing less than 25 acquisitions, the IPTA reference manual recommends the use of the spectral diversity criterion for point target identification. As mentioned in Chapter 2, an object on the ground is imaged approximately 1000 times during image acquisition by an ERS platform. The forward motion of the satellite enables the observation of the object from different perspectives. The amount of incident electromagnetic radiation reflected back to the satellite is recorded while observing the object from each of these different perspectives. Point targets identified using the spectral diversity criteria correspond to those pixels exhibiting a very low variation in backscatter intensities when imaged from different vantage points in the trajectory followed by the satellite during image acquisition. In contrast to the temporal variability approach, which is applied to the entire data stack, the spectral diversity approach can be applied to a single acquisition.

In this method, point targets are identified as those pixels that maintain a constant intensity of backscatter irrespective of the fractions of range and azimuth bandwidth used to process the selected SLC. Processing an SLC with fractions of the range and azimuth bandwidths translates into a reduced resolution of the resulting SLC. Hence, point targets detected using the spectral diversity criteria are those that correspond to high backscatter irrespective of the resolution of the processed SLC.

A fraction of the azimuth bandwidth can be realized by utilizing only a fraction of the 1000 returns from scatterers in a ground resolution cell during for

SLC formation. While utilizing all the 1000 returns in processing raw data into an SLC results in high azimuth resolution, using only one-fifth of the total number of returns results in a degraded resolution. Hence five SLCs of the same area can be made by utilizing one-fifth of the number of returns available for each scatterer located in the imaged area. In other words, this operation corresponds to taking five spectral looks in the azimuth direction with the resolution of the SLC formed using each spectral look equaling that which can be realized by one-fifth of the azimuth bandwidth.

In order to achieve robustness in the identification of point targets, the spectral diversity criterion can also be applied to all scenes in a given data stack (say all 25 scenes covering the same study area) and the degree of correlation between the spectral diversity estimates derived for a particular pixel in all SLCs in a data stack can be used for point target identification.

Candidate points identified using the two criteria are combined into one single point list that is subjected to quality control for point target identification. Details on the quality control procedure used in this study will be provided in the Chapter 4, in which the IPTA processing flow adopted for this study will be discussed in detail. On applying the persistent scatterer approach adopted for ERS -1/2 data to RADARSAT-1 and JERS-1 SAR data, Colesanti et al. (2003b), concluded that permanent scatterer distribution depends on the operating frequency of the SAR system, the imaging geometry of the platform, and the polarization of the electromagnetic radiation used during imaging.

In a study performed by Ferretti et al. (2004) and aimed at evaluating the effect of satellite repeat cycle on the density of point targets detected, higher persistent scatterer densities were inferred from an ERS dataset containing 26 acquisitions over Rome and defined by a 3-day repeat cycle when compared to the density inferred from a similar ERS dataset consisting of 26 scenes but defined by a 35-day repeat cycle. In addition, Ferretti et al. (2004) define *semi-permanent scatterers* (SPS) and *temporary permanent scatterers* (TPS) and list approaches that can be adopted in their identification. SPS are defined as those that exhibit persistent-scatterer-like behavior over temporal baselines less than or greater than a particular threshold value whereas TPS are defined as those that exhibit persistent-scatterer-like behavior over temporal baselines bracketed by specific lower and upper bounds. Ten percent of the total permanent scatterers in ERS acquisitions over urban settings are reported to be SPS while the ratio of TPS is reported to be 1% over similar settings.

3.4 Differential Interferogram Calculation

The conventional processing flow involved in point target analysis using the IPTA module of the GAMMA Remote Sensing software is shown in Figure 3.4. Successful identification of point targets using methods outlined in Section 3.3.2 is followed by combining complex values at the point target locations for all SLCs in the data stack to generate complex interferograms. It is important to note that interferograms can be computed using a single SLC as the master or by considering all possible interferometric combinations. The basis for choice between the two possibilities depends on the degree of robustness that can be

associated with the derived phase model. Generally, a single master is adopted when large SLC data stacks (> 40 SLCs) are available for analysis. In such cases, a data stack with (n) complex acquisitions yields (n-1) differential interferograms. On the other hand, when dealing with small data stacks (approximately 10 to 15 SLCs), improved statistical robustness can be achieved by considering all possible interferometric combinations. In such cases, a data stack with (n) complex acquisitions yields $n(n-1)/2$ differential interferograms.

Every interferogram in the stack is characterized by an interferometric baseline. As can be recalled from Chapter 2, the baseline is the distance between the satellites when the two acquisitions used to calculate an interferogram were acquired. Therefore, a stack containing 40 interferograms, for example, can be associated with 40 different baselines. As mentioned in Chapter 2, the phase contribution in an interferogram that results due to the topography in the area for which the interferogram is calculated is a function of the baseline defining the two SLCs used to calculate the interferogram. Hence, the baseline can be perceived as the scaling factor that controls the phase contribution resulting from topography in an interferogram. As mentioned in Chapter 2, an important step in deformation studies involves the simulation of the topographic phase contribution using estimates of the interferometric baseline. Hence, for each interferogram in the stack, the topographic phase corresponding to the baselines characterizing the SLC-pair used to calculate the interferogram is simulated, from initial baseline estimates.

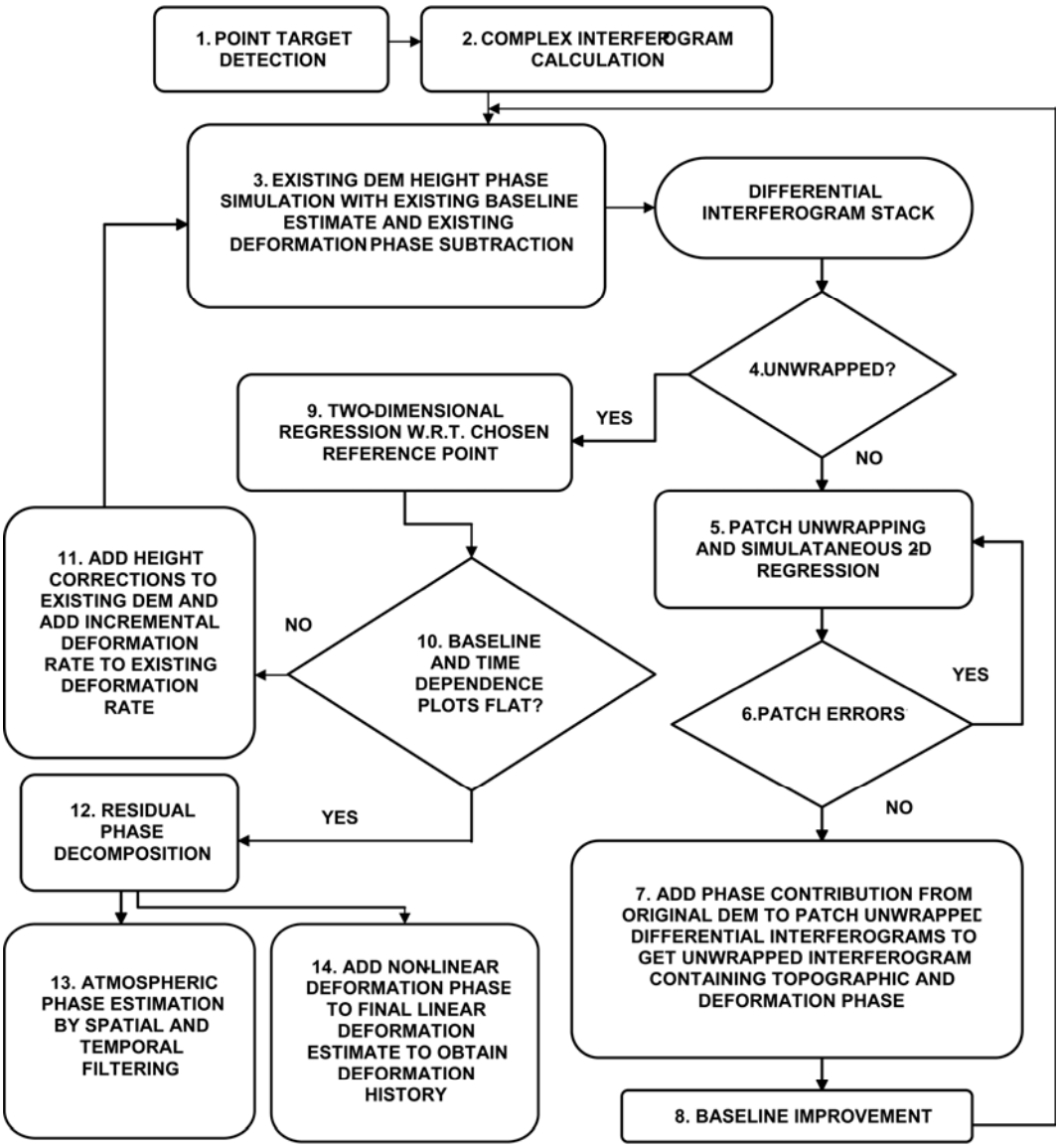

Figure 3.4 IPTA processing flow

The initial baseline estimates are derived based on satellite orbit information. The number of topographic phase estimates will correspond with the number of interferograms calculated. The topographic phase estimates are then subtracted from the corresponding interferograms to obtain a stack of differential interferograms.

Any residual topographic phase contribution that may be present in the differential interferograms due to inaccurate baseline estimates used for topographic phase simulation are compensated for at a later stage of the analysis when a least-squares improvement of the baseline is performed using the unwrapped interferometric phase (Step 8 in Figure 3.4).

3.4.1 Patch Unwrapping

As can be seen from the flowchart in Figure 3.4, correct unwrapping of the interferometric phase must be achieved before baseline improvement can be performed and is hence a very critical step. As mentioned in Section 3.4, the interferograms to be unwrapped are formed by utilizing complex values at the point target locations for interferogram calculations. The IPTA package accomplishes unwrapping of such point-wise interferograms by adopting a *patch unwrapping* technique and spatial smoothness of the unwrapped surface is accomplished by means of a region growing algorithm. The patch unwrapping step forms an integral part of the regression step where the regression solves for the integer number of whole cycles of phase that need to be added to the wrapped phase of a point target in all interferograms comprising the stack of interferograms available for analysis while simultaneously solving for the baseline and time dependence of the phase.

The patch unwrapping step in the IPTA command flow is critical in ensuring robustness of the two-dimensional regression analysis that follows. The patch unwrapping step in IPTA is sought to negate spatial sampling issues that arise from the irregular distribution of point targets in a given study area. This

irregular spatial distribution of point targets makes the conventional phase unwrapping techniques based on assumptions of adequate spatial sampling of the inherent unwrapped phase surface susceptible to unwrapping errors in the form of skipped cycles. Regression analyses performed with such erroneous unwrapped phase values can lead to incorrect phase dependence inferences.

The patch unwrapping approach used in IPTA relies on the available temporal phase history of a particular point target to achieve phase unwrapping in the temporal domain or, in other words, through the data stack adopted for IPTA analysis. The *multi_def_pt* command within the IPTA module simultaneously solves for the unwrapping problem and the baseline and time dependence of the resulting unwrapped phase of a point target with respect to a user specified reference point.

More specifically, the command divides the study area into several user-specified patch sizes. Point targets within each patch are analyzed for feasibility to serve as a local patch reference. Once a reference point is chosen within each patch, the regression analysis is performed for all point targets within each patch with respect to the local reference point for that patch. The unwrapped phase, height corrections and linear deformation rates inferred for all point targets within a patch with respect to the local patch reference are then referenced to the global user specified reference point.

As mentioned in the IPTA reference manual, the deviation of the point target phase values from the best fit 2-D linear regression solution increases with increasing distance of the point targets from the chosen global reference point.

This deviation is attributed to baseline errors and atmospheric path delay phase, both of which vary as a function of distance between two points. Therefore, the reliability of the regression is lower for points located farther from the reference point than for points located closer to the reference point. The patch-wise approach to the accomplishment of phase unwrapping ensures the reliability of the solution by using local patch references in order to maintain short distances between the local reference and other points within the patch.

Unreliable solution of the 2-D regression for some interferograms in the stack results in erroneous unwrapping which translates into “patchy” looking unwrapped surfaces like those shown in Figure 3.5. It is very critical to ensure the proper unwrapping of all interferograms included in the IPTA analysis in order to ensure correctness of the final deformation rates obtained from IPTA.

3.5 Unwrapped Phase Analysis

After accomplishment of unwrapping all differential interferograms in the differential interferogram stack without patch errors, the topographic phase contribution in each interferogram that was calculated using the initial baseline estimates corresponding to each interferogram, is added back to the now unwrapped differential interferogram stack to obtain an *unwrapped interferogram stack*. Each interferogram in this unwrapped interferogram stack, now contains phase contributions from all components outlined in Eq. 3.1 and Eq. 3.2.

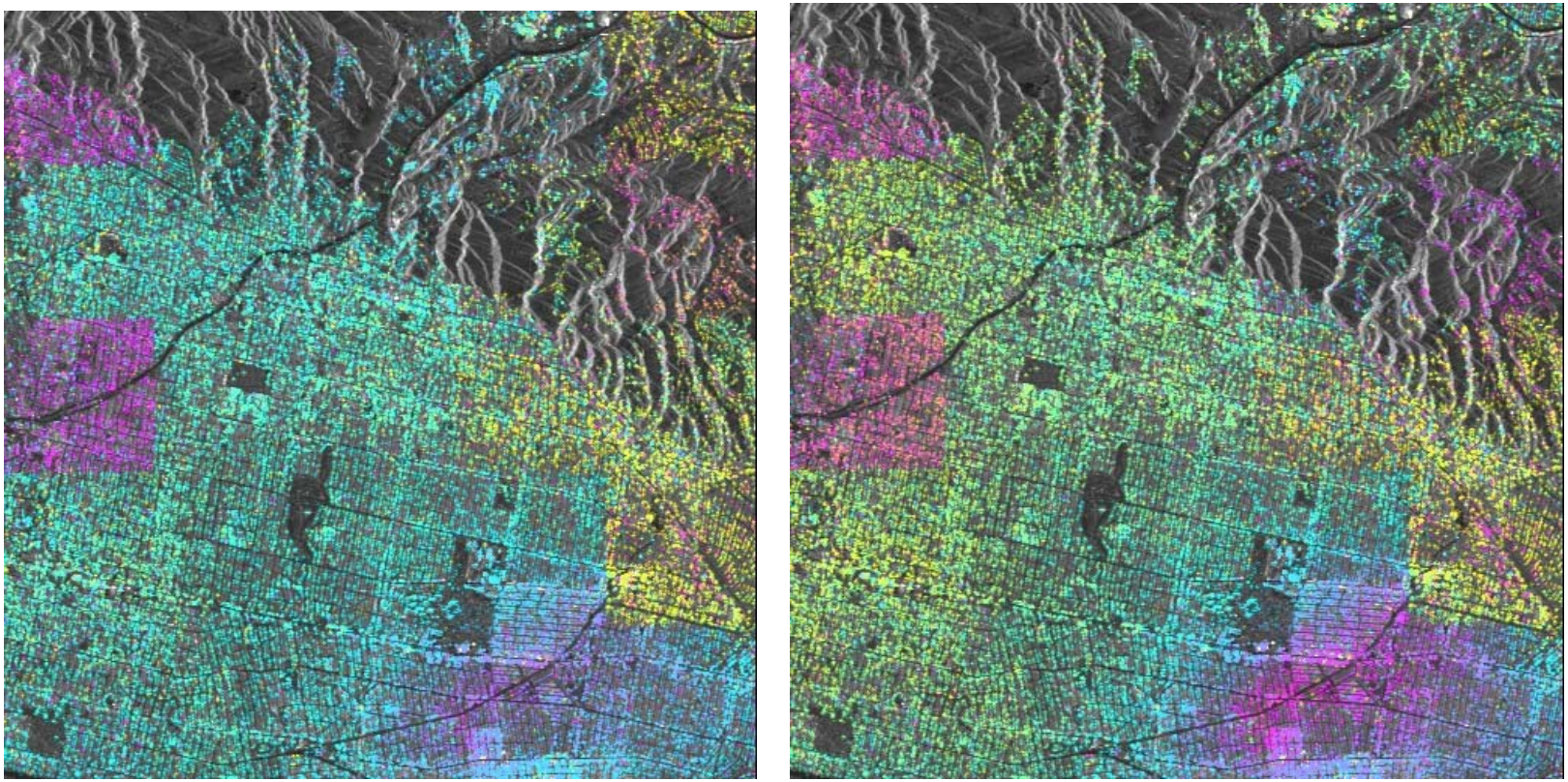

(a) **(b)**

Figure 3.5 Patch unwrapping errors in two unwrapped differential interferograms for a section of Los Angeles. The square patches outline the size of the patches into which the area represented in the interferograms were divided into for patch unwrapping. Each patch measures 100 pixels x 100 pixels. In the two examples shown, the unwrapped phases for the some patches did not fit well with the unwrapped phases for other patches in the interferogram. These erroneous patches are clearly visible in (a) and (b).

In other words, this unwrapped interferogram stack represents an unwrapped version of the complex interferogram calculated in Step 2 of the flowchart shown in Figure 3.4. This unwrapped interferogram stack representing the unwrapped version of the complex interferogram calculated in Step 2, is then used for baseline improvement. The least-squares baseline improvement approach mentioned in Chapter 2 is used to accomplish baseline improvement. After least-squares baseline improvement, a precise baseline estimate is available for each interferogram in the unwrapped interferogram stack. These improved baseline estimates are then used to re-estimate the topographic phase contribution in each interferogram. The improved topographic phase contribution estimates corresponding to each interferogram that is derived from the improved baseline estimates are then subtracted from the corresponding unwrapped interferograms in the unwrapped interferogram stack to derive an *unwrapped differential interferogram stack*.

3.5.1 Two-Dimensional Regression

Since the interferometric phases are now unwrapped, the remainder of the IPTA processing flow focuses on performing statistical analysis of the unwrapped phase associated with all point targets. The statistical analysis accomplishes iterative improvement of the estimates of sources of interferometric phase contribution until all phase in the unwrapped differential interferograms is attributed to its components, namely, linear deformation, non-linear deformation, DEM height corrections, atmospheric path delay phase, or phase noise. Each

interferogram in the unwrapped differential interferogram stack that is used for regression analysis is characterized by

1. a baseline, and
2. a time period.

The baseline, as mentioned before, is the distance between the satellites when the two acquisitions used to calculate an interferogram were acquired. As mentioned in Chapter 2, the interferometric baseline can be defined by its perpendicular and parallel components or by its across-track and parallel components. The time period is defined by the time separating the acquisition times of the two SLCs used to calculate the interferogram. In the IPTA regression analysis, the unwrapped phase is analyzed for dependence on two parameters, namely, perpendicular baseline and time (Figure 3.6). The statistical approach is hence two-dimensional in nature. It should be noted that since point targets are detected by using information from all SLCs available to perform IPTA, the point target locations will be the same for all SLCs and all interferograms calculated from the SLCs. It is important to note that although the two dimensional regression is performed on the unwrapped phase data, the two dimensional regression plots generated by GAMMA show the result of the regression in terms of phase data that has been re-wrapped after being unwrapped. This is reason for the phase axis in Figure 3.6 showing values ranging between $-\pi$ and $+\pi$.

As mentioned in Section 3.4.1, temporal unwrapping of the complex differential interferogram stack is accomplished for point target locations in all

interferograms with respect to a user-defined point target reference. As mentioned in Section 3.4.1, point target analysis is performed with respect to a reference point in order to ensure the reliability of the solution as derived from two-dimensional regression. Robustness of the regression is a function of distance between a point target and the reference point target with smaller distances resulting in greater robustness.

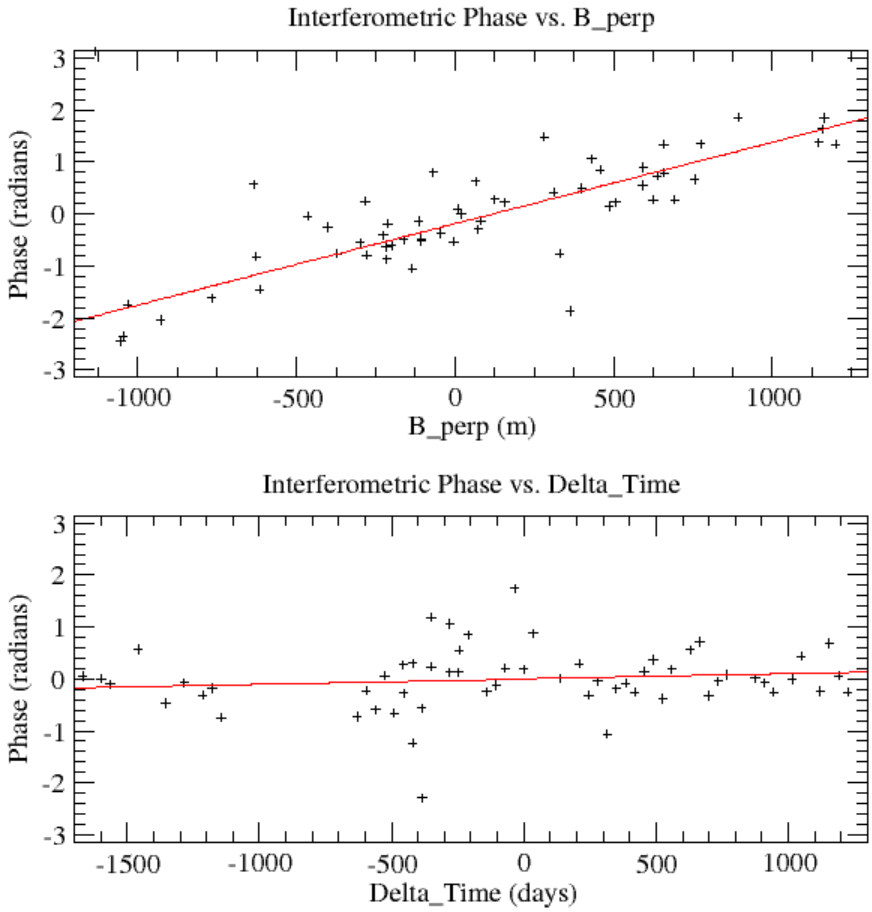

Figure 3.6 Baseline and temporal dependence of differential interferogram phase (Gamma Remote Sensing, 2003).

Each data point in the plots in Figure 3.6 represents the rewrapped differential interferogram phase value at a specific point target location (at different times) with respect to the reference point target location. The number of

data points in the plots, shown by cross marks in Figure 3.6, reflects the number of interferometric combinations used to constrain the phase model. In other words, the number of cross marks defines the number of interferograms in the differential interferogram stack used for statistical analysis. More specifically, in a stack of 40 unwrapped differential interferograms, for example, every point target can be associated with 40 values of unwrapped phase which were calculated with respect to the user-defined reference point. Since the phases are unwrapped with respect to the reference-point, it follows that the height corrections and linear deformation rate estimates inferred from the two-dimensional regression, shown by Steps 9 through 11 of the IPTA processing flowchart (Figure 3.4), are referenced to the user-defined reference point.

For example, if there are 60,000 point targets in a study site, the choice of a reference point among the 60,000 available point target locations, will mean that in steps 9 through 11, the unwrapped phase of all other 59,999 point targets will be analyzed with respect to the user-defined reference point, to infer baseline and time dependence. This is depicted with the help of an illustration in Figure 3.7. The pixel sizes are exaggerated to enhance visualization. Figure 3.6 shows the two-dimensional regression for one such point target when analyzed with respect to a user-defined reference point. The baseline dependence of the unwrapped differential interferometric phase for a given point target with respect to a reference point, as can be inferred from the Phase vs. Baseline plot shown in Figure 3.6(a), translates into a height correction. This height correction is

applied to the given point target assuming that the DEM-derived height of the reference point target is correct.

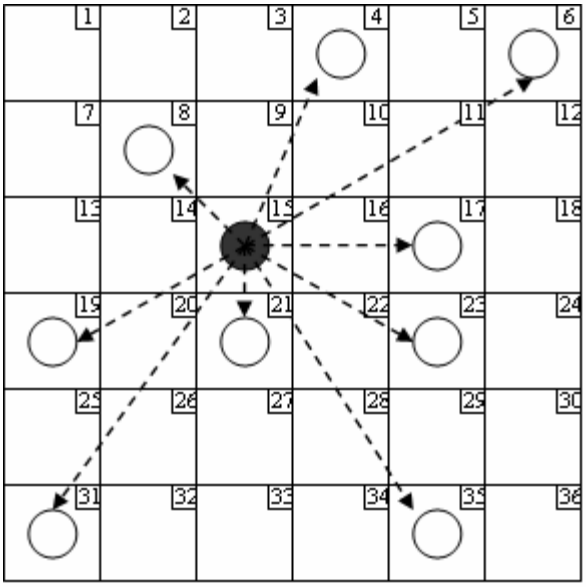

Figure 3.7 Illustration of point target pairs for which regression is conducted. Squares denote individual pixels. The numbers at the top right of each square represent pixel numbers. Pixels with circles in them depict point targets. Pixel number 15 with a solid circle depicts the reference point target. The arrows illustrate that regression is conducted for all point targets relative to the reference point target.

Time dependence of the unwrapped differential interferometric phase for a given point target with respect to a reference point, as can be inferred from the Phase vs. Time plot shown in Figure 3.6(b), translates into the linear deformation rate for a given point target with respect to the reference point.

3.5.2 Phase Model Improvement

As can be seen from Figure 3.6, the baseline and time dependence of unwrapped phase is modeled by linear regression. The difference between the original unwrapped phase values and the phase values modeled by the two

trends shown in Figure 3.6, defines the deviation of the unwrapped phase values from the two linear trends. In order to ensure that all baseline and time dependence of the unwrapped phase is modeled, any such deviation of phase values from the linear regression is subjected to additional iterations of Steps 9 through 11 shown in Figure 3.4. Any height corrections and linear deformation rates derived from these successive iterations are added to the original estimates derived from the first iteration of Steps 9 through 11.

As can be seen from the IPTA processing flowchart (Figure 3.4), the iterative loop formed by Steps 9 through 11 terminates when the baseline and time dependence plots for all point targets, with respect to the user-defined reference point, are characterized by a linear regression trend having zero slope. The zero slope indicates that all baseline and time dependence inherent in the unwrapped phase values has been modeled. This iterative process defines the phase model improvement stage wherein estimates of DEM height corrections and linear deformation rates are continually appended until estimated incremental corrections become negligible, as can be perceived from the slope of the baseline and time dependence plots.

3.5.3 Residual Phase Decomposition

Any deviation of the unwrapped phase values from the zero slope linear regression trends obtained at the end of the phase model improvement step is termed residual phase. The components constituting the residual phase are outlined in Eq. 3.2. Spatial and temporal filtering techniques are used to decompose residual phase into atmospheric phase, non-linear deformation

phase and phase noise. Residual phase decomposition is comprised of the following steps:

1. Spatial filtering of the residual phase to reduce phase noise.
2. Temporal filtering of the spatially filtered residual phase to identify phase contributions correlating with time periods associated with the temporal window chosen for filtering. Phase values identified during the temporal filtering stage are associated with non-linear deformation.
3. The non-linear deformation phase is subtracted from the spatially filtered residual phase obtained in Step 1 above.
4. This is followed by appropriate spatial filtering to reduce any remaining noise to obtain phase contribution induced by atmospheric path delay.

The non-linear deformation estimate for each point target is added to the corresponding linear deformation estimates to obtain the final deformation history for each point target with respect to the user-defined reference point. Figure 3.8 illustrates the results obtained from IPTA processing as applied to a differential interferogram stack calculated by SLCs acquired by the ERS platform on Track 368 over Northern Chile. Figure 3.8(a) shows one unwrapped differential interferogram. Figure 3.8(b) shows the linear deformation component of Figure 3.8(a) as estimated from IPTA. Figure 3.8(c) shows the height corrections that were inferred for all points in the interferogram at the end of the IPTA analysis. Figure 3.8(d) shows a map of the residual phase component present in the unwrapped differential interferogram shown in Figure 3.8(a).

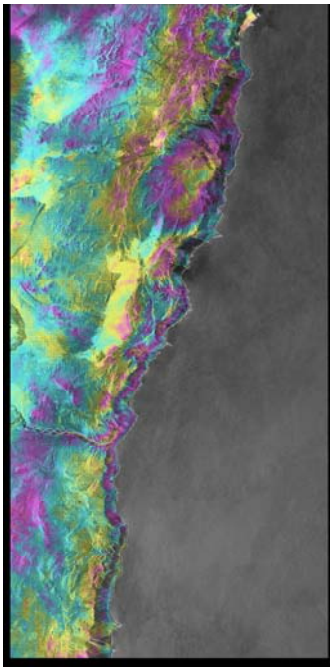

(a) Unwrapped Differential Interferogram

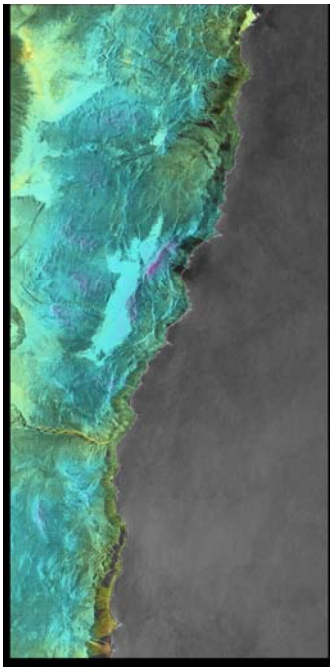

(b) Linear Deformation

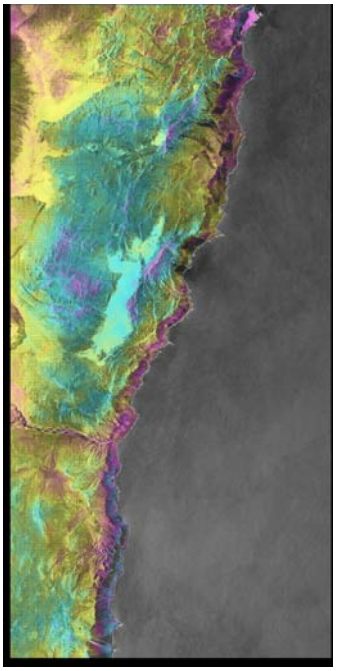

(c) Height Correction

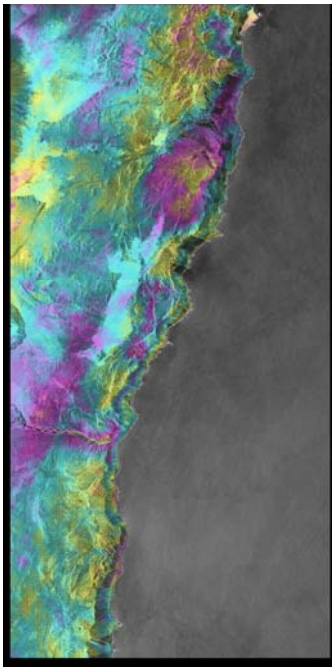

(d) Residual Phase

Figure 3.8 Unwrapped differential interferogram phase resolved into its components using IPTA. All images are in satellite viewing geometry. One color cycle in (a) corresponds to 2π radians of phase.

Recall that the residual phase is composed of non-linear deformation, atmospheric phase and phase noise whose maps have not been shown in Figure 3.8.

As can be inferred from the processing flow described above, the final deformation rates are obtained by the summation of deformation trends derived by means of linear regression of updated differential interferogram phases in each of the iterations, while atmospheric phase and non-linear deformation regimes are derived by making use of their spatial and temporal spectral signatures.

Other advanced methods that use non-linear models to derive deformation estimates is provided in Ferretti et al. (2000) with illustrations relating to non-linear temporal deformation signature resulting from ground water pumping in Pomona, California.

3.6 Accuracy of Method

Sub-millimeter accuracy of deformation inferred from InSAR time series was verified by Ferretti et al. (2007) by means of a “blind experiment” in which line-of-sight (LOS) motion of one dihedral reflector which was moved with respect to another which was kept motionless, was derived using interferometric methods and compared to ground truth data. The two pairs of man-made dihedral reflectors were placed 50 m apart and designed to dominate the backscatter of the resolution element they were placed in. In addition, the two pairs of reflectors were oriented such that they could be imaged by both ascending and descending Radarsat-1 and Envisat orbits with the purpose of being able to derive the

components of LOS motion projected in all three dimensions for comparison with ground truth. Standard deviations of error of 0.58 mm and 0.75 mm were reported for the East-West and vertical components.

Colesanti et al. (2001) compare the persistent scatterer technique to Global Positioning System (GPS) and optical leveling techniques of measuring displacements. Very good agreement of line of sight deformation estimates inferred from persistent scatterers are reported for targets identified in the vicinity of optical leveling benchmarks that are reported to have been used during surveying operations performed in South-West Ancona, Italy. The region is characterized by gradual landslide induced ground deformation. Also, similarity in deformation rates inferred from persistent scatterer and GPS techniques is reported with reference to deformation recorded in the Los Angeles basin using the Southern California Integrated GPS Network (SCIGN). In their study, Colesanti et al.(2001), projected the deformation estimates inferred from optical leveling and GPS onto the satellite line of sight (LOS) to facilitate comparison.

In their effort to investigate the effect of the 30 MHz operating frequency shift between ERS and Envisat SAR's, on the feasibility of extending an ERS-1/2 persistent scatterer time series by means of cross platform interferograms between ERS-2 and Envisat acquisitions, Colesanti et al. (2003c) conclude that persistent scatterers in ERS acquisitions having coherence values above 0.95 exhibit persistent scatter like behavior in Envisat acquisitions despite the discrepancy in the carrier frequencies of the two platforms. Moreover, it has been shown that the phase shift resulting in ERS-Envisat interferograms, that varies as

a function of slant range location of the targets, can be used to obtain high precision location of the scatterers.

Perissin et al. (2004) show that 60-70% of the points identified as point scatterers using ERS acquisitions are detected as persistent scatterers in Envisat acquisitions and can thus be used to extend the temporal extent of the time series by means of computing ERS-Envisat interferograms for the points identified as persistent scatterer by both platforms.

3.7 Applications to Non-Tectonic Problems

Due to the achievable precision associated with point target time series approaches, the method has found use in inferring both spatial and temporal deformation signatures resulting from various tectonic and non-tectonic processes. A brief overview related to the monitoring of ground deformation due to various non-tectonic processes using point target or persistent scatterer time series as reported in the literature is presented. Persistent scatterers are referred to by different names by different authors. In the literature review presented in the following section, these stable scatterers are referred to by the naming convention chosen by the respective authors.

3.7.1 Landslide Monitoring

Farina et al. (2006) report the use of the “permanent scatterer” technique to facilitate landslide inventory mapping and monitoring slopes known to exhibit movements related to instability in the Arno river basin in Italy. Colesanti and Wasowski (2006) present a case study where the permanent scatterers

technique was used to discern slope instability related movements in the Liechtenstein Alps. The authors state that the strengths of the technique lie in its ability to aid in:

1. distinguishing stable and unstable regions on a large scale, and
2. hazard mapping.

Bovenga et al. (2006) and Wasowki et al. (2006) present an optimized approach aimed at identifying “persistent scatterers” in Caramanico where standard persistent scatter methods yielded low persistent scatterer densities. The optimized approach is termed Stable Point Interferometry over Un-Urbanized Areas (SPINUA). The authors verify the deformation estimates derived from the detected stable scatterers by verifying the conformity of their location with previously identified regions of landslide activity.

3.7.2 Mining Related Subsidence

Kircher et al. (2004) present the use of the IPTA analysis in inferring ground deformation in the Rhine river embayment in Germany resulting from large-scale groundwater drawdown during mining. The authors confirm the validity of the deformation estimates derived at point target locations using IPTA by comparing them with leveling measurements in the area.

Colesanti et al. (2005) have applied the persistent scatterer technique to assess ground deformation occurring in a 300 m x 300 m area in Roncourt located in the iron mining basin of Lorraine, France.

Walter et al. (2005) present the results of an extensive analysis used to verify permanent scatterer inferred subsidence due to coal mining at the Prosper-

Haniel mine in the Ruhr region, Germany with ground truth. The authors report the use of 78 ERS-1/2 scenes to constrain their interferometric analysis.

Jung et al. (2007) applied the persistent scatterer technique to infer subsidence rates at an abandoned coal mine in the Gaeun coal mining region in Korea. Twenty-five JERS-1 images acquired between 1992 and 1998 over the region were analyzed for deformation. The authors report the inference of a maximum subsidence of 11.2 cm over the time period of analysis. It is reported that the mean deformation rates derived from the interferometric analysis is consistent with the deformation rates associated with the extent of ground cracking levels measured at the site.

3.7.3 Other Studies

Meisina et al. (2006) use the permanent scatterer approach for deformation monitoring in the complex geological and structural setting of Oltrepo Pavase in Northern Italy which is also characterized by clay-rich sediment. The study area is reported to be characterized by both shallow and deep landslides and movements related to shrinkage and swelling of clayey soils. The study was carried out using SAR imagery acquired between 1992 and 2001 and detected deformation rates are reported to vary between + 5 mm/yr to -16 mm/yr where "+" indicates uplift and "-" indicates subsidence. The use of the permanent scatter technique is reported to have enabled the detection of some previously unknown regions characterized by slope instability.

Yue et al. (2005) report the use of the permanent scatterer technique to derive deformation rates and an improved DEM of Las Vegas using ERS-1/2 SAR data stacks.

Declercq et al. (2006) use a data stack containing seventy-four ERS-1/2 SAR scenes acquired between 1992 and 2003 to identify 173,000 permanent scatterers and investigate ground water pumping related subsidence in a 900 km^2 area located in the Ottignies-Wavre area in Brussels, Belgium. The detected regions of subsidence are reported to correspond to water-catchment regions and aquifers subjected to ground water withdrawal.

Allievi et al. (2003) report the use of permanent scatterers in monitoring slow mass movements in the Lombardy alpine region of Italy between 1993 and 2000. The authors report identification of more than 380,000 permanent scatters for use in the analysis despite the reasonably un-urbanized nature of the study area. The data used in identifying the permanent scatters is reported to consist of two stacks, one containing 51 scenes in the ERS descending imaging mode and the other containing 29 scenes in the ERS ascending mode of imaging.

Riedmann and Haynes (2005) present the use of millimeter precision achievable from persistent scatterer interferometry to supplement traditional surveying techniques for ground stability detection. The usefulness of the technique to aid in the effective selection of locations suitable for pipeline network installation is demonstrated.

3.8 Summary

This chapter presented an overview of the point target time series analysis technique, recent developments in the field and its applications in monitoring non-tectonic spatial and temporal deformation signatures. The specifics of how this method was used to accomplish the objectives of this study are described in detail in the next chapter.

4. METHODS

4.1 Introduction

This chapter introduces the study area and provides details pertaining to the point target analysis performed to achieve the objectives of this study. As can be recalled from Chapter 1, this study was designed to fulfill the following objectives:

1. Evaluate the feasibility of using IPTA to detect small spatial-scale deformation features by computing the deformation time histories resulting from the construction of the Red Line in Los Angeles,
2. Investigate the influence of dataset characteristics on the application of the conventional IPTA processing flow, and
3. Quantify the dependence of the IPTA-derived deformation time history on the number of satellite acquisitions used to constrain the analysis.

The first objective was designed to investigate the feasibility of using IPTA to detect deformations on spatial scales typical of civil engineering construction activities. The second and third objectives were motivated by situations confronted when limited numbers of SAR acquisitions or SLCs are available to constrain an IPTA processing flow. Given that IPTA enables utilization of SLCs separated by very long spatial as well as temporal baselines, such situations arise mainly due to limited imagery being available for a particular study area.

The first objective was addressed by performing an IPTA analysis using all SLCs acquired over the study area between 1992 and 2000. The second and third objectives were addressed by applying the IPTA processing flow to subsets of data that were derived from the stack of SLCs acquired over the study area between 1992 and 2000. The ease of application of the conventional IPTA processing flow in the second objective was evaluated by investigating the possibility to temporally unwrap or patch unwrap a subset of available data without obtaining patch unwrapping errors. For reasons provided later in the chapter, the average baseline of these subsets was used as the quality measure to investigate the second objective.

In addition to details about the study area and experimental processing details, a list of SAR acquisitions used for the study and details pertaining to the software used for analysis has been provided.

4.2 Study Area

Characteristics of the study area and criterion governing its choice for this study are discussed in the following sections.

4.2.1 Site Selection Criteria

Suitability of a site for the study aimed at addressing the above-mentioned objectives was assessed based on the following desired characteristics:

1. Availability of extensive SAR data for the study area with sufficient spatial and temporal coverage,

2. Study area characterized by an urban setting (due to the quality and density of point targets that can be identified in such a setting), and
3. Known occurrence of localized ground deformation resulting from civil engineering construction activities.

Due to (a) reported subsidence encountered along Hollywood Boulevard (Figure 4.1 and Figure 4.2) during construction of the Los Angeles Metro Rail Red Line, and (b) availability of 52 SAR scenes spanning the time between 1992 and 2000, SAR imagery of Los Angeles was used for Interferometric Point Target Analysis (IPTA) presented study.

4.2.2 Characteristics of the Red Line

Key features of the Red Line construction as described by Stirbys et al. (1999) can be summarized as follows:

The 37-km long Los Angeles Metro Rail Red Line subway, which was developed under the supervision of the Metropolitan Transportation Authority (MTA), forms an important segment of the 480 km rail system that was designed to serve the Los Angeles area. The Red Line was constructed in three segments, namely segments 1, 2 and 3 shown in Figure 4.2. Construction on segment 1 was performed between 1987 and 1993. Construction along the Wilshire Boulevard section of segment 2 was performed between 1991 and 1996 while the Vermont and Hollywood sections of segment 2 were scheduled to be completed in 1998. Construction along segment 3 was performed between 1994

Figure 4.1 Google Earth image of study area. Los Angeles Metro Rail Red Line is delineated in red.

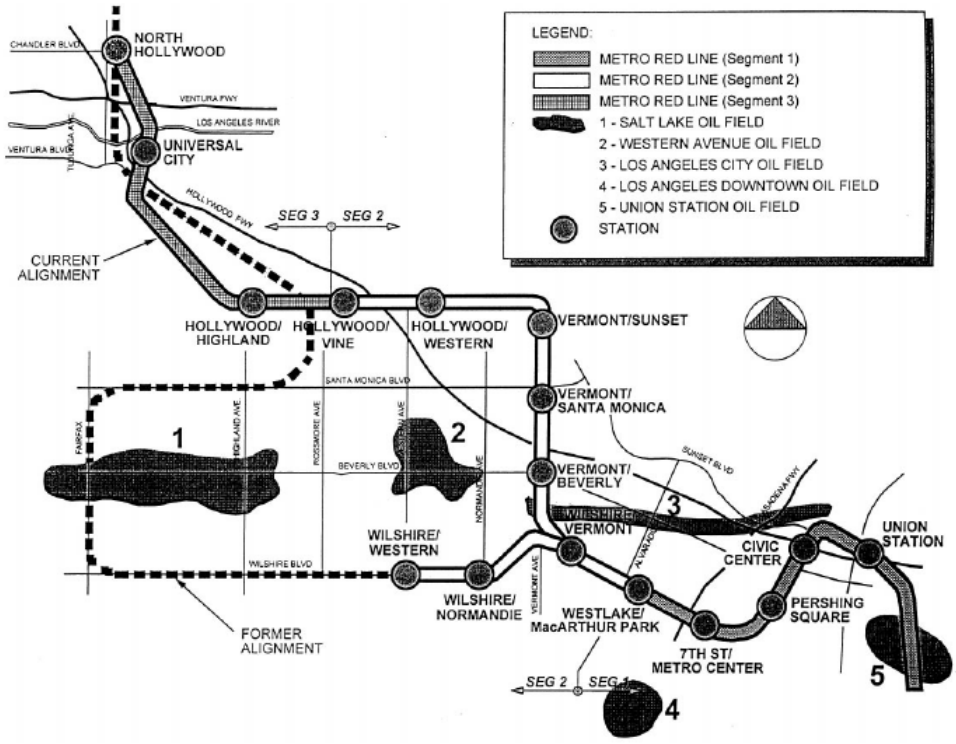

Figure 4.2 Layout and stages of construction of Los Angeles Red Line (Stirbys et al., 1999).

and 2000. The imaged area covered by the section of SAR imagery used in this study (Figure 4.1) is representative of sites where construction of the entire second segment and a part of the third segment of the Red Line was pursued. Segment 2 is comprised of 11-km-long twin tunnels connecting eight subway stations, whereas Segment 3 is comprised of 10-km-long twin tunnels connecting three subway stations. The subway stations are marked by concentric circles in Figure 4.2. Each of the twin tunnels had a post-boring diameter of 6.6 m which was reduced to 5.5 m after finishing. The pillar separating the side walls of the two tunnels had a width that varied between 4.4 m and 6.1 m. The depth of the tunnels varied between 11 m below ground level at subway stations to 300 m

along the third segment of Red Line that was routed through the Santa Monica Mountains.

As shown in Figure 4.3, sections of segment 2 were bored through the following sub-surface conditions at various points along the alignment:

1. Alluvial deposits varying in age from the Pleistocene to the Holocene, and
2. Upper Miocene to Plio-Pleistocene aged sandstone, siltstone and claystone formations.

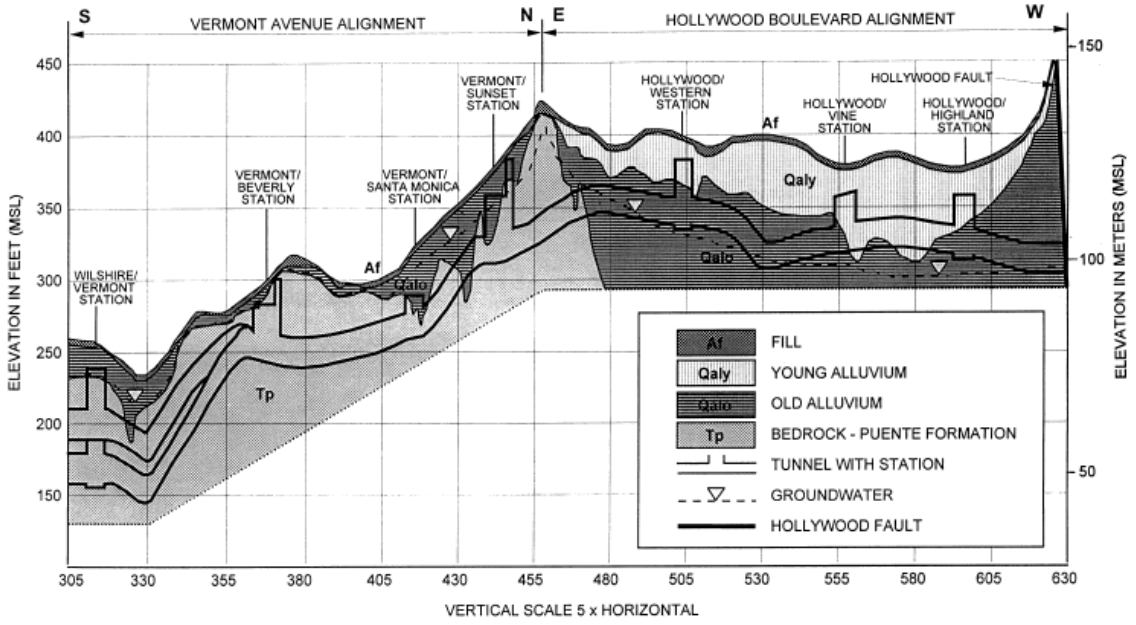

Figure 4.3 Geologic profile along segment 2 of the Red Line (Stirbys et al., 1999). Note that Vermont Avenue tends North-South whereas Hollywood Boulevard tends East-West.

Prevalence of these geological features throughout most of the area represented in Figure 4.1, necessitated soft-ground tunneling techniques to be adopted during the construction of most of the Red Line, excluding the portion of Segment 3 that

passed through the Santa Monica Mountains, where hard rock tunneling methods were used.

The Salt Lake Oil Field located on Beverly Boulevard between Fairfax and Highland Avenue, and the Western Avenue Oil Field located on Beverly Boulevard between Western Avenue and Normandie Avenue, as shown in Figure 4.2, are two abandoned oil fields situated in the vicinity of the Red Line alignment. Their location is of importance in the context of deformation features that were detected on analyzing SAR imagery of the study area while assessing the first objective of the study.

4.2.3 Subsidence Features in Study Area

According to Bell (1999), instances of ground deformation observed following the beginning of tunneling beneath Hollywood Boulevard include:

1. Subsidence of 2” occurred during the construction of the first of two tunnels located 80’ below Hollywood Boulevard in August 1994, as opposed to the expected subsidence of ½”.
2. Construction of the second tunnel that began three weeks later was accompanied by subsidence ranging from 5” to 10” with buildings on the section between Vine and the El Capitan Theater incurring severe damage.
3. Occurrence of an 80’ wide sinkhole on the 6300 block of Hollywood Boulevard on June 22, 1995 accompanied by cracking of the tunnel near the sinkhole.

Although these settlements are substantial, they likely occurred over a very localized region. The feasibility of detecting these small spatial scale settlements was investigated as part of the first objective of this study.

4.3 Data

The following raw data were used for interferometric analysis of the study area:

1. A stack of 52 SAR images acquired by the ERS-1 and ERS-2 platforms over Los Angeles, California. Although data for the entire 100 km x 100 km area defined by ERS Track 442, Frame 2925 were obtained, a 500 pixel x 2500 pixel area containing the Los Angeles Red Line was clipped from the full frame image for interferometric point target analysis (IPTA) using the GAMMA Remote sensing software. A list of all SAR images used in the analysis is provided in Table 4.1. The SAR images are denoted by their respective ERS orbit numbers and acquisition dates. The geographic coordinates of the four corners defining the clipped section of the SAR image used for IPTA are listed in Table 4.2.
2. A Digital Elevation Model (DEM) of the study area as acquired during the Shuttle Radar Topography Mission (SRTM) and sampled at 1 arc-second. The 1 arc-second sampling translates into a 30 m x 30 m DEM pixel.

4.4 Software Used in Study

The IPTA software package, developed and distributed by GAMMA Remote Sensing, was used for point target analysis performed in this study.

Table 4.1 List of SAR scenes of Los Angeles used for point target analysis.

#	Platform	Orbit	Date	#	Platform	Orbit	Date
1	ERS1	4595	1-Jun-92	27	ERS2	7811	17-Oct-96
2	ERS1	6098	14-Sep-92	28	ERS2	8312	21-Nov-96
3	ERS1	6599	19-Oct-92	29	ERS2	8813	26-Dec-96
4	ERS1	7100	23-Nov-92	30	ERS2	9815	6-Mar-97
5	ERS1	7601	28-Dec-92	31	ERS2	10316	10-Apr-97
6	ERS1	11108	30-Aug-93	32	ERS2	10817	15-May-97
7	ERS1	11609	4-Oct-93	33	ERS2	11318	19-Jun-97
8	ERS1	12110	8-Nov-93	34	ERS2	11819	24-Jul-97
9	ERS1	19468	5-Apr-95	35	ERS2	13322	6-Nov-97
10	ERS1	19969	10-May-95	36	ERS2	13823	11-Dec-97
11	ERS1	20470	14-Jun-95	37	ERS2	14324	15-Jan-98
12	ERS1	20971	19-Jul-95	38	ERS2	14825	19-Feb-98
13	ERS1	21472	23-Aug-95	39	ERS2	17330	13-Aug-98
14	ERS1	21973	27-Sep-95	40	ERS2	17831	17-Sep-98
15	ERS1	22474	1-Nov-95	41	ERS2	18332	22-Oct-98
16	ERS1	22975	6-Dec-95	42	ERS2	18833	26-Nov-98
17	ERS1	23476	10-Jan-96	43	ERS2	19334	31-Dec-98
18	ERS1	23977	14-Feb-96	44	ERS2	19835	4-Feb-99
19	ERS1	24979	24-Apr-96	45	ERS2	20336	11-Mar-99
20	ERS1	25480	29-May-96	46	ERS2	22340	29-Jul-99
21	ERS2	2801	2-Nov-95	47	ERS2	23342	7-Oct-99
22	ERS2	3302	7-Dec-95	48	ERS2	24344	16-Dec-99
23	ERS2	3803	11-Jan-96	49	ERS2	26348	4-May-00
24	ERS2	4304	15-Feb-96	50	ERS2	26849	8-Jun-00
25	ERS2	6308	4-Jul-96	51	ERS2	27851	17-Aug-00
26	ERS2	7310	12-Sep-96	52	ERS2	29354	30-Nov-00

Table 4.2 Coordinates of SAR scene corners.

Azimuth Pixel #	Range Pixel #	WGS84 Latitude (degrees)	WGS84 Longitude (degrees)
0	0	34.04	-118.29
0	499	34.06	-118.40
2499	0	33.95	-118.31
2499	499	33.97	-118.43

GAMMA Remote Sensing, based near Bern, Switzerland, was founded in 1995 by Dr. Charles Werner and Dr. Urs Wegmuller. In addition to the IPTA package, the Modular SAR Processor (MSP) - used for processing raw SAR data into SLCs, the Interferometric SAR Processor (ISP) - used for interferometric computations, Differential SAR Interferometry and Geocoding (DIFF&GEO)- used for differential interferometry, and Land Application Tools (LAT)- used for adopting SAR imagery for land applications, are other software packages that are provided by GAMMA Remote Sensing. Programs comprising the IPTA software package that were used in this study were run on a Dell Precision 690 Workstation operating on an Intel Xeon processor.

4.5 Datasets Analyzed

Although the IPTA processing flow and IPTA programs that were used to accomplish the different objectives of this study were essentially the same, the datasets to which these programs were applied were different depending on the objective being addressed. All future references to the sizes of datasets analyzed will be made with respect to the number of interferograms that were used for point target analysis. All interferograms comprising the datasets analyzed to accomplish the three objectives of this study were calculated with respect to a common reference SLC, namely, ERS1-11609, and included the auto-interferogram. Datasets comprised of fewer than 52 interferograms are referred to as subsets and were computed from a stack of SLCs that contained a subset of all the available 52 SLCs shown in Table 4.1

The auto-interferogram is an interferogram calculated between the common reference SLC and itself. The auto interferogram enables atmospheric phase quantification, as will be explained in more detail in Section 4.6.2.1. Therefore, a dataset containing a total of n interferograms was calculated from n SLCs. All SLCs were coregistered and resampled to the geometry of ERS1-11609 (master SLC) before interferogram calculations.

4.5.1 Detection of Subsidence over Red Line

To investigate the feasibility of using IPTA to detect subsidence resulting from tunneling during the construction of the Los Angeles Red Line, all steps comprising the IPTA processing flow shown in Figure 3.4 in Chapter 3, were applied to a dataset containing 52 interferograms that were computed from all 52 SLCs listed in Table 4.1. As mentioned in Section 4.5, the count of 52 interferograms is inclusive of the auto-interferogram.

4.5.2 Dependence of Temporal Unwrapping on Average Baseline of Dataset

To investigate the influence of acquisition parameters (namely, number of scenes and average baseline) on the ability to successfully patch unwrap all interferograms comprising a dataset, a total of 94 subsets of data were initially analyzed using Steps 2 through 6 from the IPTA processing flow shown in Figure 3.4 in Chapter 3. Accomplishment of successful patch unwrapping was assessed based on the ability to unwrap all interferograms comprising a dataset without patch errors. For reasons mentioned in Section 4.6.1, the point targets detected

using all 52 available SLCs while addressing the first objective, were used for processing related to this part of the study.

Not counting the auto-interferogram, which was included in all datasets analyzed for patch unwrapping errors, datasets containing 15, 20, 25, 30, 35, 40 and 45 interferograms were analyzed in this part of the study. Figure 4.4 summarizes the total number of datasets generated containing each of the above mentioned number of interferograms. Each dataset generated was initially analyzed for feasibility in unwrapping without patch errors.

Datasets that could be unwrapped successfully were then subjected to the remainder of the conventional IPTA processing flow, namely Steps 7 through 14 as outlined in Figure 3.4 in Chapter 3. Details pertaining to patch unwrapping and the two-dimensional regression analysis have been provided in Section 4.6.

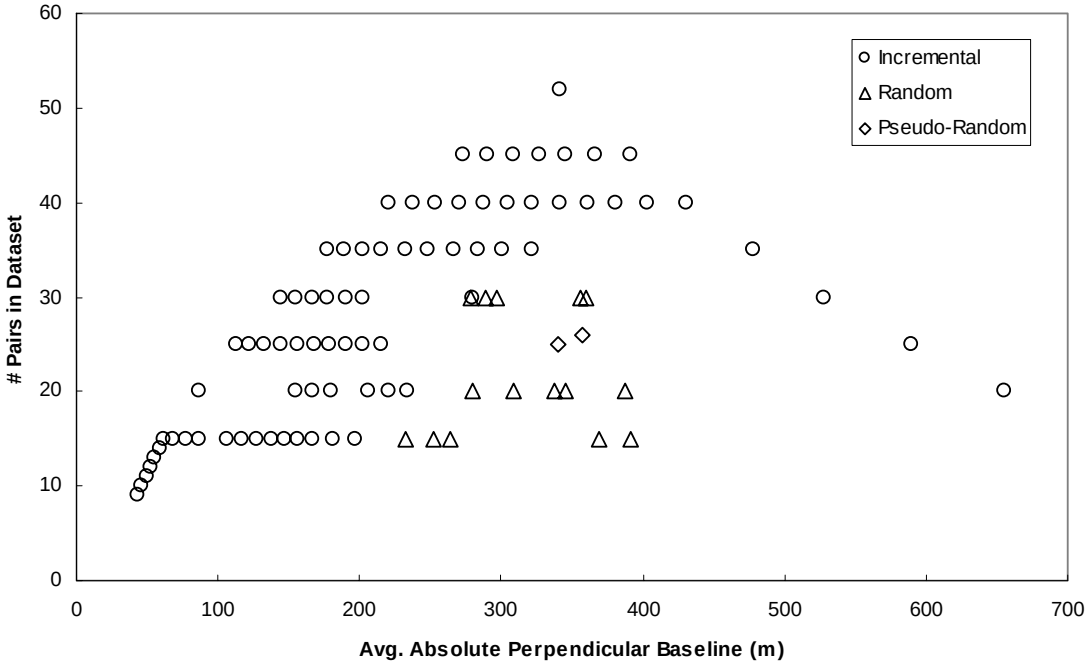

Figure 4.4 Datasets generated for point target analysis.

In Figure 4.4, the datasets are categorized as *incremental*, *random* and *pseudo-random*, based on the method in which they were generated.

1. The incremental method corresponds to that by means of which interferograms comprising datasets were chosen on the basis of increasing order of absolute perpendicular baselines characterizing them. This method of choice has been illustrated in Figure 4.5 by means of a hypothetical example wherein twenty interferograms were assumed to be available for dataset generation. In the example shown in Figure 4.5, numbers 1 through 20 represent twenty available interferograms sorted in increasing order of their absolute perpendicular baselines. So, pair 1 represents an interferogram with the lowest absolute perpendicular baseline whereas pair 20 represents an interferogram with the highest absolute perpendicular baseline among the twenty available interferograms. The brackets represent a sliding window of a fixed size wherein interferogram numbers bracketed by the window represent interferograms that constitute a dataset. Hence, a unique dataset can be associated with each new position of the sliding window.

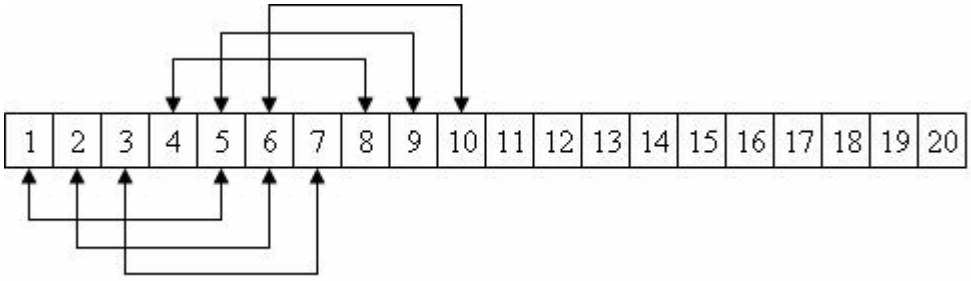

Figure 4.5 Illustration of incremental method of generating datasets using sliding window.

Specifically, in Figure 4.5, the size of the sliding window is five. The size of window is chosen according to the size of the dataset desired. Moreover, it can be seen from Figure 4.5 that the sliding window was chosen to move to the right in steps of one until no more datasets of the desired size could be generated.

For this study, the number of available non-zero baseline interferograms was 51. Sliding window sizes of 15, 20, 25, 30, 35, 40 and 45 were chosen to generate incremental datasets for analysis. Hence, a dataset containing 45 interferometric pairs and corresponding to the lowest average baseline, for example, contained interferograms representing the 45 lowest absolute perpendicular baselines of the available 51 non-zero perpendicular baselines. Similarly, the 45 interferogram dataset corresponding to the second-lowest average baseline was generated by moving the sliding window to the right by one interferogram. Hence, it was possible to generate seven such datasets containing 45 interferograms defined by non-zero perpendicular baselines. Similarly, the dataset corresponding to the lowest average baseline of all datasets analyzed and containing 15 interferograms, contained those interferograms that were defined by the 15 lowest perpendicular baselines among the available 51 non-zero perpendicular baseline interferograms.

2. The random method of choice corresponds to datasets formed by random number generation as was achieved using Microsoft Excel. Non-repeating random numbers between 1 and 52 were generated using Excel. The

generated random numbers were then associated with the corresponding interferograms to which the IPTA processing flow would be applied. Table 4.3 lists the interferometric combinations corresponding to numbers between 1 and 52 as used in the IPTA analysis.

Perpendicular baseline values shown in Table 4.3 correspond to the component of the distance between the satellites when the center of the master and slave SLCs were acquired. The perpendicular baseline values are positive or negative depending on the relative positions of the satellites at the time of acquisition of the center of the master and slave SLCs. A positive perpendicular baseline implies that the satellite with which the slave SLC was acquired was positioned to the right of the look vector of satellite with which the master SLC (ERS1-11609) was acquired (Hanssen, 2001).

3. The two pseudo-random datasets shown in Figure 4.4 contained every other combination of the possible 51 non-zero baseline interferograms listed in Table 4.3, ie., excluding the auto-interferogram. Hence, one pseudo-random set contained 26 non-zero interferometric pairs numbered 1,3,5,7,…,51 in Table 4.3 whereas the other contained 25 that were numbered 2,4,6,8,…,50 in Table 4.3.

The average perpendicular baseline corresponding to each dataset shown in Figure 4.4 was calculated by the ratio of the sum of absolute perpendicular baselines of interferograms comprising the dataset to the number of non-zero

baseline interferograms in the dataset. Hence the auto-interferogram was not accounted for in the average perpendicular baseline calculations.

Table 4.3 List of Interferograms used in study. Only slave images are listed since all interferograms were calculated with respect to a common master-ERS1, Orbit11609.

	Slave		Perp.		Slave		Perp.
#	Platform	Orbit	Baseline (m)	#	Platform	Orbit	Baseline (m)
1	ERS1	4595	234.72	27	ERS2	8312	1171.35
2	ERS1	6098	599.71	28	ERS2	8813	-79.42
3	ERS1	6599	-151.31	29	ERS2	9815	23.25
4	ERS1	7100	328.06	30	ERS2	10316	657.01
5	ERS1	7601	-421.99	31	ERS2	10817	53.27
6	ERS1	11108	-313.37	32	ERS2	11318	-46.70
7	ERS1	12110	209.31	33	ERS2	11819	76.28
8	ERS1	19468	-214.52	34	ERS2	13322	-716.81
9	ERS1	19969	-986.10	35	ERS2	13823	-638.58
10	ERS1	20470	-80.63	36	ERS2	14324	-216.50
11	ERS1	20971	113.70	37	ERS2	14825	-304.08
12	ERS1	21472	12.79	38	ERS2	17330	65.01
13	ERS1	21973	214.79	39	ERS2	17831	-773.67
14	ERS1	22474	859.03	40	ERS2	18332	-362.14
15	ERS1	22975	217.72	41	ERS2	18833	-110.49
16	ERS1	23476	184.21	42	ERS2	19334	-819.73
17	ERS1	23977	674.87	43	ERS2	19835	-395.25
18	ERS1	24979	876.63	44	ERS2	20336	-35.58
19	ERS1	25480	-335.79	45	ERS2	22340	452.04
20	ERS2	2801	711.02	46	ERS2	23342	-360.98
21	ERS2	3302	67.19	47	ERS2	24344	512.79
22	ERS2	3803	68.08	48	ERS2	26348	-18.05
23	ERS2	4304	695.18	49	ERS2	26849	-210.40
24	ERS2	6308	337.99	50	ERS2	27851	-103.83
25	ERS2	7310	-153.31	51	ERS2	29354	-89.20
26	ERS2	7811	430.25	52	ERS1	11609	0.00

The generated datasets were then used for differential interferogram generation and subsequent patch-unwrapping and two-dimensional regression analysis. In cases where unwrapping could not be achieved without patch errors

for some interferograms in an analyzed dataset, the specific pairs within the analyzed datasets that were affected by patch unwrapping errors were excluded from the dataset and hence further analysis. This resulted in a reduction in the number of interferograms constituting the dataset and hence a modification in the average baseline corresponding to the dataset. The patch unwrapping step was then applied to the resulting modified dataset and any patch unwrapping errors were checked for. This procedure was repeated until no patch unwrapping errors were found in any of the interferograms constituting a dataset. The modified average baseline and the number of interferograms characterizing the dataset having no patch unwrapping errors were recorded.

4.5.3 Influence of Number of Interferograms on Derived Deformation Rates

Quantification of the dependence of the IPTA-derived deformation rates on the number of interferograms used to constrain the analysis was accomplished by generating the following datasets:

1. one thousand datasets comprised of 15 randomly selected interferograms,
2. one thousand datasets comprised of 25 randomly selected interferograms,
3. one thousand datasets comprised of 35 randomly selected interferograms, and
4. one thousand datasets comprised of 40 randomly selected interferograms

It should be noted that the number of interferograms comprising datasets reported above does not take the auto-interferogram into account. As can be recalled, the auto-interferogram is included in all datasets in order to facilitate atmospheric phase estimation. Hence, a total of 4000 datasets were generated

to evaluate the dependence of IPTA-derived deformation rates on the number of interferograms analyzed. Point target analysis of all datasets was performed using the same command flow in order to facilitate comparison.

One thousand datasets, each having a specific number of interferograms, were generated to ensure that statistics defining the deformation rates, derived by applying the IPTA command flow to each of the one thousand datasets, were calculated from a representative sample size. Due to the infeasibility of ensuring that temporal unwrapping was accomplished without patch errors for each of the total of four thousand datasets analyzed, the IPTA command flow was applied to datasets that were generated by randomly sampling the 52 interferograms that were unwrapped without patch errors when accomplishing the first objective. Random sampling of the unwrapped interferograms as obtained while addressing the first objective meant that the point targets detected using all 52 available SLCs while addressing the first objective, were used for processing related to this part of the study. This procedure of dataset generation is shown in Figure 4.6.

While generating these random datasets of unwrapped interferograms, it was ensured that each generated dataset contained the first and the last interferograms defined by record numbers 1 and 51 in Table 4.3**,** in addition to the auto-interferogram that is defined by record number 52 in Table 4.3. This was done to ensure that the deformation rates, derived from IPTA as applied to each of the datasets analyzed, were representative of the same time period. Since these randomly generated datasets were already unwrapped without patch errors, deformation rates from these datasets were derived by running programs

in the IPTA package aimed at accomplishing Steps 9 through 14 outlined in the IPTA processing flowchart shown in Figure 3.4 in Chapter 3.

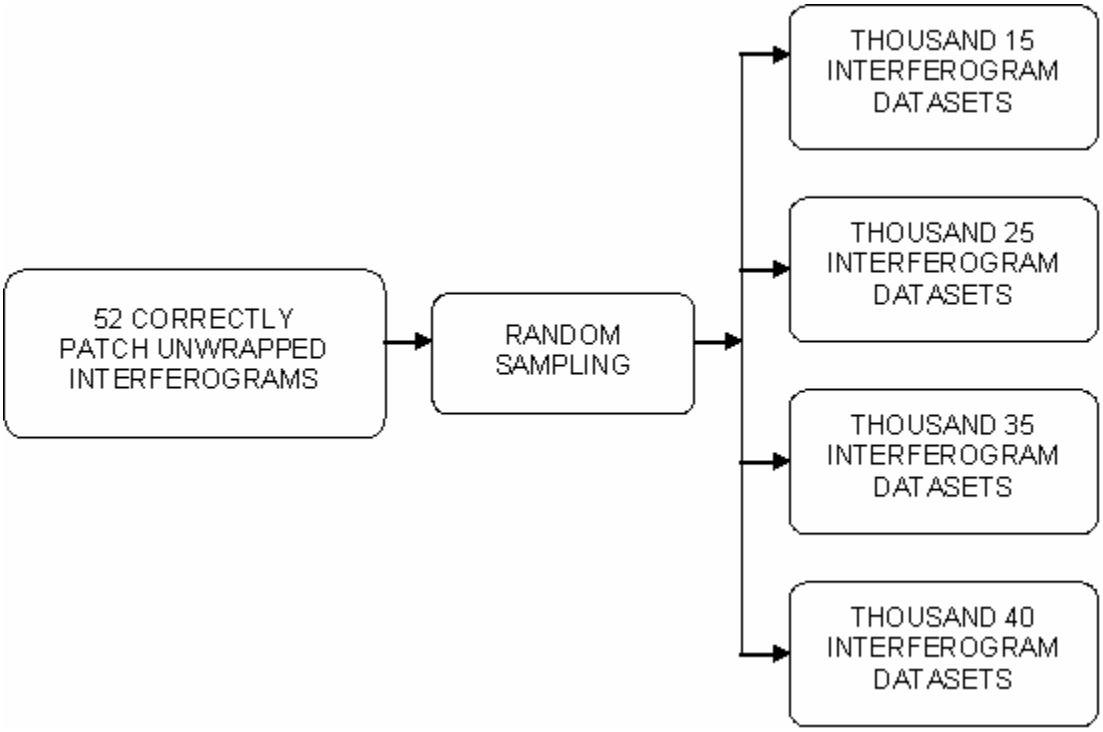

Figure 4.6 Random dataset generation.

The random samplings used to generate the datasets analyzed for this part of the study were accomplished using MATLAB.

4.5.3.1 Statistical Analysis

The linear deformation rate and associated uncertainties, as obtained for each point target after IPTA analysis of each dataset analyzed, were used to statistically quantify the variability of the linear deformation rate estimates and corresponding uncertainties. The mean and standard deviation were the two statistical measures used for quantification of variability.

IPTA analysis of four groups of datasets, with each group containing one thousand datasets, wherein all datasets within a group were associated with a specific number of interferograms (15, 25, 35, 40), resulted in four groups of one thousand estimates of linear deformation and the associated uncertainty for each point target. Every group of one thousand estimates, derived from datasets containing a specific number of interferograms, was used to derive estimates of the following parameters for each point target:

1. Mean and standard deviation of linear deformation rate, and
2. Mean and standard deviation of uncertainty of linear deformation rate.

Hence, for every point target, four estimates of mean and standard deviation of linear deformation rate and four estimates of mean and standard deviation of the uncertainty of linear deformation rate were obtained. These four estimates were used to investigate the influence of the number of interferograms characterizing the four different groups of datasets analyzed.

The linear deformation rates, in millimeters-per-year, used for statistical analysis were those that were obtained by adding all incremental linear deformation rate estimates until two-dimensional regression was terminated (Step 10, in Figure 3.4 in Chapter 3). The uncertainty estimates used for statistical analysis, also expressed in millimeters-per-year, were those associated with the linear deformation estimates obtained as explained above.

4.6 IPTA Processing Parameters and Examples

This section provides details about the point target analysis of the datasets used in this study. Examples of outputs corresponding to different stages of the processing flow are presented for illustration.

4.6.1 Point target selection

The point target candidates were chosen using the Mean-to-Standard deviation ratio (MSR) and spectral diversity criterion as explained in Section 3.3.2 in Chapter 3. Point target candidates identified in this study using the MSR criteria correspond to those with MSR values greater than or equal to 1.4 and a backscatter intensity relative to a spatial average greater than or equal to 0.5.

As mentioned is Section 3.3.2.2 in Chapter 3, point targets identified using the spectral diversity criteria correspond to those exhibiting a very low variation in backscatter intensities when imaged from different vantage points during satellite image acquisition. MSR values greater than or equal to 1.2 between four spectral looks, a spectral correlation greater than or equal to 0.4, and a backscatter intensity greater than or equal to 0.5 relative to the spatial average were used to identify point target candidates in each image in the data stack. Higher spectral correlation values are representative of lower spectral diversity.

The final list containing point target candidates identified using spectral diversity contained points corresponding to an average spectral correlation of 0.33. The average spectral correlation is the average of the spectral correlation values determined for a point in each record of the data stack. The candidates identified using both the criteria were merged to form a single point target

candidate list. The point targets identified using the above mentioned criteria are shown in Figure 4.7. SLC phase values and DEM heights corresponding to the coordinates of the point target candidates were extracted for point-wise complex interferogram and differential interferogram calculations.

As mentioned in Section 4.5, all interferometric calculations were made between a common master, namely, ERS1-Orbit 11609, and all other images constituting the datasets. All datasets analyzed included the auto-interferogram. The complex phase values of the initial differential interferograms were subjected to a quality control procedure in order to choose the final point target list for use in further regression analysis. The quality of points were assessed using the IPTA program *qc_pt* that uses the standard deviation of the unwrapped phase of a point from a two-dimensional regression model relating the unwrapped differential phase of the point to the perpendicular baseline and time.

The *qc_pt* program performs a regression for all possible point pairs with respect to all possible reference points within a user-specified search radius. A phase standard deviation threshold value of 0.7 radians and a search radius of 8 pixels, as recommended by the GAMMA IPTA reference manual, were used for the quality control step in this study. In order to facilitate the comparison of deformation rates obtained from the point target analysis, the point target candidates identified using all 52 SLCs, and that passed the quality control step were used as point targets for the analysis of all other datasets used in this study, i.e., datasets having 15, 20, 25, 30 etc. combinations.

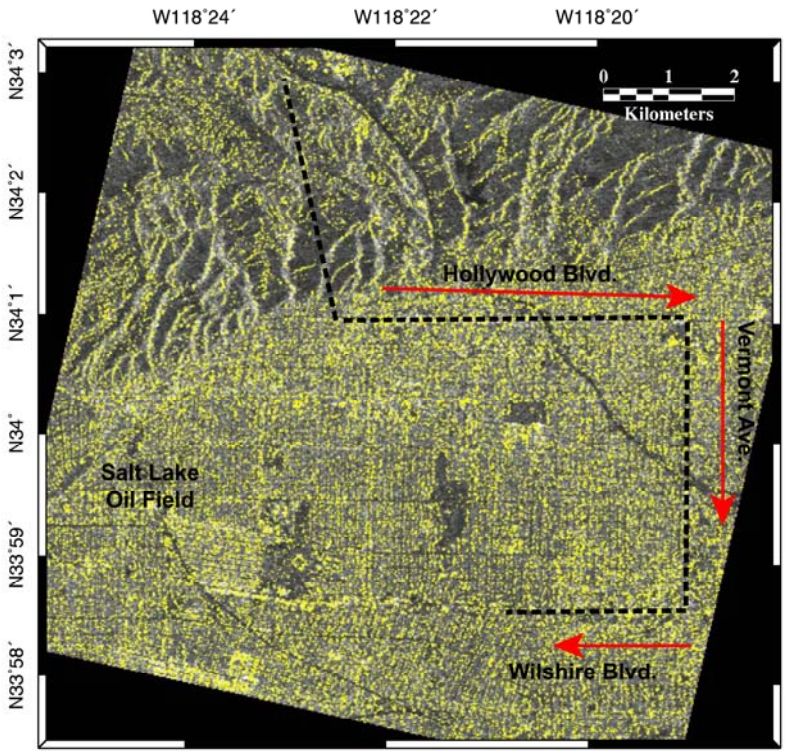

Figure 4.7 Point targets detected for the study area. Point targets are shown in yellow. The grey scale image in the background is the amplitude image of the study area. The bold dotted line shows the alignment of the Red Line.

It should be noted that the number of point targets identified using different numbers of scenes would have yielded different estimates of MSR for the same pixels on the scene and could have resulted in a lesser reliability in the identification of point targets.

4.6.2 Two-dimensional Regression Analysis

This stage of the analysis is represented by Step 9 in Figure 3.4 shown in Chapter 3. The initial complex differential interferograms generated using topographic phase simulated from the original DEM, were unwrapped in the temporal direction using the IPTA program *multi_def_pt*. This program, whose

algorithm is similar to that of *qc_pt*, performs a regression of complex values or wrapped phase values of all point targets with respect to a user-defined reference point target.

In this study, the point target with index number 30251 was used as the reference in all runs of the IPTA command flow. The program *multi_def_pt* ensures robustness of regression by performing a patch-wise operation in which all interferograms are divided into several patches and point targets within these user-defined patches are subjected to regression with respect to a local reference point within the patch, as identified by the program. Subsequently, the program performs a regression between the user-defined reference point (30251 in this study) and the patch-wise local reference points chosen by the program in order to match the patches at the edges and yield a smooth unwrapped phase field.

The *multi_def_pt* program solves for the temporal unwrapping besides resolving the perpendicular baseline and temporal dependence of the unwrapped phase values. As mentioned in Chapter 3, the linear estimate of unwrapped phase dependence on time translates into a linear deformation rate of a particular point target with respect to the user-defined reference point, whereas the linear estimate of the unwrapped phase dependence on perpendicular baseline translates into a height correction that needs to be added to or subtracted from the DEM height at the location of a point target with respect to the user-defined reference point.

Similar to the *qc_pt* program, the point targets to which the two dimensional regression was applied were chosen based on the standard deviation of the unwrapped phase of a point target from a two dimensional regression model. It may be recalled that the two dimensional regression model relates the unwrapped phase of a point target, calculated with respect to a reference point, to the perpendicular baseline and time characterizing all interferograms chosen for analysis. An example of two-dimensional regression between a pair of point targets has been shown in Figure 3.6 in Chapter 3.

The adoption of a patch-wise approach to ensure robustness of the solution necessitates the selection of point targets located within each patch that would be subjected to the two dimensional regression with respect to the local patch reference. The *multi_def_pt* program allows for such a selection to be made based on the standard deviation of unwrapped phase values of the point targets located within the patch from the two regression planes that relate the unwrapped phase to baseline and time. In this study, a phase standard deviation of 1.2 radians from such best fit regression planes was chosen to facilitate point target selection within patches. The unwrapped phase values and the resulting linear deformation rates and height corrections for all point targets located within a patch, as derived from the patch-wise approach, are referenced to the local patch reference.

As mentioned before, a regression between the user-defined reference point target (30251 in this study) and all patch reference points targets is performed in order to transform the unwrapped phase and the resulting height

corrections and linear deformation rates of all point targets such that they are referenced to the user-defined reference point. A standard deviation of 0.75 radians between patch references was used as a threshold value in order to accomplish such a transformation. The standard deviation thresholds of 1.2 radians and 0.75 radians are the default values that are recommended for use by the IPTA reference manual and were hence adopted for all *multi_def_pt* runs in this study.

A patch size of 100 pixels in the range direction and 500 pixels in the azimuth direction was adopted in all *multi_def_pt* runs applied to all datasets analyzed in this study. Once all differential interferograms in a dataset were unwrapped without patch unwrapping errors, the phase values corresponding to updated DEM heights (obtained after the application of height corrections estimated from the regression), were added back to yield a stack of unwrapped interferograms having both topographic and non-topographic phase contributions. This operation represents Step 7 shown in Figure 3.4 in Chapter 3.

A least squares improvement of baselines, as shown in Step 8 of Figure 3.4, of all interferograms in a dataset was accomplished using the stack of unwrapped interferograms containing both topographic and non-topographic phase contributions and by masking regions on the interferogram corresponding to significant deformation. In brief, at this stage, a stack of unwrapped interferograms representing the unwrapped version of the initial point-wise complex interferograms and precise estimates of the baseline associated with

each of these interferograms were obtained. The improved baseline estimates were used to simulate the phase contribution due to the initial DEM heights.

The stack of precise topographic phase estimates was then subtracted from the stack of complete unwrapped interferograms to yield a stack of unwrapped differential interferograms. This stack was referred to as *pint_diff* in the IPTA command flow adopted for analysis of the study area.

A two dimensional regression analysis, as shown by Step 9 of Figure 3.4 in Chapter 3, was performed on the stack of unwrapped differential interferograms (*pint_diff*) using the IPTA program *def_mod_pt*. The unwrapped differential interferograms were generated by subtracting the topographic phase contribution, as calculated from improved baseline estimates, from the unwrapped interferogram containing phase contributions from topography, deformation and other sources.

The *def_mod_pt* program is similar to *multi_def_pt* program, except that it does not use patch-wise regression to solve for perpendicular baseline and time dependence of phase values. Since initial unwrapping was accomplished by means of a robust regression analysis using *multi_def_pt*, all subsequent regression analysis on the unwrapped data was accomplished using the IPTA program *def_mod_pt*.

Figure 4.8 illustrates results of the two-dimensional regression analysis as applicable to the *pint_diff* phase of point target number 19655 located on Hollywood Boulevard with respect to the reference point target number 30251. The height corrections and deformation rates for all point targets were estimated

with respect to point target number 30251 in a way similar to that illustrated in Figure 4.8. The estimated height corrections were added to existing DEM height values for all points and the deformation rates estimated for all points were taken as initial deformation rate estimates.

These updated DEM height values and initial deformation rates were subtracted from the initial stack of complete unwrapped interferograms containing both topographic and non-topographic phase contributions to obtain a new stack of unwrapped differential interferograms. This new stack was denoted as *pdiff4_unw* in the IPTA command flow adopted for analysis. Figure 4.9 illustrates the results of the two-dimensional regression as applied to the phase of point 19655 in *pdiff4_unw* with respect to reference point number 30251. The height corrections and incremental deformation rates for all point targets as obtained from two-dimensional regression analysis of *pdiff4_unw* were added to updated DEM heights and deformation rates as obtained after the previous run of *def_mod_pt*. The resulting new DEM heights and deformation rates corresponding to all point targets were subtracted from the initial stack of complete unwrapped interferograms containing both topographic and non-topographic phase contributions to obtain a new stack of unwrapped differential interferograms.

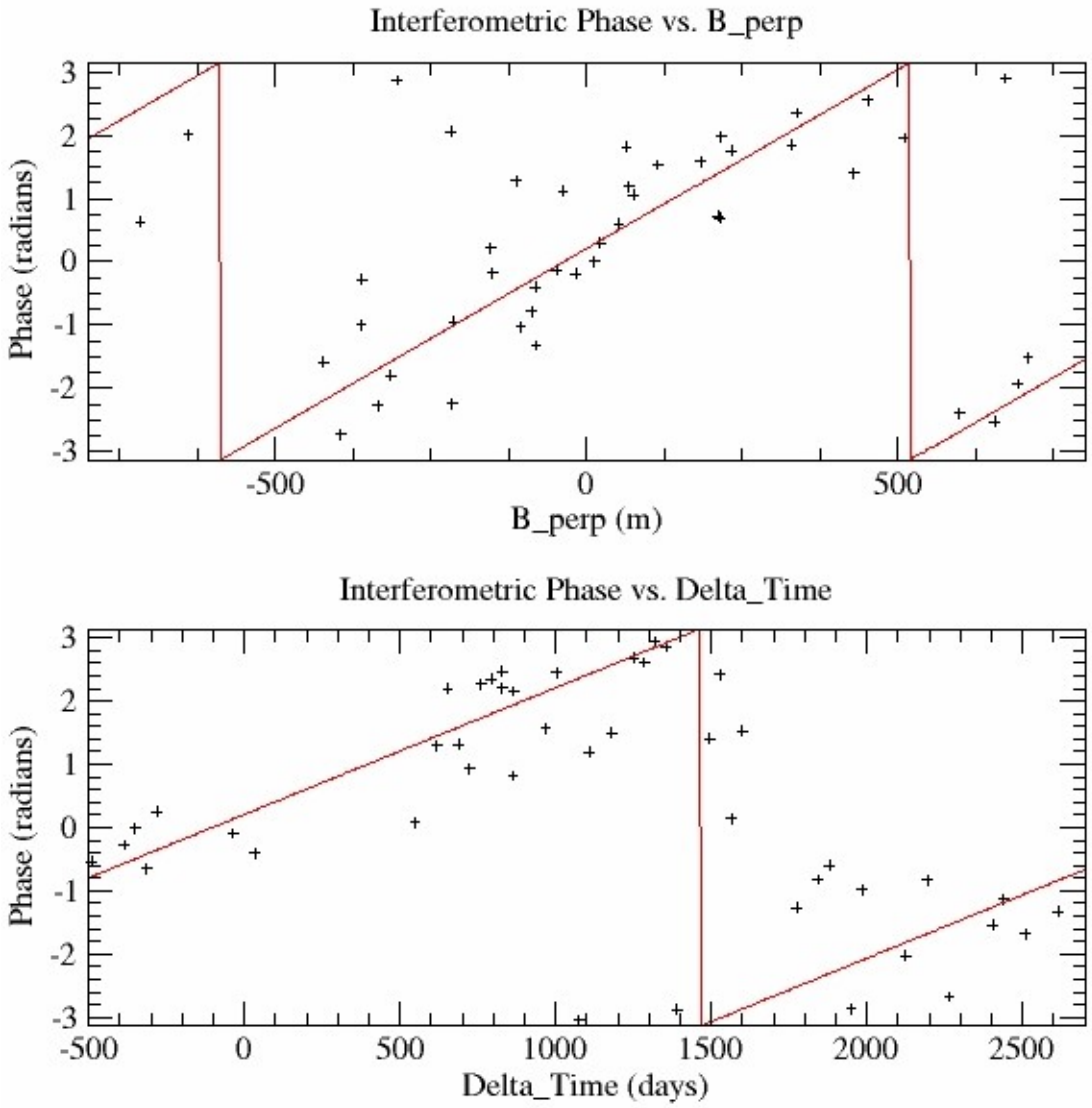

Figure 4.8 Two dimensional regression performed using pint_diff phase for point target number 19655 with respect to reference point number 30251. The baseline dependence plot on top corresponds to a height correction of -7.99 m to be applied to the DEM height of point 19655 with an uncertainty of 0.61 m, whereas the temporal dependence plot at the bottom corresponds with a deformation rate corresponding to point 19655 of -3.29 mm/yr with an uncertainty of 0.29 mm/yr. The negative sign associated with the deformation rate indicates subsidence.

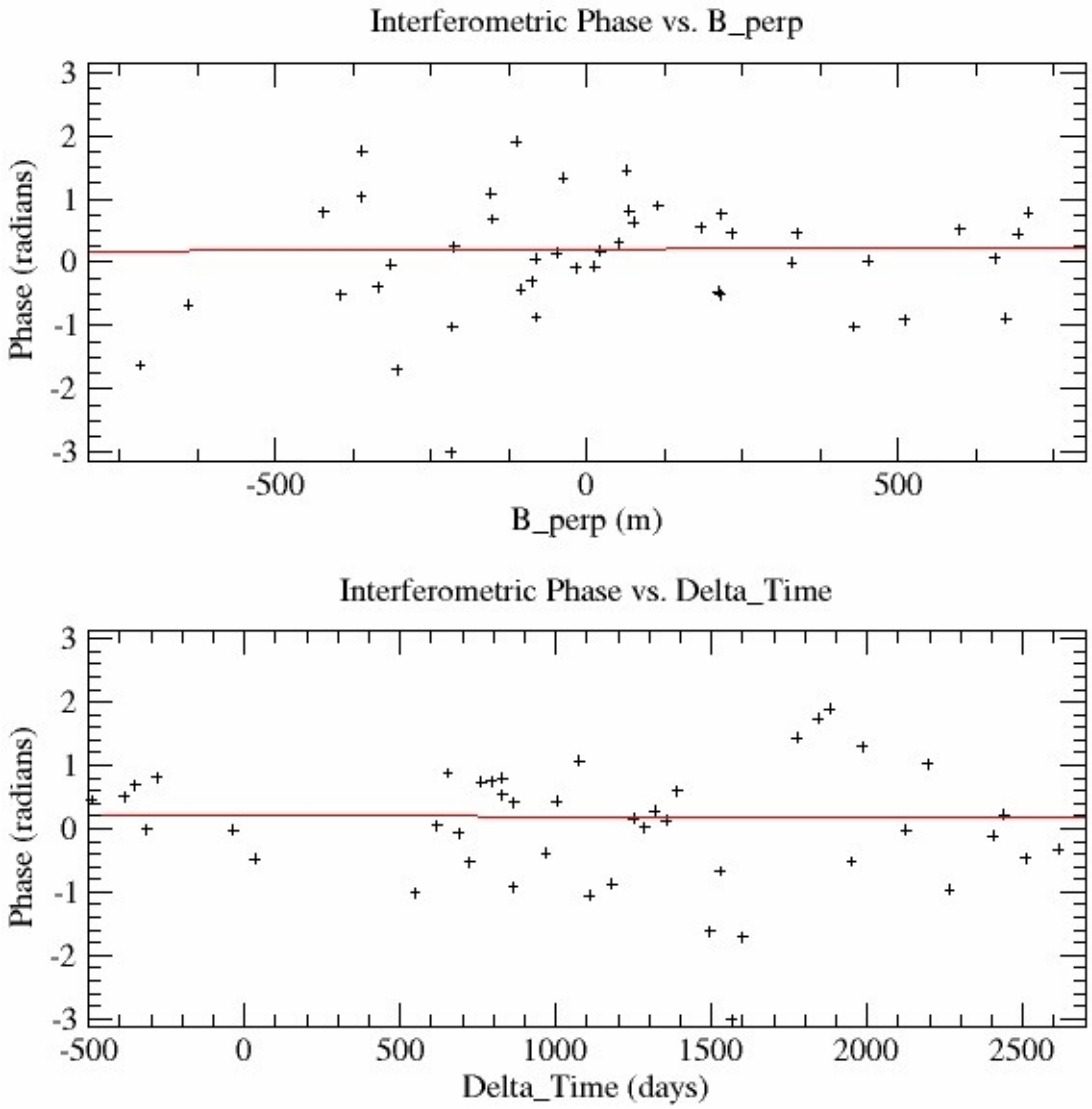

Figure 4.9 Two dimensional regression performed using pdiff4_unw phase for point target number 19655 with respect to reference point number 30251. The baseline dependence plot on top corresponds to a height correction of -0.06 m to be applied to the DEM height of point 19655 with an uncertainty of 0.61 m, whereas the temporal dependence plot at the bottom corresponds with an incremental deformation rate corresponding to point 19655 of 0.02 mm/yr with an uncertainty of 0.29 mm/yr.

This new stack was denoted as *pdiff5_unw* in the IPTA command flow adopted for analysis. Figure 4.10 illustrates the results of the two-dimensional regression as applied to the phase of point 19655 in *pdiff5_unw* with respect to reference point number 30251.

It should be noted that *pdiff4_unw* and *pdiff5_unw* are the differential interferogram stacks resulting from additional iterations of the loop formed by Steps 3, 9, 10 and 11 of the IPTA processing flow shown in Figure 3.4 in Chapter 3. The incremental DEM height corrections and deformation rates for all point targets as obtained from two-dimensional regression of phase values of *pdiff5_unw* were added to improved DEM heights and deformation rate estimates obtained after two-dimensional regression of phase values of *pdiff4_unw*. As can be seen from horizontal line fits on the perpendicular baseline dependence and time dependence plots in Figure 4.9 and Figure 4.10, the estimated improvements to the DEM heights and deformation rates were negligible, hence, the two dimensional regression was terminated.

As mentioned in Chapter 3, the phase values deviating from the regression at this stage were assumed to be residual phase containing contributions from non-linear deformation, atmospheric path delay, and noise.

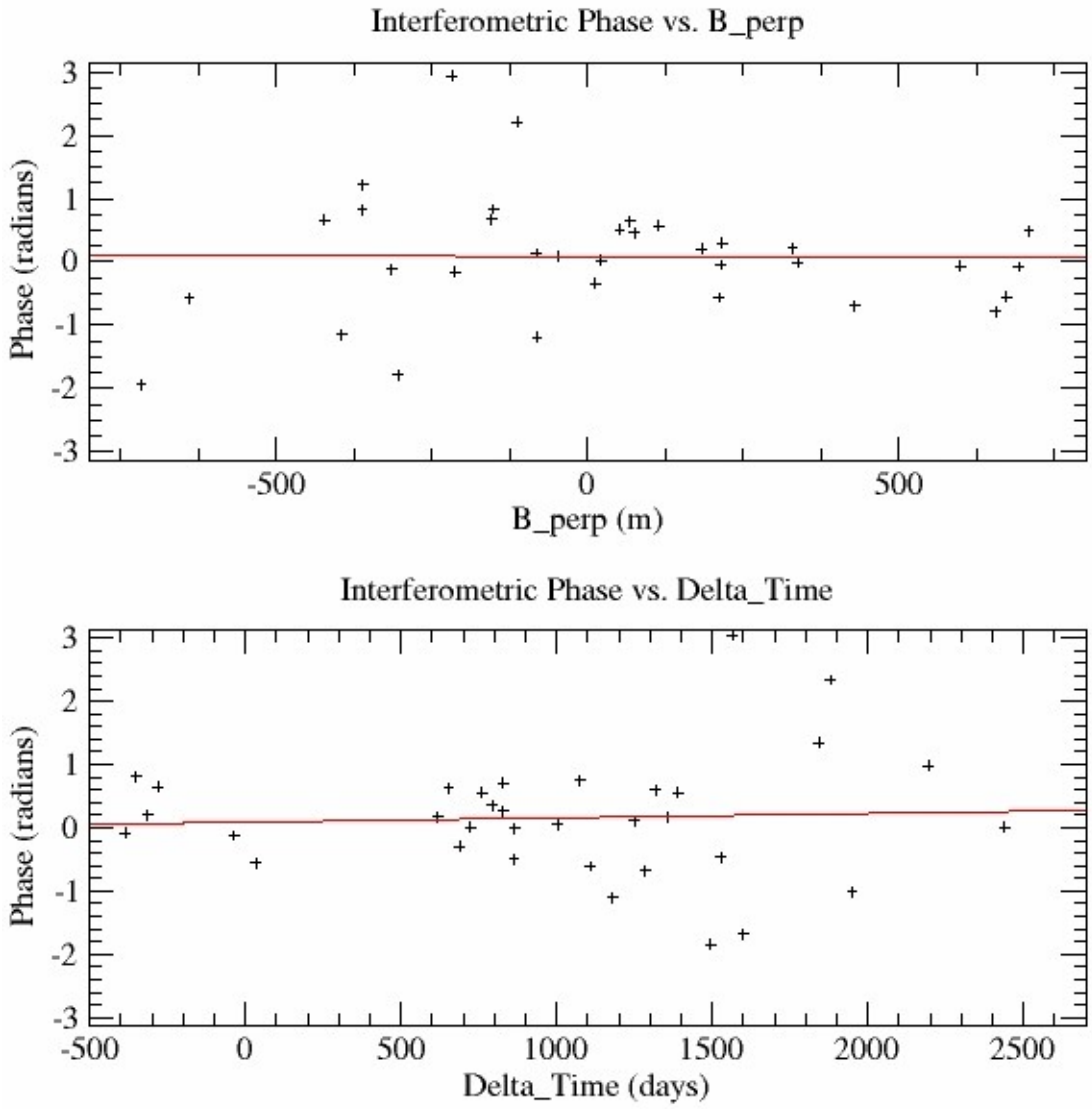

Figure 4.10 Two dimensional regression of pdiff5_unw phase for point target number 19655 with respect to reference point number 30251. The baseline dependence plot on top corresponds to a height correction of 0.02 m to be applied to the DEM height of point 19655 with an uncertainty of 0.69 m whereas the temporal dependence plot at the bottom corresponds with an incremental deformation rate corresponding to point 19655 of -0.11 mm/yr with an uncertainty of 0.41 mm/yr.

4.6.2.1 Atmospheric Phase Estimation

The residual phase estimate, obtained after termination of two-dimensional regression, was subjected to spatial low-pass filtering using the program *spf_pt*. This step was aimed at reducing phase noise. All frequency components of the residual phase that are smaller than that represented by the user-defined radius are passed through the filter for further processing. A radius of 7 pixels was used for spatial low-pass filtering of the residual phase obtained from IPTA processing as applied to all datasets analyzed in this study.

The temporal variation of the spatially filtered residual phase corresponding to all point targets analyzed was then analyzed for temporal correlation. This was accomplished using a temporal filter characterized by a user-defined temporal window. Temporal filtering was applied to the spatially filtered residual phase. The IPTA program *tpf_pt* was used to accomplish temporal filtering wherein the program analyzes spatially filtered residual phase estimates from interferograms spanning the user-defined temporal window and determines those components of the phase signal that correlate with time. The temporal filtering was constrained by using a time window that included three interferograms nearest in time to every interferogram comprising the interferogram stack.

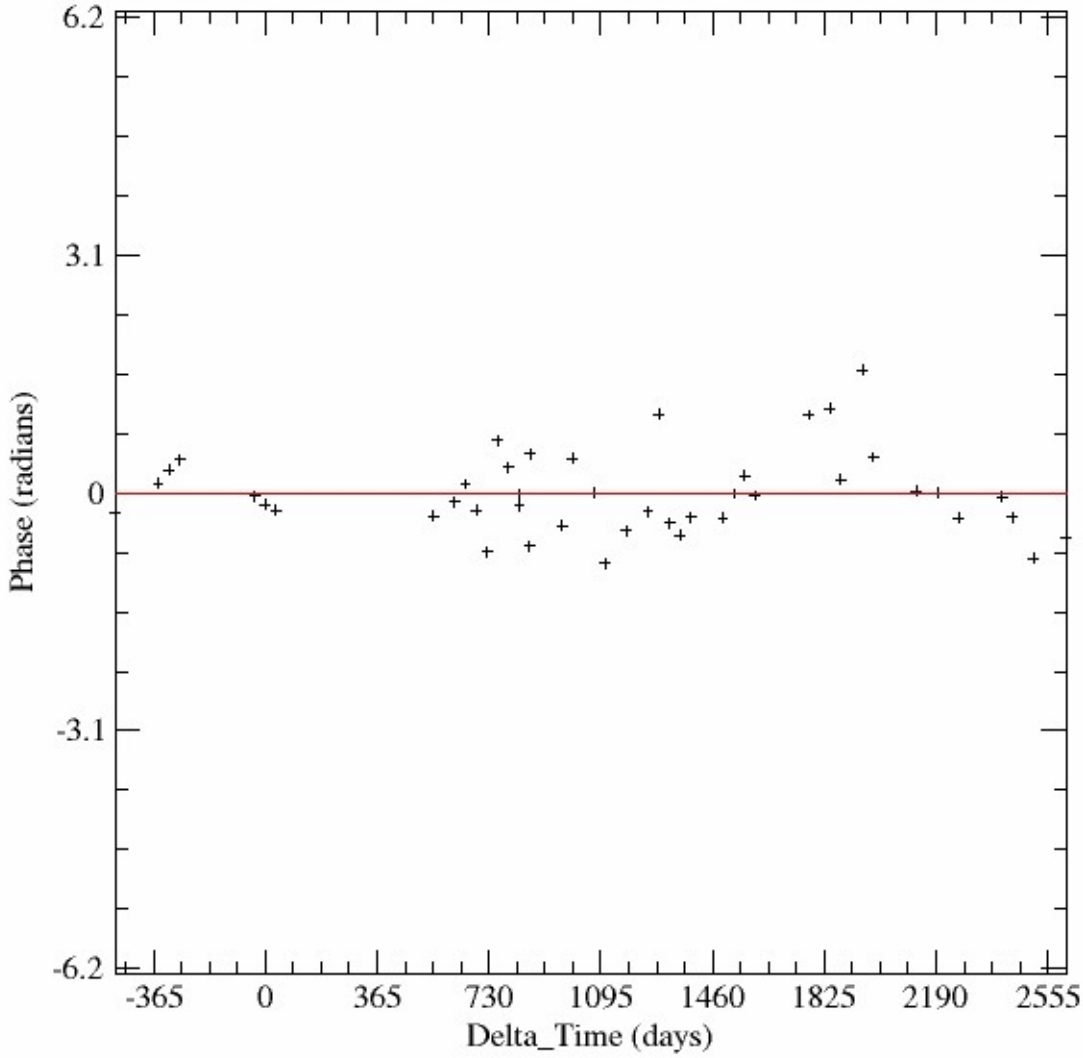

Figure 4.11 Time series showing spatially filtered residual phase of point target number 19655 obtained after two dimensional regression of its phase in pdiff5_unw.

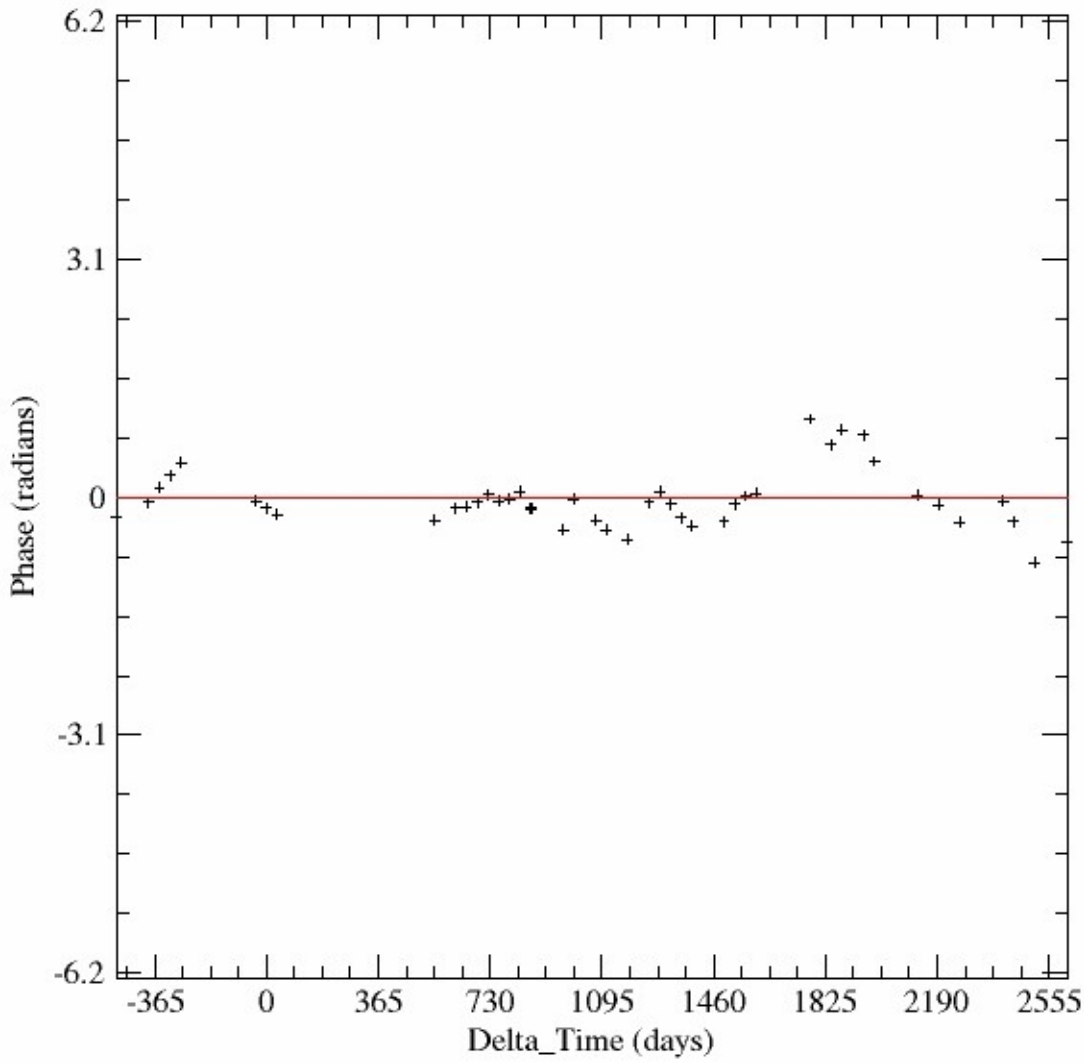

Figure 4.12 Component of spatially filtered residual phase of point target number 19655 correlating with time over a temporal window of 72 days. Zero time indicates the date of acquisition of master SLC (E1-11609).

Phase estimates derived after temporal filtering correspond to those that are filtered for noise minimization and that correlate with time. As explained in Section 3.2.2 in Chapter 3, by definition, it is assumed that atmospheric phase can be spatially correlated while being temporally uncorrelated. Hence, the temporally correlated estimate of phase derived from *tpf_pt* was subtracted from the spatially filtered estimate to derive atmospheric phase estimates.

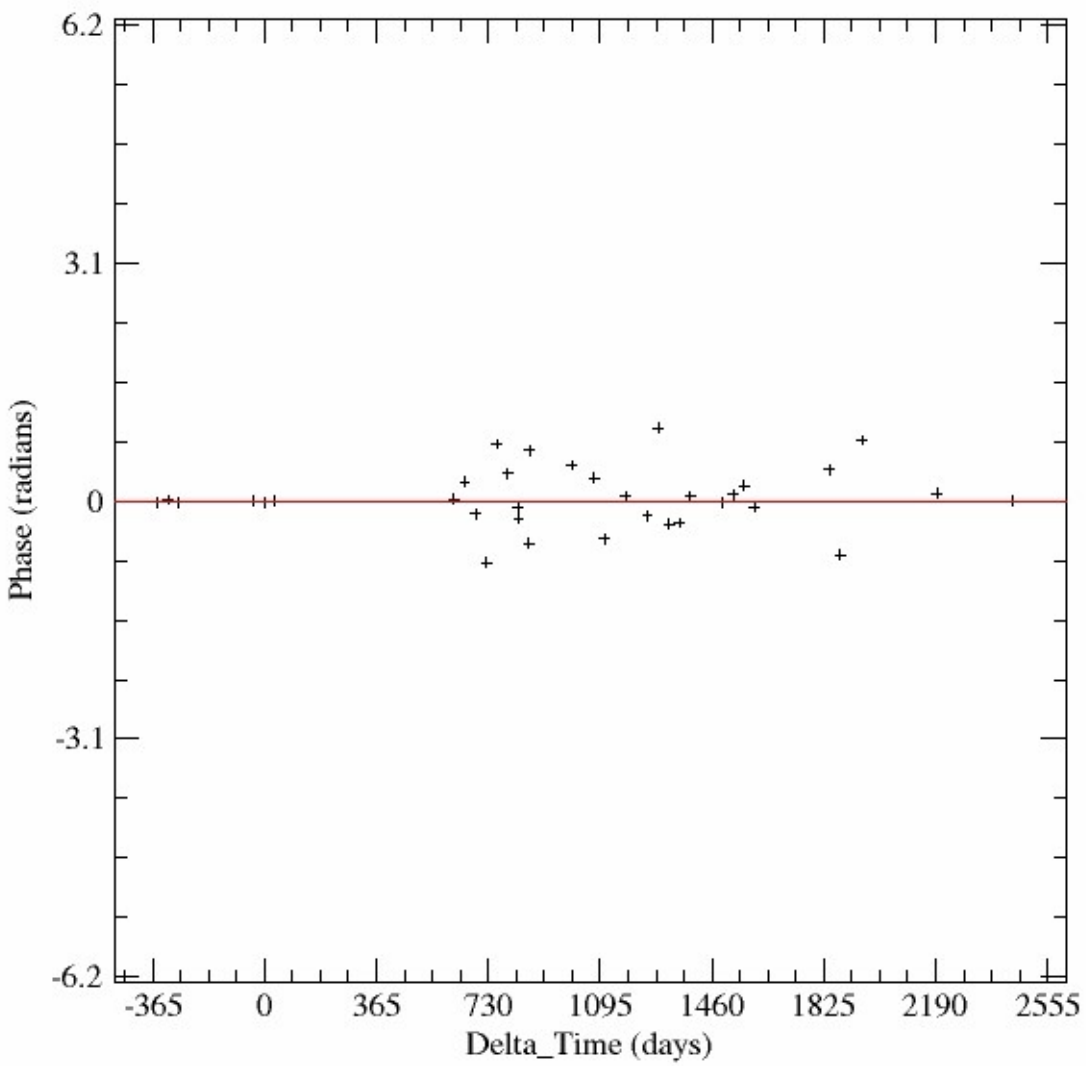

Figure 4.13 Difference between spatially filtered and temporally filtered residual phase as a function of time. Zero time indicates the date of acquisition of master SLC (E1-11609).

It is of importance to recall that the auto-interferogram was included in all of the datasets analyzed. The auto-interferogram is an interferogram having the reference scene (ERS1-11609) as both master and slave and hence represents zero baseline and zero time. Owing to the best fit regression line not passing through zero time and zero baseline, it is sometimes possible to have an estimate for the residual phase for the auto-interferogram.

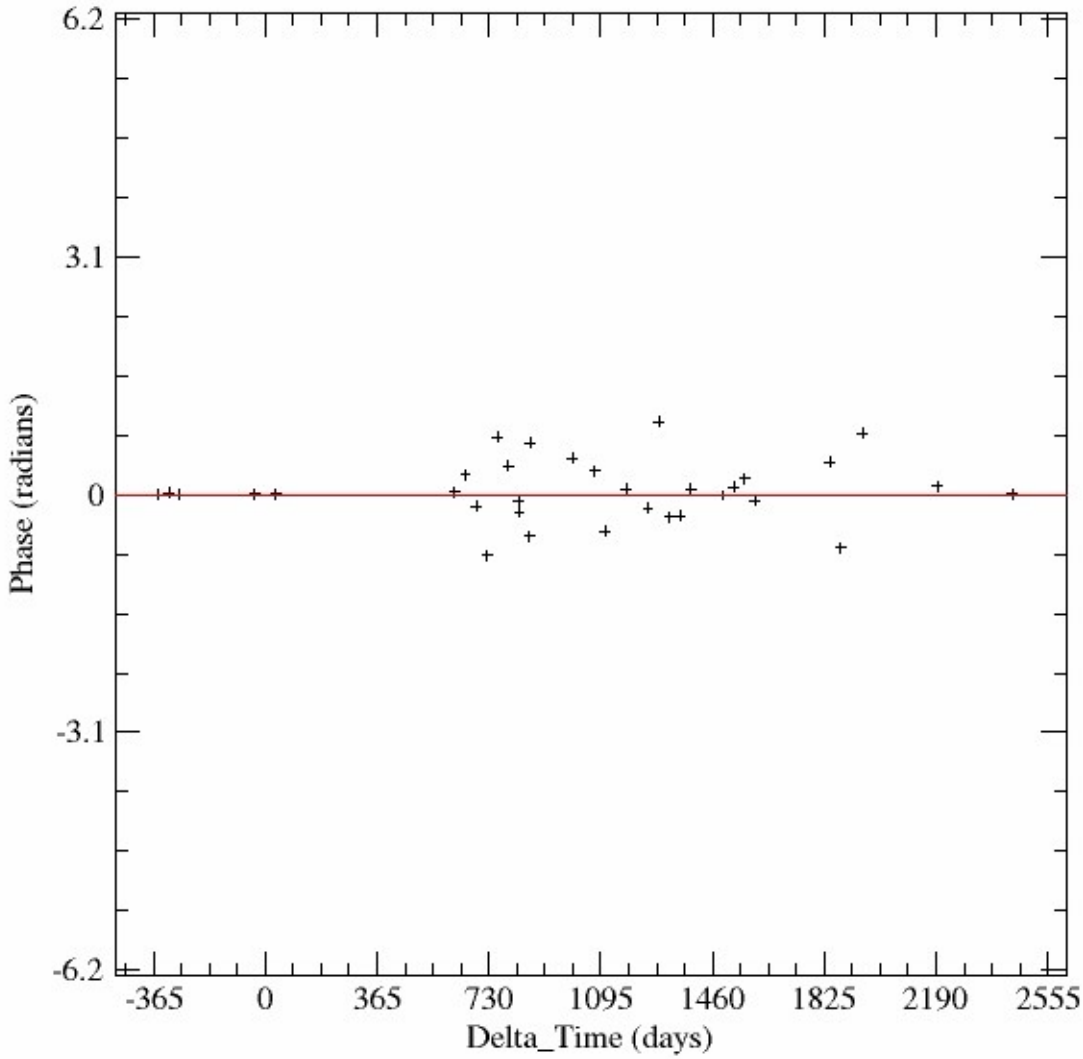

Figure 4.14 Atmospheric phase as a function of time. Zero time indicates the date of acquisition of master SLC (E1-11609).

Having an estimate for the residual phase in an auto-interferogram, results in an estimate of atmospheric phase for the auto-interferogram when in reality there should be none. Hence, any atmospheric phase contribution estimated for points in the auto-pair are subtracted from the atmospheric phase estimates of corresponding points representing all other interferometric pairs. An updated stack of differential interferograms were calculated by subtracting the estimated

atmospheric phase, updated DEM heights and deformation rates of all point targets analyzed from the initial stack of complete unwrapped interferograms containing both topographic and non-topographic phase contributions. A final two-dimensional regression was performed on the differential interferogram stack using *def_mod_pt*. Similar to the cases shown in Figure 4.9 and Figure 4.10, the incremental estimates at this stage were observed to be very low.

The incremental estimates were added to already existing DEM height map and deformation rate estimates to obtain final estimates of the same. Since atmospheric phase contribution was already modeled, the residual phase estimate obtained from the final two-dimensional regression was assumed to have contributions from non-linear deformation and a very low phase noise. Since *def_mod_pt* yields estimates of deformation rate in units of mm/yr and residual phase estimates were obtained in radians, the linear deformation rates were converted to phase rates and added to the non-linear phase estimates. The sum was then converted into final displacement rate estimates in mm/yr for further analysis. The final displacement time series of point target number 19655 with respect to the reference point target 30251 is shown in Figure 4.15. Figure 4.8 through Figure 4.15 illustrate step-wise results obtained for point target number 19655, with respect to the user-defined reference point, by executing the IPTA processing flow. The IPTA programs subject all other identified point targets to the same procedure. A detailed comparison of deformation rates and related statistics is presented in detail in the next chapter.

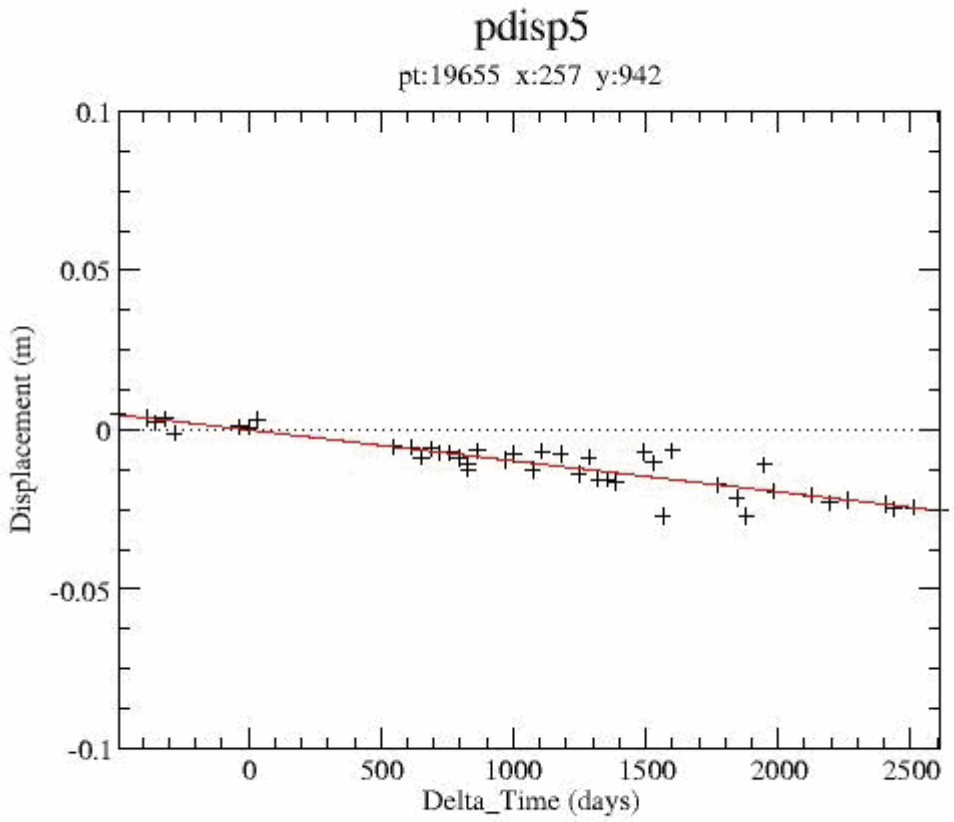

Figure 4.15 Displacement of point target number 19655 with respect to reference point target number 30251 as a function of time. Zero time indicates the date of acquisition of master SLC (E1-11609).

4.7 Summary

An introduction of the study area and the list of SAR data used for point target analysis of the study area have been provided in this chapter. The processing flow adopted to address each of the three objectives has also been provided. A graphical representation of outputs derived from each step of the processing flow has been provided for illustration. Results obtained by applying

the methods presented in this chapter to SAR data obtained for the study area are presented in the next chapter.

5. RESULTS AND DISCUSSION

5.1 Introduction

The results obtained from point target analysis of the study area are presented in this chapter. The three objectives of the study were accomplished by adopting the methods that were outlined in detail in Chapter 4. In addition to the obtained results, a detailed analysis and discussion of the results are presented. The results obtained for each objective and the related analyses are presented in separate sections within the chapter.

5.2 Deformation Detection

The first objective of the study was to investigate the feasibility of using point target analysis to detect and compute the deformation history corresponding to small-scale deformation features. Results obtained by performing point target analysis of the study area with 52 interferograms are presented in this section. As mentioned in Chapter 4, the 52 interferograms used to constrain the analysis for this part of the study were calculated between a common master SLC, namely ERS1-11609, and all other SLCs acquired over the study area between 1992 and 2000.

5.2.1 Spatial Extent of Detected Deformation

Figure 5.1 and Figure 5.2 show satellite line-of-sight displacement maps for the study area that correspond to four distinct time periods during the construction of the Red Line.

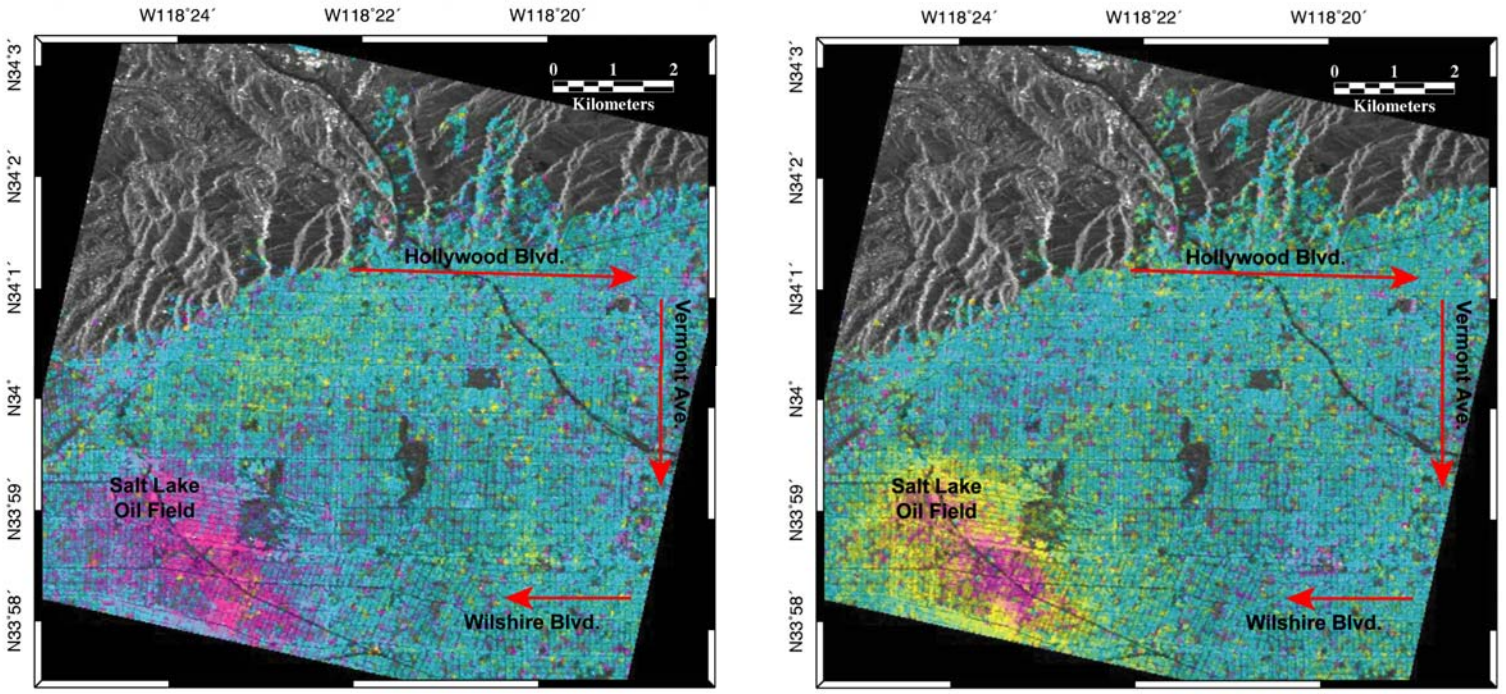

Figure 5.1 Line-of-sight displacement for the study area corresponding to (a)1st June, 1992 and (b) 1st November, 1995. Both displacement fields were calculated relative to ERS1-11609 acquired on 4th October, 1993. One color cycle corresponds to 28 mm of displacement in the satellite line-of-sight direction. The line-of-sight direction corresponds with a descending satellite viewing geometry.

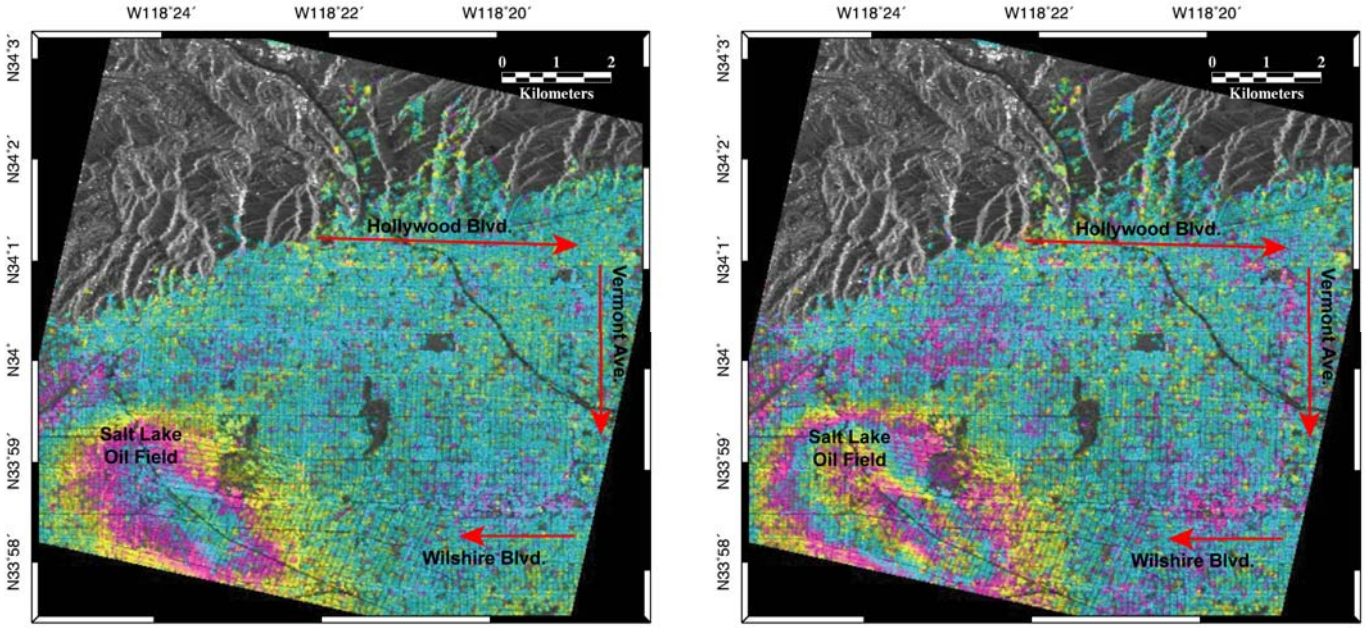

Figure 5.2 Line-of-sight displacement for the study area corresponding to (a) 10th April, 1997 and (b) 4th May, 2000. Both displacement fields were calculated relative to ERS1-11609 acquired on 4th October, 1993. One color cycle corresponds to 28 mm of displacement in the satellite line-of-sight direction. The line-of-sight direction corresponds with a descending satellite viewing geometry.

Two distinct deformation features are evident in Figure 5.1 and Figure 5.2. The first is a large region of deformation, which is consistent with the location of the abandoned Salt Lake oil field. It may be recalled from Chapter 4 that the Salt Lake Oil field is one among the several abandoned oil fields that are situated in the vicinity of the study area. The spatial deformation signature corresponding to the Salt Lake oil field is present in all displacement maps shown in Figure 5.1 and Figure 5.2. Also important to note from Figure 5.1 and Figure 5.2, is the increase in the number of color cycles that can be associated with deformation in the vicinity of the oil field as a function of time. Each color cycle corresponds to 28 mm of displacement resolved along the satellite line-of-sight.

A series of spatially linear deformation features that are consistent with the alignment of the Red Line tunnels represent the second set of deformation features that were detected in the study area. It is interesting to note the absence of these linear features in 1992/1993 (Figure 5.1(a) and Figure 5.1(b)) and its strong emergence between 1997 and 2000 (Figure 5.2(a) and Figure 5.2(b)). The time periods of emergence of the deformation features along the Red Line alignment are consistent with the dates of construction along segment 2 and segment 3.

The limited spatial extent of the subsidence detected along the Red Line alignment can be explained in the context of the 20 m resolution achievable from ERS SAR data. It may be recalled from Chapter 4 that each of the twin tunnels had a post-boring diameter of 6.6 m while the pillar separating the side walls of the two tunnels had a maximum width of 6.1 m. The cross-sectional width of the

entire setup hence equaled approximately 20 m, which is effectively equivalent to one pixel on the map. The extent of the spatial deformation signature caused by subsidence during construction of the tunnels can be expected to depend on the zone of influence, and can hence be expected to be greater than 20 m in a direction perpendicular to the alignment of the tunnel.

5.2.2 Temporal Signature of Detected Deformation

A second important result from this phase of the study concerns the deformation-time relationship for different regions in the study area. The temporal deformation signatures that might be expected in these different regions can be summarized as follows:

1. **Along Red Line Alignment:** A deformation time series with a step or ramp that correlates distinctly with the time of tunneling would be expected for point targets located along the alignment of the Red Line,
2. **Over Salt Lake Oil Field:** Considering that the oil filed is abandoned (Stirbys et al., 1999), the temporal signature of deformation corresponding with point targets located in the vicinity of the oil field can be expected to correspond with gradual settlement. In other words, the deformation time history for point targets near the oil field can be expected to be different from those for point targets along the Red Line alignment, and
3. **Other Points:** Assuming no other deformation in the study area, the deformation signature for point targets located away from the Red Line and the oil field would be expected to represent zero deformation.

The deformation time series for point targets located along the Hollywood Boulevard section (segment 3) of the Red Line are shown in Figure 5.3. Figure 5.4 presents the deformation time series for point targets located in the vicinity of the oil field and Figure 5.5 shows the deformation time series for point targets located away from the deformation fields corresponding to the Red Line and the Salt Lake oil field. It can be observed from these plots, that three different deformation time series signatures were observed in regions representing different deformation sources within the study area. A detailed discussion of these deformation time series signatures is presented in the next section.

5.2.3 Discussion

The first important observation from the first phase of this study is that the small deformation associated with the construction of the Red Line tunnels can be detected using IPTA. Although the deformation occurred over a region covering the width of a few pixels, the linear trend, which correlates spatially with the tunnel alignment, is evident (Figure 5.2).

The second important observation is that the expected deformation-time trend that can be associated with tunnel construction is present in the deformation history plots for point targets along the tunnel alignment (Figure 5.3). All deformation time history plots shown in Figure 5.3 through Figure 5.5 have a discontinuity between 8th November 1993 and 5th April 1995 due to unavailability of SAR data during that time period. It is important to note that despite this discontinuity in the time series, a distinct step in the deformation series can be observed in most of the time series plots shown in Figure 5.3.

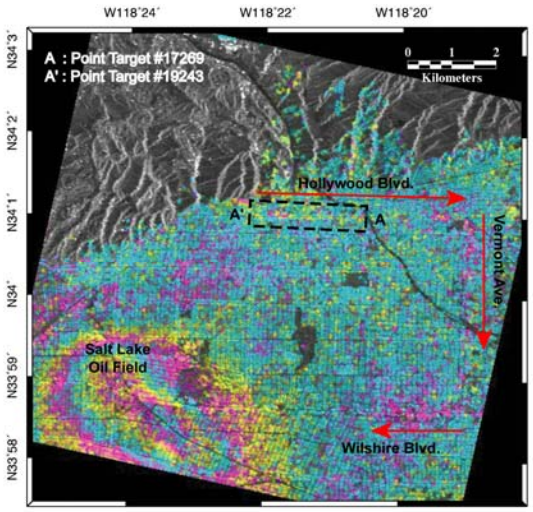

(a)

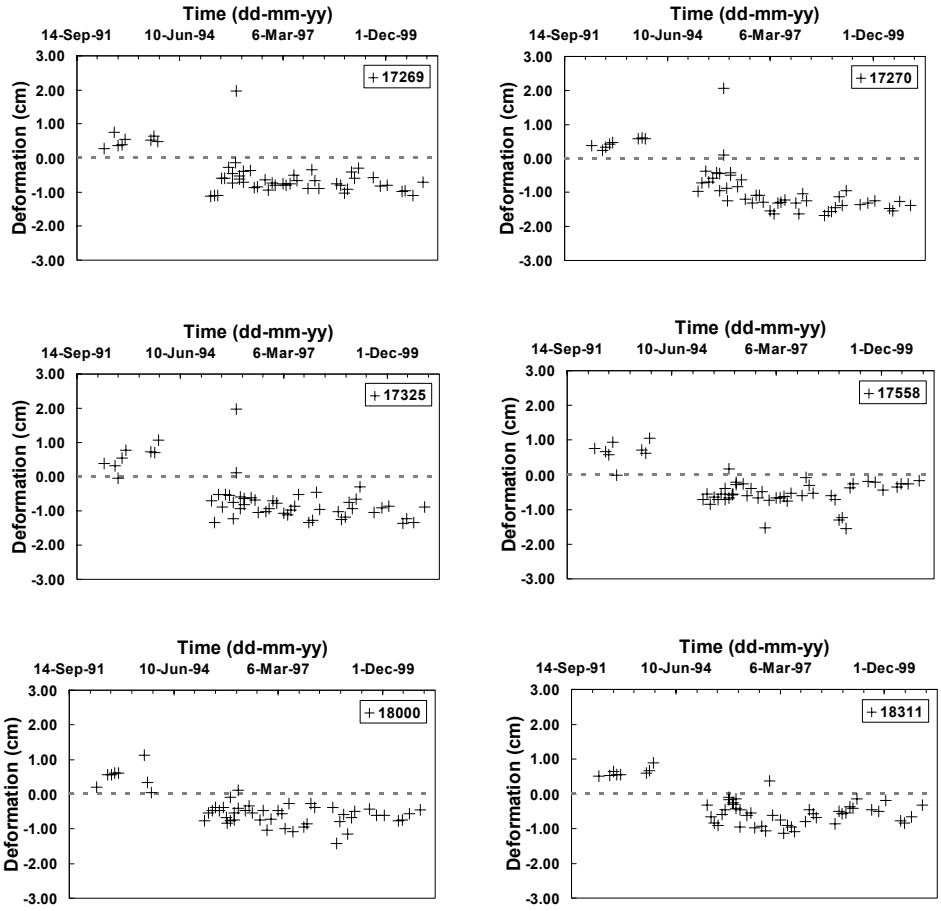

(b)

Figure 5.3 (a) Line of sight displacement field (descending view) for time period between 4th October, 1993 and 4th May, 2000 (b) Deformation time series for point targets along Section A-A' on Hollywood Boulevard.

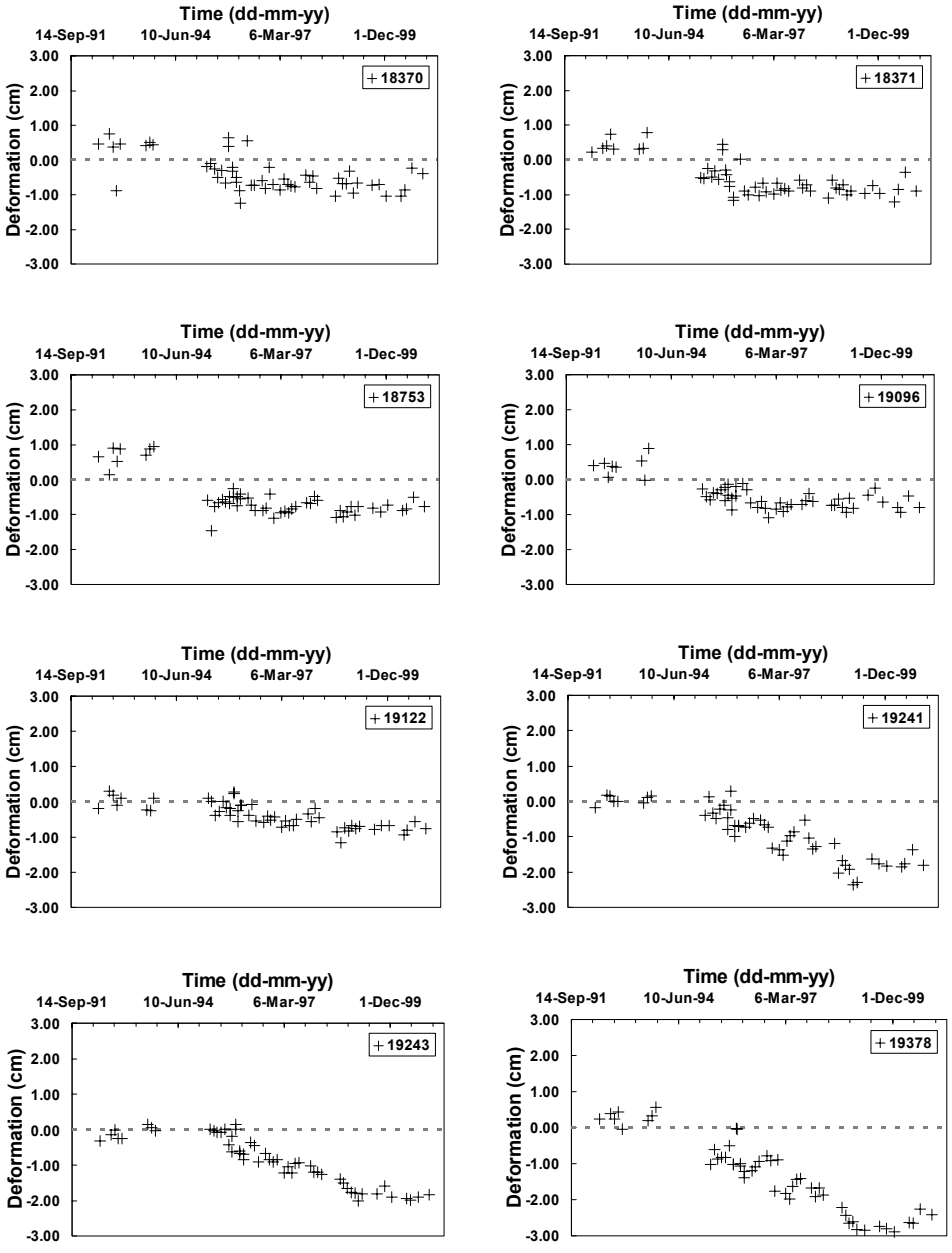

(c)

Figure 5.3 contd. Deformation time series for point targets along Section A-A' on Hollywood Boulevard.

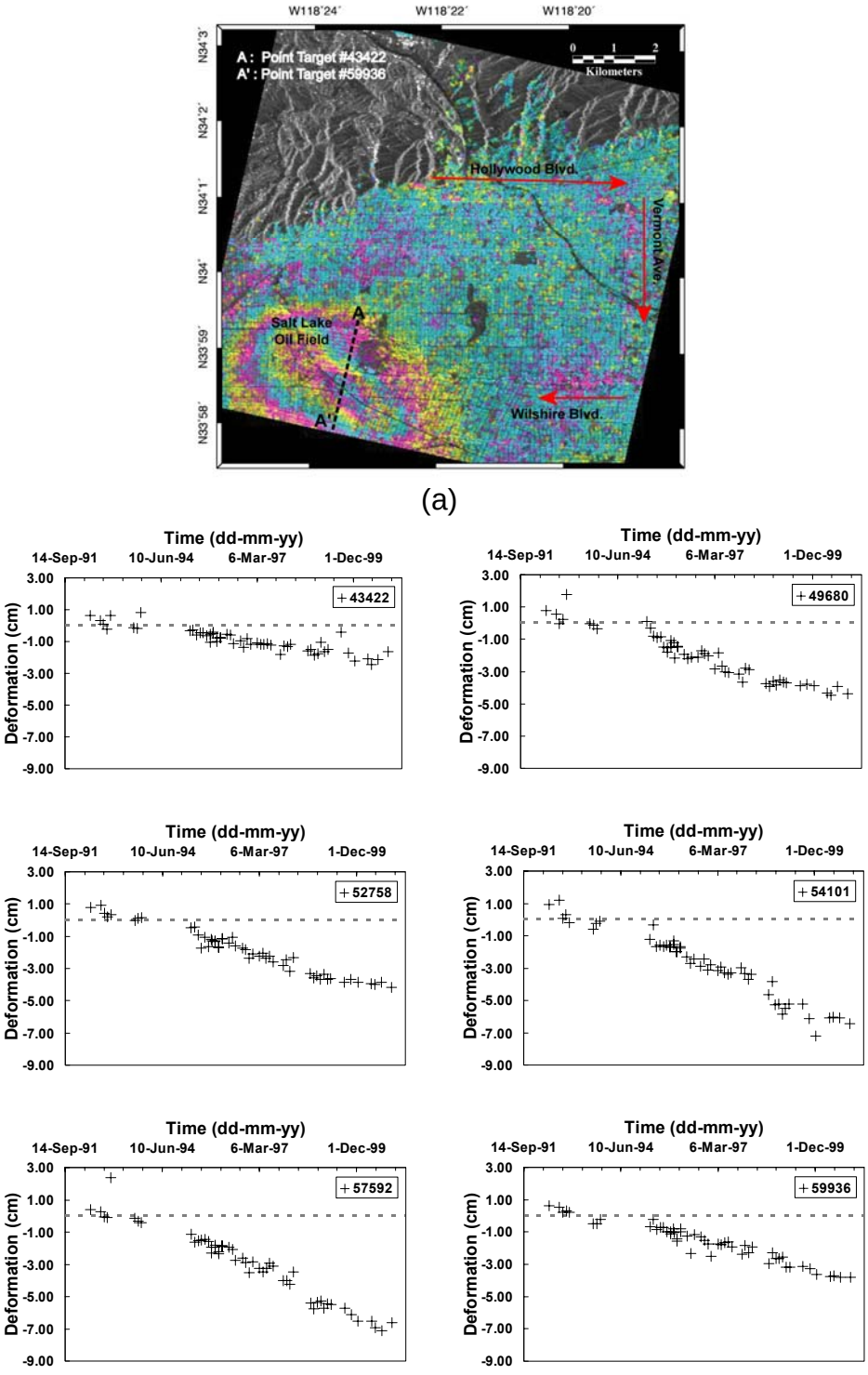

Figure 5.4 (a) Line of sight displacement field (descending view) calculated for time period between 4th October, 1993 and 4th May, 2000 (b) Deformation time series for point targets along Section A-A' in the vicinity of the Salt Lake Oil Field.

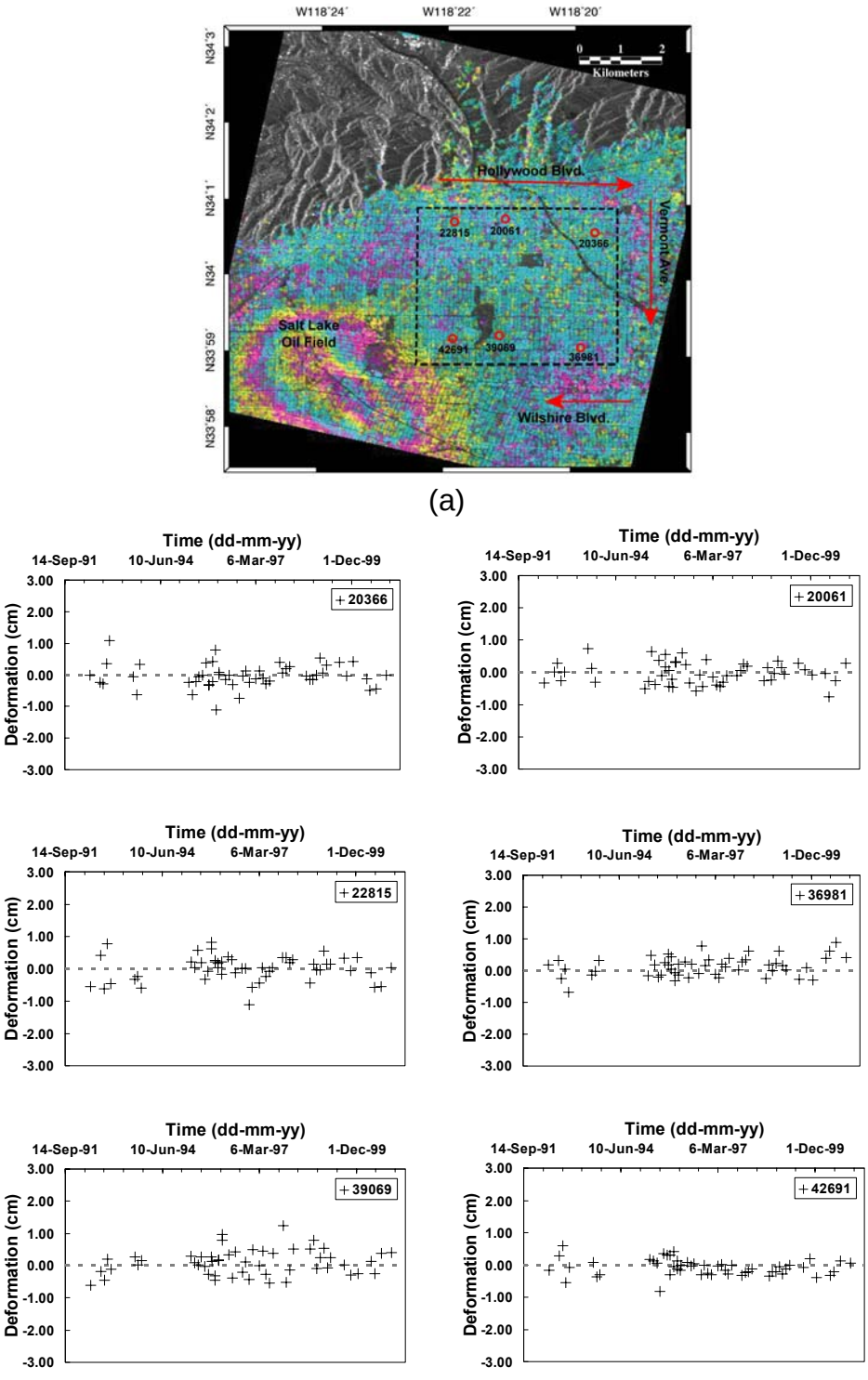

Figure 5.5 (a) Line of sight displacement field (descending view) for time period between 4th October, 1993 and 4th May, 2000 (b) Deformation time series for point targets located away from the Red Line and oil field deformation fields.

Subsidence ranging between ½” to 1” in the satellite line of sight direction can be inferred from the step in the deformation time series plots of some point targets along Section A-A’ in Figure 5.3. This is consistent with the 2 inches of subsidence that was observed during construction along Hollywood Boulevard (Bell, 1999).

On comparing the deformation time history plots shown in Figure 5.3, it is observed that the time period of occurrence of the step in the deformation history shifts from 1993 for point 17269 to 1995 for point 19243. This time progression of the step, indicates that tunneling along Hollywood Boulevard may have progressed from A to A’ (right to left with reference to the Figure 5.3). It is also important to note that the steps in deformation time history plots for all point targets shown in Figure 5.3 occur between 1994 and 2000, which is consistent with the time period of tunneling along Hollywood Boulevard. Comparing the location of Section A-A’ shown in Figure 5.3(a) with the layout of the Red Line as shown in Figure 4.2 in Chapter 4, it can be observed that the point targets showing the strongest deformation signature along Section A-A’ in Figure 5.3(a) are located between the Hollywood/Vine station and Hollywood/Highland station. From the geologic profile shown in Figure 4.3 in Chapter 4, it can be observed that the alignment between the Hollywood/Vine and Hollywood/Highland stations passes mainly through young alluvium, which may be the reason for the observed high magnitude of subsidence.

In comparison with the deformation time history corresponding to point targets located along the Red Line alignment, the deformation time history for

point targets located in the vicinity of the Salt Lake oil field shows much larger settlements with a time linear trend. This indicates continuous deformation that was prevalent during the time period bracketed by acquisition dates of SAR data used in this study.

For point targets located away from the Red Line and Salt Lake oil field deformation fields, data points in the deformation time history plots vary about zero and do not show the step that was observed in deformation time history for point targets situated along the tunnel. The random nature implied by the qualitative and quantitative signature of time series plots for these point targets are likely indicative of system noise as opposed to actual deformation. Given the location of these point targets, such a deformation time history conforms to the general expectation and more importantly, confirms that the time history plots for point targets located along the Red Line and the Salt Lake oil field are representative of deformation.

5.3 Influence of Number of Scenes and Average Baseline on Data Processing Feasibility

As explained in Chapter 3, the patch unwrapping step in the IPTA processing flow is critical in ensuring the robustness of the two-dimensional regression analysis that follows. The patch unwrapping step in IPTA is aimed at accomplishing phase unwrapping in the temporal domain. The temporal unwrapping approach is adopted in order to negate spatial sampling issues that arise from the irregular distribution of point targets in a given study area. This irregular spatial distribution of point targets renders the conventional spatial

phase unwrapping techniques of InSAR susceptible to unwrapping errors in the form of skipped cycles. It may be recalled from Chapter 2 that conventional phase unwrapping techniques are based on the assumption that the inherent unwrapped phase surface is adequately sampled in the spatial domain. Regression analyses performed with such erroneous unwrapped phase values can lead to incorrect phase dependence inferences.

In practice, unless a satellite platform is tasked for regular SAR image acquisition over a region of interest, the number of SLCs available for IPTA analysis of any area, and the spatial and temporal baselines defining the resulting dataset, is dependent on the acquisition history associated with that area. In such instances, and given the criticality of phase unwrapping in obtaining reliable deformation histories of point targets, it would be very useful to quantify the characteristics of datasets that can be unwrapped successfully, i.e., without patches. Such quantification can be useful in determining the following:

1. The feasibility of using IPTA for a study area based on the available SAR imagery, and
2. Choice of specific SLCs that will be used for IPTA analysis of a study area given that sufficient SAR images of the study area are available for analysis.

Keeping the above mentioned objectives in mind, it was sought to investigate the degree of success in unwrapping all records of datasets of varying sizes by characterizing the success or failure in unwrapping a dataset as a function of the average baseline of the dataset. As mentioned in Chapter 1, it was hypothesized

that the number of interferograms comprising a dataset and the resulting average baseline of the dataset are the most critical parameters affecting the success or failure of patch unwrapping. This section provides details pertaining to this second portion of the study.

5.3.1 Patch Unwrapping Analysis

As mentioned in Chapter 4, subsets of the 52 availabe SLCs acquired over the study area between 1992 and 2000 were generated for analysis.

Table 5.1Table 5.1 provides the details of all the 94 datasets that were analyzed in this part of the study (Figure 5.6). Both initial and modified average absolute perpendicular baselines of the analyzed datasets are provided. The interferograms in the initially generated datasets that had patch unwrapping errors and those interferograms that were removed from the corresponding initially generated datasets in order to negate the patch unwrapping errors are indicated by their record numbers in the table. The record numbers indicated in Table 5.1 correspond to the interferograms represented in Table 4.3 in Chapter 4. It can be seen from Table 5.1 and Figure 5.7 that, regardless of the method in which the datasets were generated, all the datasets analyzed can be classified into two groups:

1. Datasets in which all constituent interferograms could be unwrapped without patch errors, and
2. Datasets in which either some or all constituent interferograms were characterized by patch unwrapping errors.

Table 5.1 Details of datasets analyzed for patch unwrapping errors. "*" indicates datasets analyzed after masking point targets in the Santa Monica mountains.

	Before				After		Generation
#	# Pairs	B-perp (m)	Patches in	Records Omitted	# Pairs	B-perp (m)	Method
1	9	43.32	All	Unsuccessful			Incremental
2	10	46.62	All	Unsuccessful			Incremental
3	11	49.60	All	Unsuccessful			Incremental
4	12	52.19	All	Unsuccessful			Incremental
5	13	55.03	All	Unsuccessful			Incremental
6	14	58.52	All	Unsuccessful			Incremental
7	15	61.98	None	None	15	61.98	Incremental
8*	15	68.71	All	Unsuccessful			Incremental
9*	15	77.60	All	Unsuccessful			Incremental
10*	15	86.27	All	Unsuccessful			Incremental
11*	15	107.02	All	Unsuccessful			Incremental
12*	15	117.49	All	Unsuccessful			Incremental
13*	15	127.46	All	Unsuccessful			Incremental
14*	15	137.30	All	Unsuccessful			Incremental
15*	15	147.19	All	Unsuccessful			Incremental
16*	15	156.62	All	Unsuccessful			Incremental
17	15	166.98	All	Unsuccessful			Incremental
18	15	181.87	All	Unsuccessful			Incremental
19	15	196.82	All	Unsuccessful			Incremental
20	15	252.57	All	Unsuccessful			Random
21	15	264.33	All	Unsuccessful			Random
22	15	368.66	All	Unsuccessful			Random
23	15	390.78	All	Unsuccessful			Random
24	15	232.12	All	Unsuccessful			Random
25*	20	87.08	48,50,51	48,50,51	17	90.03	Incremental
26*	20	154.98	1,28,49,50,51	1,3,51	17	154.38	Incremental
27*	20	167.29	1,28,37	1,50,51	17	171.65	Incremental
28*	20	180.29	All	Unsuccessful			Incremental
29	20	206.20	All	Unsuccessful			Incremental
30	20	220.21	All	Unsuccessful			Incremental
31	20	233.86	All	Unsuccessful			Incremental
32*	20	280.11	Most	Unsuccessful			Random
33*	20	307.99	All	Unsuccessful			Random
34*	20	337.95	All	Unsuccessful			Random
35*	20	344.99	All	Unsuccessful			Random
36	20	387.03	All	Unsuccessful			Random
37*	20	655.76	All	Unsuccessful			Incremental
38*	25	112.62	3	3,21,51	22	113.99	Incremental
39*	25	121.50	1,3	1,3,21,50,51	20	119.56	Incremental
40*	25	132.94	28,51	1,3,28,51	21	131.85	Incremental
41*	25	144.54	1,50,51	1,7,21	22	141.02	Incremental
42*	25	156.24	1,3,4,28	1,3,4,49,50,51	19	146.77	Incremental
43*	25	167.81	1,21,28	1,51	23	168.32	Incremental
44*	25	179.20	1,3,4,21,28	1,3,4,7,51	20	173.37	Incremental

Table 5.1 contd.

	Before				After		Generation
#	# Pairs	B-perp (m)	Patches in	Records Omitted	# Pairs	B-perp (m)	Method
45*	25	191.04	1,4,28	1,4,7,21,28	20	192.86	Incremental
46*	25	202.83	1,3	1,3,4,50,51	20	208.19	Incremental
47*	25	215.92	1,4,25	1,4,25,28,50	20	224.93	Incremental
48	25	339.92	40	40	24	338.99	Pseudo
49*	25	589.38	Most Records	2,35	23	586.79	Incremental
50	26	357.18	None	None	26	357.18	Pseudo
51*	30	144.39	1,4,7,28	1,21	28	143.92	Incremental
52*	30	155.23	1,7,21	1,21	28	155.53	Incremental
53*	30	166.66	1,21,28	1,7,21,50,51	25	171.82	Incremental
54	30	177.95	21	21	29	181.77	Incremental
55	30	189.94	21	21	29	194.17	Incremental
56	30	202.45	3,21	21	29	207.12	Incremental
57*	30	279.24	All	Unsuccessful			Incremental
58*	30	360.42	1,4	1,4,28	27	376.68	Random
59*	30	355.61	8,21	1,2,4,14,21,45	24	338.65	Random
60*	30	289.17	All	Unsuccessful			Random
61*	30	296.19	18,30	None	30	296.19	Random
62*	30	278.99	18, 30	1,3,4,20,48,50,51	23	309.09	Random
63*	30	527.76	4,35,47	4,35,47	27	531.60	Incremental
64	35	177.43	1,21	1,21	33	179.03	Incremental
65	35	189.35	21	21	34	192.95	Incremental
66*	35	201.75	21	1,3,49,50,51	30	209.06	Incremental
67*	35	215.74	21	4,7,21,50,51	30	225.11	Incremental
68*	35	231.86	1,21,28	1,21,28	32	241.68	Incremental
69	35	248.77	21,35	21,35	33	242.46	Incremental
70*	35	266.02	21,35	1,5,21,28,30,35	29	248.68	Incremental
71*	35	283.44	35	21	34	289.80	Incremental
72	35	301.39	7	35	34	291.47	Incremental
73	35	321.68	44,46,50	1,35	33	314.71	Incremental
74*	35	478.32	35	35	34	473.61	Incremental
75	40	221.08	21	21	39	225.03	Incremental
76	40	237.18	21	21,35	38	231.10	Incremental
77	40	253.61	21	7,21	38	259.68	Incremental
78*	40	270.41	21	4,7,21,35	36	265.92	Incremental
79	40	287.29	21,35	7,21	37	295.14	Incremental
80	40	304.05	21,35,50	21	38	310.12	Incremental
81	40	322.06	21,35	21	38	328.59	Incremental
82	40	340.92	21,35	21,35	37	340.29	Incremental
83	40	360.72	None	None	40	360.72	Incremental
84*	40	380.93	None	None	40	380.93	Incremental
85*	40	403.68	28	28	39	411.99	Incremental
86*	40	430.98	35	35	39	425.65	Incremental
87	45	273.29	21	21	44	277.98	Incremental
88	45	290.20	21	21	44	295.27	Incremental

Table 5.1 contd.

#	Before				After		Generation
	# Pairs	B-perp (m)	Patches in	Records Omitted	# Pairs	B-perp (m)	Method
89	45	308.02	21	21	44	313.49	Incremental
90	45	326.59	21	21	44	332.48	Incremental
91	45	345.28	21	21,35	43	344.93	Incremental
92	45	366.15	21	21,35	42	352.03	Incremental
93	45	391.00	21	21,35	43	392.77	Incremental
94	52	342.00	None	None	52	342.00	All Pairs

While patch unwrapping of some datasets classified into the first group could be accomplished without modification of the size of the initially generated datasets, patch unwrapping others necessitated modification of the initial dataset by means of discarding some interferograms from the analysis. As can be seen from Figure 5.7, the smallest dataset that could be unwrapped without patch errors contained 15 interferograms. The 15 interferogram dataset contained interferograms that were characterized by the lowest absolute perpendicular baselines among those characterizing the 51 single master interferograms computed for the study area.

The 15 interferogram dataset was arrived at by beginning with a dataset containing the 10 lowest absolute perpendicular baseline interferograms computed for the study area and continually appending this dataset with an interferogram characterized by the least absolute perpendicular baseline among the interferograms not already in the dataset. The flowchart depicting this method of dataset generation is shown in Figure 5.8. This approach for generating datasets is analogous to the incremental method of dataset generation using a sliding window as shown in Chapter 4.

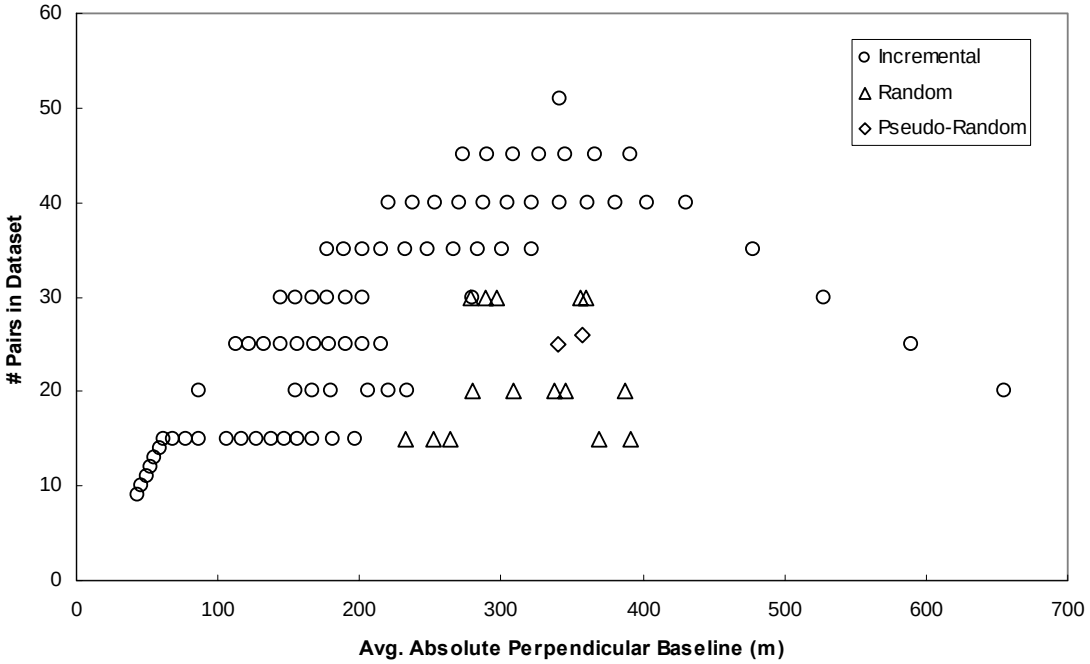

Figure 5.6 All datasets analyzed for patch unwrapping errors characterized by the number of interferograms in the dataset and the resulting average baseline.

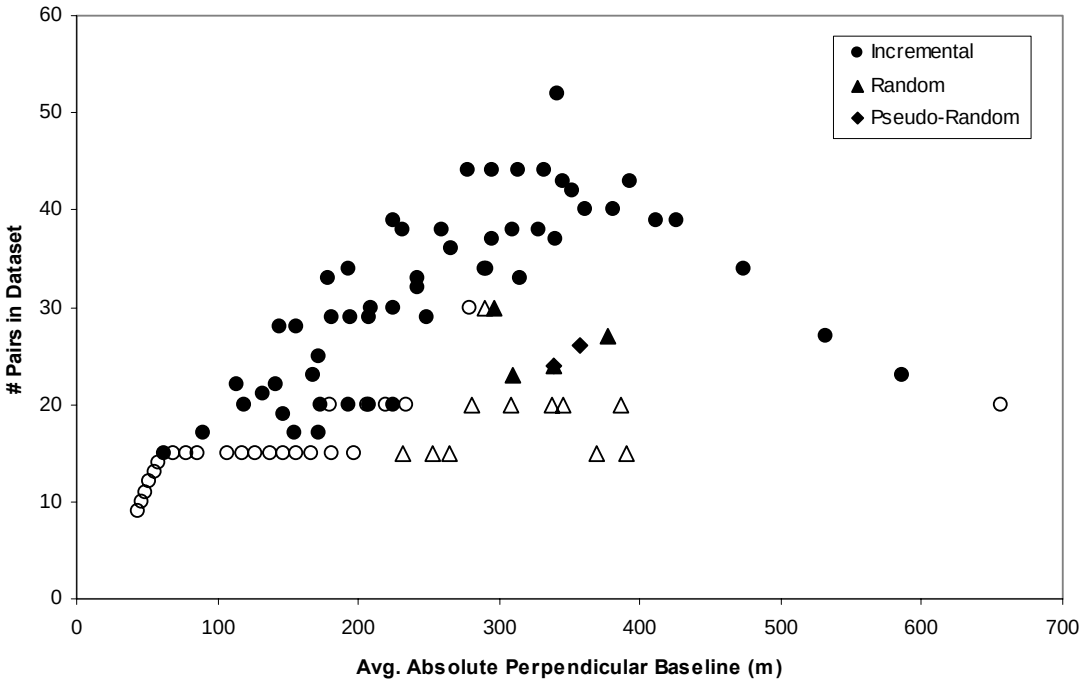

Figure 5.7 Datasets grouped based on success in patch unwrapping. Open symbols depict unsuccessful patch unwrapping while closed symbols depict successful patch unwrapping.

The only dissimilarity between the methods is that in this approach, the size of the sliding window was increased in steps of one rather than keeping its size the same and moving the sliding window to the right in steps of one.

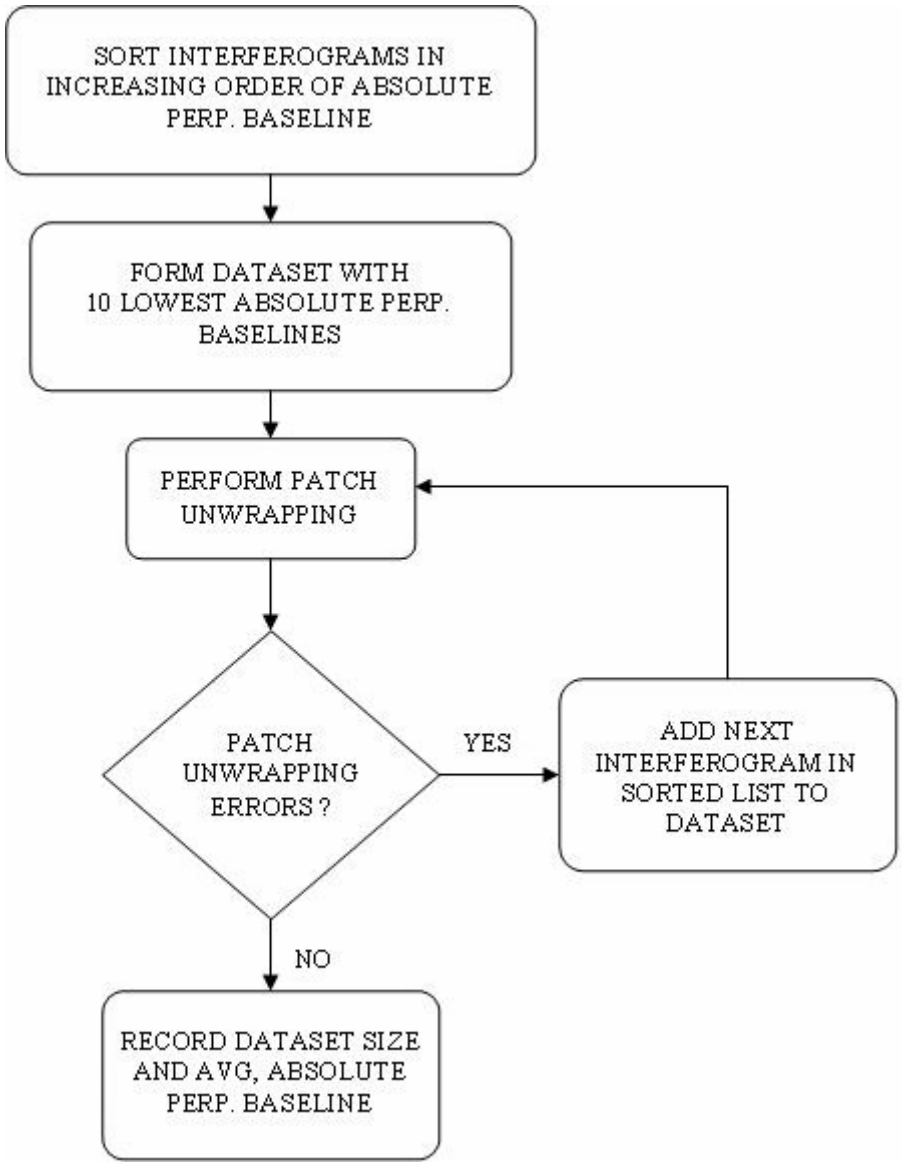

Figure 5.8 Dataset generation method adopted to establish dataset having least number of interferograms which patch unwrapped successfully.

The appended datasets were patch unwrapped and all interferograms in the dataset were checked for patch unwrapping errors. This cycle of appending and patch unwrapping a dataset was continued until all interferograms in the dataset could be unwrapped without patch errors. The subset that eventually unwrapped without patches contained 15 pairs. The average absolute perpendicular baseline of this subset was approximately 62 m with the absolute perpendicular baselines characterizing the interferograms in the dataset ranging between 12 m and 111 m. The IPTA reference manual states that patch unwrapping of small datasets (less than 25 interferograms) could be infeasible due to the lack of reliability of a solution constrained by so few interferograms. In this context, the ability to successfully unwrap a dataset having only 15 interferograms with very short baselines motivated the generation and analysis of the remainder of the datasets (as shown in Figure 5.6) to investigate the existence of a relationship between the average absolute perpendicular baseline of a dataset and the ability to successfully patch unwrap a dataset.

5.3.2 Discussion

The findings of this part of the study can be summarized as follows:

1. As can be inferred from Table 5.1, the removal of some of the interferograms from the original datasets in order to facilitate unwrapping without patches sometimes resulted in an increase in the average perpendicular baseline of the modified dataset and sometimes did not change the average perpendicular baseline significantly in comparison with the average baseline of the original dataset. This suggests that the

average perpendicular baseline of the dataset might not be the dominant parameter influencing the occurrence of patches in the unwrapped interferograms.

2. It is important to recall that the study area is located in an urban setting, where the quality of detected point targets has been proven to be suitable for point target interferometry. From Figure 5.7, it can be inferred that even with a priori information about the location of such point targets, unwrapping without patch errors can be very challenging when the number of interferograms available to constrain the regression is less than or equal to about 20. It may be recalled from Chapter 4 that the point targets detected using all the 52 SLCs were used for analysis of datasets generated from subsets of the SLC data stack.
3. While it was possible to successfully patch unwrap a dataset initially containing 23 of the 25 highest absolute perpendicular baseline interferograms computed for the study area, doing the same with a dataset containing the 20 highest absolute perpendicular baseline interferograms was not possible. Excluding a few cases, and considering that a priori knowledge about the location of point targets was used to constrain the analysis for this part of the study, this indicates that at least 20 - 25 interferograms are needed to constrain the regression reliably.
4. As can be seen from Table 5.1, record number 21 which had a perpendicular baseline of 67.2 m was consistently difficult to unwrap without patch errors. This can be attributed to most of the area in the

interferogram represented by record 21 having phase contribution from atmospheric path delay. In the context of the multi-patch unwrapping approach being an attempt to solve the unwrapping problem in the temporal domain, atmospheric phase can be visualized as a jump in the temporal phase history of point targets. This phase jump can be difficult to resolve and results in unwrapping errors. Such unwrapping errors are similar to the unwrapping errors encountered while trying to solve the unwrapping problem in the spatial domain, where phase jumps resulting from irregular topographic relief can be difficult to resolve, given that the unwrapped phase field is assumed to be spatially smooth. As outlined in the IPTA reference manual, in some cases the best approach was to exclude interferograms with severe atmospheric distortions from the analysis in order to avoid patch unwrapping errors.

5. As mentioned before, datasets that could not be unwrapped without patch errors were modified by removing interferograms. This resulted in datasets with size and average baseline values that were modified relative to the original dataset analyzed. When the datasets before and after removal of interferograms were plotted on the same graph (Figure 5.9), it was not possible to demarcate a distinct boundary separating all the datasets that could be unwrapped from the datasets that could not be unwrapped. This can be used as additional information to confirm that the average baseline of a dataset might not be the most dominant parameter influencing the ability to unwrap a dataset with the multi-patch approach.

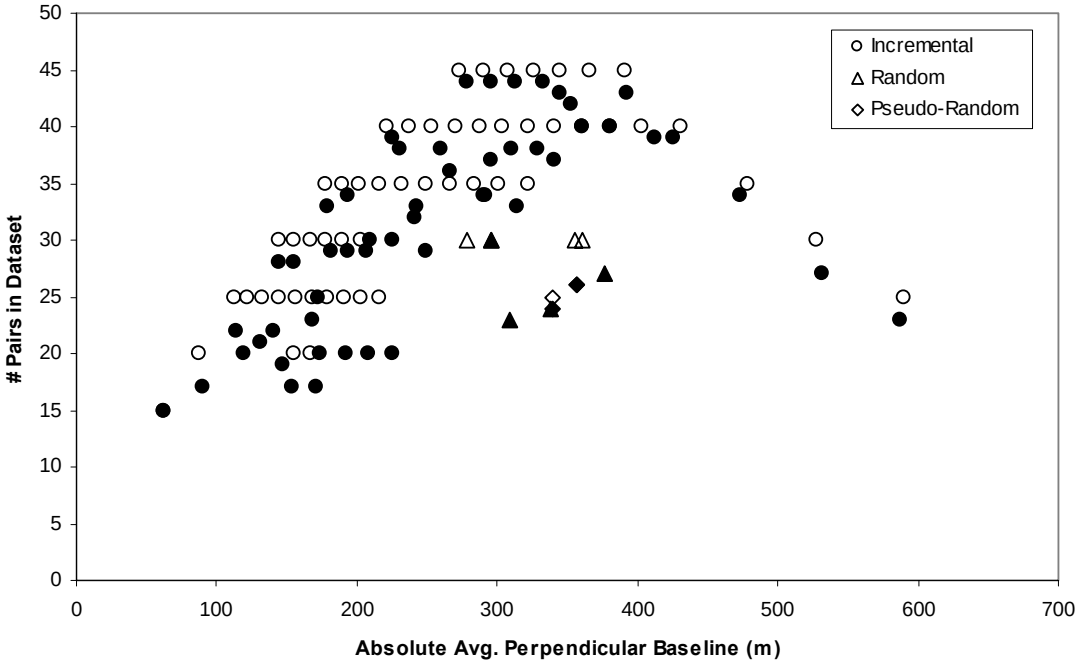

Figure 5.9 Datasets with patch unwrapping errors and the corresponding datasets that resulted from omitting some interferograms to make patch unwrapping possible. Open symbols depict unsuccessful patch unwrapping while closed symbols depict successful patch unwrapping.

6. As can be seen in Figure 5.10, while analyzing the 52 scene dataset with the default standard deviation parameters suggested in the IPTA reference manual, the point targets located in the rugged region to the north-west of all interferograms were rejected from the analysis due to their standard deviations from the two dimensional regression model being greater than the threshold for acceptance.

   However, in cases where the size of datasets analyzed was less than 52, the point targets in the north-west region did not get masked out. This could be attributed to the estimated standard deviation from the regression model being lesser than the specified threshold of 1.2 radians.

The discrepancy in the standard deviation estimates derived for the same point targets when the analysis was constrained by differing numbers of interferograms exhibits that the list of point targets accepted for analysis of a study area can vary depending on the size of the dataset analyzed and hence the standard deviation threshold should be adjusted accordingly. In most cases, when the standard deviation threshold was not enough to reject point targets in the north-west region from analysis, it was found that interferograms affected by patch unwrapping errors had patches in only this region whereas the entire region representing the urban part of the study area was free of such errors. In some cases, the number of point targets in this region that were accepted for analysis based on the standard deviation threshold were so few that the existence of patches in the this part of the interferograms were difficult to discern by means of visual inspection.

In cases where the standard deviation from the regression model as derived from the dataset was not sufficient to reject these point targets from the analysis, information from the 52 scene analysis was used and all point targets in the north-west region were masked out by user interaction. This was done in order to ensure the robustness of unwrapping in all datasets. Such datasets are represented by * in the first column of Table 5.1.

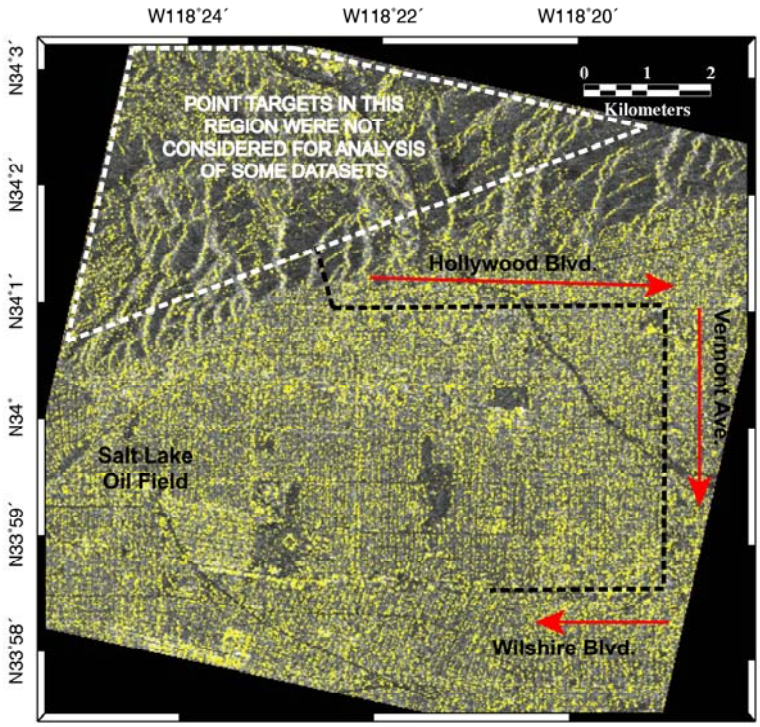

Figure 5.10 Part of the SLC over the study area that was masked from point target analysis of some datasets.

5.4 Analysis of Deformation Rates

The slope of the best fit linear regression line that corresponds to the data points defining the deformation history of a point target yields an estimate of the deformation rate corresponding to that point target. The number of data points defining the deformation history of a point target is given by the number of interferograms used for IPTA analysis. In this section, results obtained on analyzing the deformation rates derived from IPTA for dependence on the number of interferograms constituting a dataset are presented.

5.4.1 Deformation Rate Comparison for Point Targets in Datasets without Patch Unwrapped Errors

While analyzing for dependence of the ability to patch unwrap a dataset on the average baseline parameter (presented in Section 5.3), the datasets that patch unwrapped successfully were subjected to the remainder of the IPTA flow to obtain deformation rate estimates for all point targets located in the study area.

The deformation rates obtained at the end of the IPTA processing flow were then compared to investigate for dependence on the average baseline of the dataset or dependence on the number of interferograms used for IPTA analysis. The deformation histories compared contain both time linear and non-linear deformation components. To facilitate the comparison, point targets were selected at random locations in the study area and their deformation histories as obtained from different IPTA runs were plotted. The point target locations chosen for deformation history comparison are shown in Figure 5.11. In order to analyze dependence of the deformation histories on the average absolute perpendicular baseline defining the datasets, all datasets that patch unwrapped successfully were divided into two groups, namely

1. Datasets with average absolute perpendicular baseline less than 200 m, and
2. Datasets with average absolute perpendicular baseline greater than 200 m.

Figure 5.12 through Figure 5.20 compare the deformation histories of selected point targets as obtained when the study area was analyzed with datasets having (a) average absolute perpendicular baselines less than 200 m and (b) average

absolute perpendicular baselines greater than 200 m. The deformation history as obtained from the 52 pair dataset was chosen as the reference for comparison and hence is shown on all plots in Figure 5.12 through Figure 5.20.

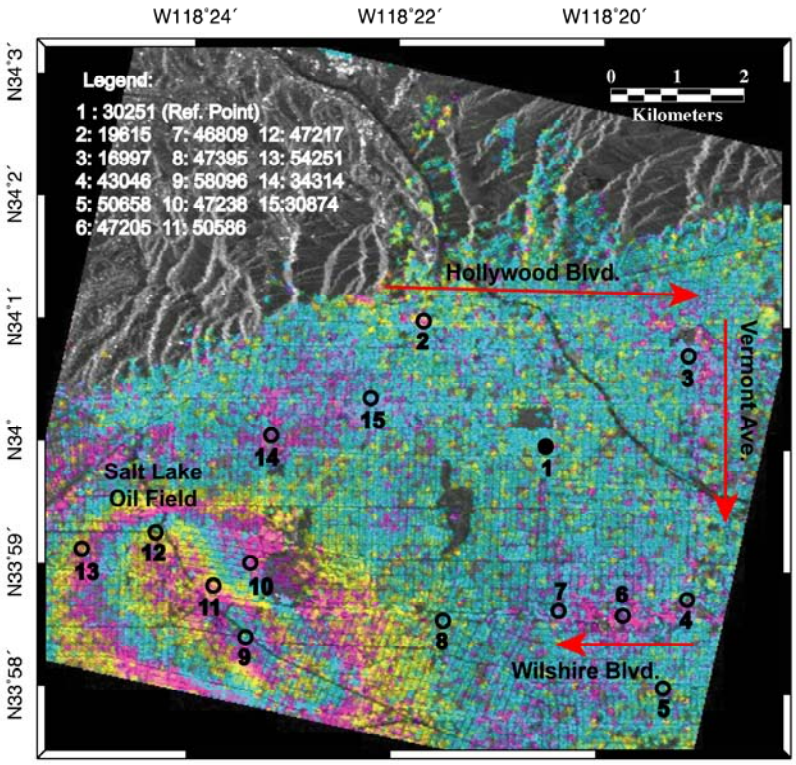

Figure 5.11 Point targets chosen for deformation rate comparison.

The convention used in Figure 5.12 through Figure 5.20 was chosen in order to represent the datasets by the number of constituent interferograms, excluding the auto-pair, as well as the inherent average absolute perpendicular baseline. Hence, 51_349, for example, represents the 52 pair dataset (51 plus the auto-interferogram) that had an average absolute perpendicular baseline of 349 m. The average absolute perpendicular baseline shown on the plots was rounded to the next integer for convenience in representation.

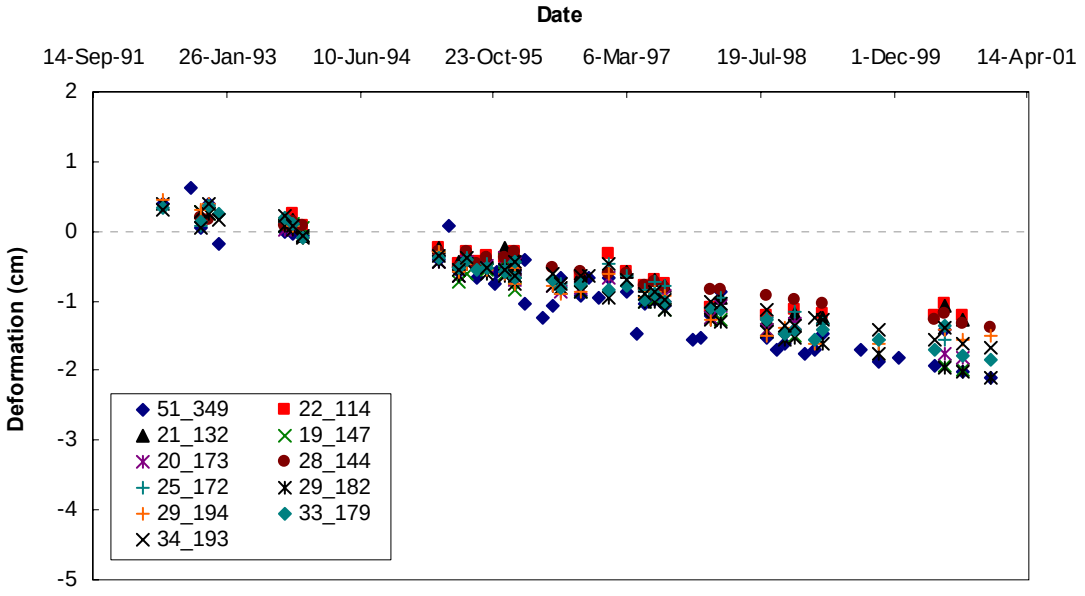

(a)

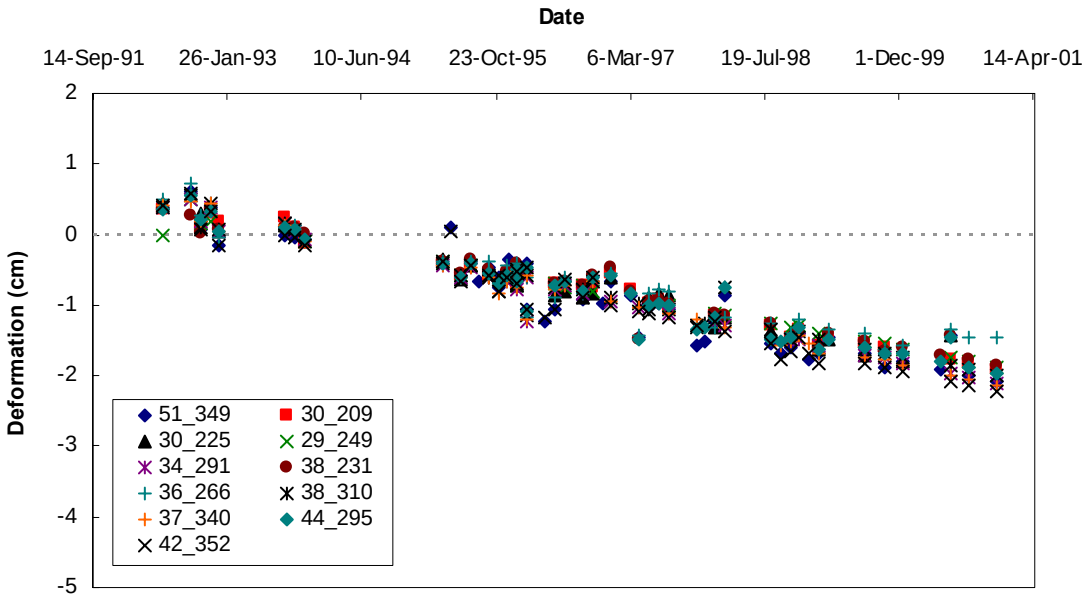

(b)

Figure 5.12 Deformation history for point 47238. (a) Average perpendicular baseline less than 200 m, (b) Average perpendicular baseline greater than 200 m. 51_349 indicates 51 non-zero baseline interferogram dataset with an average baseline of 349 m.

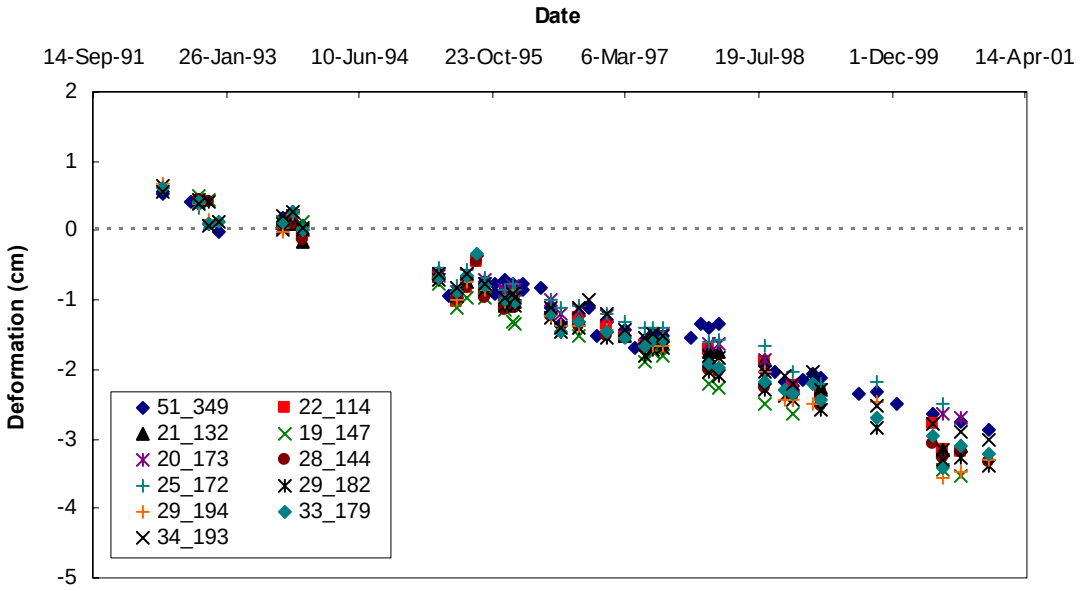

(a)

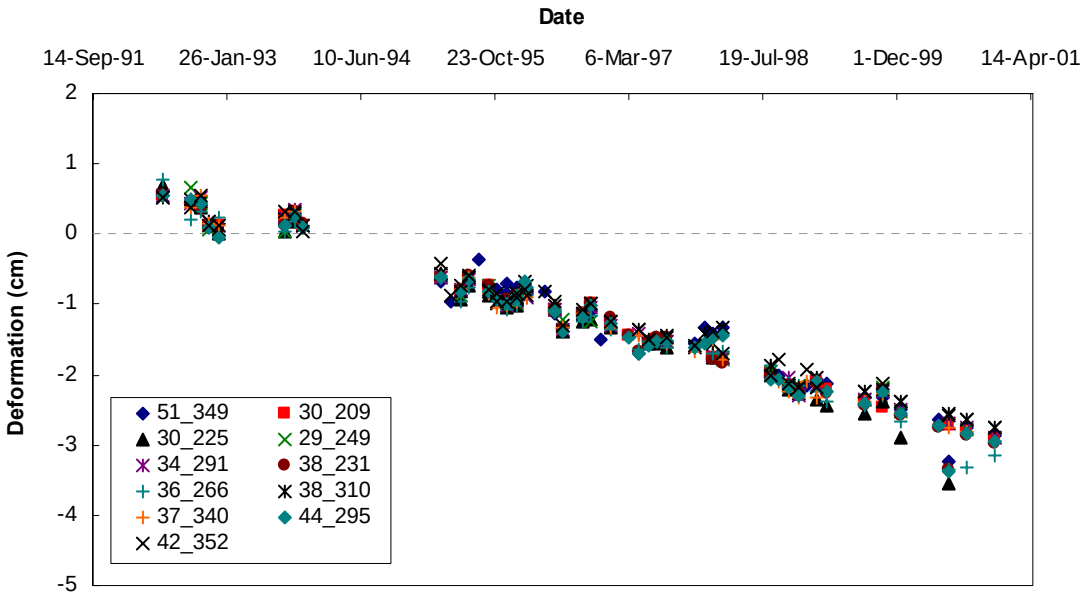

(b)

Figure 5.13 Deformation history for point 47217. (a) Average perpendicular baseline less than 200 m, (b) Average perpendicular baseline greater than 200 m. 51_349 indicates 51 non-zero baseline interferogram dataset with an average baseline of 349 m.

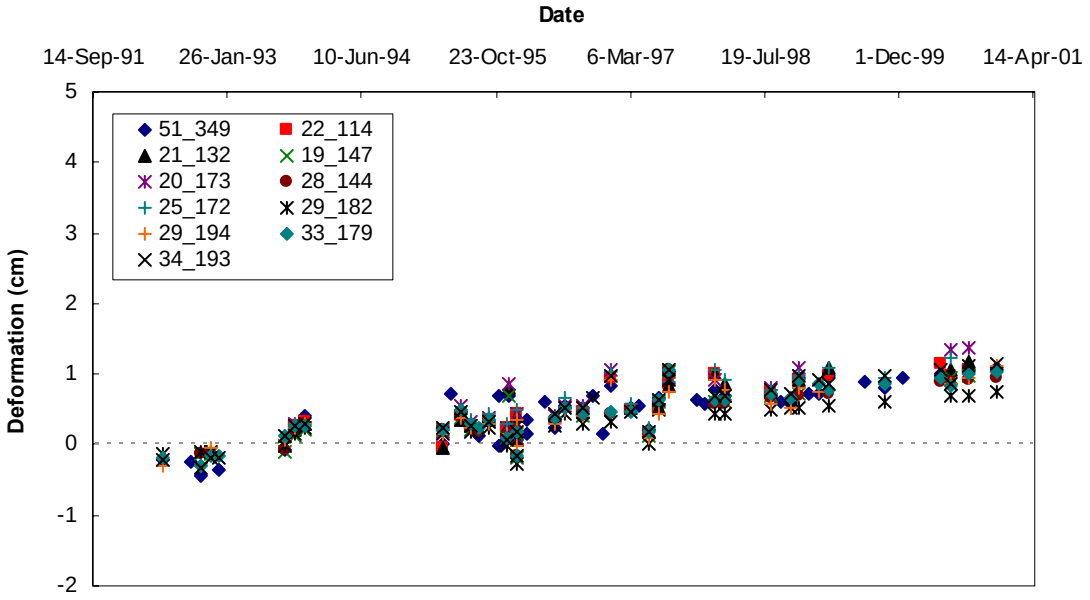

(a)

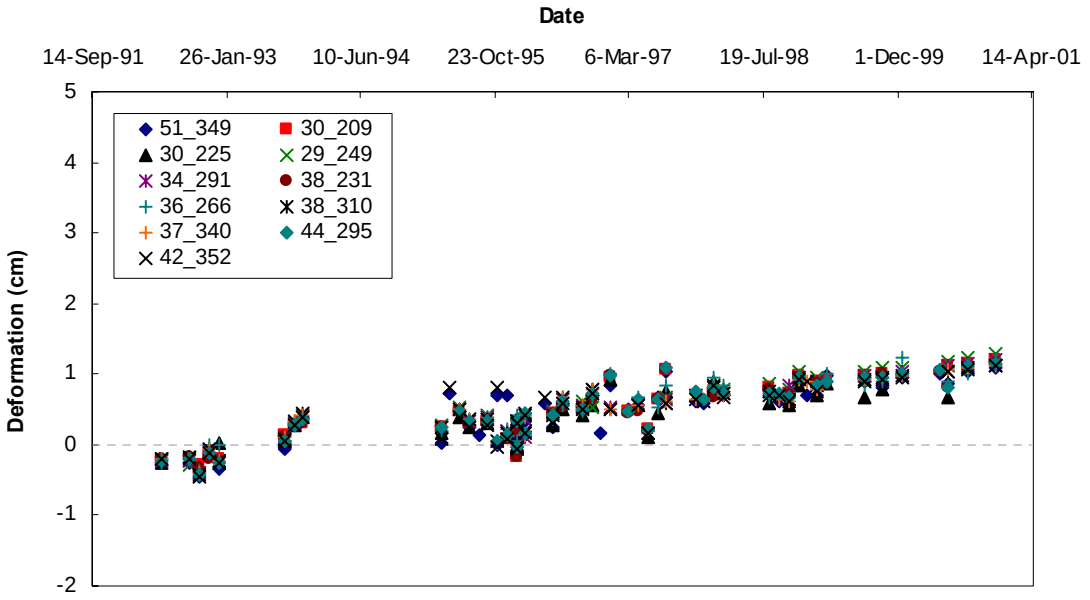

(b)

Figure 5.14 Deformation history for point 47205. (a) Average perpendicular baseline less than 200 m, (b) Average perpendicular baseline greater than 200 m. 51_349 indicates 51 non-zero baseline interferogram dataset with an average baseline of 349 m.

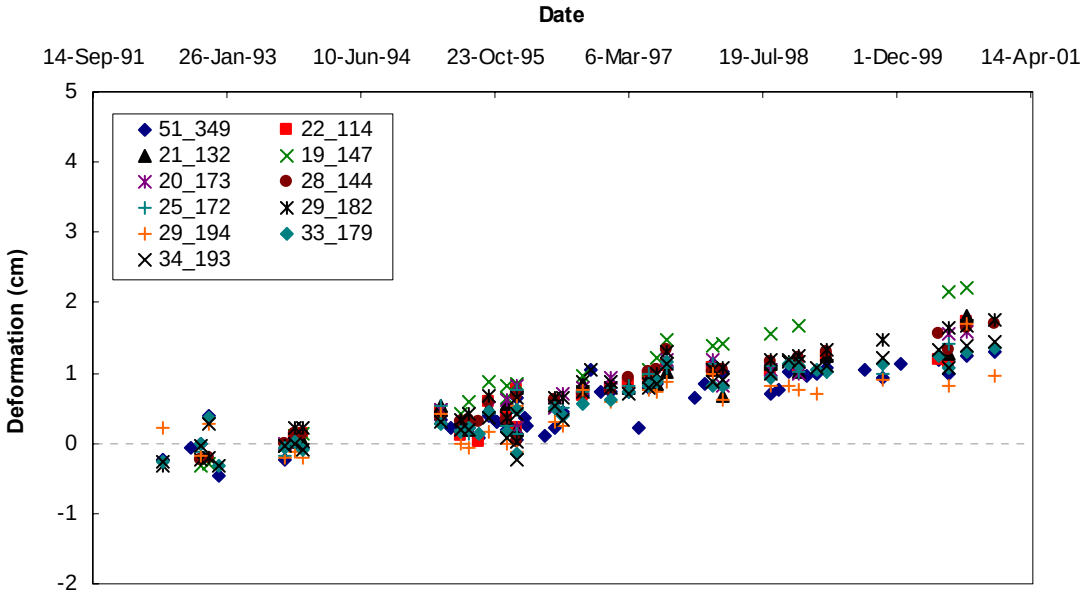

(a)

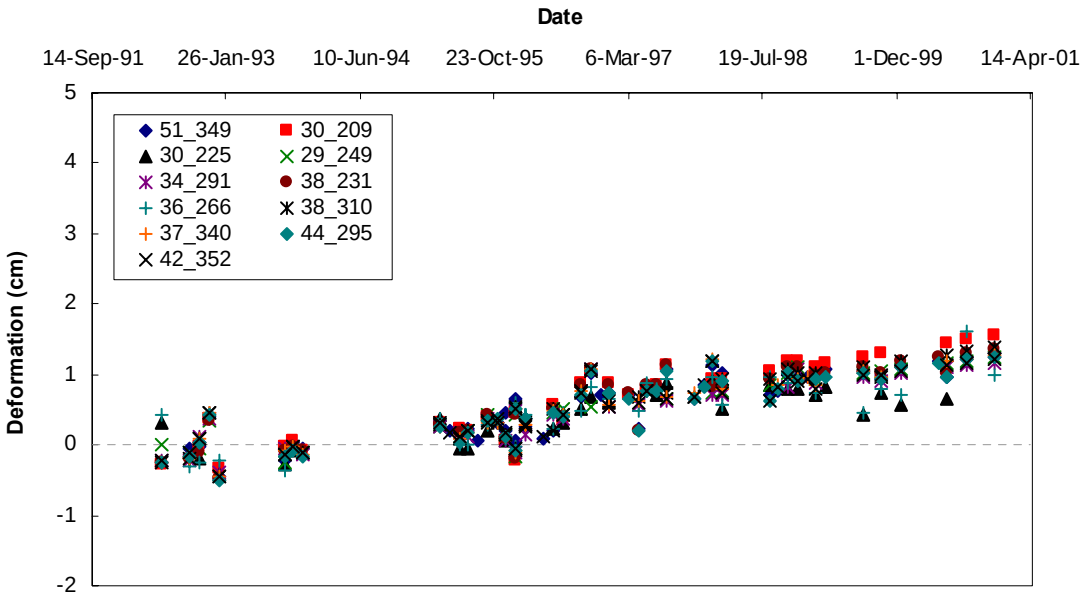

(b)

Figure 5.15 Deformation history for point 43046. (a) Average perpendicular baseline less than 200 m, (b) Average perpendicular baseline greater than 200 m. 51_349 indicates 51 non-zero baseline interferogram dataset with an average baseline of 349 m.

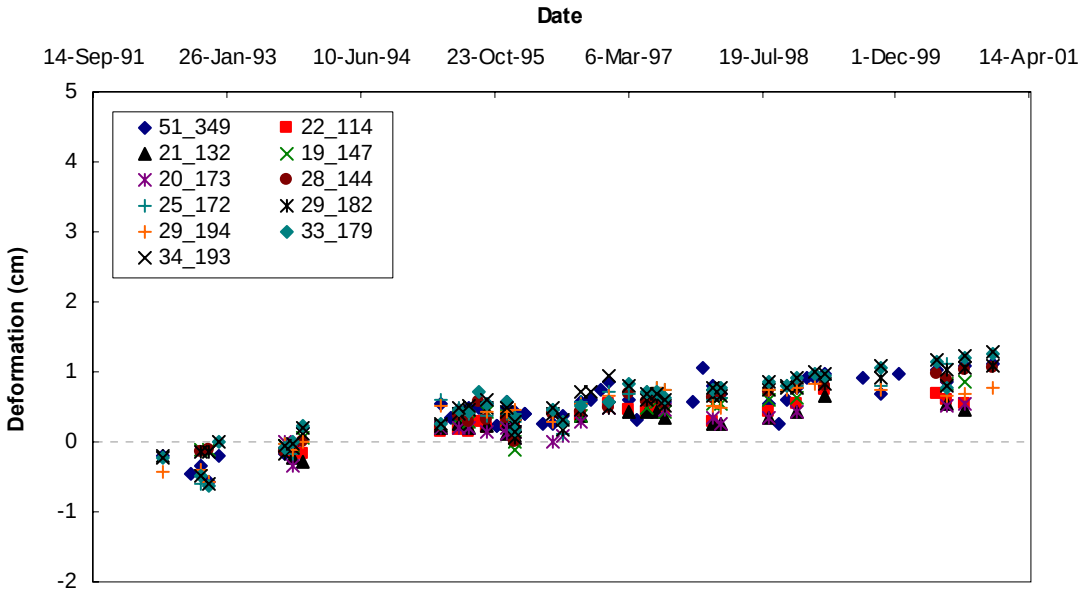

(a)

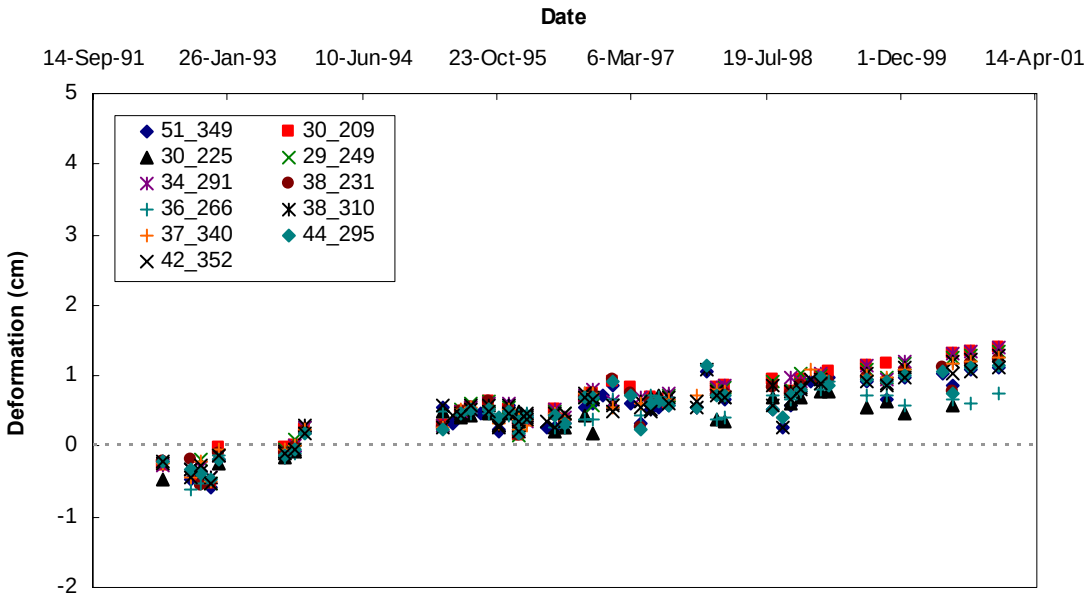

(b)

Figure 5.16 Deformation history for point 34314. (a) Average perpendicular baseline less than 200 m, (b) Average perpendicular baseline greater than 200 m. 51_349 indicates 51 non-zero baseline interferogram dataset with an average baseline of 349 m.

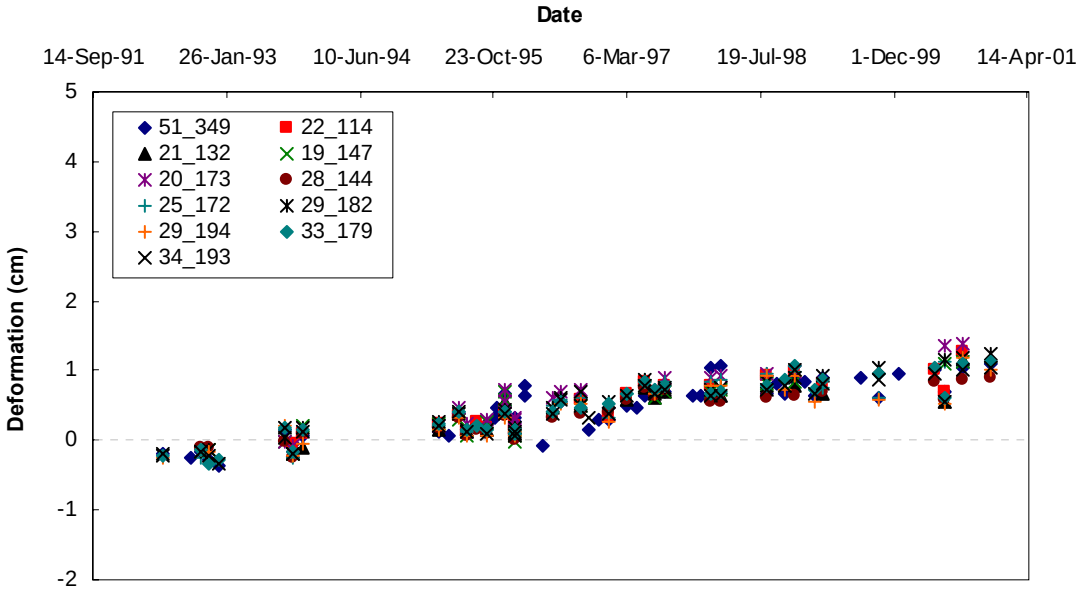

(a)

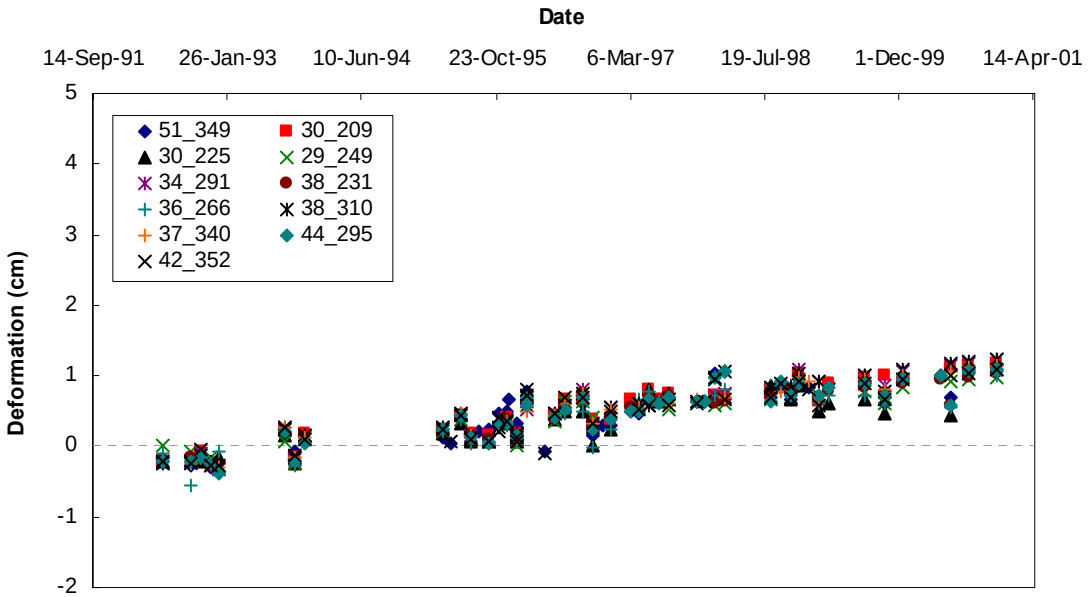

(b)

Figure 5.17 Deformation history for point 30874. (a) Average perpendicular baseline less than 200 m, (b) Average perpendicular baseline greater than 200 m. 51_349 indicates 51 non-zero baseline interferogram dataset with an average baseline of 349 m.

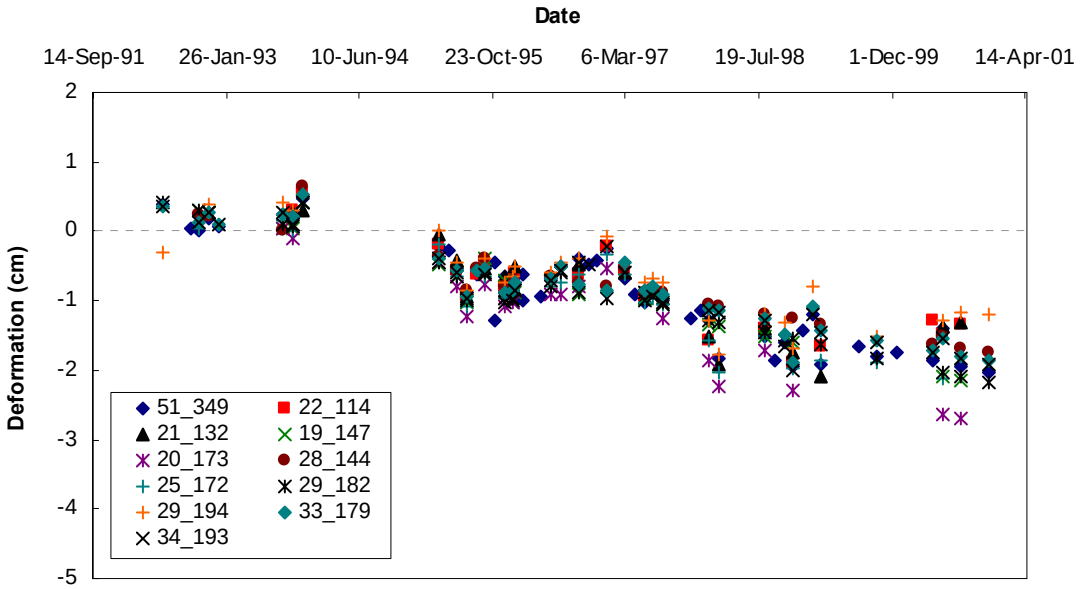

(a)

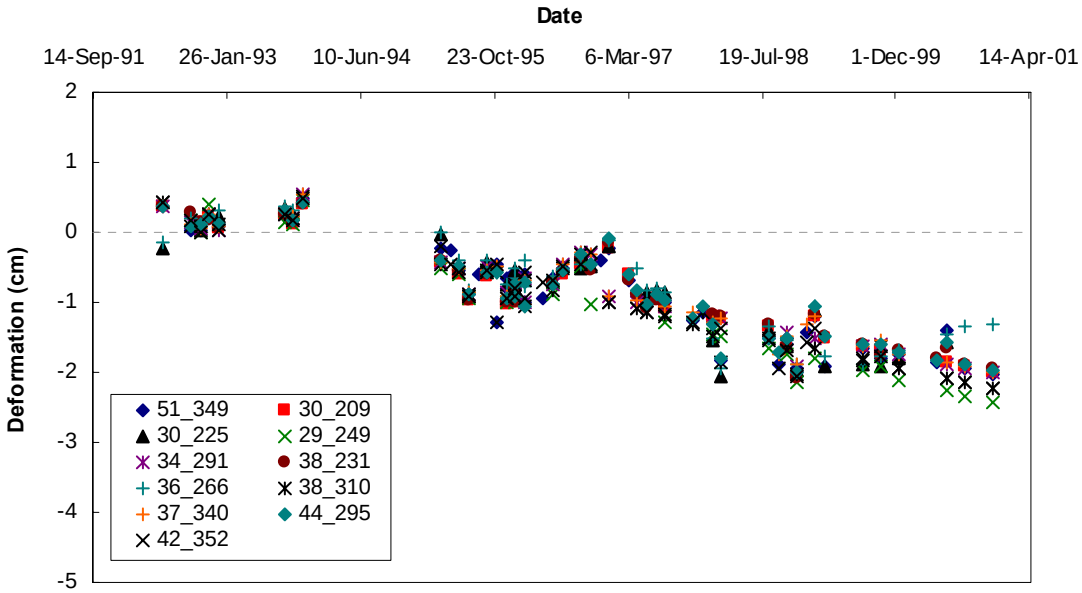

(b)

Figure 5.18 Deformation history for point 19615. (a) Average perpendicular baseline less than 200 m, (b) Average perpendicular baseline greater than 200 m. 51_349 indicates 51 non-zero baseline interferogram dataset with an average baseline of 349 m.

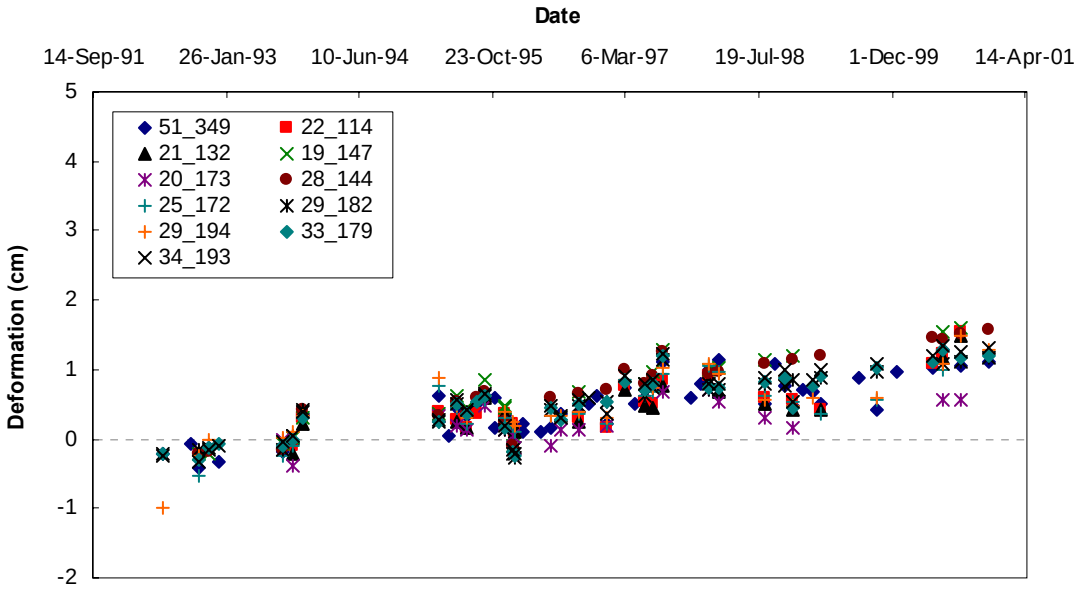

(a)

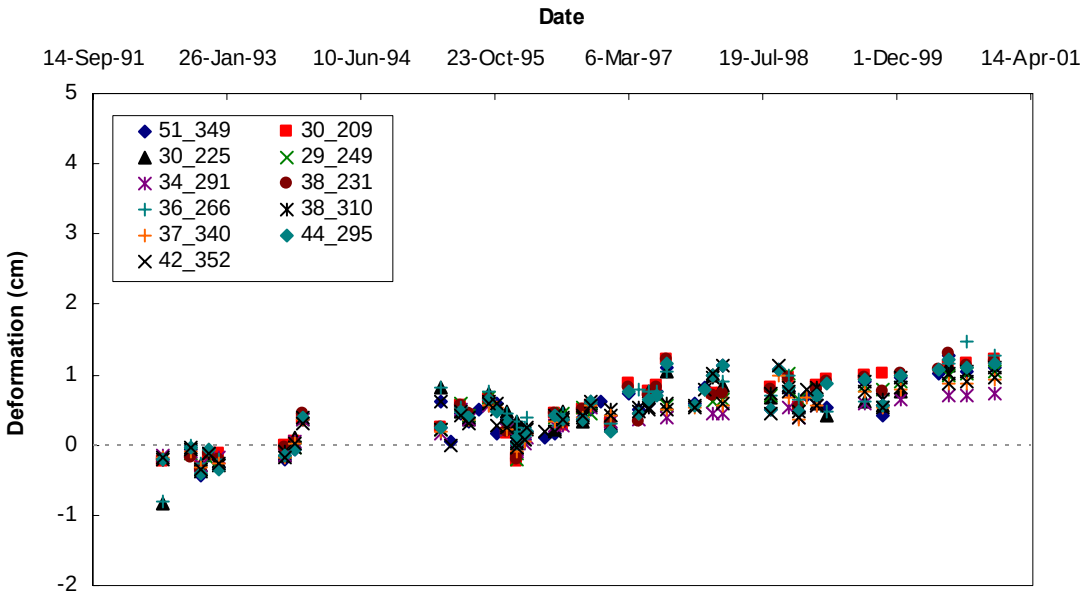

(b)

Figure 5.19 Deformation history for point 16997. (a) Average perpendicular baseline less than 200 m, (b) Average perpendicular baseline greater than 200 m. 51_349 indicates 51 non-zero baseline interferogram dataset with an average baseline of 349 m.

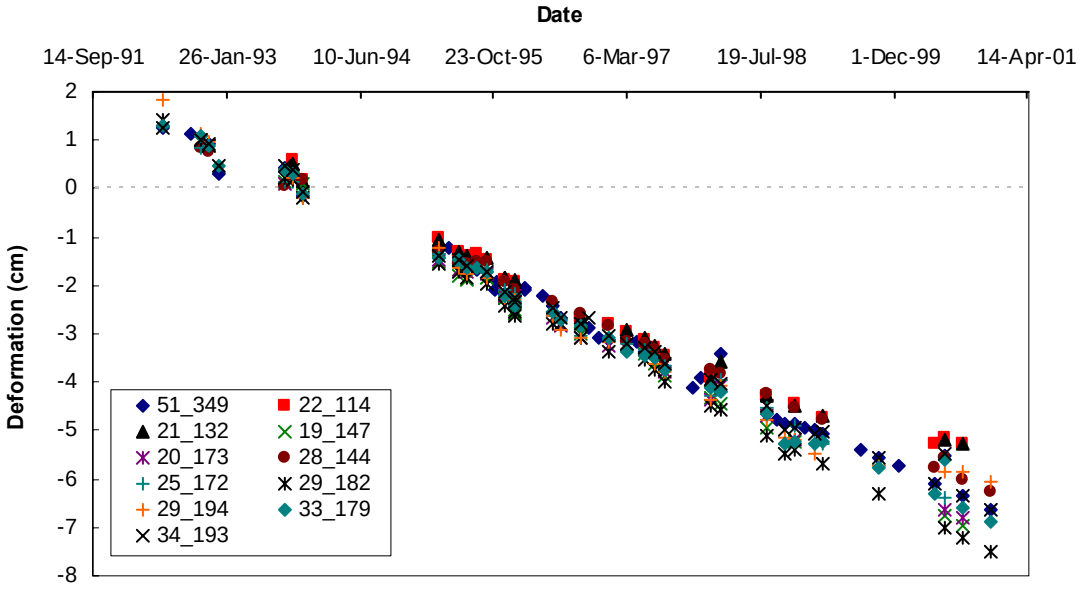

(a)

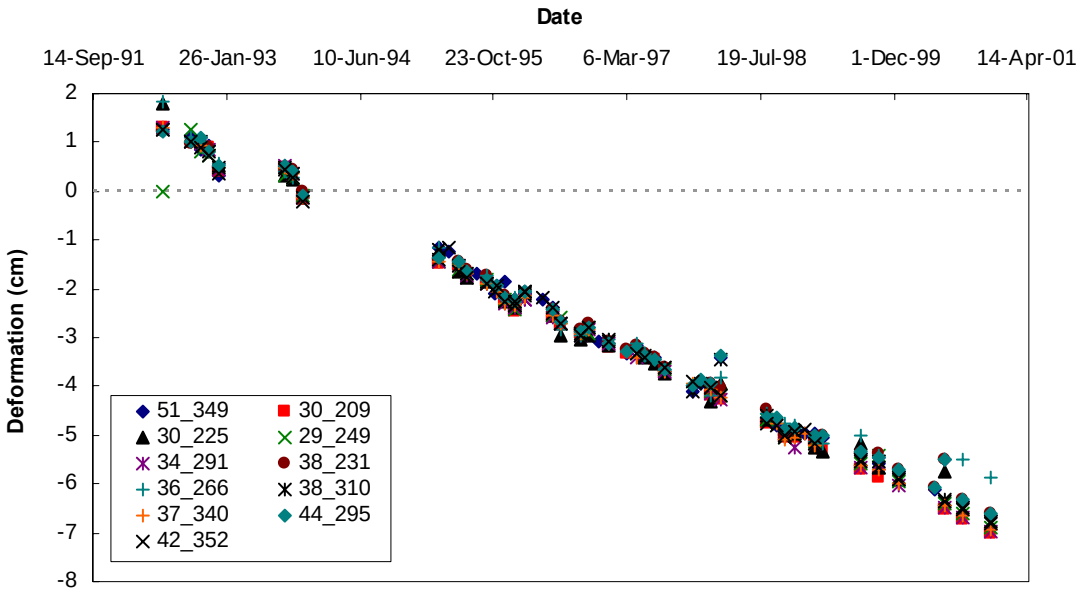

(b)

Figure 5.20 Deformation history for point 58096. (a) Average perpendicular baseline less than 200 m, (b) Average perpendicular baseline greater than 200 m. 51_349 indicates 51 non-zero baseline interferogram dataset with an average baseline of 349 m.

From the deformation history comparison plots shown above, it can be observed that the deformation (in centimeters) of a point target relative to

1. the user-defined reference point 30251, and
2. relative to the user defined temporal reference ERS1-11609,

at a specific point in time is slightly different when derived from different subsets of data. However, the overall sense of the deformation (uplift or subsidence) and the deformation rate that can be inferred from the slope of the best-fit straight line through the deformation history are generally consistent with the 51 interferogram dataset results.

For a statistically robust quantification of the variability of the deformation time history as obtained from IPTA analysis using different datasets, a sample size greater than the number of datasets that patch unwrapped successfully is needed. The results obtained by statistically comparing deformation rates of point targets as obtained from an increased number of datasets is presented in Section 5.4.2.

5.4.1.1 Deformation Rate Discrepancies for Point Targets

In contrast to the observation of deformation rates that were consistent between IPTA analyses constrained by varying dataset sizes, comparing deformation rates obtained from different datasets yielded large discrepancies for some point targets. More specifically, it was found that subsidence as derived from some datasets, including the dataset having 51 interferograms, was being mapped as uplift and vice-versa.

A detailed examination of the outputs derived from each IPTA processing step for the point targets showing deformation rate discrepancies was performed. It was found that the unwrapped phase values being assigned to the point target at different points in time, as accomplished by patch unwrapping in the temporal domain, was different from the unwrapped phase values that were assigned to the same point target when temporal unwrapping was constrained by a dataset containing all 51 interferograms. In other words, inconsistent unwrapped values were obtained for some point target locations when the IPTA analysis was constrained with different datasets. These inconsistent unwrapped phase values translated into inconsistent deformation rates that were obtained at the end of the IPTA processing flow.

It must be noted that the inconsistent values of unwrapped phase did not result in patch errors and hence could not be detected in the part of the study outlined in Section 5.3.1. Recall that unwrapping in the temporal domain was accomplished by means of the multi-patch method that relies on simultaneously resolving the phase unwrapping problem and dependence of the resulting unwrapped phase on time and perpendicular baseline by means of the two-dimensional regression. Figure 5.21 and Figure 5.22 show the results of two-dimensional regression for one such point target with respect to the reference point, when the solution was

1. Constrained with a dataset having 18 non-zero baseline interferograms, and
2. Constrained with all 51 non-zero baseline interferograms.

The results of the two-dimensional regression shown in Figure 5.21 and Figure 5.22 correspond to the first iteration of the IPTA processing flow. The multi-patch approach solves the unwrapping problem and infers baseline and time dependence of the unwrapped phase simultaneously. However, as mentioned in Chapter 3, although the baseline and time dependencies are inferred from the unwrapped phase, the GAMMA IPTA module rewraps the unwrapped phase in the graphical representation of the two-dimensional regression analysis. Hence, it must be noted that the relative phase values represented by the cross marks in Figure 5.21 and Figure 5.22 are rewrapped versions of the unwrapped phase.

Due to the difference in the unwrapped phase values that were inferred for point target # 19655 for different points in time, the inferred baseline dependence- which translates into an incremental relative height correction, and the inferred time dependence- which translates into an incremental linear deformation rate, are different for the 51 interferogram case and the 18 interferogram case. Due to the iterative nature of the IPTA processing flow, an inconsistency in the inferred linear deformation rate and height correction at the end of the first iteration propagates into the rest of the process, thus resulting in a discrepancy in the inferred linear deformation rates and height corrections at the end of the analysis. Such discrepancies are illustrated in Figure 5.23 through Figure 5.26.

The star and the open circle represent deformation in terms of radians of phase as inferred from two IPTA analyses constrained by different datasets. The open triangles indicate the difference between the unwrapped phase values at

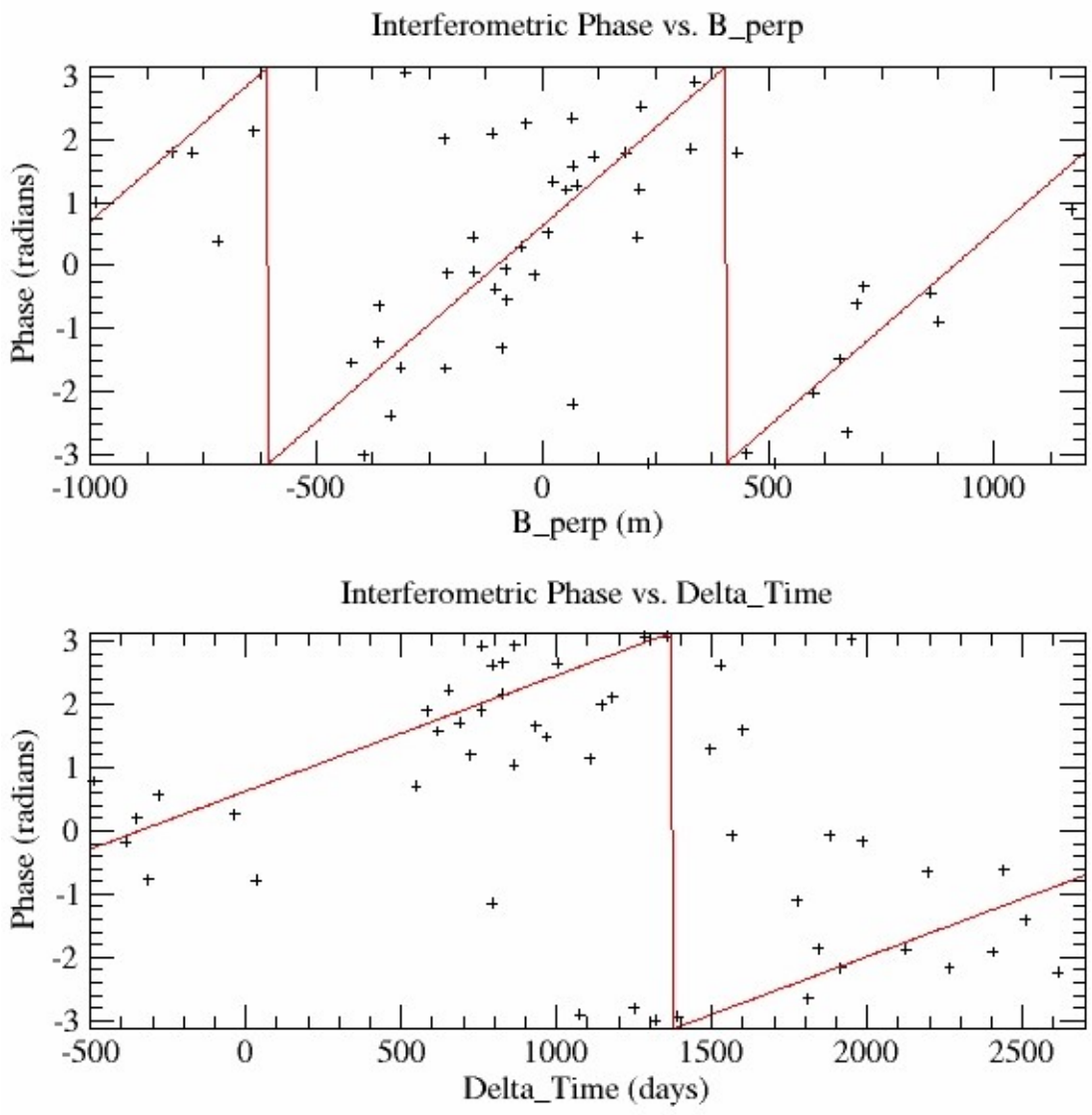

Figure 5.21 Two dimensional regression analysis for point target 19655 with respect to point target 30251 constrained with 51 interferograms.

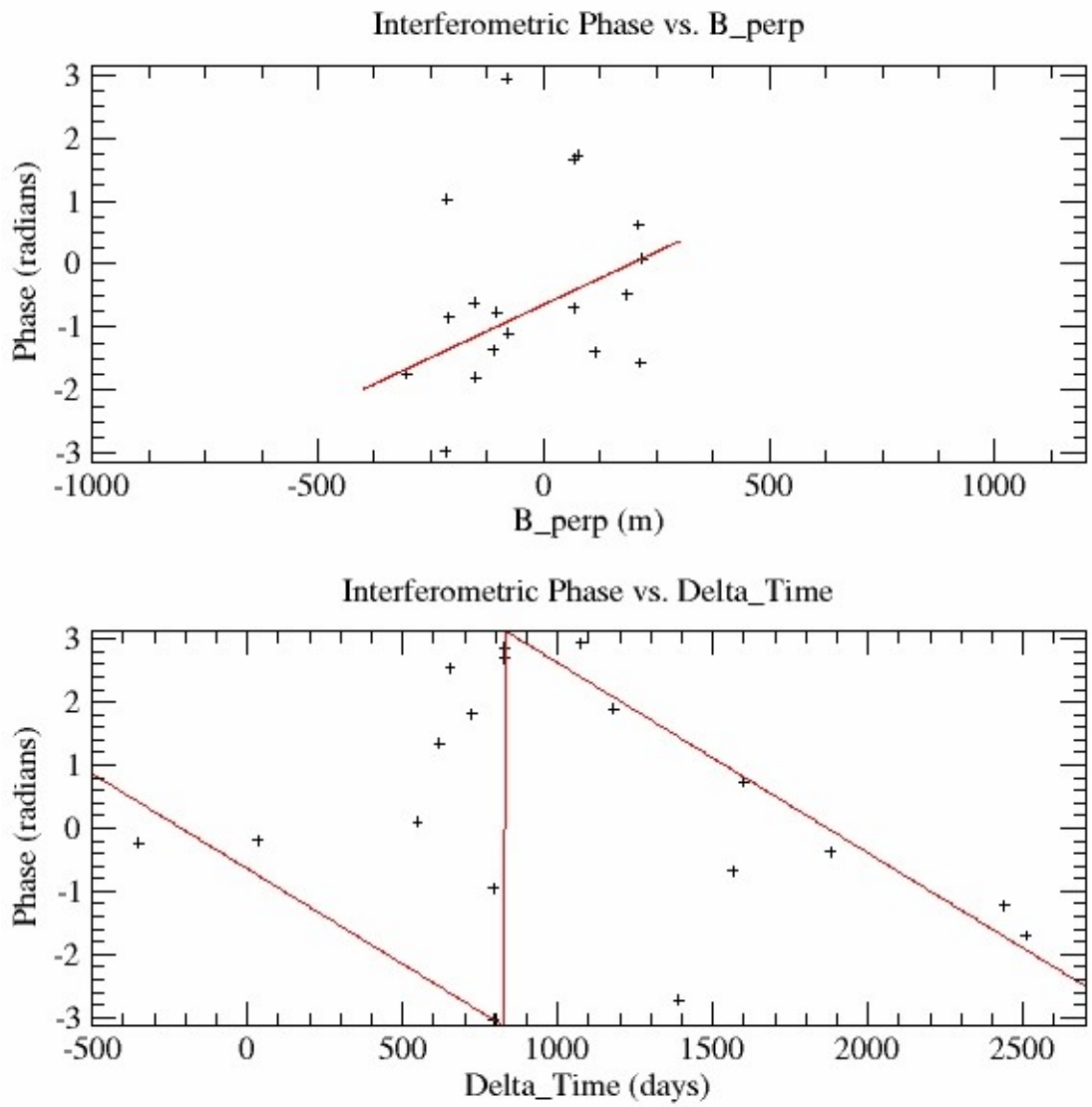

Figure 5.22 Two dimensional regression analysis for point target 19655 with respect to point target 30251 constrained with 18 interferograms.

specific points in time. Similar unwrapped phase values as obtained from the two IPTA analyses being compared would result in the triangles being plotted along the zero axis. It can be seen from Figure 5.23 through Figure 5.26 that any difference in the unwrapped phase values as obtained from the two IPTA analyses, translates into a difference in the deformation rates inferred. It can be

inferred from the deformation history that the deformation phase shown in Figure 5.23 through Figure 5.26 have both time linear and non-linear components.

From Figure 5.23 through Figure 5.26, it can also be observed that such unwrapped phase discrepancies do not correspond to only very small datasets. Figure 5.24 shows an example where a discrepancy in the inferred deformation rate of a point target was observed even when IPTA analysis was constrained with 44 interferograms. The significance of this finding can be evaluated in the context of the situation when only those SAR scenes that would result in inconsistent deformation rate inference are available for analysis. In order to mitigate such instances, it is recommended that

1. The values of standard-deviation-from-linear-fit parameters that can be used to mitigate such inconsistent unwrapped phase values as obtained from *multi_def_pt* must be investigated, and
2. Keeping in mind that the choice of point target candidates and that their quality control was accomplished by means of using the default parameters recommended in the IPTA reference manual, the parameter values that can help reject point targets corresponding to such inconsistent deformation rate inferences should be investigated.

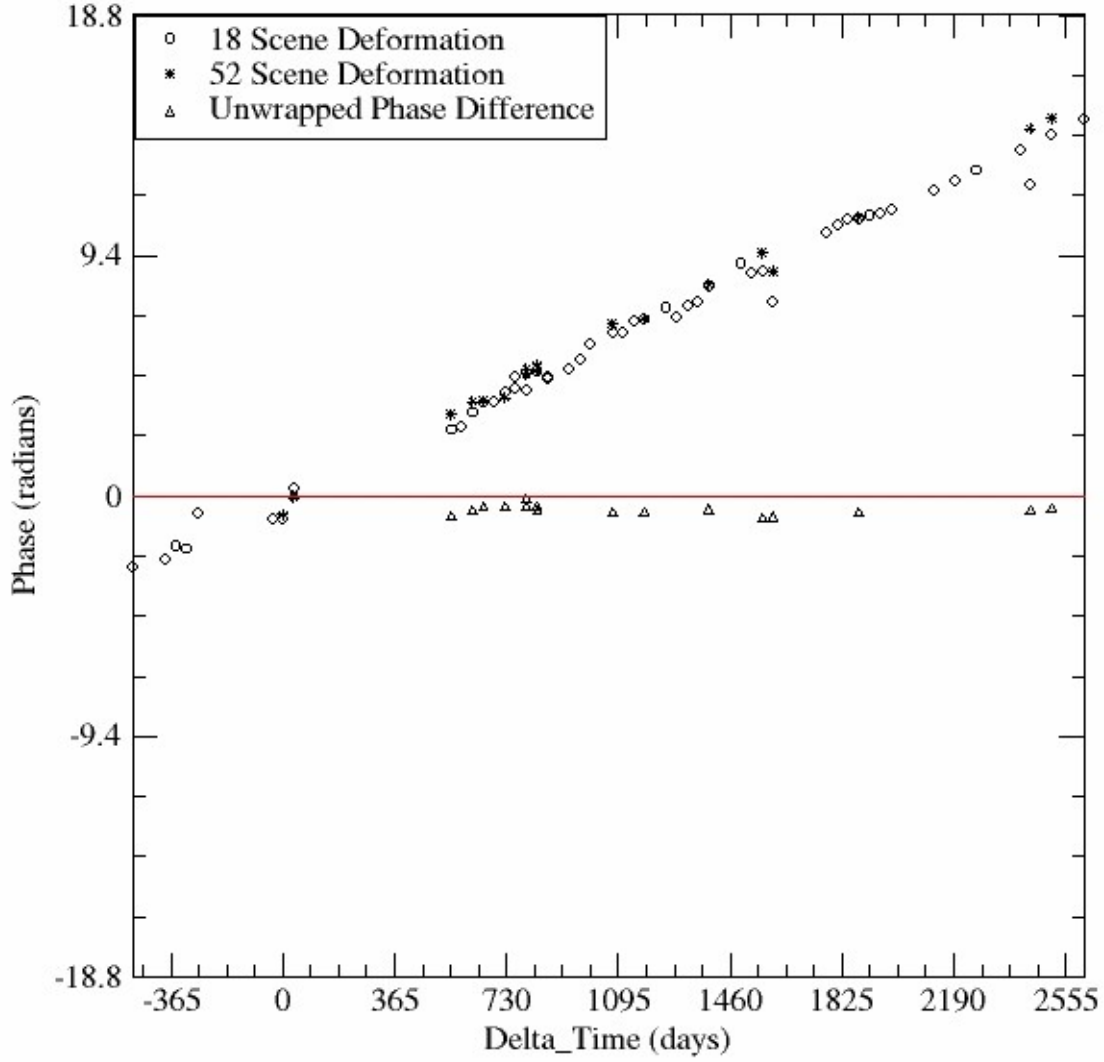

Figure 5.23 Deformation phase comparison for point target number 58096 located at the middle of the subsidence zone resulting due to oil pumping.

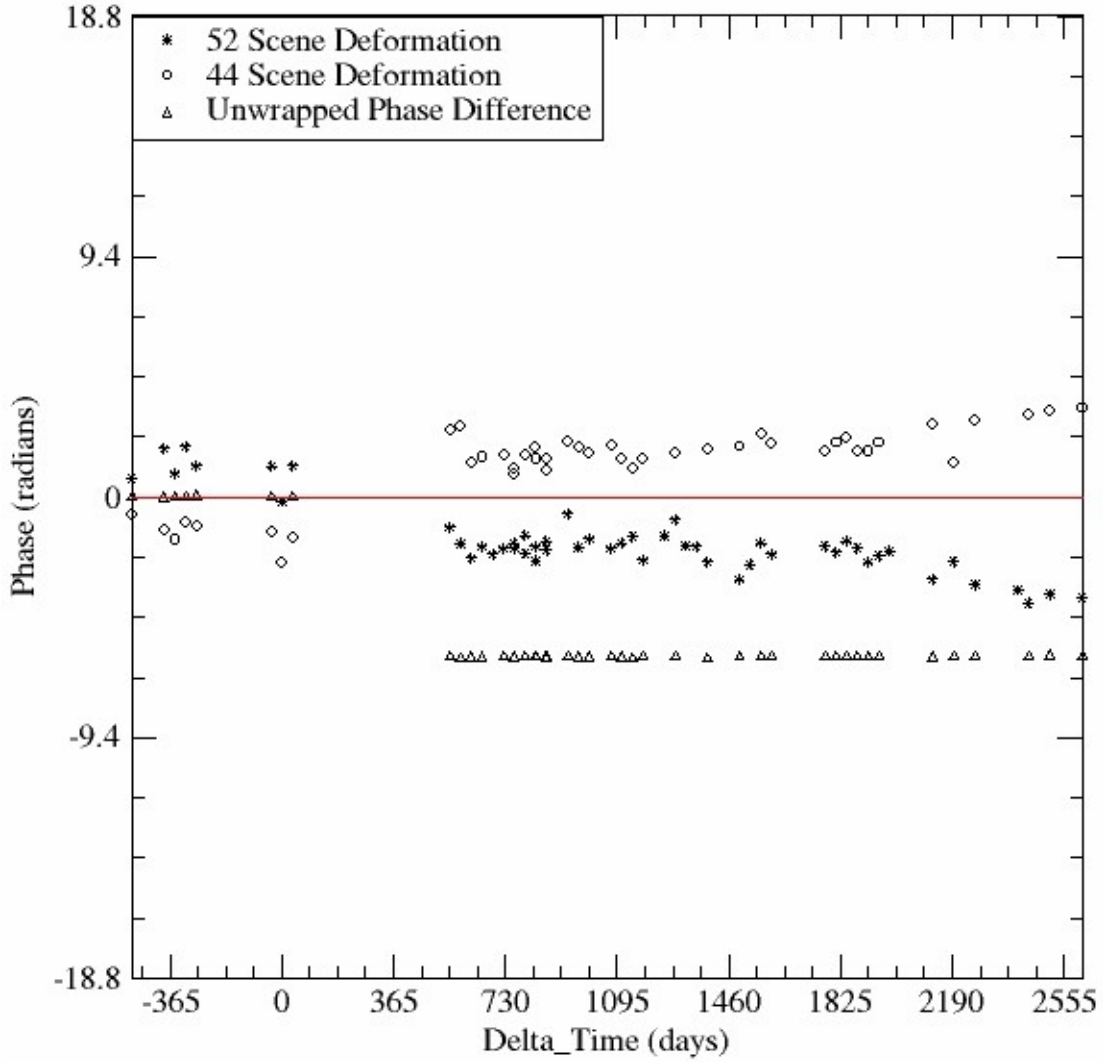

Figure 5.24 Deformation phase comparison for point number 16928.

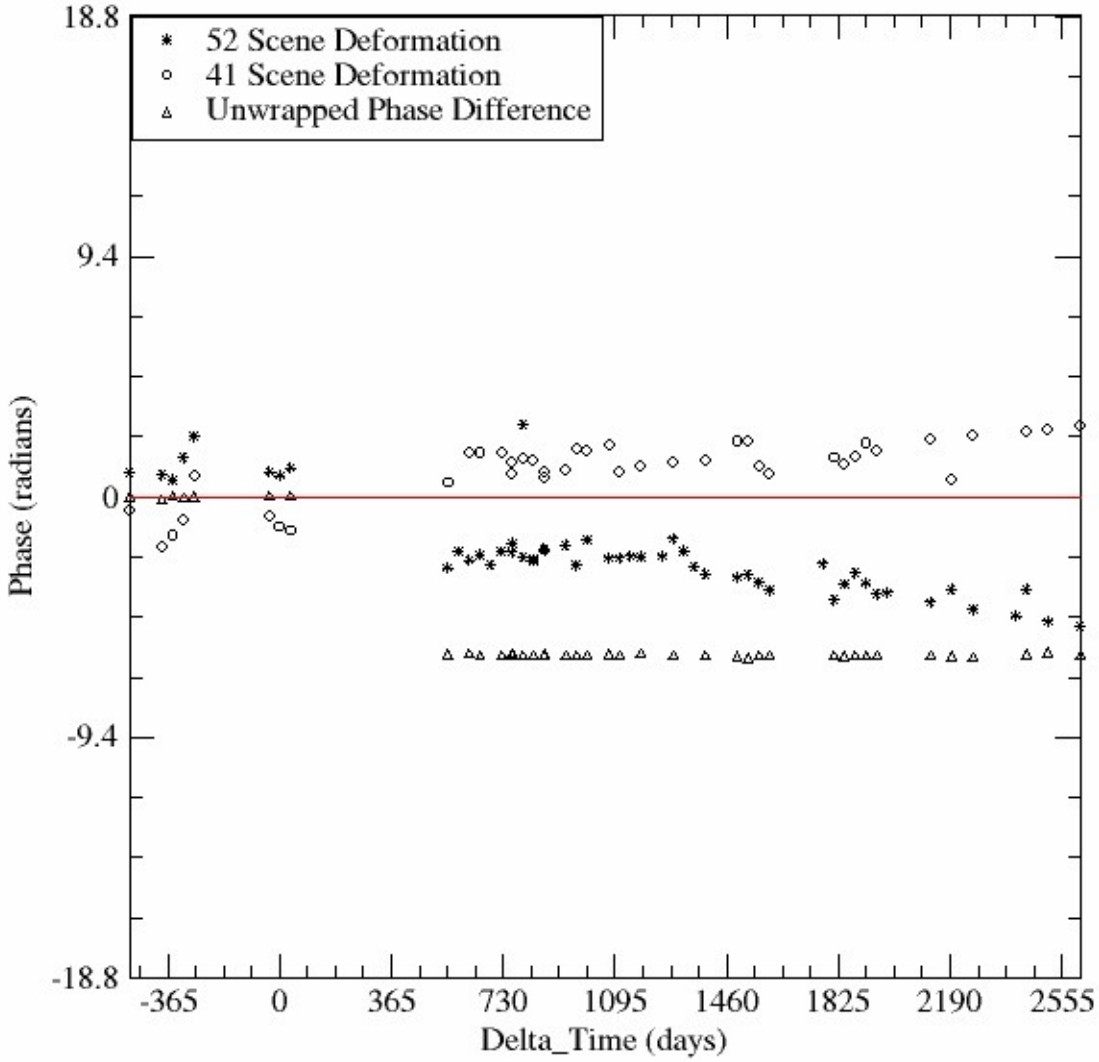

Figure 5.25 Deformation phase comparison for point number 14858.

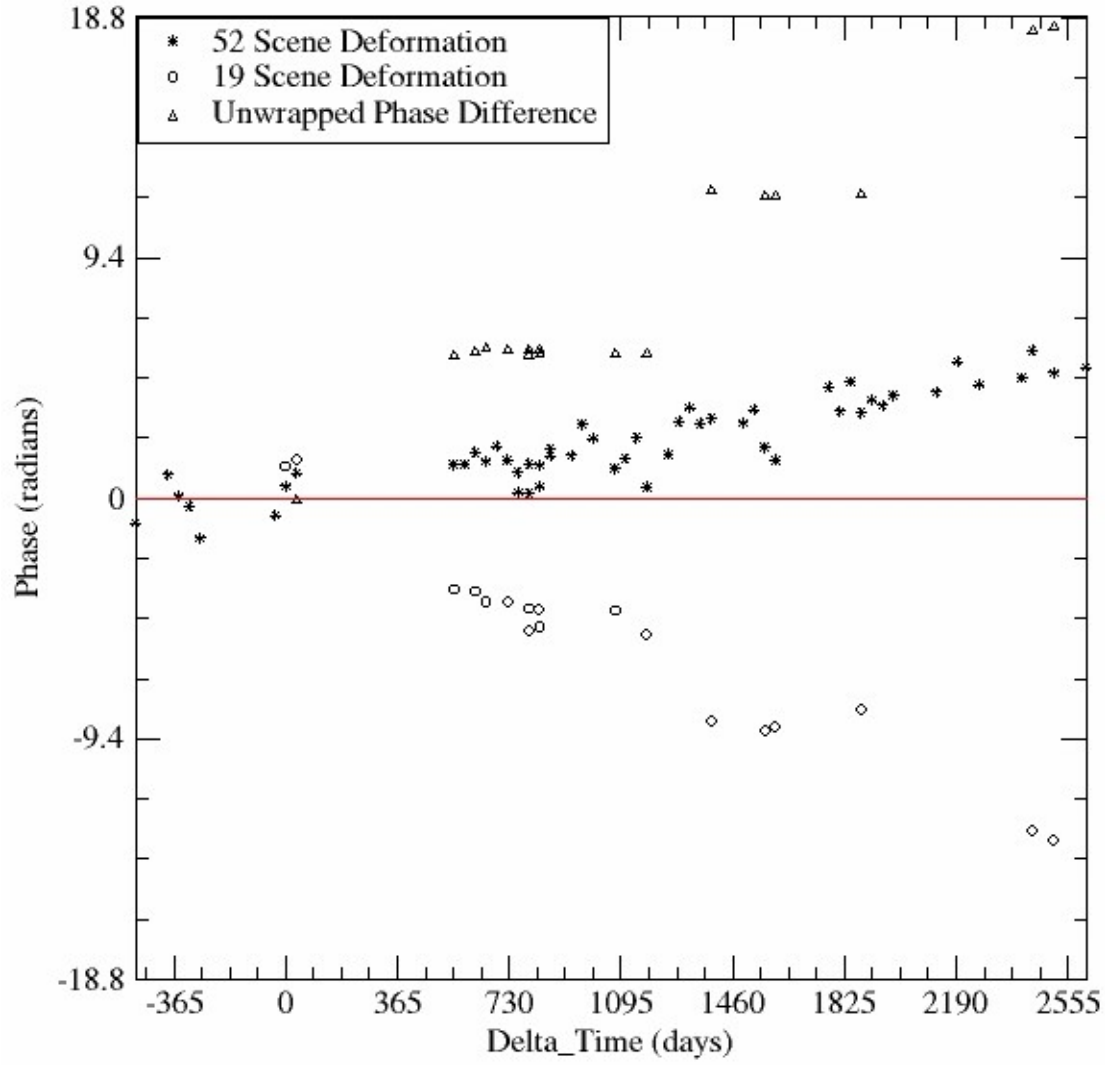

Figure 5.26 Deformation phase comparison for point number 44204.

5.4.2 Statistical Assessment of Dependence of Deformation Rate Estimates on the Size of Dataset

In practice, the size of a dataset used for point target analysis of a site depends on the number of SAR images available for analysis. In such an event, having an estimate of the variability associated with the deformation rates derived from point target analysis as a function of the size of the dataset would be valuable to quantify the associated reliability.

Motivated by the value of such information, the third objective of the study was to assess and quantify the variation of deformation rates associated with point targets as a function of the number of interferograms used to constrain the point target analysis. Point target analysis for this part of the study was applied to four groups of datasets that were generated by random sampling of the 51 correctly patch-unwrapped interferograms (obtained from point target analysis aimed at accomplishing the first objective of the study). The four groups were classified depending on the size of the datasets comprising each group. Not counting the auto-interferogram, the four groups of datasets that were used in this part of the study consisted of: (1) 15 interferograms, (2) 25 interferograms, (3) 35 interferograms and (4) 40 interferograms. Each group consisted of one thousand datasets. Figure 5.27 shows a schematic illustrating the method adopted to calculate the mean and standard deviation of deformation rates of all point targets considered for analysis in this part of the study. In effect, the random sampling method adopted for sensitivity analysis represents a modified bootstrap approach.

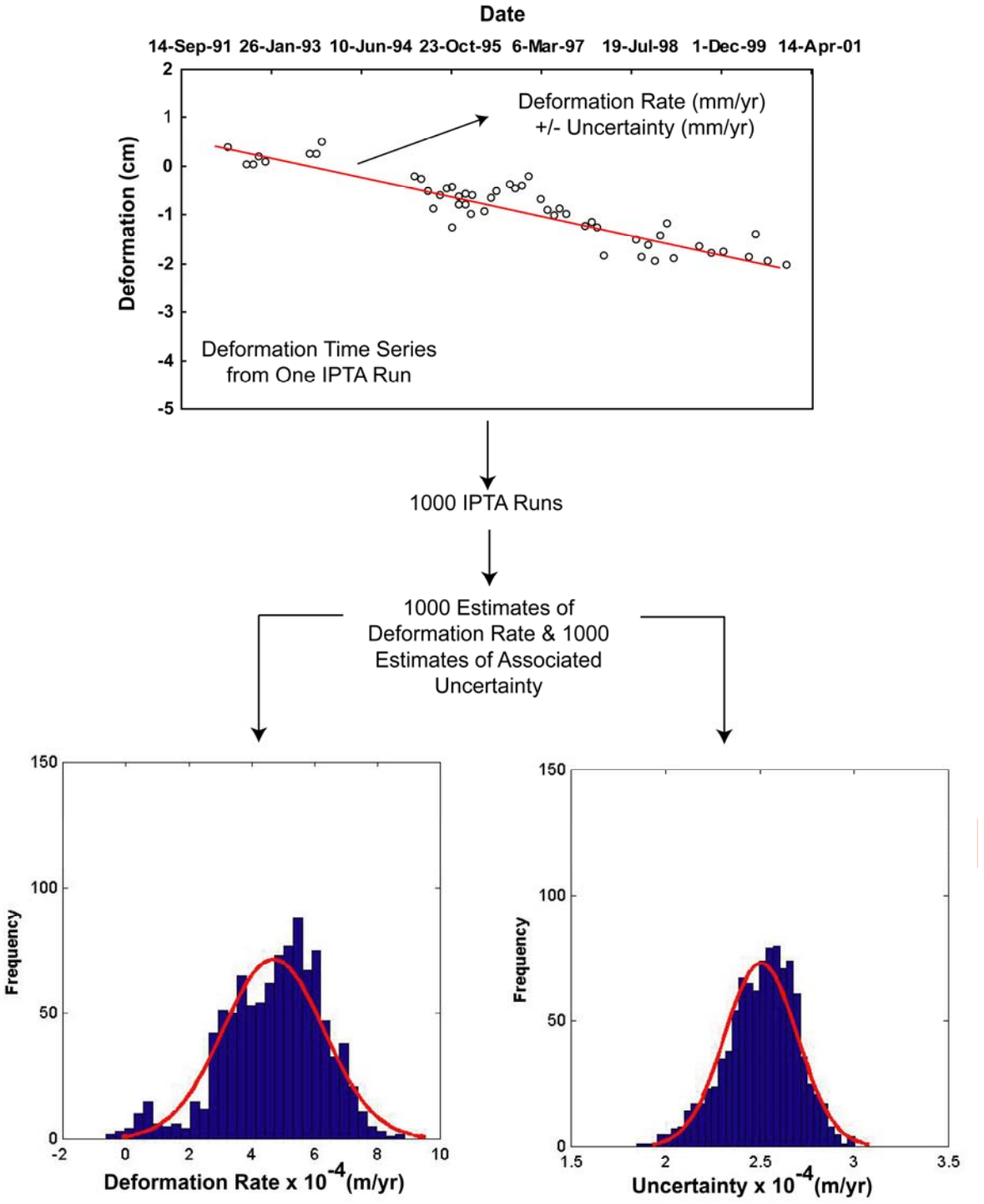

Figure 5.27 Illustration of the method adopted to calculate the mean and standard deviation of deformation rates of all point targets considered for analysis. The uncertainty is obtained from the GAMMA IPTA module and represents the standard error of the slope of the best fit linear regression line.

5.4.2.1 Analysis of Linear Deformation Rates

The point target locations chosen for deformation rate comparison are the same as those represented in Figure 5.11. Figure 5.28 shows the mean deformation rate corresponding to datasets of varying sizes as obtained for the point targets considered for analysis. The deformation rates corresponding to the 51 interferogram dataset, shown in Figure 5.28, correspond to the deformation rates obtained while assessing the first objective. The deformation rates corresponding to the 51 interferogram dataset are plotted as a reference for comparison with the mean deformation rates for the same point targets as obtained from datasets of varying sizes. The mean deformation rates corresponding to each dataset size, as represented in Figure 5.28, were derived from one thousand estimates since it may be recalled that four groups of one thousand datasets were generated with the number of interferograms in each dataset depending upon the group to which the dataset belonged, i.e., 15, 25, 35 and 40. It can be seen from Figure 5.28 that the mean deformation rates for all point targets chosen for analysis are consistent with the deformation rates derived for the same point targets when point target analysis was constrained with 51 interferograms.

The standard deviation of the one thousand estimates of deformation rates about the mean corresponding to each dataset group is presented in Figure 5.29. As can be seen from Figure 5.29, the standard deviation of deformation rates from the mean is consistently less than 0.5 mm/yr for all point targets considered for analysis and decreases monotonically with an increase in the

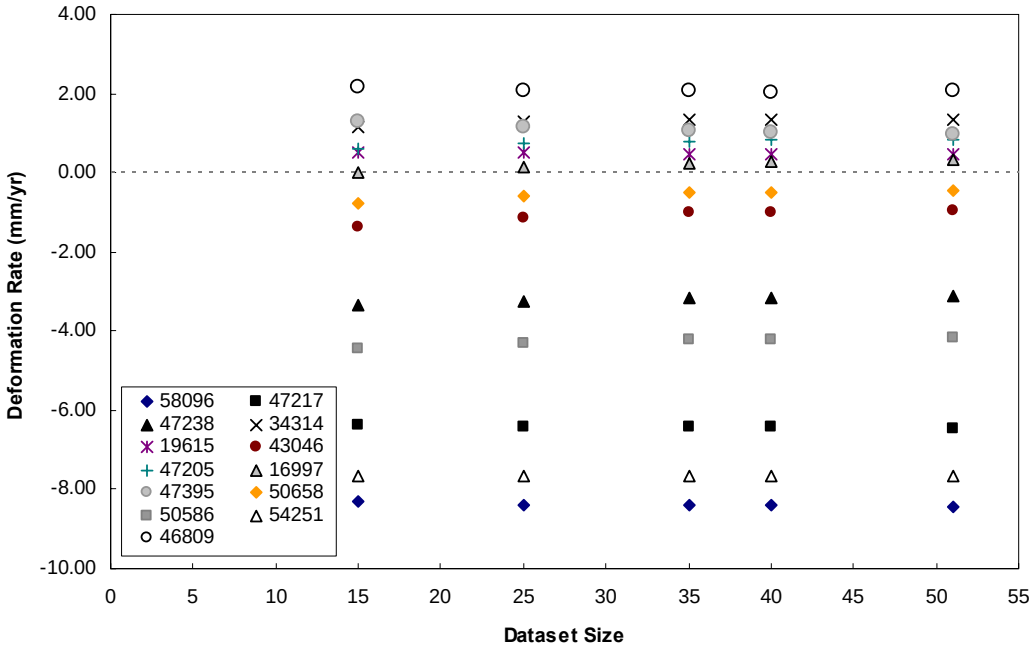

Figure 5.28 Mean of linear deformation rate estimates calculated from one thousand datasets. Symbols shown in the legend represent point target numbers.

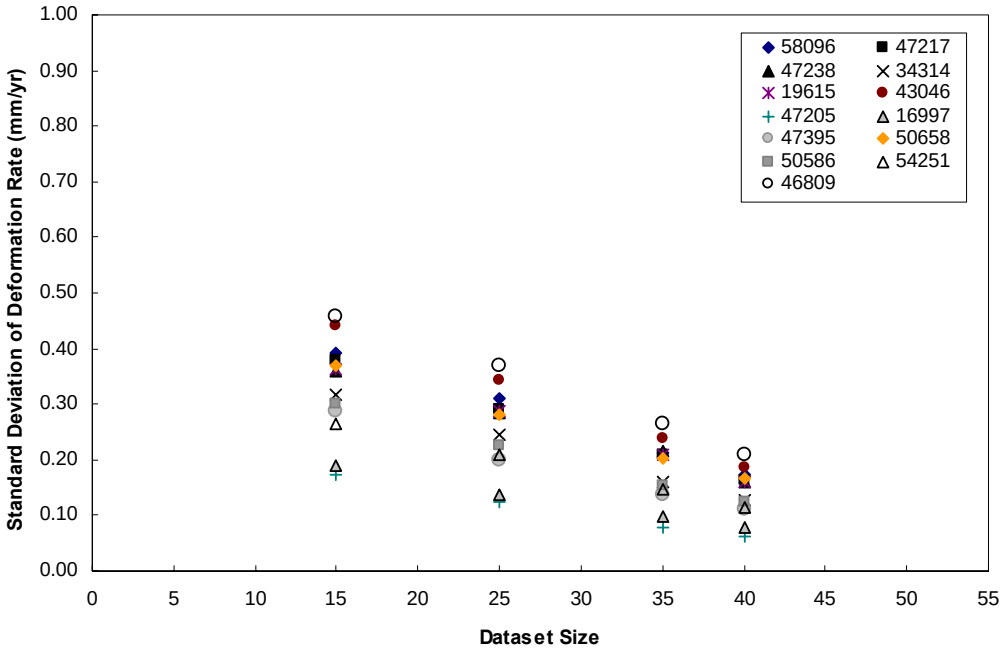

Figure 5.29 Standard deviation of linear deformation rate estimates calculated from one thousand datasets. Symbols shown in the legend represent point target numbers.

number of interferograms used for point target analysis.

5.4.2.2 Analysis of Linear Deformation Rate Uncertainty

As can be inferred from any of the two-dimensional regression analysis plots shown in Chapters 3 and 4, some uncertainty can be associated with the best-fit linear regression line that relates the independent and dependent variables. Hence, the final estimates of DEM height corrections and linear deformation rates derived from point target analysis can be associated with corresponding estimates of uncertainty. These estimates of uncertainty, as obtained from the GAMMA IPTA module, represent the standard error of the best fit linear regression line, and are expressed in mm/yr. Future references to this term are made using the symbol U_G. At the end of the IPTA processing flow, estimates of U_G are obtained for each point target considered for analysis. Since this study emphasizes on the deformation rates derived from point target analysis, the uncertainties (U_G) associated with the deformation rates were analyzed for dependence on the number of interferograms used for analysis. This comparison was developed for the point targets shown in Figure 5.11. As can be seen from Figure 5.30, the mean derived from one thousand estimates of U_G corresponding to one thousand estimates of the deformation rate associated with a point target, (a) is less than 0.7 mm/yr for all point targets considered for analysis and (b) decreases monotonically with an increase in the number of interferograms used for point target analysis. As can be seen from Figure 5.31, the standard deviation of U_G as derived from one thousand estimates shows a similar trend with the magnitude of estimates for all point targets considered for

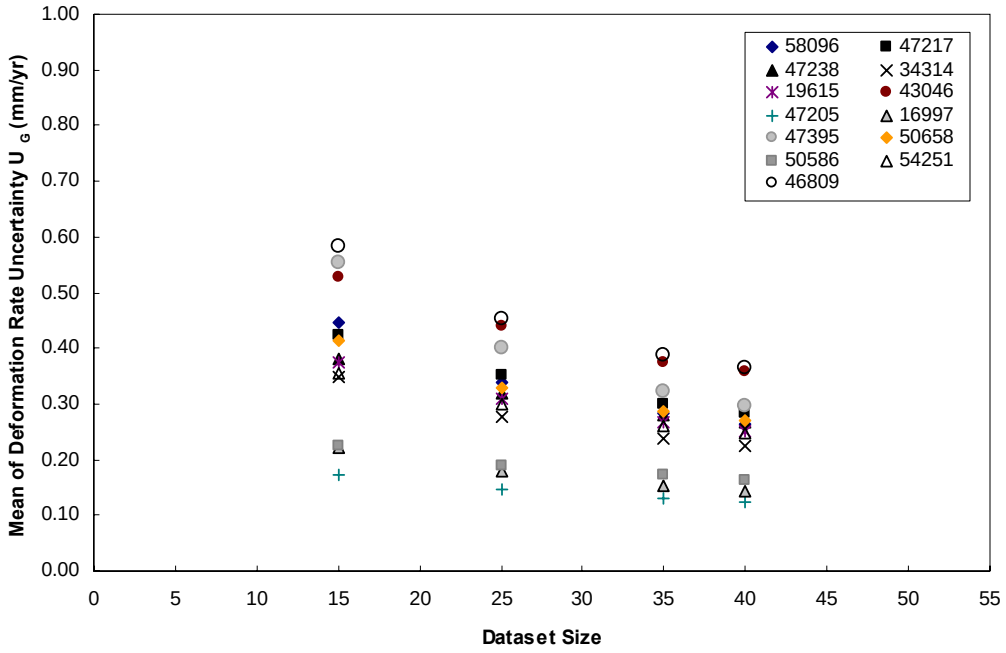

Figure 5.30 Mean of uncertainty (U_G) associated with linear deformation rate estimates. Each estimate of the mean shown in the plot was calculated from one thousand datasets. Symbols shown in the legend represent point target numbers.

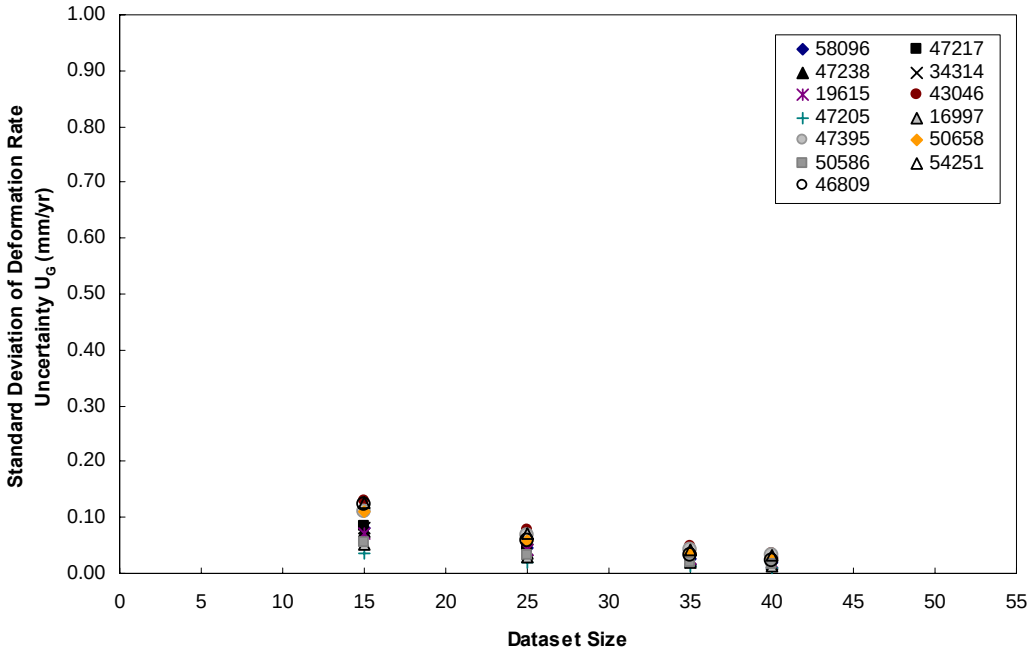

Figure 5.31 Standard deviation of uncertainty (U_G) associated with linear deformation rate estimates. Each standard deviation estimate shown in the plot was calculated from one thousand datasets. Symbols shown in the legend represent point target numbers.

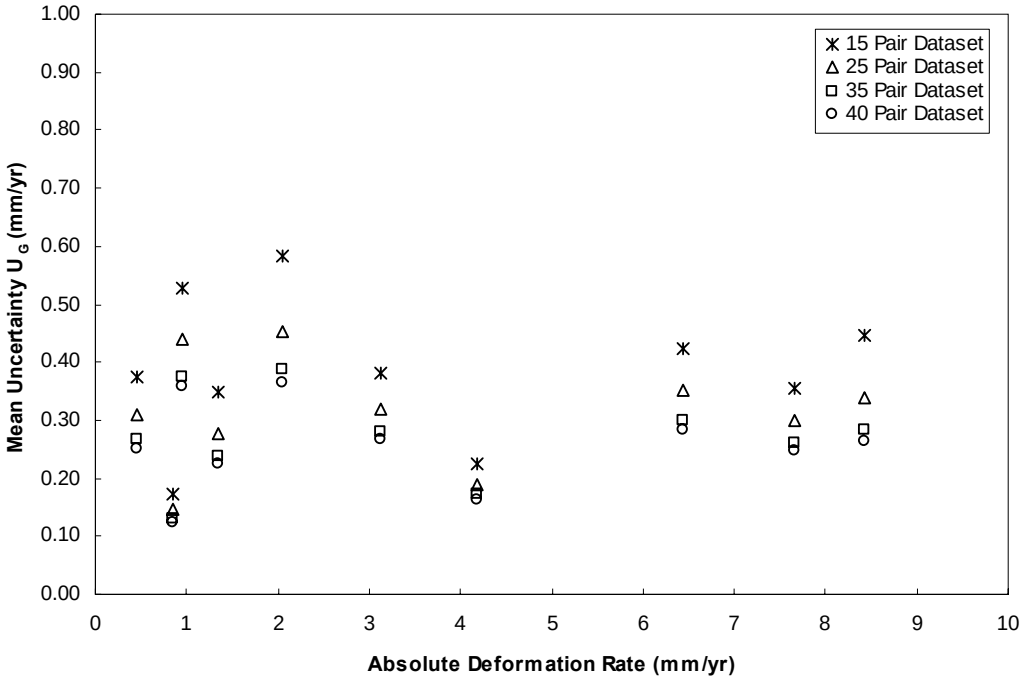

Figure 5.32 Dependence of the mean of uncertainty (U_G) on the associated absolute deformation rates and the size of the dataset used for analysis.

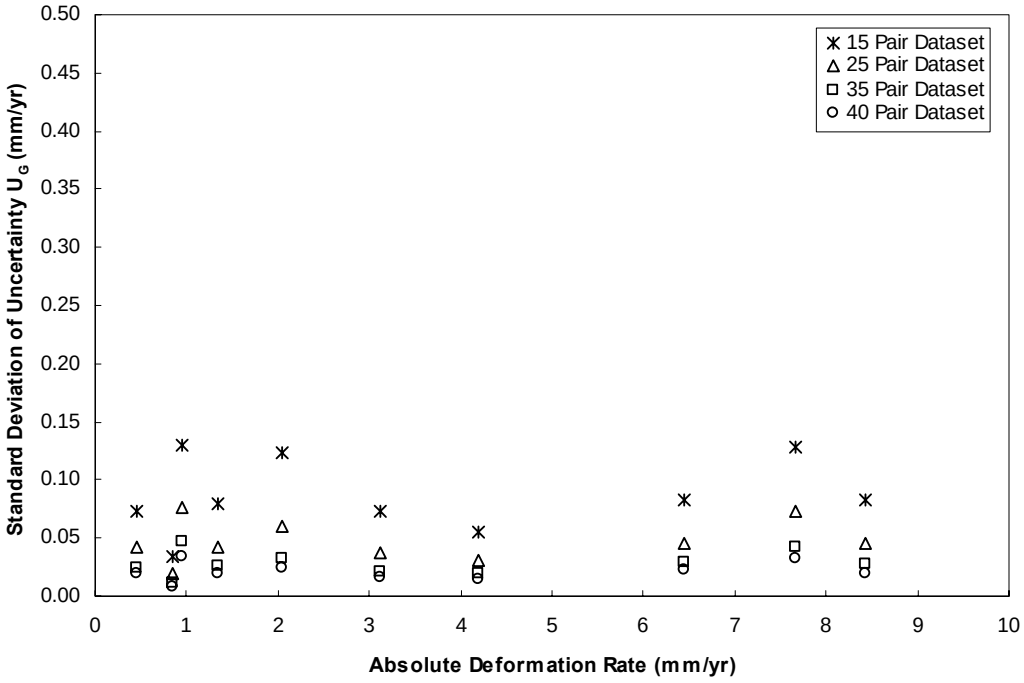

Figure 5.33 Dependence of the standard deviation of uncertainty (U_G) on the associated absolute deformation rates and the size of the dataset used for analysis.

analysis being less than 0.2 mm/yr.

Irrespective of the deformation rate of a point target, the mean of the associated uncertainty (U_G), as derived from one thousand estimates, is shown to decrease with an increase in the size of the dataset used for IPTA analysis (Figure 5.32). However, no relation between the mean of the uncertainty (U_G) and the corresponding deformation rates is evident. Similarly, irrespective of the deformation rate of a point target, the standard deviation of the associated uncertainty (U_G), as derived from one thousand estimates, is shown to decrease with an increase in the size of the dataset used for IPTA analysis (Figure 5.33). However, no relation between the standard deviation of the uncertainty (U_G) and the corresponding deformation rates is evident.

5.4.2.3 Relationship between Magnitude of Deformation Rate and its Uncertainty

Figure 5.34 shows the relationship between the *coefficient of variation* corresponding to a range of linear deformation rates and the size of the dataset used for point target analysis. The coefficient of variation shown in Figure 5.34 is the ratio of the standard deviation to the mean of the absolute linear deformation rates corresponding to a point target. The absolute value of the mean deformation rates were considered because deformation rates derived with respect to the user defined reference point-30251, were associated with a positive or a negative sign depending on whether the nature of deformation in question was uplift or subsidence. It may be recalled that both the mean and the standard deviation associated with linear deformation rate estimates

corresponding to a point target analyzed with a particular dataset size were derived from one thousand estimates.

As can be inferred from Figure 5.34, the effect of the size of the dataset used for point target analysis on the variability in deformation rate estimates decreases exponentially with an increase in the absolute linear deformation rate of a point target. The effect is most pronounced for point targets associated with linear deformation rates less than about 2 mm/yr. More specifically, while it was found that the standard deviation associated with deformation rates of all ranges considered for analysis varied inversely as a function of the number of interferograms used to constrain the IPTA analysis, the difference between the standard deviation estimates associated with deformation rates less than 2 mm/yr as achieved from point target analysis of varying dataset sizes was found to be more significant than the difference between standard deviation estimates associated with higher deformation rates. It must be recalled that the estimates of coefficient of variation shown in Figure 5.34 were derived by having a priori knowledge about the location of point targets in an urban setting and their corresponding unwrapped phase values and can hence be considered to represent the best case scenario. Figure 5.35 shows that the coefficient of variation of deformation rates of all point targets chosen for analysis decreased with an increase in the size of the dataset analyzed.

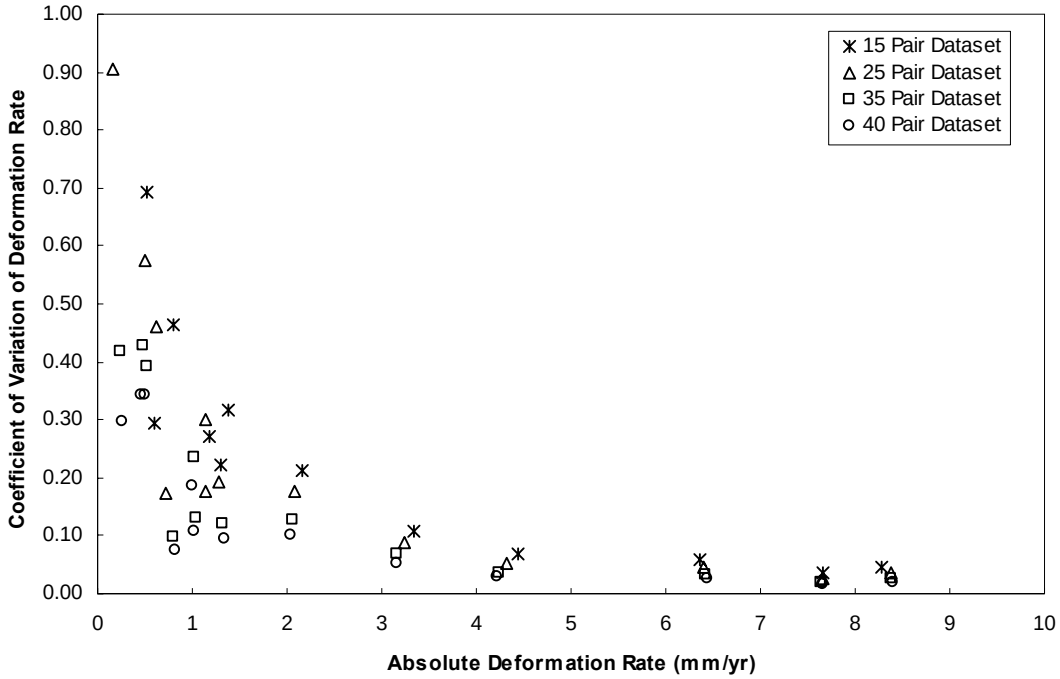

Figure 5.34 Coefficient of variation of deformation rate for a range of mean deformation rates.

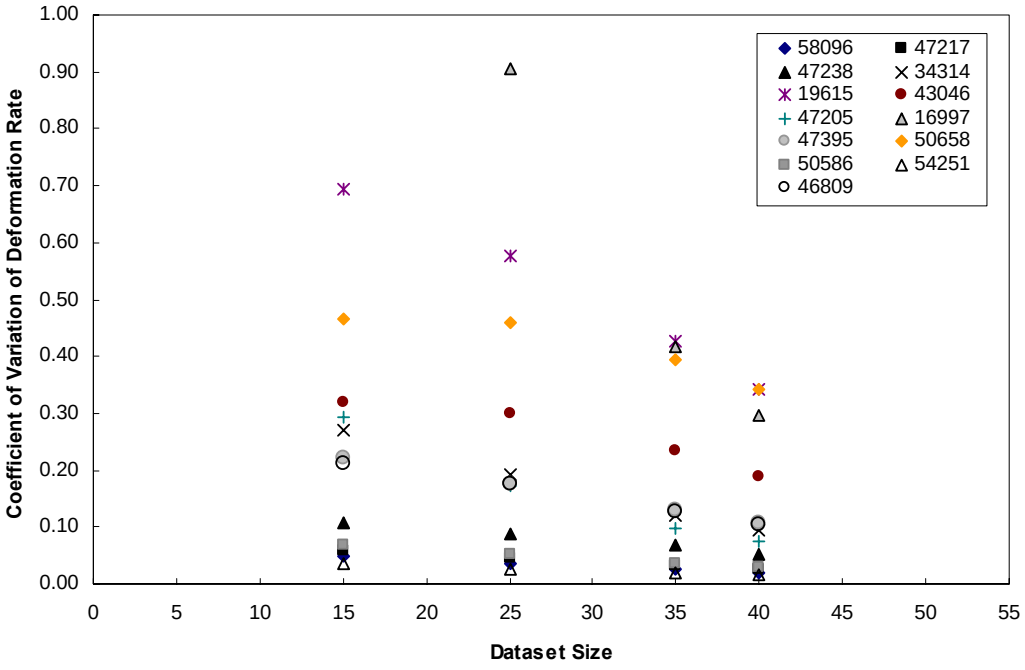

Figure 5.35 Coefficient of variation of deformation rates of point targets as obtained from the analysis of datasets of varying sizes.

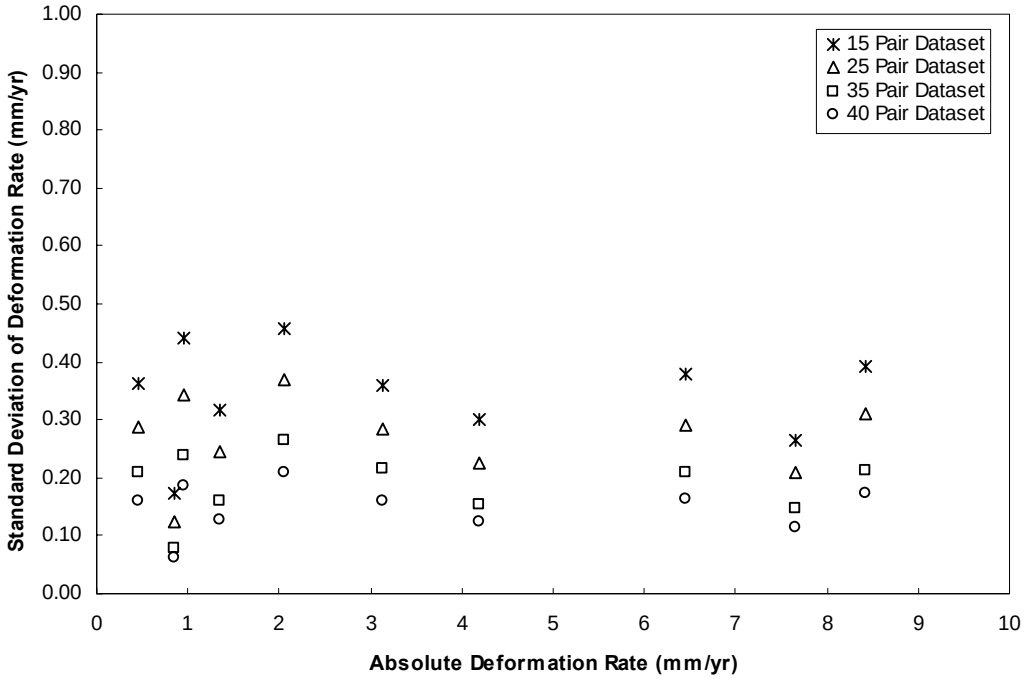

Figure 5.36 Dependence of the standard deviation of deformation rate on the associated absolute deformation rates and the size of the dataset used for analysis.

From Figure 5.36, it can be observed that, irrespective of the deformation rate of a point target, the standard deviation of the deformation rate as derived from one thousand estimates, decreases with an increase in the size of the dataset used for IPTA analysis. However, from Figure 5.36, no relation between the standard deviation of the deformation rate and the corresponding deformation rates is evident.

5.4.2.4 Discussion

The estimates of mean and standard deviation of deformation rates and related uncertainty (U_G) presented in Sections 5.4.2.1 and 5.4.2.2 were derived from a representative sample containing one thousand datasets. If only one dataset is available for IPTA analysis, the variability or precision that can be

associated with the derived deformation rates and the corresponding uncertainty (U_G), can be estimated using the mean and standard deviation estimates reported in Sections 5.4.2.1 and 5.4.2.2.

For this study, estimates of such precision are expressed in terms of the range of values bounding 95% of the one thousand estimates of deformation rate and associated uncertainty (U_G). Since the estimates of the standard deviation of deformation rates and the associated uncertainty (U_G) were derived from one thousand samples, it was assumed that the sample standard deviation was representative of the population standard deviation.

Provided that the underlying population is normally distributed, the range of values bounding 95% of the one thousand estimates of deformation rate and associated uncertainty (U_G) can be expressed as:

$$Range_{0.95} = \bar{x} \pm 1.96(\sigma) \tag{5.1}$$

where, $\bar{x}$ and σ represent estimates of the mean and standard deviation respectively. As can be seen from Equation 5.1, the interval defined by the range of values bounding 95% of the one thousand estimates of deformation rate, is a function of the standard deviation that can be associated with the mean (Ang and Tang, 1975).

For this study, the assumption of normality of the distributions defining one thousand estimates of deformation rates and one thousand estimates of the associated uncertainty (U_G), was validated by means of plotting a histogram and the corresponding normal probability plot. The histogram and normal probability plots corresponding to deformation rates and associated uncertainty (U_G), as

obtained for point target number 58096, are shown in Figure 5.37 through Figure 5.40 below. The data shown in Figure 5.37 through Figure 5.40 represent the deformation rates and associated uncertainty (U_G) that were obtained from one thousand IPTA runs, wherein each IPTA run was constrained with 15 interferograms and 25 interferograms respectively. The histograms and normal probability plots corresponding to the estimates of the deformation rate of all other point targets considered for analysis and the associated uncertainty (U_G) are shown in Appendices A and B.

The histogram represents the number of occurrences of a range of data values (deformation rates, associated uncertainty(U_G)). The distribution outlined by the solid line in the histogram plot corresponds to the normal distribution with a mean and standard deviation equal to the ones estimated from the data represented by the histogram. The data represented in the histogram are denoted by cross marks on the normal probability plot. The dashed line on the normal probability plot denotes the straight line along which the cross marks should plot if the data represented by the cross marks are normally distributed. As can be inferred from the histograms and normal probability plots shown in Figure 5.37 through Figure 5.40 and in Appendices A and B, deviations from the normal distribution are concentrated at the tails of the histogram i.e., below 10^{th} percentile and above 90^{th} percentile, whereas the frequency of occurrence of the rest of the data follows a normal distribution.

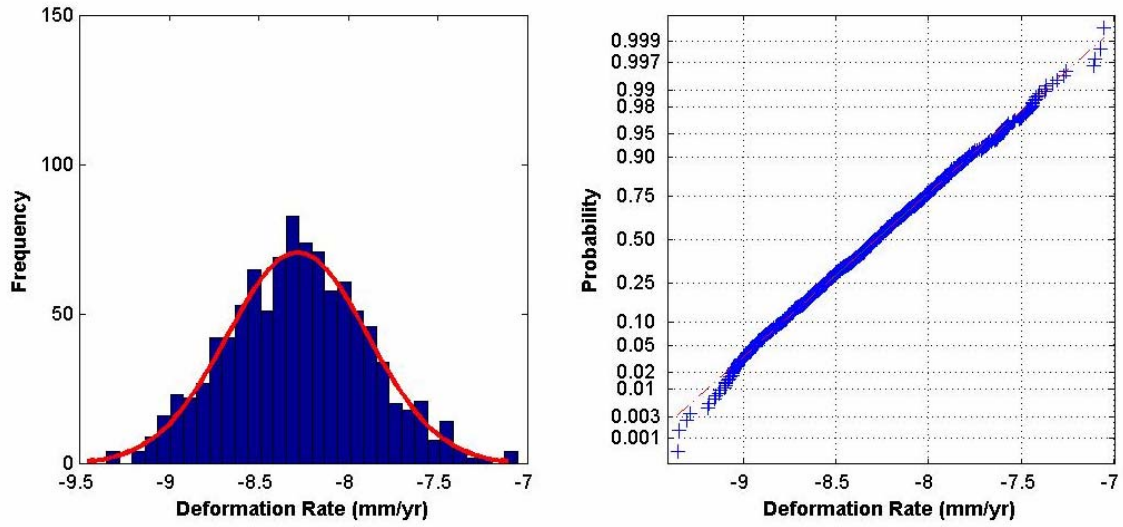

Figure 5.37 Deformation rates for point target #58096 as calculated from one thousand datasets each containing 15 interferograms. The histogram is shown to the left and the normal probability plot is shown to the right.

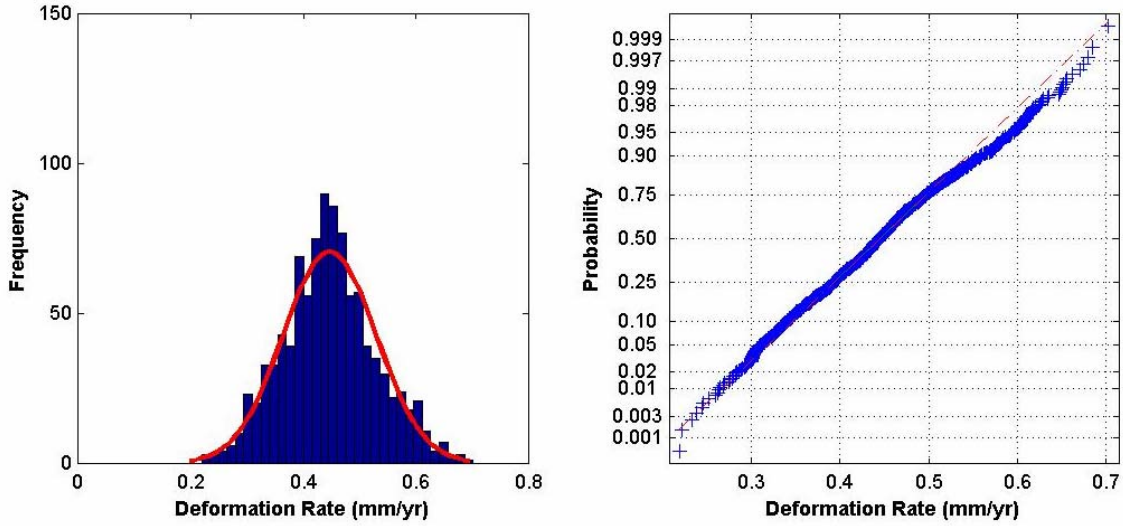

Figure 5.38 Uncertainty (U_G) associated with deformation rates for point target #58096 as calculated from one thousand datasets each containing 15 interferograms. The histogram is shown to the left and the normal probability plot is shown to the right.

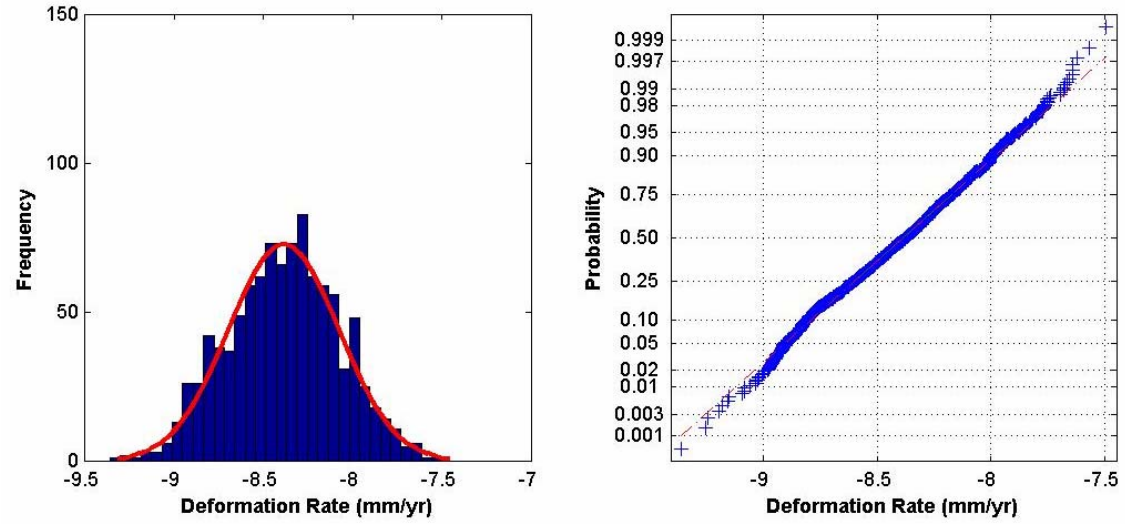

Figure 5.39 Deformation rates for point target #58096 as calculated from one thousand datasets each containing 25 interferograms. The histogram is shown to the left and the normal probability plot is shown to the right.

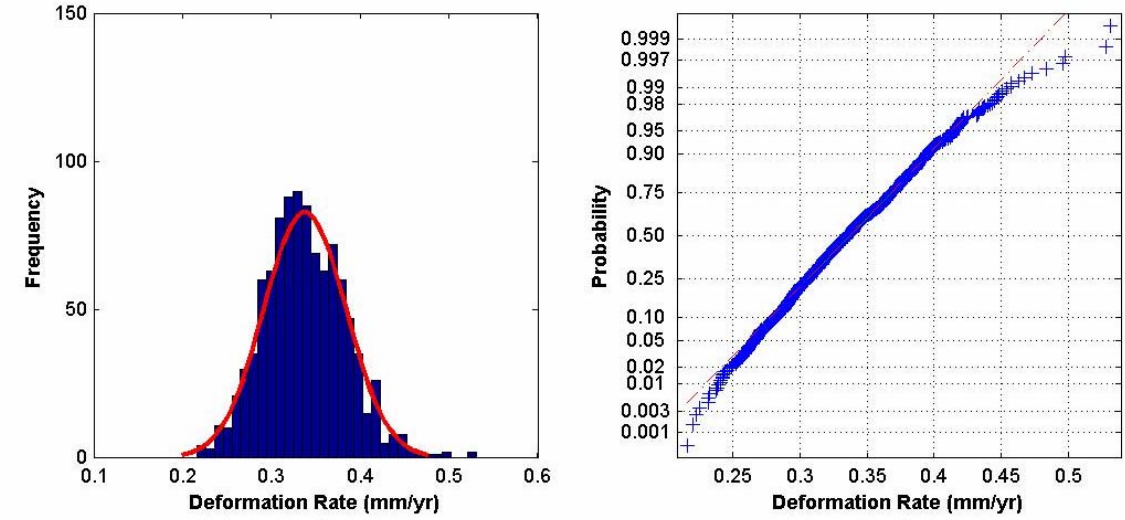

Figure 5.40 Uncertainty (U_G) associated with deformation rates for point target #58096 as calculated from one thousand datasets each containing 25 interferograms. The histogram is shown to the left and the normal probability plot is shown to the right.

This was used as sufficient proof to assume that the deformation rate and associated uncertainty (U_G) of all point targets considered for analysis follow a normal distribution. Therefore, Equation 5.1 was used to calculate the range of values bounding 95% of the data used to derive the mean and the standard deviation estimates.

The mean deformation rate, the corresponding standard deviation and the value representing the 95% interval bound corresponding to all point targets considered for analysis is shown in Table 5.2 through Table 5.5. The (95% Range/2) parameter shown in the tables represents $1.96(\sigma)$.

Table 5.2 Deformation rate statistics estimated from point target analysis of one thousand datasets containing 15 interferograms each.

Point Target #	μ (mm/yr)	σ (mm/yr)	(95%Range)/2 (mm/yr)
16997	0.00	0.19	0.37
19615	0.53	0.36	0.71
34314	1.17	0.32	0.62
43046	-1.38	0.44	0.86
46809	2.15	0.46	0.90
47205	0.59	0.17	0.34
47217	-6.35	0.38	0.74
47238	-3.34	0.36	0.71
47395	1.30	0.29	0.57
50586	-4.45	0.30	0.59
50658	-0.80	0.37	0.73
54251	-7.66	0.27	0.52
58096	-8.28	0.39	0.77

Table 5.3 Deformation rate statistics estimated from point target analysis of one thousand datasets containing 25 interferograms each.

Point Target #	μ (mm/yr)	σ (mm/yr)	(95%Range)/2 (mm/yr)
16997	0.15	0.14	0.27
19615	0.50	0.29	0.56
34314	1.28	0.24	0.48
43046	-1.14	0.34	0.67
46809	2.08	0.37	0.72
47205	0.72	0.12	0.24
47217	-6.40	0.29	0.57
47238	-3.23	0.28	0.56
47395	1.13	0.20	0.39
50586	-4.32	0.23	0.44
50658	-0.61	0.28	0.55
54251	-7.65	0.21	0.41
58096	-8.39	0.31	0.61

Table 5.4 Deformation rate statistics estimated from point target analysis of one thousand datasets containing 35 interferograms each.

Point Target #	μ (mm/yr)	σ (mm/yr)	(95%Range)/2 (mm/yr)
16997	0.24	0.10	0.19
19615	0.49	0.21	0.41
34314	1.33	0.16	0.31
43046	-1.02	0.24	0.47
46809	2.05	0.26	0.52
47205	0.80	0.08	0.15
47217	-6.42	0.21	0.41
47238	-3.16	0.21	0.42
47395	1.05	0.14	0.27
50586	-4.24	0.15	0.30
50658	-0.51	0.20	0.40
54251	-7.65	0.15	0.29
58096	-8.39	0.21	0.42

Table 5.5 Deformation rate statistics estimated from point target analysis of one thousand datasets containing 40 interferograms each.

Point Target #	μ (mm/yr)	σ (mm/yr)	(95%Range)/2 (mm/yr)
16997	0.26	0.08	0.15
19615	0.47	0.16	0.32
34314	1.34	0.13	0.25
43046	-1.00	0.19	0.37
46809	2.05	0.21	0.41
47205	0.81	0.06	0.12
47217	-6.43	0.16	0.32
47238	-3.15	0.16	0.31
47395	1.02	0.11	0.22
50586	-4.22	0.12	0.24
50658	-0.49	0.17	0.33
54251	-7.65	0.11	0.22
58096	-8.40	0.17	0.34

In section 5.4.2, the standard deviation of deformation rates of all point targets considered for analysis and standard deviation of the associated uncertainty (U_G), were shown to decrease monotonically with an increase in the number of interferograms constituting the dataset used for point target analysis. Additionally, the mean and standard deviation estimates were derived from a constant sample size of one thousand for all point targets. Given these constraints and given that estimates of the range of values bounding 95% of the data is a function of the standard deviation and the sample size used in its derivation, the precision of the mean estimates for all point targets, as inferred from the (95% Range/2) parameter, varies between ± 0.10 mm/yr and ± 0.90 mm/yr. The data presented for some point targets in Table 5.2 through Table 5.5 are summarized in Figure 5.41. From Figure 5.41 and Table 5.2 through Table

5.5, it is observed that a lower variability in the estimated deformation rates can be expected when point target analysis is constrained with larger datasets.

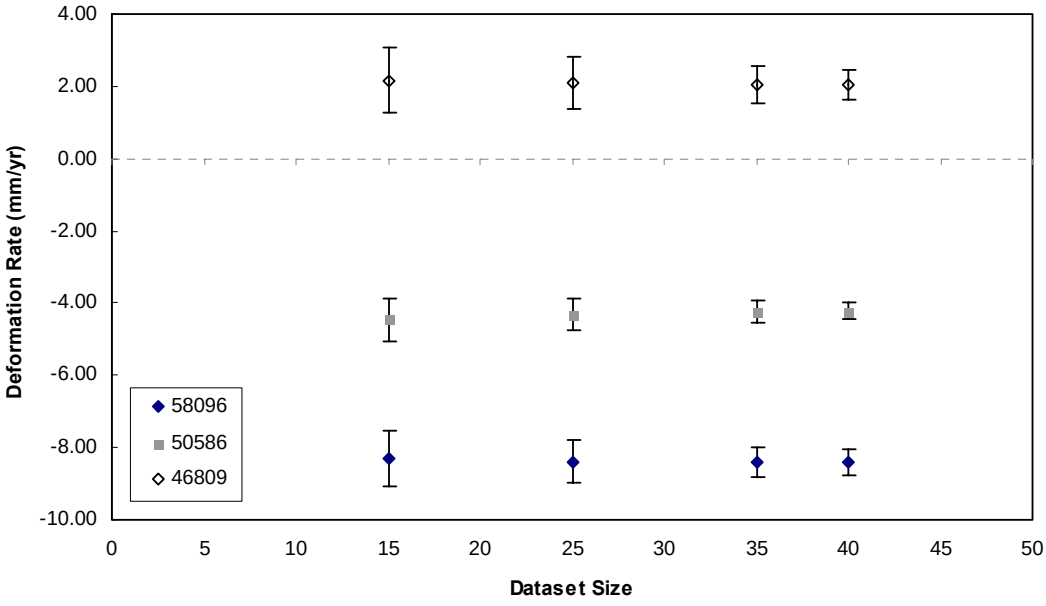

Figure 5.41 95% interval bounds ($\pm 1.96\sigma$) of deformation rates estimated from datasets of varying sizes.

The variability that can be associated with the uncertainty (U_G) corresponding to the deformation rates of all point targets considered for analysis are shown in Table 5.6 through Table 5.9. As can be inferred from the tables, estimates of the range of values bounding 95% of the data corresponding to the uncertainty (U_G) associated with the deformation rates of all point targets analyzed, ranges between ± 0.01 mm/yr to ± 0.30 mm/yr. The data presented for some point targets in Table 5.6 through Table 5.9 are summarized in Figure 5.42. Data for only two point targets are shown in Figure 5.42 to facilitate clarity in presentation.

Table 5.6 Statistics of uncertainty of deformation rate (U_G) estimated from point target analysis of one thousand datasets containing 15 interferograms each.

Point Target #	μ (mm/yr)	σ (mm/yr)	(95%Range)/2 (mm/yr)
16997	0.22	0.05	0.10
19615	0.38	0.07	0.14
34314	0.35	0.08	0.16
43046	0.53	0.13	0.25
46809	0.58	0.12	0.24
47205	0.17	0.03	0.07
47217	0.42	0.08	0.16
47238	0.38	0.07	0.14
47395	0.55	0.11	0.22
50586	0.22	0.06	0.11
50658	0.41	0.11	0.22
54251	0.36	0.13	0.25
58096	0.45	0.08	0.16

Table 5.7 Statistics of uncertainty of deformation rate (U_G) estimated from point target analysis of one thousand datasets containing 25 interferograms each.

Point Target #	μ (mm/yr)	σ (mm/yr)	(95%Range)/2 (mm/yr)
16997	0.18	0.03	0.06
19615	0.31	0.04	0.08
34314	0.28	0.04	0.08
43046	0.44	0.08	0.15
46809	0.45	0.06	0.12
47205	0.15	0.02	0.04
47217	0.35	0.05	0.09
47238	0.32	0.04	0.07
47395	0.40	0.07	0.13
50586	0.19	0.03	0.06
50658	0.33	0.06	0.12
54251	0.30	0.07	0.14
58096	0.34	0.05	0.09

Table 5.8 Statistics of uncertainty of deformation rate (U_G) estimated from point target analysis of one thousand datasets containing 35 interferograms each.

Point Target #	μ (mm/yr)	σ (mm/yr)	(95%Range)/2 (mm/yr)
16997	0.15	0.02	0.04
19615	0.27	0.02	0.05
34314	0.24	0.03	0.05
43046	0.37	0.05	0.09
46809	0.39	0.03	0.06
47205	0.13	0.01	0.02
47217	0.30	0.03	0.06
47238	0.28	0.02	0.04
47395	0.32	0.04	0.08
50586	0.17	0.02	0.04
50658	0.29	0.04	0.07
54251	0.26	0.04	0.08
58096	0.28	0.03	0.05

Table 5.9 Statistics of uncertainty of deformation rate (U_G) estimated from point target analysis of one thousand datasets containing 40 interferograms each.

Point Target #	μ (mm/yr)	σ (mm/yr)	(95%Range)/2 (mm/yr)
16997	0.14	0.01	0.03
19615	0.25	0.02	0.04
34314	0.22	0.02	0.04
43046	0.36	0.03	0.07
46809	0.36	0.02	0.05
47205	0.12	0.01	0.02
47217	0.28	0.02	0.04
47238	0.27	0.02	0.03
47395	0.30	0.03	0.06
50586	0.16	0.01	0.03
50658	0.27	0.03	0.05
54251	0.25	0.03	0.06
58096	0.26	0.02	0.04

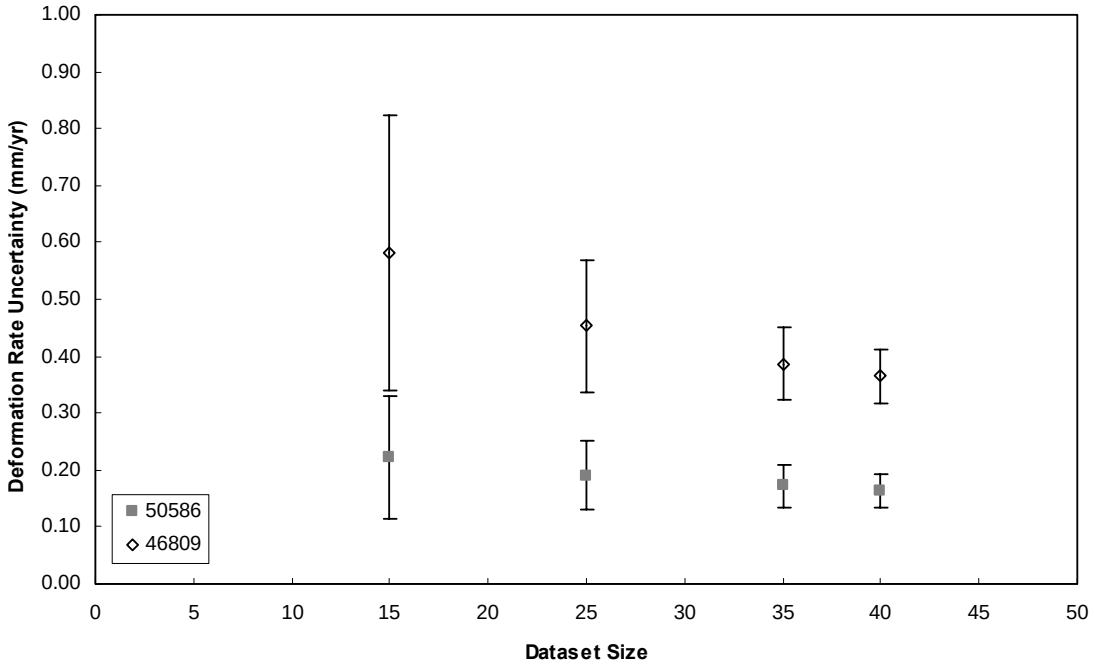

Figure 5.42 95% interval bounds ($\pm 1.96\sigma$) of the uncertainty (U_G) associated with deformation rates estimated from datasets of varying sizes.

From Figure 5.42 and Table 5.6 through Table 5.9, it is observed that a lower variability in the uncertainty (U_G) associated with the estimated deformation rates can be expected when point target analysis is constrained with larger datasets.

5.5 Summary

Results obtained on assessing the objectives of this study were presented in this chapter. A discussion of the inferred results was presented in each section.

The main findings of this study indicate that small deformation features can be detected spatially and temporally using IPTA. With respect to the influence of the dataset size on the deformation estimates derived using IPTA, it

was observed that, for a given point target, the deformation rates derived from large datasets were less variable than the deformation rates derived from smaller datasets. The dataset size was observed to have a greater influence on the variability of deformation rates for point targets associated with deformation rates less than 2mm/yr. It was also observed that the variability in the uncertainties that can be associated with the deformation rate of a point target depends on the size of the dataset used for analysis. Larger datasets were observed to yield smaller variability of the deformation rate uncertainty for a point target.

It is of importance to note that the results derived from this study are representative of a small study area situated in an urban setting. Performing similar studies for bigger sites and those located in different settings will be useful in a more comprehensive characterization of the technique. Detailed conclusions that were inferred from the findings of this study are presented in the next chapter.

6. CONCLUSIONS AND RECOMMENDATIONS

The scope of the work presented in this document was designed to address three main objectives, namely:

1. Evaluate the feasibility of using IPTA to detect small spatial-scale deformation features by computing the deformation time histories resulting from the construction of the Red Line in Los Angeles,
2. Investigate the influence of dataset characteristics on the application of the conventional IPTA processing flow, and
3. Perform an analysis to quantify:
    a. the variability associated with deformation rate estimates derived from IPTA, and
    b. the dependence of the deformation rate estimates on the number of satellite acquisitions used to constrain the analysis.

The conclusions that were derived after addressing each of the objectives are presented in this chapter.

6.1 Deformation Detection in Study Area (Objective 1)

With respect to the use of point target interferometry to detect deformation in the study area, the findings are as follows:

1. The localized deformation associated with the construction of the Los Angeles Red Line for 1992-2000 was successfully detected using IPTA. In addition, a much larger deformation feature associated with the abandoned Salt Lake oil field was also detected.

2. The temporal deformation plots corresponding to point targets located over the Red Line showed an episodic event that was distinct from the deformation signatures observed at other locations within the study area. More specifically,
    a. A distinct step in the deformation time series was observed for point targets located along segment 3 of the Red Line alignment situated along Hollywood Boulevard. The magnitude of subsidence corresponding to the step in the deformation time series ranged between ½ inch and 1 inch in the satellite line of sight direction.
    b. In contrast to the episodic nature of the temporal signature that was detected for point targets along the Red Line, the deformation time history for point targets located in the vicinity of the Salt Lake oil field showed a monotonic subsidence trend. For point targets located at the center of the oil field, a total subsidence of 8 cm in the satellite line of sight direction was detected for the time period between 1993 and 2000.
    c. Deformation time histories for randomly selected point targets located outside the two prominent deformation fields in the study area exhibited fluctuations about zero deformation.

6.2 Influence of SAR Image Acquisition Parameters on IPTA Processing (Objective 2)

With respect to the analysis of the influence of SAR image acquisition parameters on the ability to unwrap a dataset without patch errors, the findings are as follows:

1. It was not possible to establish a clear relationship between the average perpendicular baseline defining a dataset and the occurrence of patch errors during temporal unwrapping of the interferograms constituting the dataset.
2. Considering the urban setting characterizing the study area, where the quality of detected point targets has been proven to be suitable for point target interferometry, and considering that a priori information about the location of such point targets was used in the analysis of this part of the study, it was found that few datasets containing less than about 20 interferograms could be unwrapped without patch errors. Additionally, it was found that the dataset containing 23 interferograms characterized by the highest baselines, unwrapped without patch errors. This result can be used to infer the need for about 20-25 interferograms to successfully perform point target analysis of small study areas located in urban settings.

6.3 Dependence of Deformation Rates on Dataset Size (Objective 3)

With respect to the analysis that was performed to quantify the influence of the size of a dataset used for IPTA analysis on the variability of the deformation rate estimates, the findings are as follows:

1. The standard deviation of one thousand estimates of deformation rates about the mean was found to be consistently less than 0.5 mm/yr for all point targets considered for analysis and was found to decrease monotonically with an increase in the number of interferograms used for point target analysis.
2. A similar trend was observed for the mean and standard deviation of uncertainty (U_G) that was associated with one thousand estimates of the linear deformation rate of a point target. While the mean uncertainty (U_G) associated with the deformation rates of all point targets analyzed was less than 0.6 mm/yr, the magnitude of the estimates of standard deviation of uncertainty (U_G) was found to be less than 0.2 mm/yr.
3. The coefficient of variation of deformation rate for point targets associated with deformation rates greater than 2 mm/yr, was observed to be similar irrespective of the size of the dataset used in their estimation. However, the coefficient of variation of deformation rate for point targets associated with deformation rates less than about 2 mm/yr was observed to be greatly reduced when the number of

interferograms used to constrain the IPTA analysis was increased from 15 to 40.

4. The coefficient of variation of deformation rates of all point targets chosen for analysis was observed to decrease with an increase in the size of the dataset analyzed.
5. Irrespective of the deformation rate of a point target, the mean of the associated uncertainty (U_G), as derived from one thousand estimates, was observed to decrease with an increase in the size of the dataset used for IPTA analysis. However, no clear relation between the mean of the uncertainty (U_G) and the corresponding deformation rates was identified.
6. Irrespective of the deformation rate of a point target, the standard deviation of the associated uncertainty (U_G), as derived from one thousand estimates, was observed to decrease with an increase in the size of the dataset used for IPTA analysis. However, no clear relation between the standard deviation of the uncertainty (U_G) and the corresponding deformation rates was identified.

6.4 Recommendations

To facilitate further characterization of point target interferometry, the following recommendations are made:

1. The baseline separating the available SAR acquisitions for a site, and the time of their acquisition, are the two parameters that are available to aid in deciding the composition of a dataset that would be used for

point target analysis. This study addressed the influence of the baseline on successfully patch unwrapping a dataset. It is recommended that future studies investigate the dependence of patch unwrapping success on the time period separating the SAR acquisitions chosen to constitute a dataset.

2. In this study, the multi-patch approach to unwrap all datasets was performed by adopting the parameters recommended for the standard deviation of phase from the two dimensional regression. An investigation into the influence of different phase standard deviation parameters is recommended to determine the range of parameter values that can be used to successfully patch unwrap study areas located in different settings.
3. The statistical estimates of variability that were associated with deformation rates of point targets in this study area are representative of an urban setting. Investigation of similar estimates of variability associated with point targets located in different settings will be useful in further characterization of IPTA.

7. REFERENCES

Allievi, J., Ambrosi, C., Ceriani, M., Colesanti, C., Crosta, G. B., Ferretti, A., and Fossati, D. "Monitoring slow mass movements with the Permanent Scatterers technique." *International Geoscience and Remote Sensing Symposium (IGARSS)*, 215-217.

Ang, A.H.S. and Tang, W.H. (1975). "Probability concepts in engineering planning and design." W. H. Tang, ed., Wiley, New York.

Bamler, R., and Hanssen, R. "Decorellation induced by interpolation errors in InSAR processing." *International Geoscience and Remote Sensing Symposium (IGARSS). v 4 1997*, 1710-1712.

Bell, R. (1999) [Online] Available http://www.prres.net/Papers/Bell_RE_Damages_Analytical_Tools_and_Their_Application_to_High_Profile_Case_Studies.pdf, January 29, 1999.

Bovenga, F., Nutricato, R., Refice, A., and Wasowski, J. (2006). "Application of multi-temporal differential interferometry to slope instability detection in urban/peri-urban areas." *Engineering Geology*, 88(3-4), 218-239.

Burgmann, R., Rosen, P. A., and Fielding, E. J. (2000). "Synthetic aperture radar interferometry to measure Earth's surface topography and its deformation." *Annual Review of Earth and Planetary Sciences*, 28, 169-209.

Canada Centre for Remote Sensing. (2005) [Online] Available http://ccrs.nrcan.gc.ca/glossary/index_e.php?id=581, November 21,2005.

Chang, C. Y., Jin, M. Y., Yun-Ling, L., and Holt, B. A. H. B. (1996). "First SIR-C ScanSAR results." *Geoscience and Remote Sensing, IEEE Transactions on*, 34(5), 1278-1281.

Chen, C.W. and Zebker, H.A. (2000). “Network approaches to two-dimensional phase unwrapping:intractability and two new algorithms.”, *Journal of the Optical Society of America A*., 17(3), 401-414.

Colesanti, C., Ferretti, A., Locatelli, R., Novali, F., and Savio, G. (2003). "Permanent Scatterers: Precision Assessment and Multi-Platform Analysis." *International Geoscience and Remote Sensing Symposium (IGARSS)*, 1193-1195.

Colesanti, C., Ferretti, A., Novali, F., Prati, C., and Rocca, F. (2003). "SAR monitoring of progressive and seasonal ground deformation using the permanent scatterers technique." *IEEE Transactions on Geoscience & Remote Sensing*, 41(7), 1685-1701.

Colesanti, C., Ferretti, A., Prati, C., Perissin, D., and Rocca, F. (2003). "ERS-ENVISAT Permanent Scatterers Interferometry." *International Geoscience and Remote Sensing Symposium (IGARSS)*, 1130-1132.

Colesanti, C., Ferretti, A., Prati, C., and Rocca, F. (2001). "Comparing GPS, optical leveling and permanent scatterers." *International Geoscience and Remote Sensing Symposium (IGARSS)*, 2622-2624.

Colesanti, C., Le Mouelic, S., Bennani, M., Raucoules, D., Carnec, C., and Ferretti, A. (2005). "Detection of mining related ground instabilities using the permanent scatterers technique - A case study in the east of France." *International Journal of Remote Sensing*, 26(1), 201-207.

Colesanti, C., and Wasowski, J. (2006). "Investigating landslides with space-borne Synthetic Aperture Radar (SAR) interferometry." *Engineering Geology*, 88(3-4), 173-199.

Costantini, M. (1998). "A novel phase unwrapping method based on network programming." *IEEE Transactions on Geoscience and Remote Sensing,* 36(3), 813-821.

Curlander, J. C. and McDonough, R.N. (1991). *Synthetic aperture radar : systems and signal processing*, Wiley, New York.

Declercq, P. Y., Devleeschouwer, X., and Pouriel, F. "Subsidence revealed by psinsar technique in the ottignies-wavre area (Belgium) related to water pumping in urban area." *European Space Agency, (Special Publication) ESA SP Proceedings of Fringe 2005 Workshop. n 610 February 2006. 6p*.

Eineder, M., Runge, H., Boerner, E., Bamler, R., Adam, N., Schattier, B., Breit, H., and Suchandt, S. (2004). "SAR interferometry with TERRASAR-X." *European Space Agency, (Special Publication) ESA SP Proceedings of FRINGE 2003 Workshop*, 289-294.

ESA. (2007) [online] Available http://envisat.esa.int/handbooks/asar/CNTR5-2.htm, March 31, 2007.

Fang, Z., Debao, M., and Huaining, P. "A new baseline estimation approach based on the periodic interferometric phase." *Student Conference on Engineering Sciences and Technology, SCONEST 2004 Student Conference on Engineering Sciences and Technology, SCONEST 2004 - An International Multi-topic Conference by IEEE Student Branches at Jinnah University for Women, NED University of Engineering 2004*, 77-80.

Farina, P., Colombo, D., Fumagalli, A., Marks, F., and Moretti, S. (2006). "Permanent Scatterers for landslide investigations: outcomes from the ESA-SLAM project." *Engineering Geology*, 88(3-4), 200-217.

Ferretti, A., Bianchi, M., Prati, C., and Rocca, F. (2005). "Higher-order permanent scatterers analysis." *Eurasip Journal on Applied Signal Processing*, 2005(20), 3231-3242.

Ferretti, A., Colesanti, C., Perissin, D., Prati, C., and Rocca, F. (2004). "Evaluating the effect of the observation time on the distribution of sar permanent scatterers." *European Space Agency, (Special Publication) ESA SP Proceedings of FRINGE 2003 Workshop*, 167-172.

Ferretti, A., Prati, C., and Rocca, F. "Analysis of Permanent Scatterers in SAR interferometry." *International Geoscience and Remote Sensing Symposium (IGARSS). v 2 2000*, 761-763.

Ferretti, A., Prati, C., and Rocca, F. (2000). "Nonlinear subsidence rate estimation using permanent scatterers in differential SAR interferometry." *IEEE Transactions on Geoscience & Remote Sensing*, 38(5), 2202-2212.

Ferretti, A., Prati, C., and Rocca, F. (2001). "Permanent scatterers in SAR interferometry." *IEEE Transactions on Geoscience & Remote Sensing*, 39(1), 8-20.

Ferretti, A., Savio, G., Barzaghi, R., Borghi, A., Musazzi, S., Novali, F., Prati, C., and Rocca, F. (2007). "Submillimeter accuracy of InSAR time series: Experimental validation." *IEEE Transactions on Geoscience & Remote Sensing*, 45(5), 1142-1153.

Flynn, T.J. (1997). “Two dimensional phase unwrapping with minimum weighted discontinuity.” *Journal of the Optical Society of America A*., 14(10), 2692-2701.

Fornaro, G., Franceschetti, G., and Lanari, R. (1996). "Interferometric SAR phase unwrapping using Green's formulation." *IEEE Transactions on Geoscience & Remote Sensing*, 34(3), 720-727.

Fornaro, G., Franceschetti, G., Lanari, R. and Sansosti, E. (1996). “Robust phase-unwrapping techniques: a comparison.”*Journal of the Optical Society of America A.*, 13(12), 2355-2366.

Gens, R. (2003). "Two-dimensional phase unwrapping for radar interferometry: developments and new challenges." *International Journal of Remote Sensing*, 24(4), 703 - 710.

Ghiglia D.C. and Pritt, M.D. (1998). “Two-dimensional phase unwrapping: theory, algorithms and software.” John Wiley and Sons Inc., New York.

Ghiglia, D.C. and Romero, L.A. (1994). “Robust two-dimensional weighted and unweighted phase unwrapping that uses fast transforms and iterative methods.”, *Journal of the Optical Society of America A.*, 11(1),107-117.

Goldstein, R.M., Zebker, H.A. and Werner, C.L. (1988). “Satellite radar interferometry: Two-dimensional phase unwrapping.” *Radio Science*, 23(4),713-720.

Goyal, R. K., and Verma, A. K. (1996). "Mathematical formulation for estimation of baseline in synthetic aperture radar interferometry." *Sadhana-Academy Proceedings in Engineering Sciences*, 21(pt), 511-522.

Hahn Chul, J., and Min, K.-D. "Observing coal mining subsidence from JERS-1 permanent scatterer analysis." *International Geoscience and Remote Sensing Symposium (IGARSS) 25th Anniversary IGARSS 2005: IEEE International Geoscience and Remote Sensing Symposium*, 4578-4581.

Hanssen, R., and Bamler, R. (1999). "Evaluation of interpolation kernels for SAR interferometry." *IEEE Transactions on Geoscience & Remote Sensing*, 37(1), 318-321.

Hanssen, R. F. (2001). *Radar interferometry : data interpretation and error analysis*, Kluwer Academic, Dordrecht ; Boston.

Infoterra. (2007) [Online] Available http://www.infoterra-global.com/ September, 12, 2007.

Jensen, J. R. (2000). *Remote sensing of the environment : an earth resource perspective*, Pearson Prentice Hall, Upper Saddle River, NJ.

Jung, H. C., Kim, S.-W., Jung, H.-S., Min, K. D., and Won, J.-S. (2007). "Satellite observation of coal mining subsidence by persistent scatterer analysis." *Engineering Geology*, 92(1-2), 1-13.

Just, D. and Bamler, R. (1994). “Phase statistics of interferograms with applications to synthetic aperture radar.” *Journal of the Optical Society of America A*., 33(20), 4361-4368.

Kircher, M., Hoffmann, J., Roth, A., Kampes, B., Adam, N., and Neugebauer, H. J. "Application of permanent scatterers on mining-induced subsidence." *European Space Agency, (Special Publication) ESA SP Proceedings of FRINGE 2003 Workshop*, 157-160.

Madsen, S. N. and Zebker, H.A. (1999). “Synthetic aperture radar interferometry: Principles and applications.” *Manual of Remote Sensing*, 3(6), Artech House, Boston, MA.

Maini, A. K. and Agrawal, V. (2007). *Satellite technology : principles and applications*, John Wiley, Chichester, England ; Hoboken, NJ.

Mallorqui, J. J., Blanco, P., Sanz-Marcos, J., Duque, S., and Navarrete, D. "Application of the Coherent Pixels Technique (CPT) to large ERS and ENVISAT SAR images for deformation series retrieval." *European Space Agency, (Special Publication) ESA SP Proceedings of Fringe 2005 Workshop. n 610 February 2006. 6p*.

Meisina, C., Zucca, F., Fossati, D., Ceriani, M., and Allievi, J. (2006). "Ground deformation monitoring by using the Permanent Scatterers Technique: The example of the Oltrepo Pavese (Lombardia, Italy)." *Engineering Geology*, 88(3-4), 240-259.

Perissin, D., Prati, C., Rocca, F., and Ferretti, A. "ERS-ENVISAT permanent scatterers." *International Geoscience and Remote Sensing Symposium (IGARSS) 2004 IEEE International Geoscience and Remote Sensing Symposium Proceedings: Science for Society: Exploring and Managing a Changing Planet. IGARSS 2004*, 985-988.

Ren, K., Shi, X., Wang, F., and Prinet, V. (2003). "Comparison of Satellite Baseline Estimation Methods for Interferometry Applications." *International Geoscience and Remote Sensing Symposium (IGARSS)*, 3821-3823.

Riedmann, M., and Haynes, M. "Monitoring pipelines and oil & gas infrastructure using satellite radar interferometry." (2005). *16th International Conference on Pipeline Protection Papers presented at: 16th International Conference on pipeline Protection*, 367-375.

Rosen, P. A., Hensley, S., Joughin, I. R., Li, F. K., Madsen, S. N., Rodriguez, E., and Goldstein, R. M. (2000). "Synthetic aperture radar interferometry." *Proceedings of the IEEE*, 88(3), 333-382.

Scharroo, R., Visser, P., and Peacock, N. "ERS orbit determination and gravity field model tailoring: Recent developments." (2000). *European Space Agency, (Special Publication) ESA SP*, 715-725.

Schneider, R. Z., Papathanassiou, K., Hajnsek, I., and Moreira, A. "Coherent scatterers in urban areas: Characterisation and information extraction." *European Space Agency, (Special Publication) ESA SP Proceedings of Fringe 2005 Workshop. n 610 February 2006. 6p*.

Seymour, M.S. and Cumming, I.G. (1996). “An iterative algorithm for ERS baselineestimation.” *FRINGE*.

Skolnik, M. I. (1962). *Introduction to radar systems*, McGraw-Hill, New York .

Small, D., Werner, C., and Nuesch, D. (1993). "Baseline modelling for ERS-1 SAR interferometry." *International Geoscience and Remote Sensing Symposium (IGARSS). Publ by IEEE, IEEE Service Center, Piscataway, NJ, USA*, 1204-1206.

Stirbys, A. F., Radwanski, Z. R., Proctor, R. J., and Escandon, R. F. (1999). "Los Angeles metro rail project - geologic and geotechnical design and construction constraints." *Engineering Geology*, 51(3), 203-224.

Walter, D., Hoffmann, J., Kampes, B., and Sroka, A. (2005). "Radar interferometric analysis of mining induced surface subsidence using permanent scatterer." *European Space Agency, (Special Publication) ESA SP Proceedings of the 2004 Envisat and ERS Symposium*, 887-894.

Wasowski, J., Bovenga, F., Casarano, D., Nutricato, R., and Refice, A. "Application of PSI techniques to landslide investigations in the caramanico area (Italy): Lessons learnt." *European Space Agency, (Special Publication) ESA SP Proceedings of Fringe 2005 Workshop. n 610 February 2006. 6p*.

Werner, C., Wegmuller, U., Strozzi, T., and Wiesmann, A. "Interferometric Point Target Analysis for Deformation Mapping." *International Geoscience and Remote Sensing Symposium (IGARSS)*, 4362-4364.

Yue, H., Hanssen, R., Van Leijen, F., Marinkovic, P., Ketelaar, G., Guo, H., and Chen, Q. "Land subsidence monitoring in city area by time series interferometric SAR data." *International Geoscience and Remote Sensing Symposium (IGARSS) 25th Anniversary IGARSS 2005: IEEE International Geoscience and Remote Sensing Symposium*, 4590-4592.

Zebker, H. A., and Goldstein, R. M. (1986). "Topographic mapping from interferometric synthetic aperture radar observations." *Journal of Geophysical Research*, 91(B5), 4993-4999.

Appendix A

Histograms and Normal Probability Plots For Deformation Rates

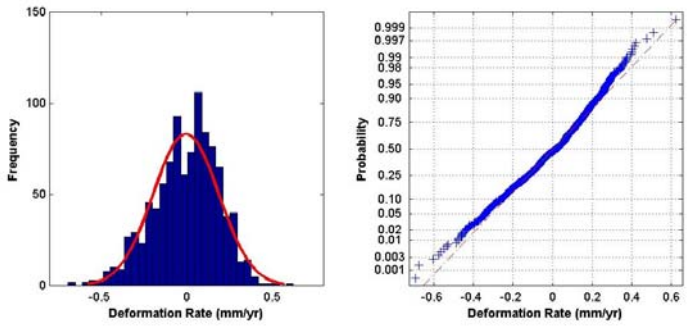

(a)

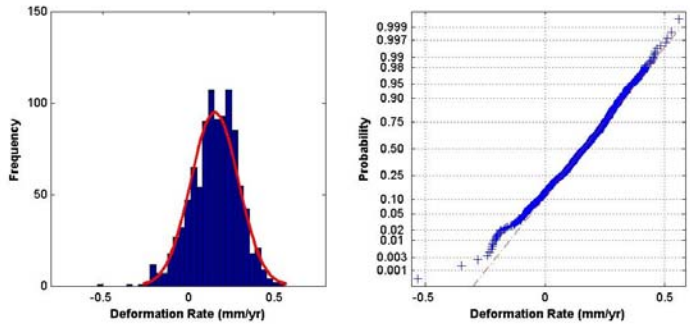

(b)

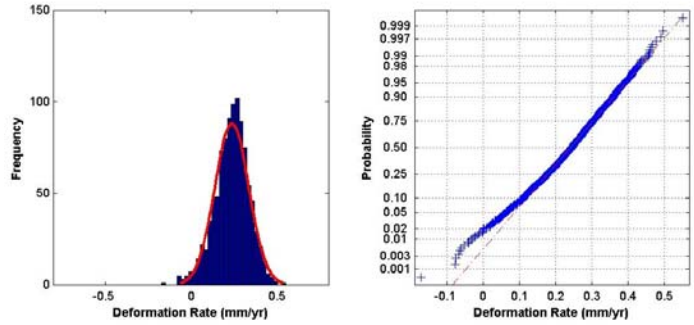

(c)

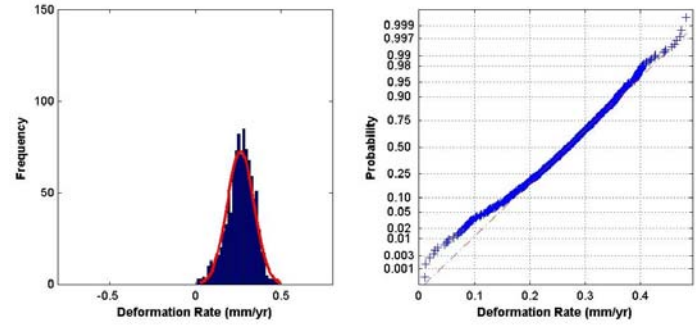

(d)

Figure A.1 Histogram and corresponding normal probability plot of deformation rate for point target #16997, as inferred from one thousand datasets containing (a)15 pairs, (b) 25 pairs, (c) 35 pairs and (d) 40 pairs.

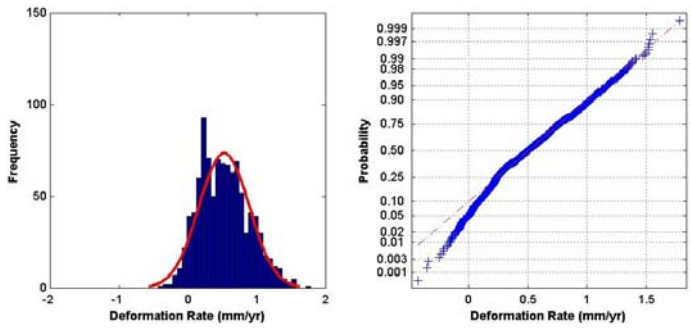

(a)

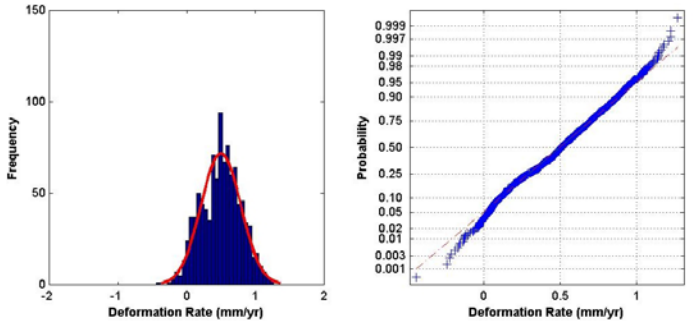

(b)

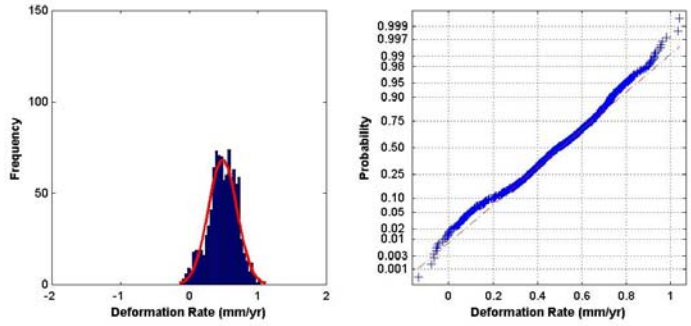

(c)

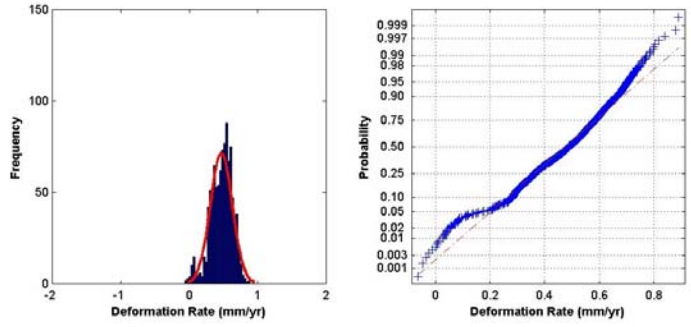

(d)

Figure A.2 Histogram and corresponding normal probability plot of deformation rate for point target #19615, as inferred from one thousand datasets containing (a)15 pairs, (b) 25 pairs, (c) 35 pairs and (d) 40 pairs.

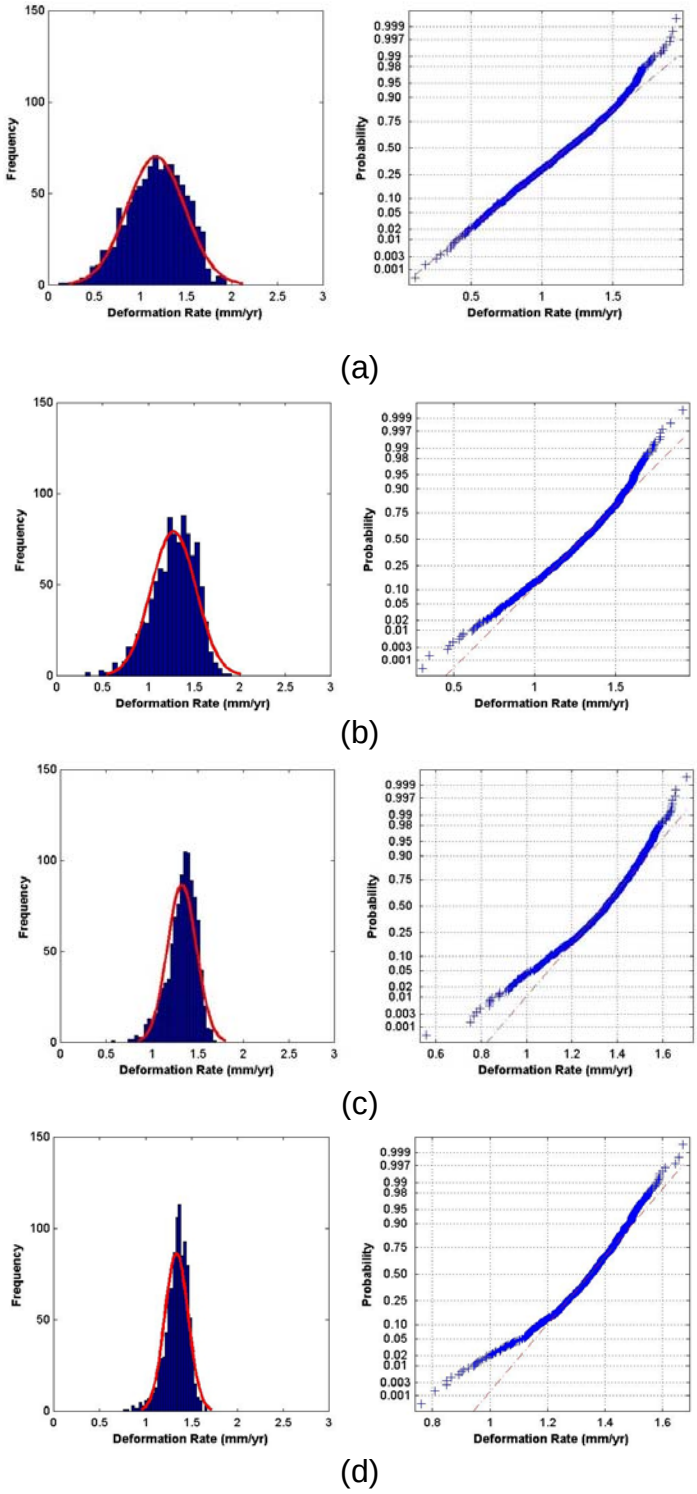

Figure A.3 Histogram and corresponding normal probability plot of deformation rate for point target #34314, as inferred from one thousand datasets containing (a)15 pairs, (b) 25 pairs, (c) 35 pairs and (d) 40 pairs.

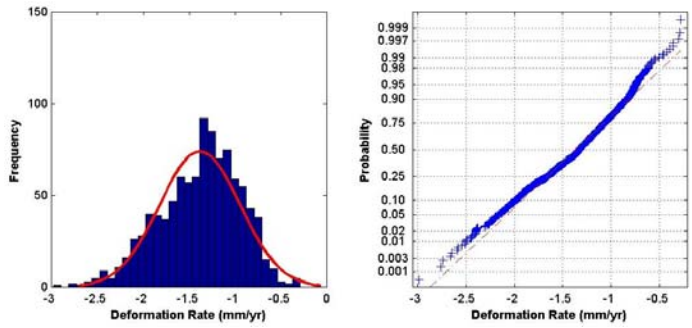

(a)

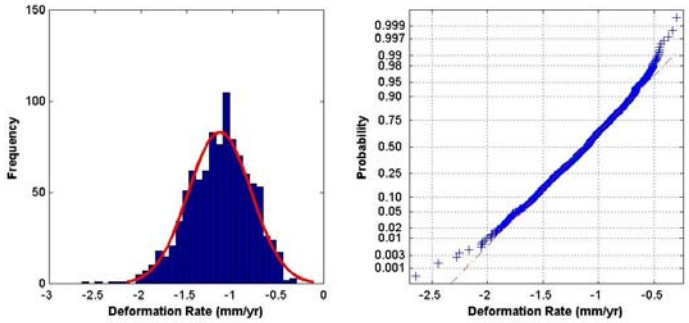

(b)

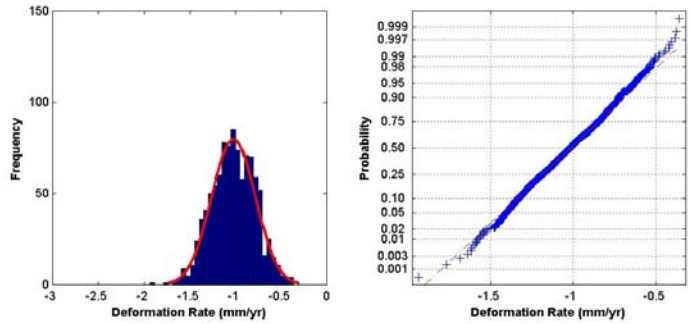

(c)

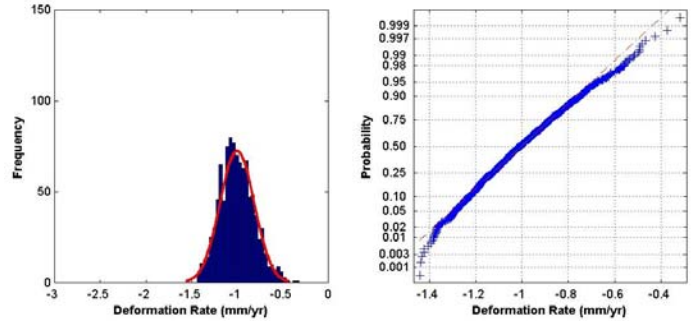

(d)

Figure A.4 Histogram and corresponding normal probability plot of deformation rate for point target #43046, as inferred from one thousand datasets containing (a)15 pairs, (b) 25 pairs, (c) 35 pairs and (d) 40 pairs.

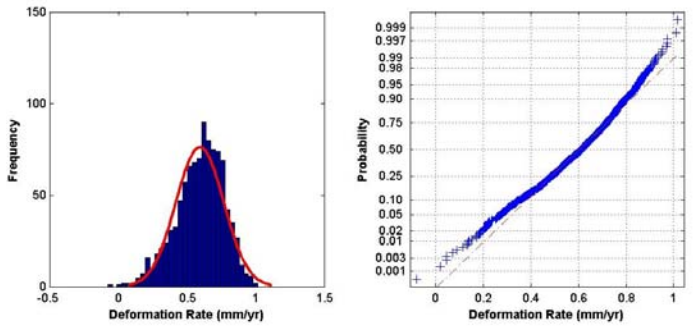

(a)

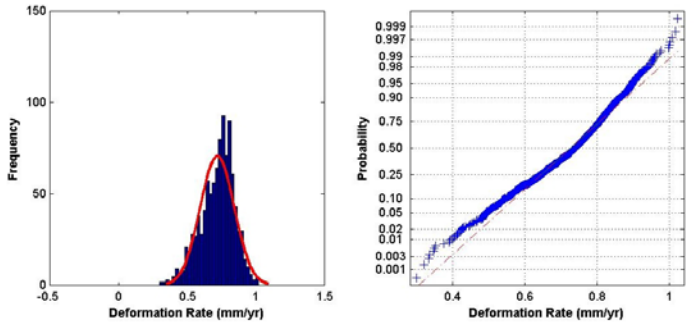

(b)

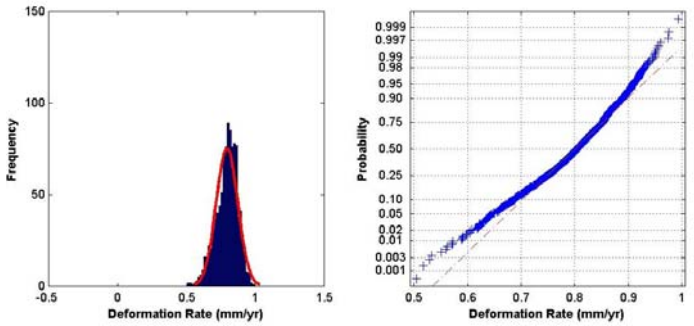

(c)

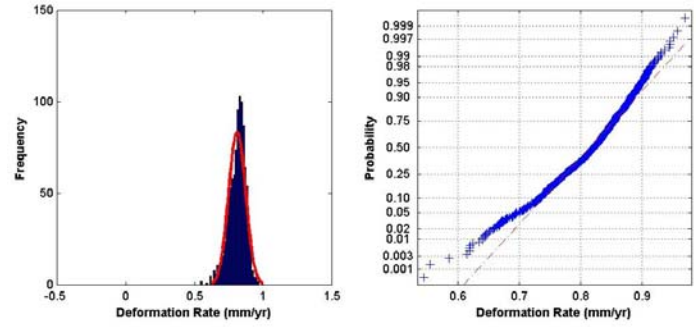

(d)

Figure A.5 Histogram and corresponding normal probability plot of deformation rate for point target #47205, as inferred from one thousand datasets containing (a)15 pairs, (b) 25 pairs, (c) 35 pairs and (d) 40 pairs.

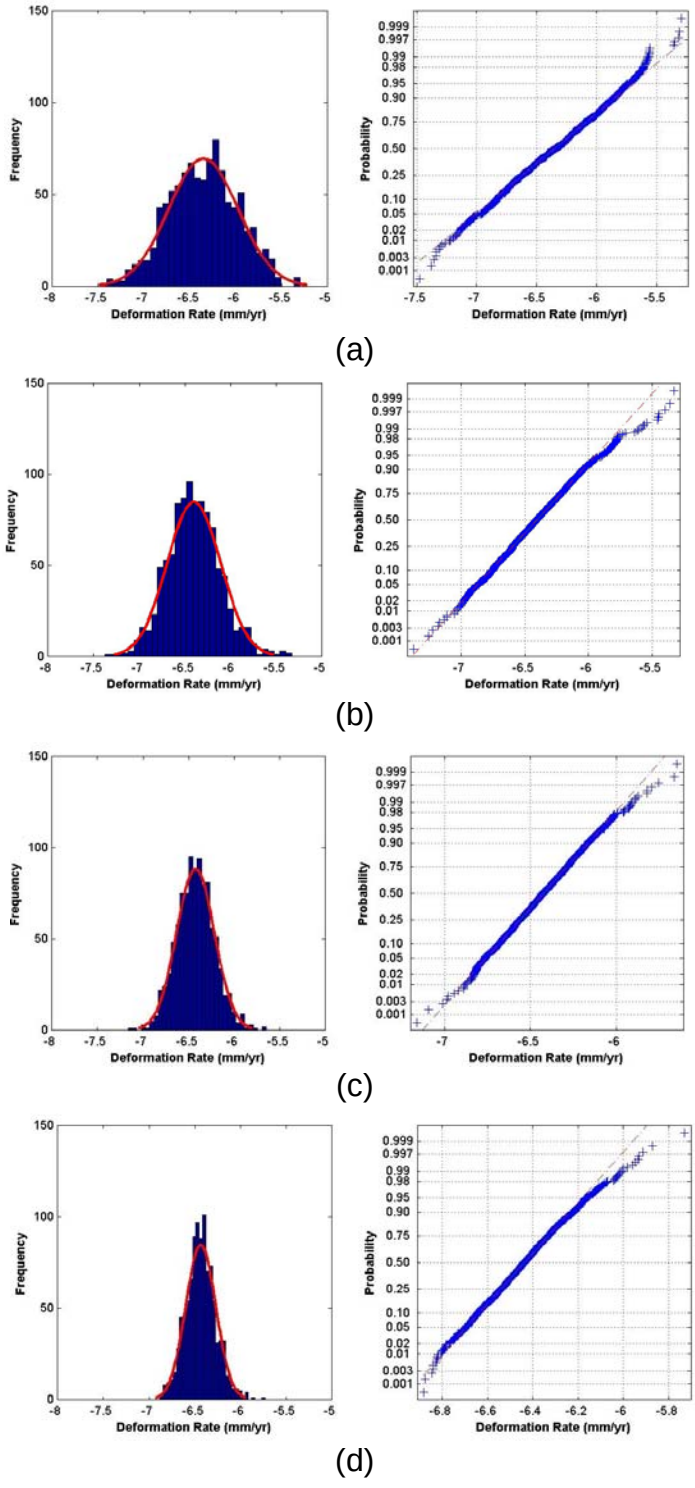

Figure A.6 Histogram and corresponding normal probability plot of deformation rate for point target #47217, as inferred from one thousand datasets containing (a)15 pairs, (b) 25 pairs, (c) 35 pairs and (d) 40 pairs.

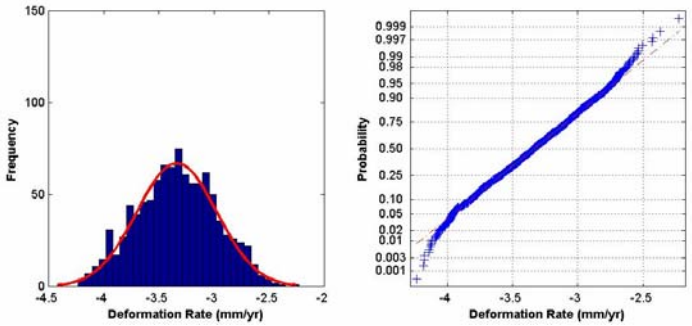

(a)

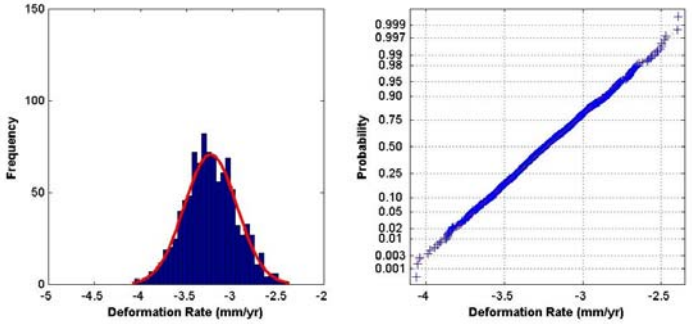

(b)

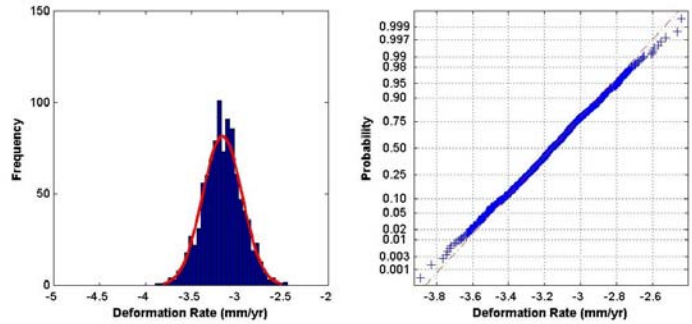

(c)

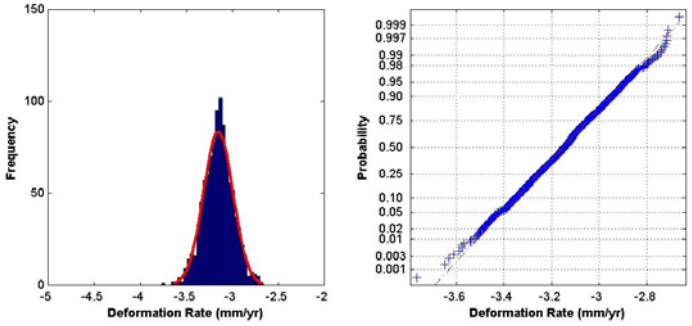

(d)

Figure A.7 Histogram and corresponding normal probability plot of deformation rate for point target #47238, as inferred from one thousand datasets containing (a)15 pairs, (b) 25 pairs, (c) 35 pairs and (d) 40 pairs.

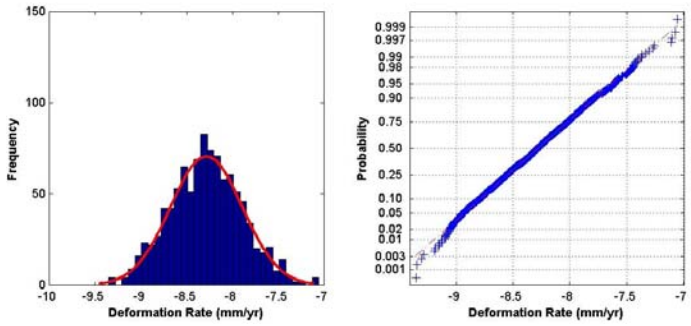

(a)

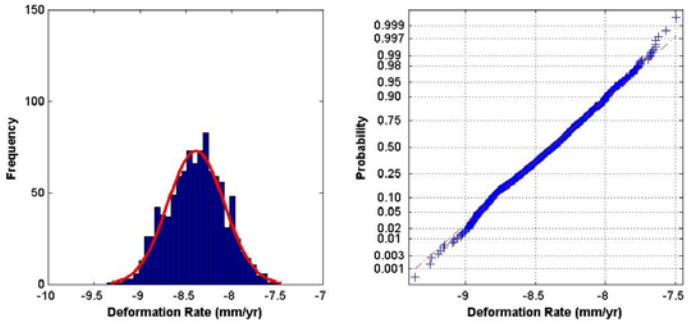

(b)

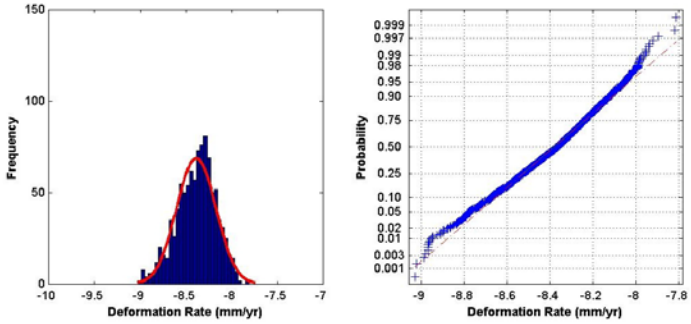

(c)

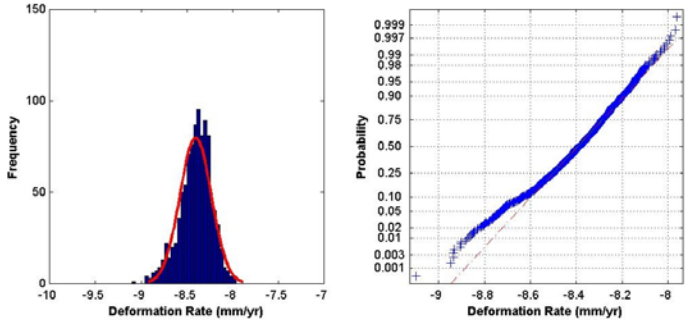

(d)

Figure A.8 Histogram and corresponding normal probability plot of deformation rate for point target #58096, as inferred from one thousand datasets containing (a)15 pairs, (b) 25 pairs, (c) 35 pairs and (d) 40 pairs.

Appendix B

Histograms and Normal Probability Plots For Deformation Rate Uncertainties (U_G)

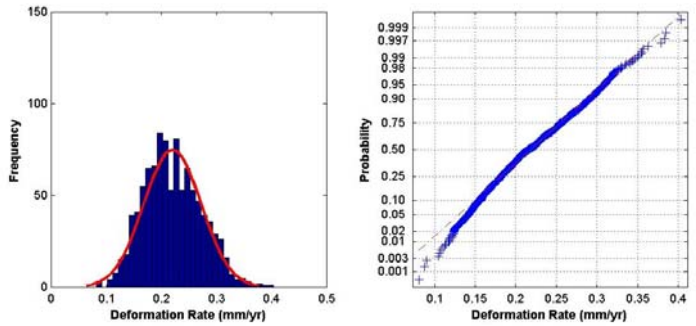

(a)

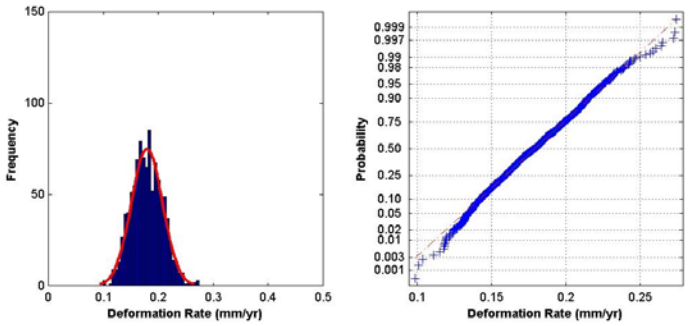

(b)

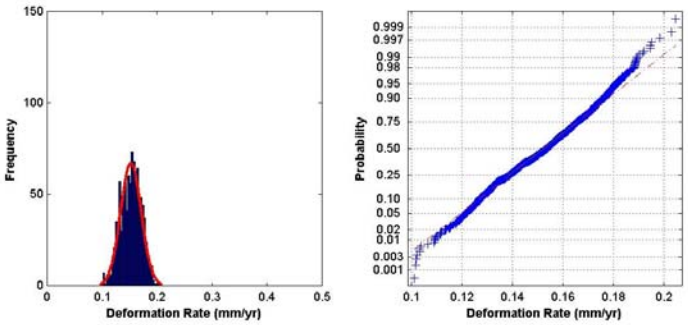

(c)

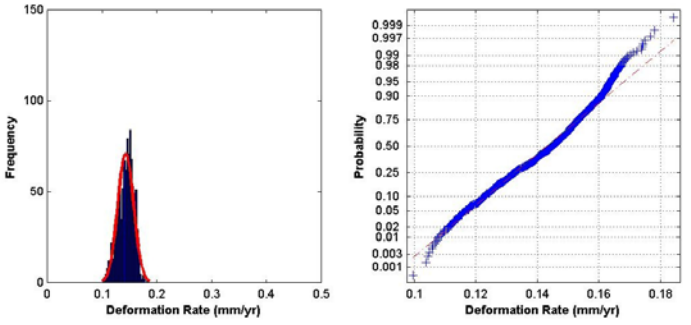

(d)

Figure B.1 Histogram and corresponding normal probability plot of deformation rate uncertainty (U_G) for point target #16997, as inferred from one thousand datasets containing (a)15 pairs, (b) 25 pairs, (c) 35 pairs and (d) 40 pairs.

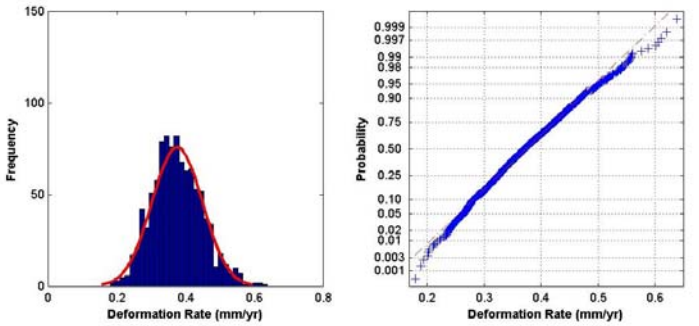

(a)

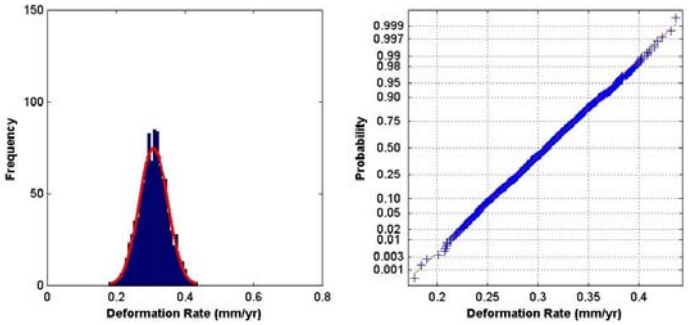

(b)

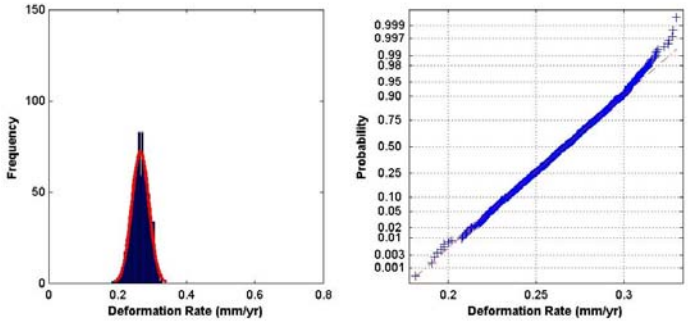

(c)

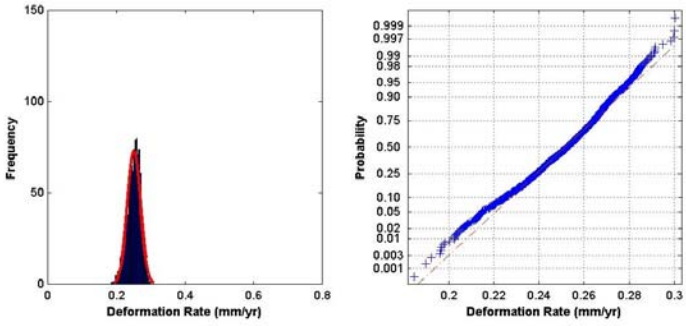

(d)

Figure B.2 Histogram and corresponding normal probability plot of deformation rate uncertainty (U_G) for point target #19615, as inferred from one thousand datasets containing (a)15 pairs, (b) 25 pairs, (c) 35 pairs and (d) 40 pairs.

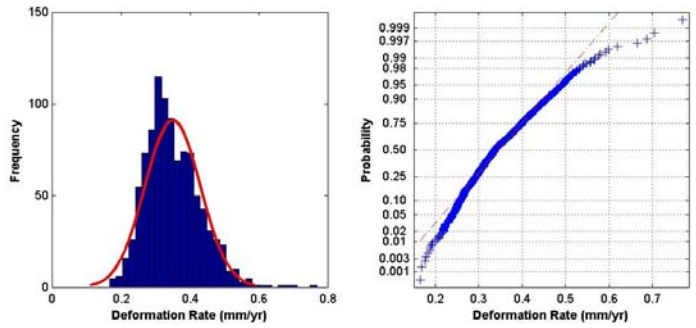

(a)

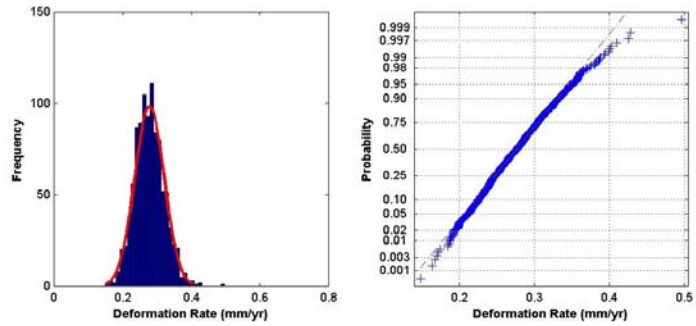

(b)

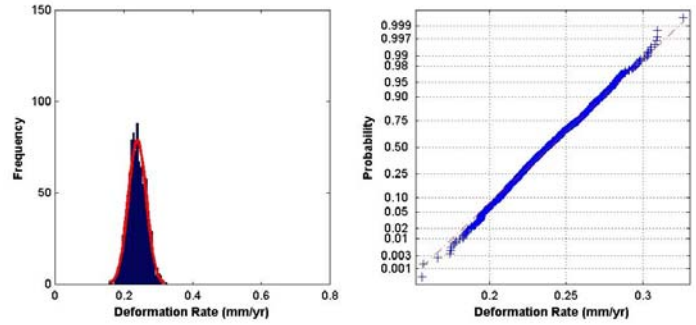

(c)

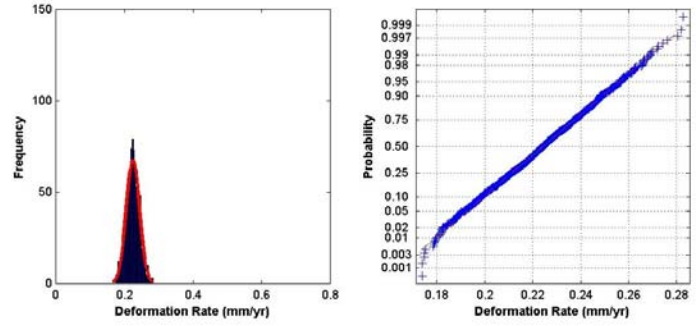

(d)

Figure B.3 Histogram and corresponding normal probability plot of deformation rate uncertainty (U_G) for point target #34314, as inferred from one thousand datasets containing (a)15 pairs, (b) 25 pairs, (c) 35 pairs and (d) 40 pairs.

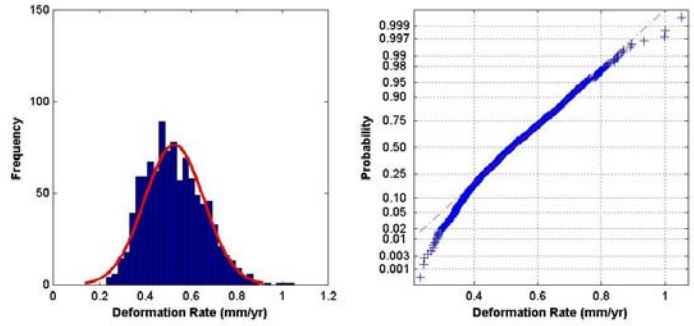

(a)

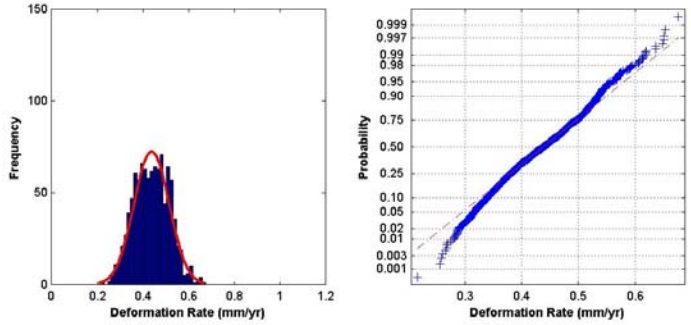

(b)

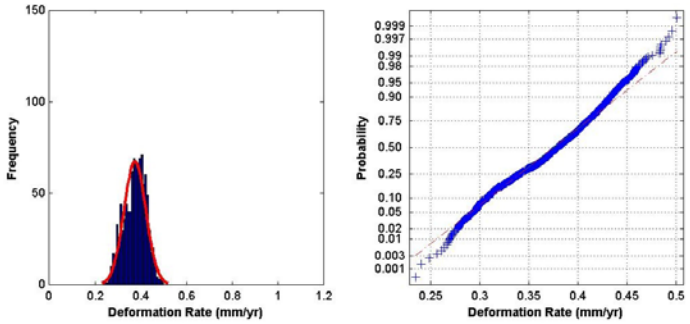

(c)

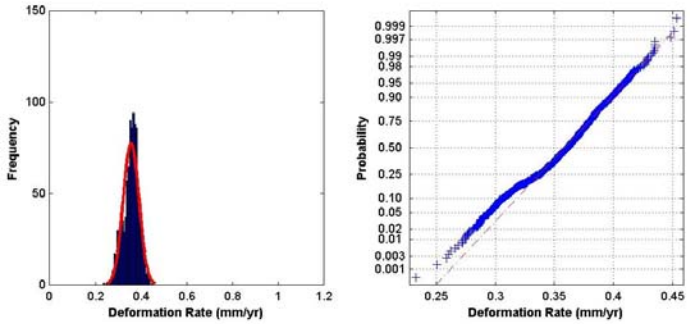

(d)

Figure B.4 Histogram and corresponding normal probability plot of deformation rate uncertainty (U_G) for point target #43046, as inferred from one thousand datasets containing (a)15 pairs, (b) 25 pairs, (c) 35 pairs and (d) 40 pairs.

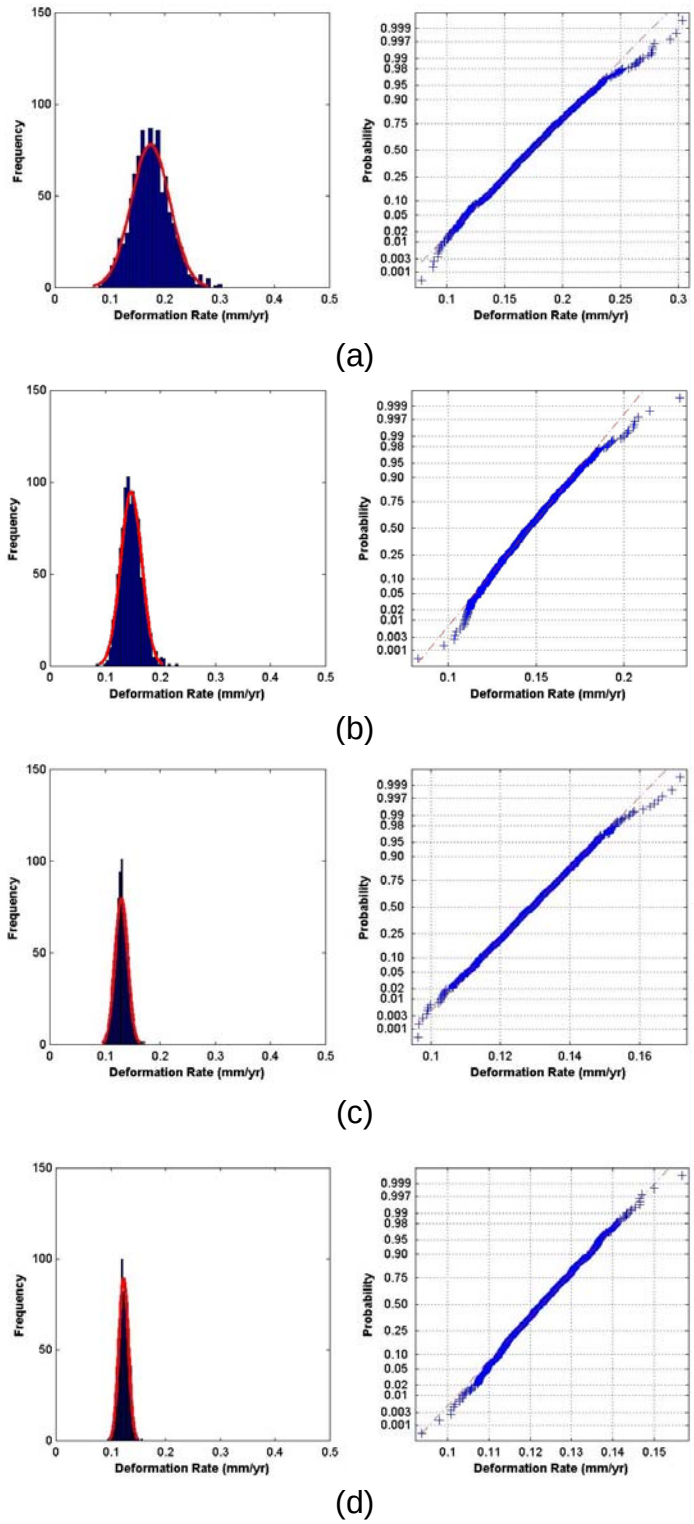

Figure B.5 Histogram and corresponding normal probability plot of deformation rate uncertainty (U_G) for point target #47205, as inferred from one thousand datasets containing (a)15 pairs, (b) 25 pairs, (c) 35 pairs and (d) 40 pairs.

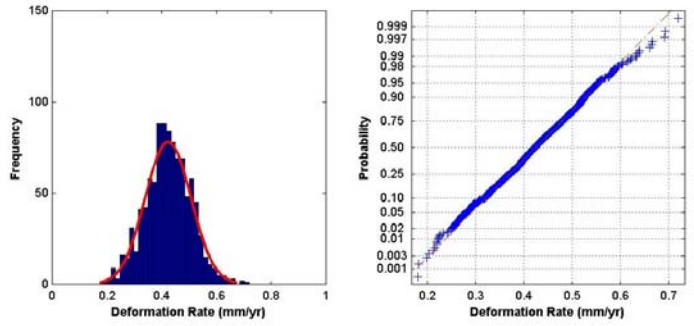

(a)

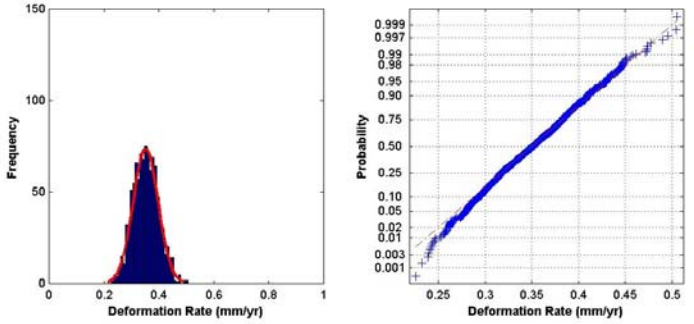

(b)

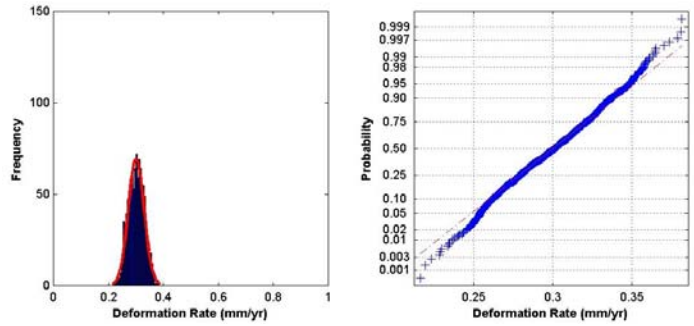

(c)

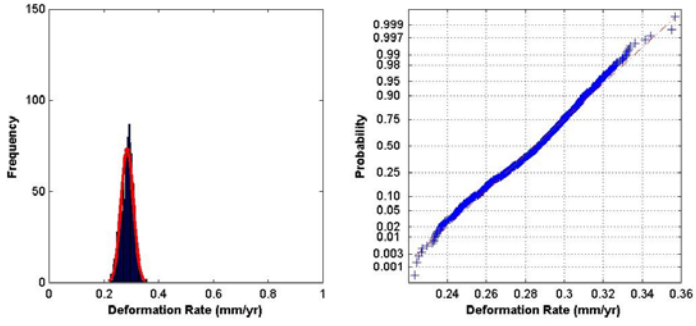

(d)

Figure B.6 Histogram and corresponding normal probability plot of deformation rate uncertainty (U_G) for point target #47217, as inferred from one thousand datasets containing (a)15 pairs, (b) 25 pairs, (c) 35 pairs and (d) 40 pairs.

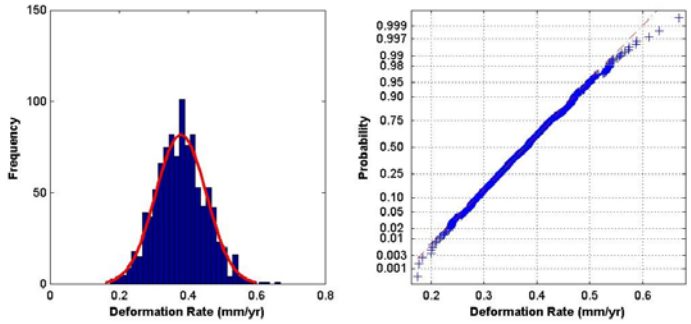

(a)

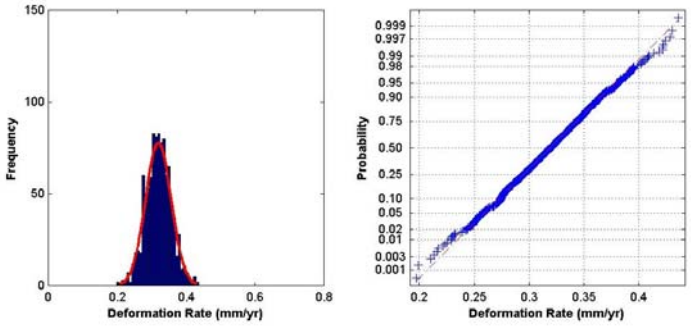

(b)

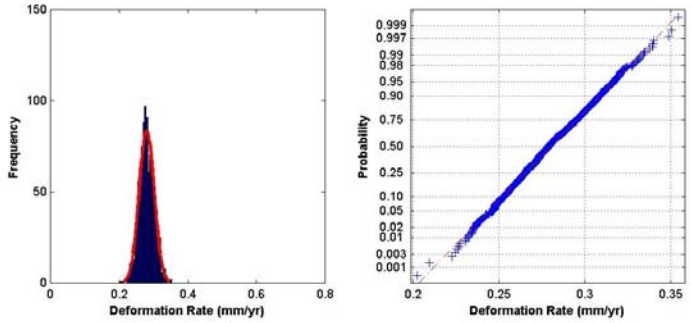

(c)

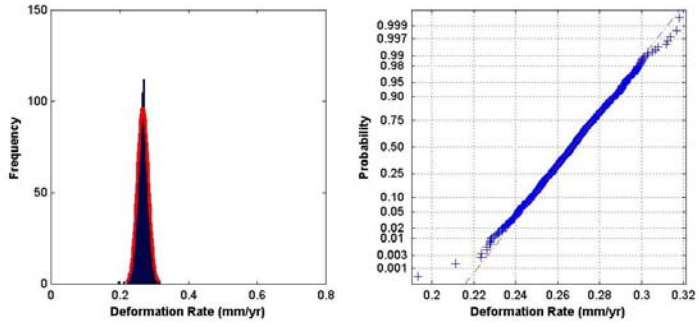

(d)

Figure B.7 Histogram and corresponding normal probability plot of deformation rate uncertainty (U_G) for point target #47238, as inferred from one thousand datasets containing (a)15 pairs, (b) 25 pairs, (c) 35 pairs and (d) 40 pairs.

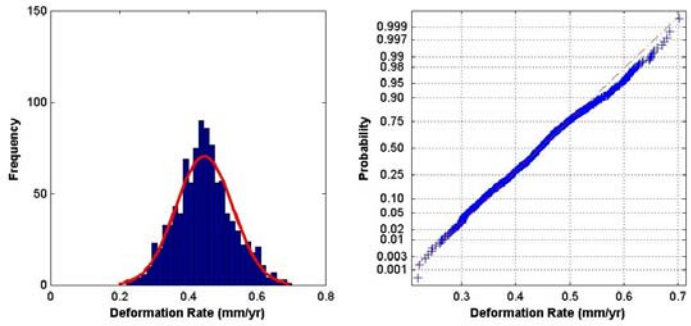

(a)

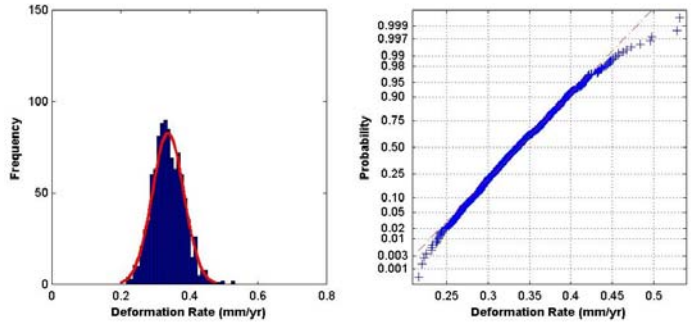

(b)

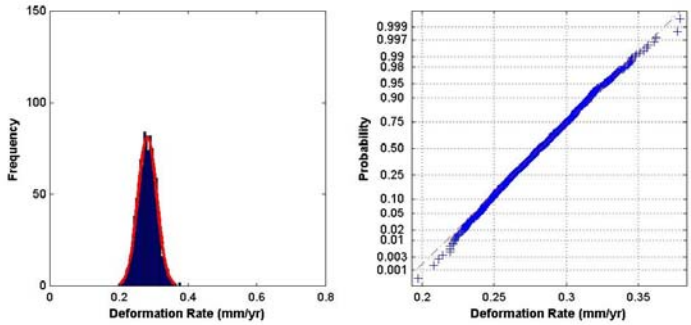

(c)

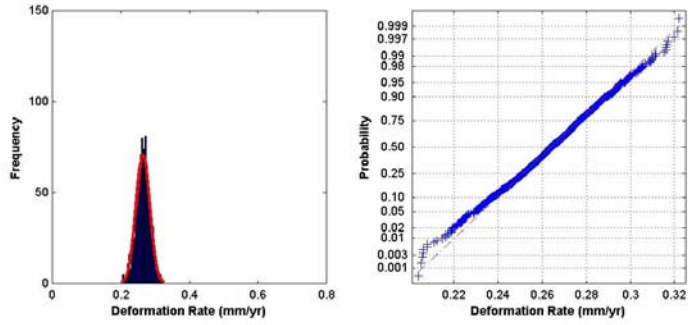

(d)

Figure B.8 Histogram and corresponding normal probability plot of deformation rate uncertainty (U_G) for point target #58096, as inferred from one thousand datasets containing (a)15 pairs, (b) 25 pairs, (c) 35 pairs and (d) 40 pairs.

VITA

Deepak Vishwanath Manjunath was born on August 1st, 1977 in the city of Dharwad, Karnataka, India. In 1999, he obtained a Bachelor of Engineering degree in the field of Civil Engineering from the Sardar Vallabhbhai Regional College of Engineering and Technology, Surat, Gujarat, India.

He obtained an MS degree in Transportation Engineering from the University of Missouri-Columbia in 2002. He obtained an MS degree in Geology in 2008 from the University of Missouri, Columbia, the work for which he pursued while simultaneously working on his PhD degree in the field of Geotechnical Engineering.